ADVERTIMENT. L'accés als continguts d'aquesta tesi queda condicionat a l'acceptació de les condicions d'ús establertes per la següent llicència Creative Commons: http://cat.creativecommons.org/?page_id=184

ADVERTENCIA. El acceso a los contenidos de esta tesis queda condicionado a la aceptación de las condiciones de uso establecidas por la siguiente licencia Creative Commons: http://es.creativecommons.org/blog/licencias/

WARNING. The access to the contents of this doctoral thesis it is limited to the acceptance of the use conditions set by the following Creative Commons license: https://creativecommons.org/licenses/?lang=en

Department of Electronic Engineering

ADVANCED NANOSCALE CHARACTERIZATION CONCEPTS FOR COPPER INTERCONNECTION TECHNOLOGIES

Ph.D. Thesis written by
Tobias Berthold

Under the supervision of
Günther Benstetter and Rosana Rodríguez Martínez

The research program was carried out in collaboration
with Deggendorf Institute of Technology,
Deggendorf, Germany

Bellaterra, June 2017

Department of Electronic Engineering

The undersigned, Dr. Günther Benstetter, professor of the Faculty of Electrical Engineering, Media Technology and Computer Science of the Deggendorf Institute of Technology and Dra. Rosana Rodríguez Martínez, professor of the Department of Electronic Engineering of the Universidad Autònoma de Barcelona,

Certify

That the thesis entitled "**Advanced nanoscale characterization concepts for copper interconnection technologies"** has been written by the PhD candidate Tobias Berthold under their supervision in fulfillment of the requirements for the PhD degree of Electrical and Telecommunication Engineering.

Dr. Günther Benstetter

Dra. Rosana Rodríguez Martínez

Tobias Berthold

Bellaterra, June 2017

Acknowledgement

I would like to thank Prof. Günther Benstetter and Prof. Werner Frammelsberger for their constant support throughout my PhD studies at the Deggendorf Institute of Technology. I'm grateful for their guidance, ideas and constructive criticism and their provision of the resources for my research.

I owe my heartfelt gratitude to my director at the Universitat Autònoma de Barcelona, Prof. Rosana Rodríguez, for supervising this thesis and the everlasting support along the stony path of doing a PhD. I also thank Prof. Montserrat Nafria and the people of Electronic Engineering Department who gave me the opportunity to do a PhD and who supported my work.

I am grateful to all my colleagues at the Deggendorf Institute of Technology and specifically at the Faculty of Electrical, Media and Computer Engineering, who supported me in many respects. My particular thanks go to my colleagues of the research group Micro- and Nanoanalytics and the Institute for Quality and Material Analysis, Prof. Raimund Förg, Alexander Hofer, Manuel Bogner, Heiko Ranzinger and Edgar Lodermeier, who were a constant source of support.

Ganz herzlicher Dank gebührt meinen Eltern, Alois und Lydia Berthold, die in jeder Hinsicht die Grundsteine für meinen Weg gelegt haben und mich immer in meinem Vorhaben unterstützt haben.

Abschließend möchte ich meiner Freundin Maria danken, dass sie mir in den Jahren immer zur Seite gestanden ist und mich an jedem Tag zur jeder Zeit unterstützt hat.

This work was partly supported by "Bundesministerium für Bildung und Forschung" and "Bayerische Staatsministerium für Umwelt und Verbraucherschutz"

Contents

Publications related to this thesis i

1. Introduction 1
1.1 Copper 1
1.2 Thermosonic Wire Bonding 2
1.3 Copper oxide 6
1.4 Oxidation protection of copper surfaces 8
1.5 Characterization techniques 11

2. Aims of the work 16

3. Experimental 18
3.1 Atomic Force Microscopy 18
3.1.1 PeakForce Tapping (Pulsed Force Mode) 20
3.1.2 Kelvin Probe Force Microscopy 22
3.1.3 Dynamic Chemical Force Microscopy 25
3.1.4 Torsional Resonance Tunneling Atomic Force Microscopy 27
3.2 Scanning Electron Microscopy 28
3.2.1 Energy Dispersive X-ray Spectroscopy 31
3.2.2 Electron Backscatter Diffraction 33
3.3 Fourier Transform Infrared Spectroscopy 35

4. Nanoscale characterization of copper oxide by KPFM 38
4.1 Experimental 39
4.2 Evaluation of PeakForce Kelvin Probe Force Microscopy 44
4.3 Correlation of topographic features and oxide type at the nanoscale 47
4.4 Summary 51

5. Numerical study of hydrodynamic forces for AFM operations in liquid 52
5.1 Numerical Model 54
5.2 Cantilever Model 57
5.3 Fluid Model 61
5.4 Results and Discussion 65
5.4.1 Evaluation of the sensor dynamics simulation model 67
5.4.2 Sensor dynamics in ultrapure water 68

5.4.3 Sensor dynamics in an ethanol-water mixture 73
5.5 Summary 78

6. Nanoscale characterization of Self-Assembled Monolayer on Cu 80
6.1 Experimental 81
6.2 Characterization of virgin SAM film on Cu 83
6.3 Advanced investigation of the SAM film degradation 86
6.4 Summary 90

7. Protective nanometer films on copper 91
7.1 Experimental 92
7.2 Structural and elemental analysis 95
7.3 Analysis at the nanoscale of the protective Pt layer 98
7.4 Nanoscale characterization of the protective C layer 101
7.5 Decrease of the C layer thickness 104
7.6 Summary 111

8. Oxidation and microstructural study of Cu free air ball formed in air 112
8.1 Experimental 113
8.2 Surface morphology and elemental analysis of FAB 114
8.3 Nanoscale characterization of the internal FAB structure 123
8.4 Summary 128

9. Conclusion 130

References 133

Publications related to this thesis

- T. Berthold, G. Benstetter, W. Frammelsberger, R. Rodríguez, M. Nafría, Nanoscale characterization of copper oxide films by Kelvin Probe Force Microscopy, Thin Solid Films 584 (2015) 310–315.
- T. Berthold, G. Benstetter, W. Frammelsberger, R. Rodríguez, M. Nafría, Nanoscale characterization of CH3-terminated Self-Assembled Monolayer on copper by advanced scanning probe microscopy techniques, Applied Surface Science 356 (2015) 921–926.

Other publications

- W. Ni, Q. Yang, H. Fan, L. Liu, T. Berthold, G. Benstetter, D. Liu, Ordered arrangement of irradiation-induced defects of polycrystalline tungsten irradiated with low-energy hydrogen ions, Journal of Nuclear Materials 464 (2015) 216–220.
- Q. Yang, H. Fan, W. Ni, L. Liu, T. Berthold, G. Benstetter, D. Liu, Y. Wang, Observation of interstitial loops in He+ irradiated W by conductive atomic force microscopy, Acta Materialia 92 (2015) 178–188.

Contributions to conferences

- T. Berthold, G. Benstetter, W. Frammelsberger, R. Rodríguez, M. Nafría: Nanoscale copper oxide characterization with Kelvin Probe Force Microscopy. The 7th International Conference on Technological Advances of Thin Films & Surface Coatings (THINFILMS2014), Chongqing, China, 2014
- T. Berthold, G. Benstetter, W. Frammelsberger, R. Rodríguez, M. Nafría: Characterization of Self-Assembled Monolayers on Copper by Scanning Probe Microscopy. 16th International Conference on Thin Films (ICTF16), Dubrovnik, Croatia, 2014
- T. Berthold, G. Benstetter, W. Frammelsberger, R. Rodríguez, M. Nafría, R. Foerg: "Analysis of copper oxide films by combined scanning microscopy", 6th International Conference on Technological Advances of Thin Films & Surface Coatings, Juli 2012, Singapore
- Alexander Hofer, Tobias Berthold, Anton Greppmair, Günther Benstetter, Martin S. Brandt: "Nanoscale characterization of laser-sintered Ge nanoparticle layers", 2nd International Conference on Functional Integrated Nano Systems, nanoFIS, June 2016, Graz Austria

- Alexander Hofer, Tobias Berthold, Anton Greppmair, Martin S. Brandt, Günther Benstetter, “Nanoscale electrical conductivity of laser-sintered Ge nanoparticle layers”, 8th International Conference on Technological Advances of Thin Films and Surface Coatings, ThinFilms 2016, Singapore
- G. Benstetter, A. Hofer, T. Berthold, „Selected Atomic Force Microscopy Methods for the Electrical Characterization of Thin Films and Devices”, 4th International Advances in Applied Physics and Materials Science Congress & Exhibition (APMAS), Fethiye, Turkey, 2014

1. Introduction

1.1 Copper

In 1999 Lloyd mentioned, that copper (Cu) was, is and will be the future for the semiconductor industry [1,2]. With this statement, he already realized that the standard aluminum (Al) metallization cannot satisfy the growing demands for more powerful devices. For years, aluminum was the standard metallization material for all semiconductor devices. However, Cu outmatches Al concerning current carrying capacity and specific resistance a lot. For the ongoing geometry shrink, these features are very important to match the reliability needs for the semiconductor devices. The resistivity of Cu is approximately 37% lower than the resistivity of Al [2]. The only disadvantage of Cu consists in the interaction with the atmospheric oxygen (O) and the missing self-passivation characteristic of the Cu oxide layer. Al also builds up an oxide layer (Al_2O_3), but this dense surface layer acts as a self-passivation layer and prevents Al from corrosion and diffusion through the SiO_2 dielectric [3]. Beside the fact that Cu is prone to corrosion, device degradation is caused by the Cu diffusion through the silicon dioxide (SiO_2) dielectric [3]. Therefore, process improvements such as additional diffusion layers were necessary for the introduction of Cu. However, because of the demand for faster and more powerful devices at a simultaneous geometry shrinking, the change to Cu as metallization material was needful. Based on the review of Waldrop et al. [4], the development of the device shrinking indicated by the number of transistors per chip and the increasing processor power in the past decades are illustrated in Fig. 1.1.

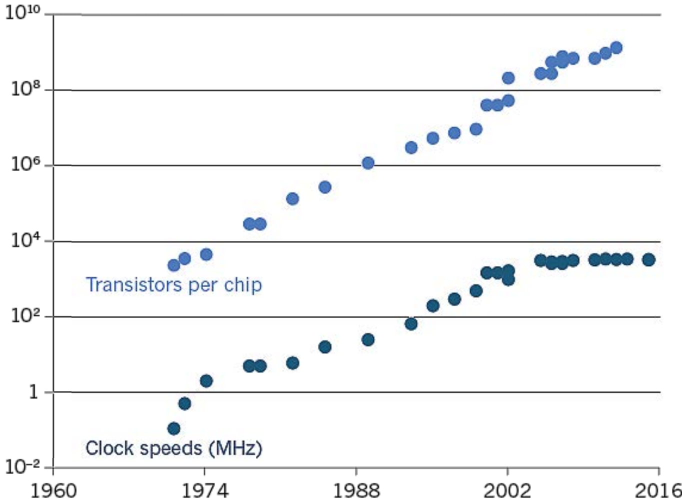

Figure 1.1. Development of transistors per microprocessor chip and the processor power in the past decades based on Moore's law [4].

For Al, the device degradation by electromigration limits the applicability for such devices. Due to the current flow, a material transport in direction of the electron flow direction can be observed which

provides areas with a depletion and areas with an accumulation of the metallization material. This effect is schematized in Fig. 1.2. In his research showed von Glasgow [5] that for the Cu metallization a maximal current densities of 30 mA/μm² could be achieved whereas for the Al metallization the maximal current densities were in the range of 2 mA/μm². The much better resistivity against electromigration is a basic requirement for the applicability in faster and smaller devices.

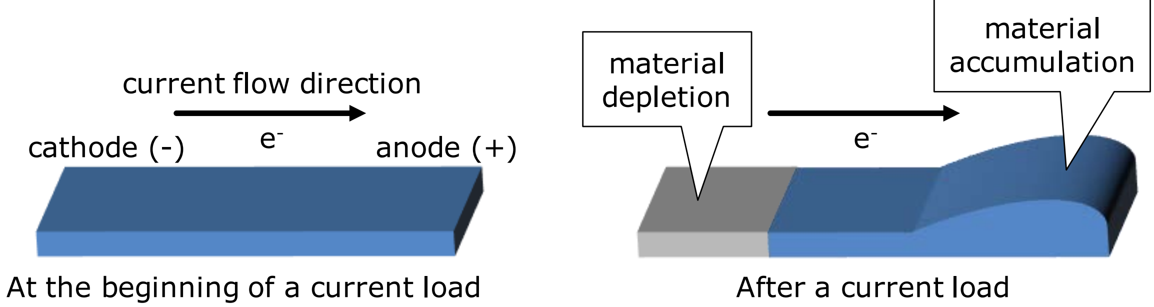

Figure 1.2. Principle of the electromigration showing the circuit path before (left) and after (right) an electromigration damage [5].

Beside the metallization, the interconnection technology in the packaging process is also an important factor for the performance and reliability of the device. Although Cu has found one's way into the semiconductor manufacturing as metallization material, the mostly used interconnection material to connect a semiconductor chip and a leadframe is gold (Au) [6,7]. The reasons providing Au as interconnection material are benefits such as self-cleaning, a high yield rate, flexibility and reliability [8]. In integrated circuit (IC) packaging the three principal electrical interconnection methods are flip-chip, tape-automated bonding and thermosonic wire bonding, at which the thermosonic wire bonding alone has been applied for more than 96% of the IC interconnections [9]. By this reason, this work focuses on the thermosonic wire bonding technology.

1.2 Thermosonic Wire Bonding

In IC packages the most popular electrical interconnection method is the thermosonic wire bonding. The connection is achieved by the combination of pressure, temperature and ultrasonic vibrations.

The general process flow of the wire bonding is depicted in Fig. 1.3. The bonding wire is mounted in a ceramic capillary. At first a so called free air ball (FAB) is formed by electric flame-off (EFO) which signifies that a high voltage spark melts the end of the wire.

In a next step the formed FAB is forced down to a preheated bond pad with a defined contact pressure. In addition, at the contact point the capillary is excited by an ultrasonic vibration. These vibrations are adopted to improve the connection of the FAB and the bond pad. For the implementation of the thermosonic wire bonding based on a Cu wire connected to a Cu bond pad, the oxidation of Cu must

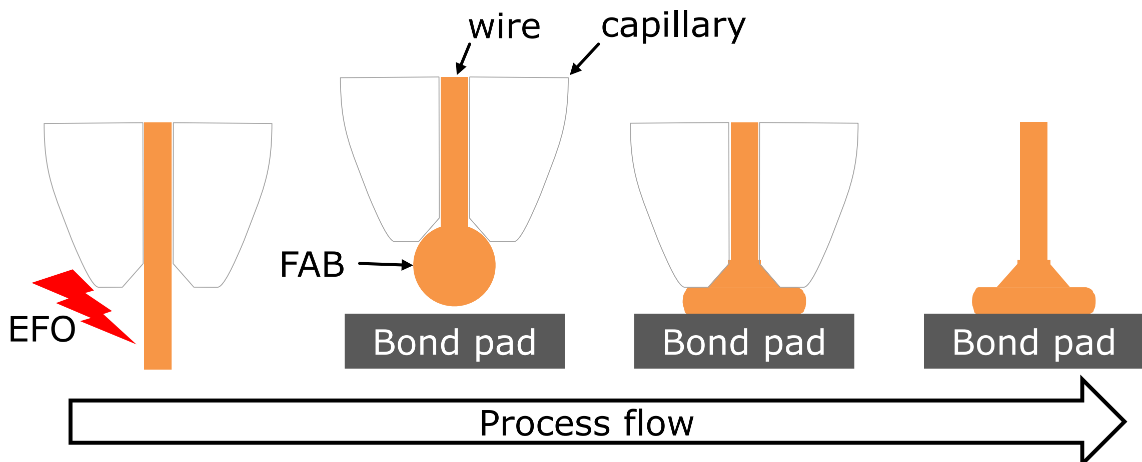

Figure 1.3. Process flow of the thermosonic wire bonding

be considered. By reviewing the process flow of the bonding process in Fig. 1.3, it can be concluded that the FAB [10] and the bond pad [11] are mainly influenced by the oxidation because both are exposed to an increased temperature treatment. The oxidation of the FAB is closely linked to its formation process. Due to the melting of the Cu wire and the subsequent solidification to the FAB a probable oxidation has to be considered. Recent studies have been focused on the FAB formation under an inert gas atmosphere to minimize or even prevent the FAB oxidation completely [12,13]. Usually a mixture of 5% hydrogen (H_2) and 95% nitrogen (N_2) or Argon (Ar) are used for the shielding gas. The hydrogen in the gas mixture reduces the oxide on the wire surface during the EFO process. Pequegnat et al. [14] investigated the influence of the gas type and the corresponding flow rate on the FAB formation. The study illustrated the importance of the hydrogen for the shielding gas because by using only N_2 a severe oxidation of the FAB could be observed. Besides applying a special shielding gas mixture with defined flow rates, the applicability of palladium (Pd) plated Cu wires was also researched in former investigations. Kaimori et al. [15] and Lim et al. [16] showed the improved reliability of Pd-plated Cu wires bonded on aluminum bond pads. In addition, the publication of Zhang et al. [17] confirmed that the Pd coating minimizes the oxidation of the formed FAB. However, it was also observed that an inhomogeneous Pd distribution in the FAB could influence the reliability of the bond connection.

Much research dealing with Cu ball bonding has been focused on the process parameters for a Cu FAB on an Al bond pad [18–21]. By using these materials, the formation of intermetallic compounds is an important issue. Zhong et al. [19] mentioned that the growing speed of the intermetallic compound (IMC) between Al and Cu is much lower than that between Al and Au, leading to lower electrical contact resistance, less heat generation, and better reliability and device performance, compared to Au/Al bonds. In a review Breach et al. [22] examined the material aspects of the Cu/Al and Au/Al compound. Based on this review the improved electrical performance is illustrated in Fig. 1.4. Additionally, the growth of the intermetallic compound is an important reliability factor for the mechanical integrity of the bond

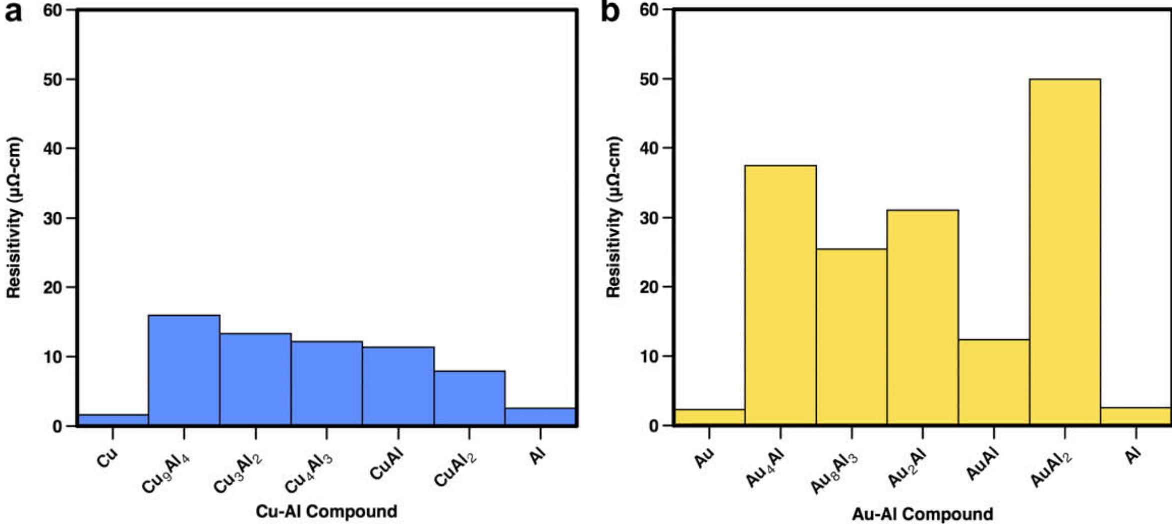

Figure 1.4. Resistivity of the various intermetallic compounds by providing a (a) Cu bond wire on an Al pad or (b) an Au bond wire on an Al pad. The data are based on the publication of Breach et al. [22].

connection [23]. The majority of recent studies has presented the growth behavior of the Cu/Al intermetallic compound [21–27]. The lower resistivity of the Cu/Al intermetallic compounds compared to the Au/Al compound is obvious and clarifies again the advantages of Cu as bonding material. However, Fig. 1.4 also presents that the application of Al as bond pad can lower the electrical performance because the resistivity is always increased compared to the pure material.

In a further development, the process must be improved to enable the bonding connection of a Cu FAB on a Cu bond pad. For the thermosonic wire bonding process the leadframe with the bond pad must be heated up. More specifically, a stage temperature of 150 °C to 200 °C is needed for Cu wire bonding [19]. In case of Cu as bond pad material such a temperature treatment immediately provokes an oxidation of the bond pad surface which influences the quality and the reliability of the bond contact. Chuang et al. [28] summarized in their work that copper oxide on the surface cannot be broken or removed by the ultrasonic power during the thermosonic bonding process to achieve a reliable Au-Cu bond. The oxidation of the bond pad is not only limited to the actual bonding process. Ho et al. [29] demonstrated that the surface oxidation already started at the wafer level and cannot be prohibited by using a vacuum oven or a nitrogen environment during the further processing. Hence, for the introduction of a direct Cu-Cu bond process the oxidation of the Cu bond pad must be further researched.

By using a passivation layer for the Cu bond pad, the problems related to the surface oxidation could be bypassed. Numerous experiments have established that different passivation schemes such as thin chromium (Cr) , titanium (Ti) or Al film [28,30], copper-silicide layers [31,32] or self-assembled monolayer [33] can be used to prohibit the Cu oxidation. In detail, possible approaches for the protection of the Cu surfaces are discussed in a subsequent section. Related to the thermosonic bonding process and the limitation caused by IMC presented in Fig. 1.4, Aoh et al. [30] found out that a thin passivation

layer can be removed using ultrasonic power during the bonding process enabling the connection of an Au wire onto a fresh Cu pad surface. In addition to the research concerning passivation methods for the oxidation protection, Jeng et al. [34] introduced an alternative approach by researching the influence of Cu oxide on top of the Cu bond pad. It could be demonstrated that an oxide layer grown by preheating the Cu bond pad under controlled conditions resulted in the same bonding strength than a Ti passivation layer. However, their findings are related to the gold-copper bonding process and they cannot be easily transferred to the Cu-Cu process. Nevertheless, such publications show that the characterization of the oxide growth must be considered in the further research.

Beside the surface modification of the Cu bond pad, microstructural information such as grain size and orientation of the free air ball formed by the electric flame-off process are very important factors. Hang et al. [35] inspected the recrystallization process of the Cu FAB and showed the evolution of the solidification process as seen in Fig. 1.5. It could be observed that a large number of fine subgrains was formed at the ball periphery. The relation between yield stress and grain size is described mathematically by the Hall–Petch equation [35,36],

$$\sigma_y = \sigma_0 + \frac{k_y}{\sqrt{D_{GB}}} \quad (1.1)$$

where σ_y is the field strength, σ_0 is a material constant for the starting stress, k_y is the strengthening constant specific for each material. The influence of the grain size is introduced by the average grain size diameter D_{GB}. Based on the Hall-Petch law it was predicted that the outer FAB is harder which could produce more stress during the bonding process. Tan et al. [37] observed that Cu-Cu connections with a grain growth across the bonding interface leads to much higher tensile strength. A varying microstructure at the outer FAB as shown in Fig. 1.5 based on [35] could limit such a grain growth.

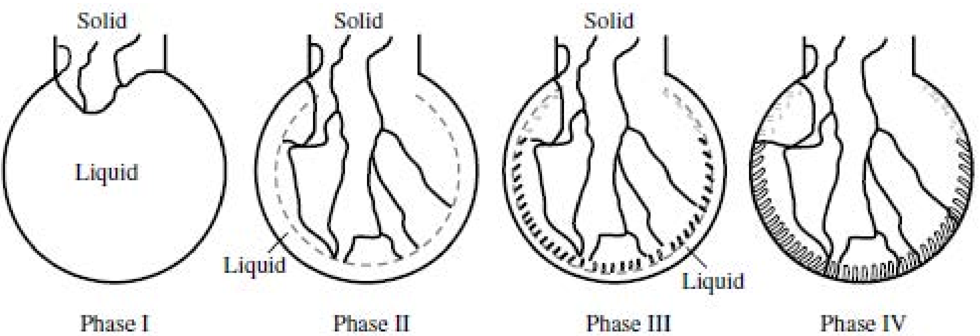

Figure 1.5. Schematic of the solidification process and the resulting recrystallization in the Cu FAB according to [35]

1.3 Copper oxide

The Cu oxidation is an important process for understanding the Cu corrosion. There are two stable oxide phases, the cuprous oxide or cuprite Cu_2O and the cupric oxide or tenorite CuO. Their different characteristics can already be observed in their different color. The cuprous oxide Cu_2O is known to form a reddish surface color, whereas the cupric oxide CuO grown on a Cu surface is black [38]. However, these observations can only be used for a first estimation. For the exact characterization of the oxidation state further analytical methods must be used. Cabrera and Mott [39] introduced a theory regarding the oxidation of metals and also of Cu. They assumed in their model that the oxide film grows in layers uniformly. Many years later, Yang et al. [40] demonstrated that the Cabrera-Mott model cannot be valid for the Cu oxidation. They presented that the Cu oxide film nucleates and grows as oxide islands, not as a uniform layer. It is generally accepted that the growth of the oxide phases, Cu_2O and CuO, can be attributed to different temperature regions. Derin et al. [38] observed the oxide film grown on Cu by thermal oxidation at 125 °C and could assign the oxide film to the Cu_2O phase. After a further increase of the temperature to 140 °C the main oxide phase remains to be Cu_2O [41]. Gosh et al. [42] found out that at temperatures below 200 °C the Cu_2O phase is dominant. For temperatures exceeding the 200°C, Cu_2O starts reacting with O_2 and forms the CuO phase. This observation could be confirmed by Honkanen et al. [43].

The different transitions of the oxidation states based on the reaction equations are detailed in Fig. 1.6. In addition, the topographic study shown in Fig. 1.7 could point out that the grain size of the CuO oxide is much larger than the grain size of the Cu_2O oxide. Referred to the results of Honkanen et al [43], a root-mean-square (RMS) surface roughness of 26 nm to 33 nm was stated for CuO and a much lower RMS roughness of 2 nm to 8 nm was named for Cu_2O.

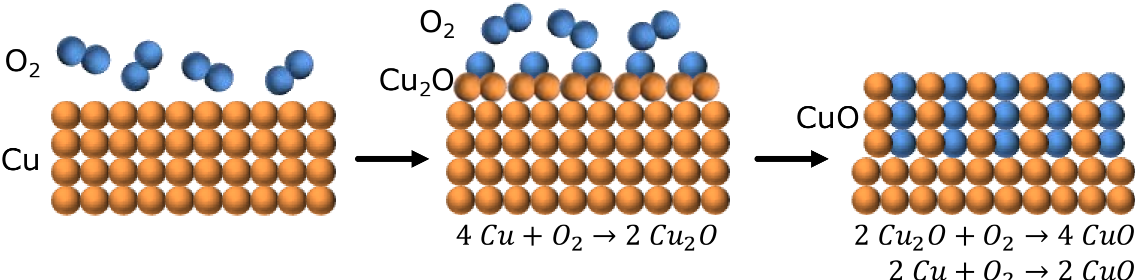

Figure 1.6. Oxidation states of the Cu surface by reacting with O_2 based on the shown reaction equations.

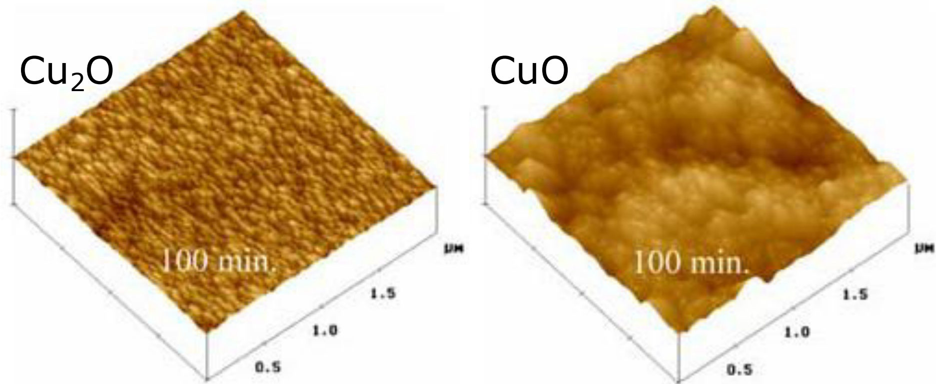

Figure 1.7. Topography images of a Cu_2O oxide and a CuO oxide as presented in [43].

Beside the main oxidation phases different researchers have mentioned the presence of the Cu_3O_2 oxide phase [44–47]. The Cu_3O_2 oxide phase is a metastable defect structure of the Cu_2O oxide phase. In the study of Lefez et al. [44] it was shown that the formation of CuO out of Cu_2O occurs via the intermediate state Cu_3O_2. Therefore, such a defect structure could exist as interfacial layer. The detection of this interface oxide Cu_3O_2 was taken into account by Mencer et al. [47]. By using sputter depth profiling, Cu_3O_2 is determined to be the oxide in the ion impact altered layer. However, the defect structure Cu_3O_2 could also originate from the ion sputtering damaging the present oxide layer.

Mostly, the researched Cu oxides were grown under controlled conditions such as pressure, oxygen content and temperature to explore the oxidation kinetics [46]. Furthermore, in addition to the thermal oxidation different methods for the oxide growth were investigated such as plasma evaporation [48], RF reactive sputtering [42] or chemical deposition [49]. Beside the reliability issue of the Cu oxide for the semiconductor manufacturing, the Cu oxides are investigated as solar cell material [50]. Hence in most cases, the aim of using controlled conditions and different deposition methods is the generation of a defect-free oxide layer for the photovoltaic application [51]. The study as possible material for photovoltaic power generation can be explained by the semiconducting properties of the Cu oxides. Their p-type conductivity and the different band gaps are shown in different experiments [49,52,53]. The observations of the oxide topography [43,53] show that the Cu surface is modified in a nanoscale structure by the oxidation. Therefore, it is evident that for a more advanced investigation of oxidation and topographic features, nanoscale characterization techniques play a key role for the further research and must be focused in this work. The mainly used methods in the literature are summarized in one of the next introducing sections. As the oxidation of the Cu surface is such a striking feature, numerous investigations have addressed the protection of the Cu surface. In the next section, various approaches to protective layers for the Cu surface are reviewed.

1.4 Oxidation protection of copper surfaces

The protection of copper surfaces is an important and advantageous procedure for many different applications to achieve a reliable and stable surface along with the development of nanotechnology and device miniaturization. Especially for the application of subsequent process steps such as connection techniques, the protection of the Cu surface is an important factor. For example, Tan et al. [37] observed that the grain growth across the bonding interface is significantly limited by the surface oxide forming a barrier. Consequently, an additional process step for a protective cap on the bond pad can be introduced to bypass a probable oxidation of the Cu pad [11]. Ratchev et al. [54] pointed out that materials such as Al, nickel (Ni)/Au or Ni/Pd/Au fulfill the demand as protective cap on the Cu pad. The cap layer thickness was specified to be 800 nm for Al, 3 µm/80 nm for Ni/Au and 5 µm/500 nm/80 nm for Ni/Pd/Au. However, by using such comparatively thick protection layers, the formation of intermetallic compounds at the interface must be considered. Due to these various materials used, the formation of intermetallic compounds is rather complex and difficult to predict. However, the growth of the intermetallic compound is an important reliability factor for the mechanical integrity of the bond connection [23]. The majority of recent studies have presented the growth behavior of the Cu/Al intermetallic compound [21–26]. Although such layers of micrometer thickness can successfully protect the Cu surface, coatings of nanometer thickness would minimize the possible growth of transition phases and additionally, they would reduce dimensional modifications, costs and weight. The challenge for novel coating techniques is to achieve a high protection efficiency while minimizing the coating thickness.

Beside the deposition of protective caps, Li et al. [55] studied the oxidation protection by alloying a copper film with titanium (Ti), palladium (Pd), chromium (Cr) or aluminum (Al). They could demonstrate that the oxidation rate of the Cu alloys is significantly reduced, but it could also be shown that the alloys provide an increased sheet resistance which lower the electrical performance. In addition, the retarding of the oxidation rate is closely linked to the compound formation and thus, there must be more effort involved in the formation process.

A further approach is the implementation of copper silicide passivation layers. Hymes et al. [31,32] researched in their studies the formation of Cu silicides, Cu_3Si and Cu_5Si, on top of a 400 nm Cu film. They found out that over time and temperature the resistance is increased which reflects that a compositional development is occurring. Two different diffusion processes could be observed over time. Silicon (Si) diffuses to the surface where it oxidizes to form a silicon dioxide (SiO_2) layer on the surface and additionally, Si diffusion into Cu increased the resistivity of the underlying Cu layer. Although the silicide layer can protect the underlying Cu surface from oxidation, the different diffusion processes lower the electrical performance and the varying composition of the silicide layer can provide different surface properties for the bonding process.

In recent publications, aluminum oxide Al_2O_3 was researched as protection layer for the Cu surface. In the review regarding the chemical vapour deposition of various material compounds, Choy [56] stated that the ceramic material Al_2O_3 can act as protection against corrosion and oxidation. Applied to the protection of a Cu surface, Chang et al. [57] and Mirhashemihaghighi et al. [58] implemented an Al_2O_3 protection layer deposited by an Atomic Layer Deposition (ALD) process. They showed in their studies that in general a 10 nm Al_2O_3 layer provides a feasible oxidation protection, but the ALD process parameters are very critical. Defects in the protective film could allow oxygen penetration and the attack of the underlying Cu surface [57]. Beside these challenges, Kukli et al. [59] investigated the modification of the mechanical properties due to the protective layer of the ceramic material Al_2O_3. The mechanical strength and resistance of the substrate material can be affected positively by the deposited Al_2O_3 film. However, it is worth noting that the mechanical properties of the film may significantly complicate a reliable bonding process.

Similar outcomes could be achieved by using graphene as protective layer on Cu surfaces. In various experiments, such layers provide promising results on Cu [60–63]. Kirkland et al. [60] as well as Prasai et al. [63] introduced in their research that single layer graphene as well as multi-layer graphene e.g. graphite can serve as barriers to electrochemical corrosion. Additionally, the protective effect caused by the atomic graphene layer goes along with an improved mechanical stability of the protected surface. Different researcher published in their study that a graphene layer effects an improved wear resistance of the coated surface [64,65]. However, especially for further applications of any interconnection methods, the modified mechanical stability of the surface may limit significantly the ability for applying such processes.

In contrast, encouraging results could be shown with very thin passivation layers deposited onto the Cu surface. In their studies showed Aoh et al. [30] that a 3.7 nm thick titanium passivation layer can protect the Cu surface and provides excellent bondability and strong bonding-strength of an Au-Cu bond. They concluded that such a thin passivation layer can be removed using ultrasonic power during the thermosonic bonding process. Therefore, novel coating materials for the application in the Cu-Cu bonding process may be deposited as a few nanometers thick protective layer to avoid the growth of interfaces and to achieve the pure Cu-Cu transition. The challenge for such thin layers is to achieve a high protection efficiency while keeping the coating thickness minimal at the same time. Furthermore, the deposition process should be easy to be implemented in the device manufacturing process structure and simultaneously it should not be time-consuming.

For this reason, the suitability of sputter coatings which are well known for the application in scanning electron microscopy experiments must be investigated. Former studies by Stokroos et al. [66] showed that various sputter materials provided different structural details such as particle size and density. chromium (Cr) provides a very smooth coating, but it is known that the Cr layer degrades in ambient

environment and can oxidize rapidly. Noble metals such as gold (Au) or platinum (Pt) could yield a surface coating inert with the ambient environment. Pt coatings tends to offer a much smaller grain size compared to an Au coating layer. Beside protective layer consisting of metals, carbon coating layer can be an interesting alternative to achieve very thin and stable protection layers. Especially for depositing thin carbon layers Ion-beam sputtering techniques must be used because DC magnetron coaters tend to build up non-conductive diamond-like carbon layers with improved mechanical stability [67].

As an alternative to the previous introduced protection layers, it is known from the literature that thin organic Self-Assembled Monolayer (SAM) can act as effective barrier to protect metal, in general and Cu, in particular, from corrosion [29,33,68–71]. In a study related to Cu-Cu thermo-compression bonding Tan et al. [37] observed that Cu surfaces passivated with a SAM film facilitate the grain growth across the bonding interface. The surface oxidation could be identified to form a barrier preventing such a grain growth. Therefore, they concluded that the SAM film can protect the Cu surface from oxidation. In Fig. 1.8 the oxidation protection of the SAM film is schematized. The molecules forming the SAM layer are bound to the Cu surface via thiol (-SH) groups and thus, the Cu surface cannot interact with the oxygen molecule.

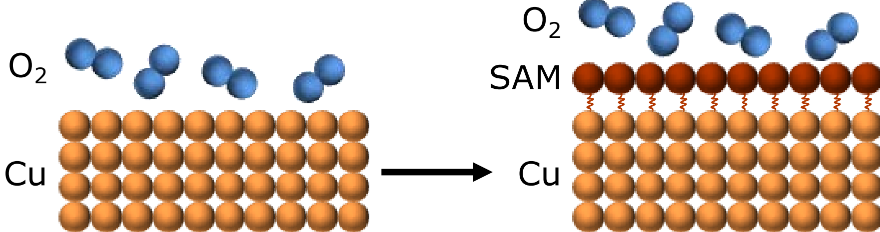

Figure 1.8. Schematic of the oxidation protection of the Self-Assembled-Monolayer on a Cu surface. The molecules forming the SAM layer are bound to the Cu surface via thiol groups.

Summarized, it is obvious that several passivation techniques and materials can protect the Cu surface from oxidation. However, in combination with the subsequent bonding process, thin sputter coatings and Self-Assembled Monolayer provide already promising results. Fundamental for the application in the thermosonic bonding process is the temperature stability of the protection layers. As mentioned before, a stage temperature in the range of 150 °C to 200 °C is needed for the process [19]. Consequently, the characterization of the film integrity at these temperatures is very important and must be researched. In detail, it must be ensured that even a very local degradation can be detected without damaging the protective films. For this reason, several characterization methods used in the literature are considered in the next section.

1.5 Characterization techniques

In recent studies, the investigation of the Cu surface and especially, the determination of the Cu oxide were mainly performed by using X-ray diffraction (XRD) [42,53,57,72–78]. The fundamental of XRD is the usage of monochromatic X-rays collimated to the sample surface. As illustrated in Fig. 1.9, the X-rays incoming with a defined angle theta Θ are deflected from the crystal structure with the lattice distance d and produce a reflection peak which is dependent on the path-length difference $2d\sin(\Theta)$. In this case, the incoming beam is deflected by an angle of 2Θ producing a specific reflection peak which is characteristic for the crystalline structure of the material.

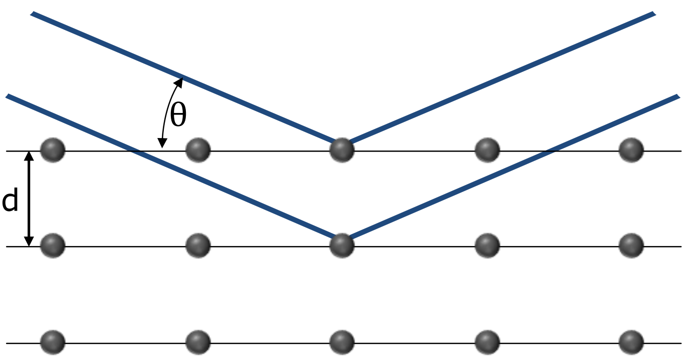

Figure 1.9. Schematic principle of the X-ray diffraction (XRD) illustrating X-rays deflected by a crystalline atomic lattice structure.

Related to the characterization of crystalline Cu oxides grown on Cu, an example of a XRD result based on the investigations in [57] is shown in Fig. 1.10. Different reflection peaks at distinct angles 2Θ can be attributed to the different crystal orientations of CuO, Cu_2O and the crystalline Cu substrate. This presented example and other experiments [42,53,72–78] evidence that the Cu oxide phases can be determined by an XRD analysis. However, it is worth noting that the material under investigation must be grown in a crystallographic structure because in case of an amorphous grown oxide layer, the incoming X-rays are scattered in various directions and consequently an XRD analysis does not provide any characteristic reflection peaks.

In general, XRD results are very advantageous for the determination of an oxidation occurrence, because the analytical volume achieved by an XRD analysis can be several micrometers in all directions. The intensity of the X-ray beam decreases exponentially with the distance traveled in the material and strongly depends on the mass absorption coefficient and the density of the material. However, it must be noted that the analysis of nanostructures is limited strongly by the comparatively large analytical volume.

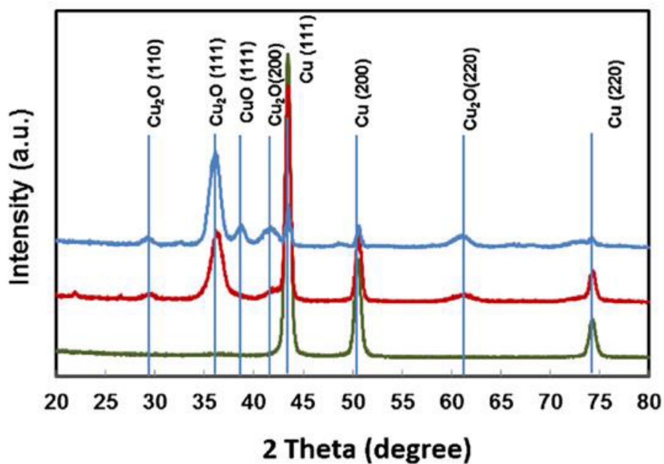

Figure 1.10. XRD spectra after three different periods of oxidation of a bare Cu surface based on[57]. Various Cu, Cu_2O and CuO peaks respectively belonging to different crystal orientations.

X-ray Photoelectron Spectroscopy (XPS) [33,53,68–70,78] is another measurement technique based on the irradiation of the sample by an X-ray beam. This surface-sensitive spectroscopic technique measures the elemental composition as well as the chemical state and electronic state of the elements existing within the material. The surface sensitivity of XPS can be explained by the limited free path of photo-emitted electrons in the material.

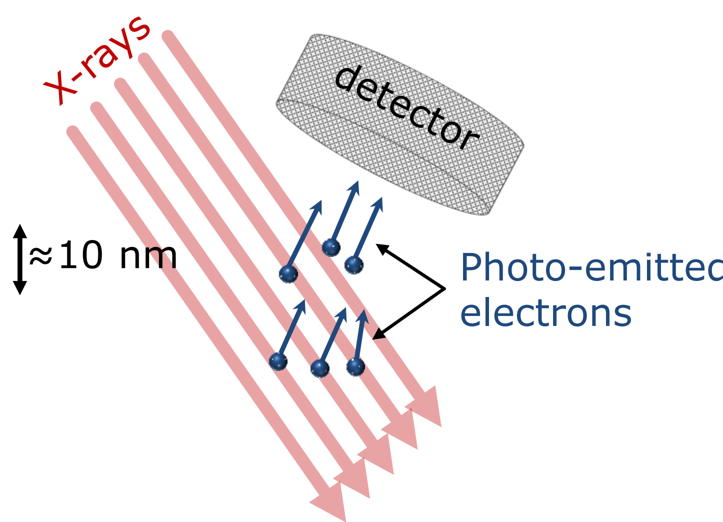

Figure 1.11. Basic schematic principle of the surface characterization by X-ray Photoelectron Spectroscopy (XPS).

As illustrated in Fig. 1.11 photo-emitted electrons near the surface can escape easily to the detector whereas electrons emitted in deeper regions can undergo inelastic collision, recombination or trapping in various excited states within the material. Therefore, the signal from the surface is much stronger than

the signal from the inside of the sample. The fundamental of the XPS analysis is the measurement of the binding energy of the detected electrons. These binding energies are characteristic for each element and correspond to the electron configuration within the atom.

For the investigation of Cu surfaces, Fig. 1.12 shows a suitable XPS result based on [53] achieved by an X-ray beam with a 600 μm diameter spot size. The presence of the oxides can be confirmed by the Cu_2O peak at 932.5 eV and the CuO peak at 934.7 eV together with several satellite peaks from 940 to 945 eV.

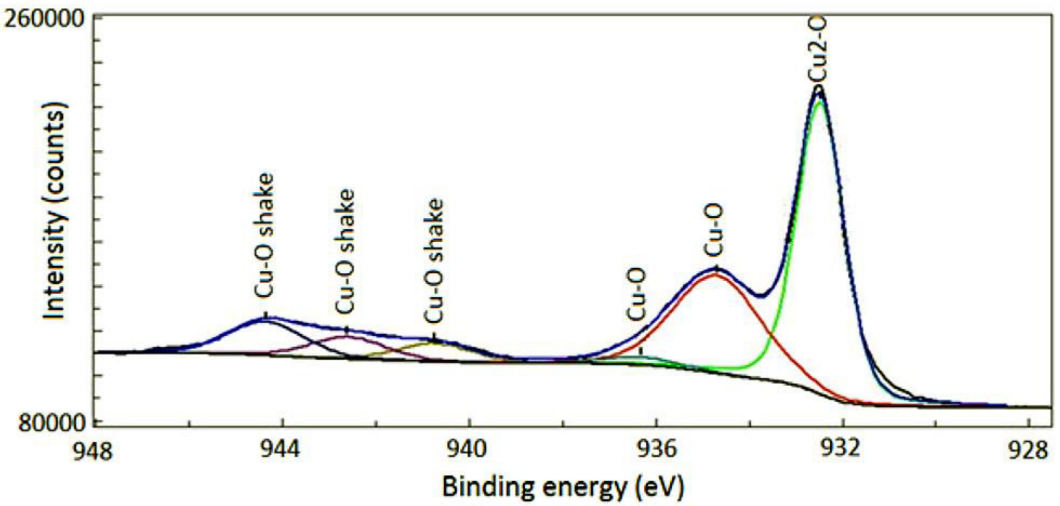

Figure 1.12. XPS result based on [53] indicating the presence of Cu_2O (~932.5 eV) and CuO (~934.7 eV and satellite peaks from 940 to 945 eV) on a Cu surface.

As stated in the literature and shown in Fig. 1.12, XPS enables the exact characterization of the Cu surface because of the assignment of the binding energy and the suitable surface sensitivity. Additionally, it is worth noting that in contrast to XRD, XPS is not limited to the identification of a solely crystalline material structure and can also be applied for investigating the presence and the composition of any amorphous grown materials.

Summarized, XPS as well as, with the restrictions to crystalline substances and larger analytical volumes, XRD are appropriate tools for the general characterization of the Cu surface. However, the major disadvantage of both tools is the limited lateral resolution based on the excitation by an X-ray beam.

Alternative characterization techniques mentioned in previous examinations are Electron Probe Microanalysis (EPMA) [45,57] and Fourier Transform Infrared Spectroscopy (FTIR) [74,77,79]. EPMA is based on the energy dispersive X-ray spectroscopy (EDX) and enables the quantitative identification of the element composition of the sample by detecting the characteristic X-ray spectrum of each element. EDX or EPMA is a suitable method to characterize any protective coatings as well as the oxidation of the Cu surface by the presence of oxygen (O). Furthermore, the different oxide phases can be distinguished by their absolute Cu:O ratio. Due to the penetration depth of the electron beam, the nanoscale investigation of samples may be limited. Monte Carlo simulations [80,81] confirm that for the

identification of layers in the nanometer range an acceleration voltage below 1 kV would have to be applied, but for the detection of Cu, the lowest X-ray emission line is the L-alpha line at 0.930 keV. Since the X-ray generation is also subject to various losses, a much higher electron acceleration voltage must be applied to reliably detect Cu and its oxidation states. Consequently, thin layers with few nanometers cannot be examined solely by EDX. However, it is worth noting that EDX can correlate topographic features to their element analysis. Few researchers [8,27,37,82] have shown in their studies that EDX maps enable the investigation of the distribution of certain elements on an imaged surface.

The characterization by FTIR is based on the detection of the molecular absorption of an infrared beam irradiating the sample and enables thereby the investigation of any molecules on the Cu surface by the detection of their vibration modes. Especially for the distinct Cu oxide phases, Cu_2O and CuO have different vibration modes which provide different absorption peaks. The possible analysis of protective coatings on the Cu surface by FTIR is very limited. As the presence of any molecular compound is essential, it cannot be applied to protective sputter coatings. In contrast, as mentioned in literature [70,71] FTIR is able to identify the composition of a Self-Assembled Monolayer. It is important to note that like XPS, both techniques, EDX and FTIR, are not restricted to the analysis of crystalline structures and can thereby also characterize amorphous materials.

Especially for the examination of SAM films, an additional characterization technique is mentioned in literature. Whelan et al. [33] and Rao [70] show that high quality SAM films correlate with a high hydrophobicity of the coated surface. As an evaluation of the hydrophobic properties, Contact Angle Measurements (CAM) can be performed. In Fig. 1.13, the principle of CAM is schematized. The contact angle defines the interface between a sessile drop to the surface under investigation and provides distinct surface properties such as the surface energy. In their studies, Rao [70] and Lukose et al. [83] report that CAM is a suitable tool to provide valuable information about the hydrophobicity of a surface.

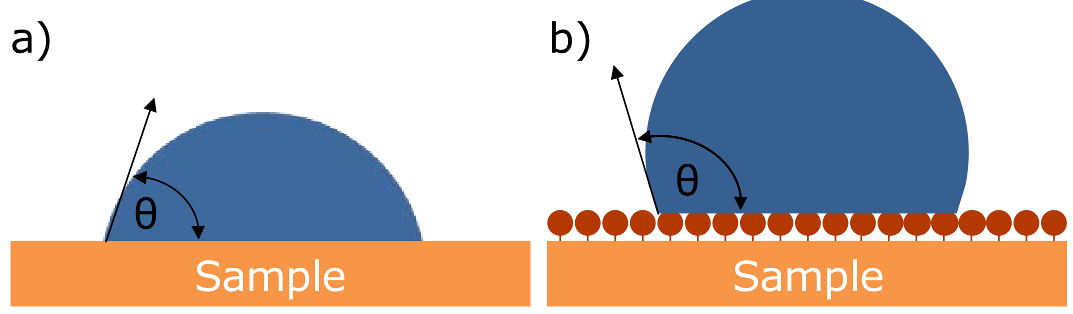

Figure 1.13. Schematic principle of the Contact Angle Measurement determining the contact angle Θ of a) bare Cu and b) SAM film covered Cu surface

Even though the reviewed characterization techniques mentioned in recent literature provide valuable information about important surface properties, it could be shown that they are not able to achieve very local information in the nanoscale. For the nanoscale imaging of the topography, techniques such as the

scanning electron microscopy (SEM) [27,58,77,78,84,85] or the atomic force microscopy (AFM) [41,43,53,70,85,58] are used. Especially, AFM based techniques can monitor surface properties in the nanoscale because the probe tip can obtain a high-resolution image of the surface.

The AFM based method Kelvin Probe Force Microscopy (KPFM) [86–90] enables the measurement of the Contact Potential Difference (CPD) of material surfaces with high lateral resolution at ambient environment. Sugimura et al. [91] have addressed the problem that local variations of surface potentials are shielded by the presence of a surface water layer in ambient environment. Since such disturbances can influence the capability of KPFM significantly, more work is needed to develop a novel analysis package for the nanoscale surface characterization based on the combination of appropriate measurement techniques.

A further AFM based technique, the conductive-AFM, enables the nanoscale characterization of local current flow or the local conductivity of a sample surface. Chintala et al. [92] focused on conductive-AFM (C-AFM) to investigate the electrical properties of SAM films on silicon substrate. They report that SAM films are isolating and that film homogeneity may be monitored by local tunneling current measurements. For C-AFM, the appropriate probe tip is in contact with the sample surface and is moved to scan a specific region. It is important to note that this contact mode application provides high lateral and vertical forces acting on the sample surface. Beside a significant wear of the probe tip, such forces may damage the sample surface under investigation [93,94] and must be considered critically. Therefore, especially for the nanoscale examination of soft samples such as protective coatings on the Cu surface, more advanced characterization techniques featuring reduced vertical and lateral forces must be introduced.

2. Aims of the work

The implementation of a connection technology based on a direct Cu-Cu connection is a desirable progress in the semiconductor manufacturing and especially in the packaging of integrated circuits. However, the different properties of Cu, especially the oxidation behavior compared to standard materials such as aluminum or gold impede the easy transition to the direct Cu-Cu connection. Since the Cu surface is subject to oxidation, even at room temperature, the advanced characterization of the surface state is very important and must be researched. In recent studies, the Cu surface was investigated by measurement techniques with a very limited lateral resolution. Research is now necessary to investigate very local topography features and their correlation to the corresponding oxidation phase. Atomic Force Microscopy techniques have the potential to address these needs, but combined analytical methods are required to develop a novel analysis package for the nanoscale surface characterization.

The introduction of passivation layers for the Cu surface is an interesting approach for the practicability of a direct Cu-Cu connection because such a layer can protect the bond pad from oxidation. A protective film must meet certain requirements to be suitable for the bonding process. The protection must also be effective at elevated temperatures up to 200 °C without increasing the mechanical stability of the Cu surface. Additionally, the thickness of the passivation layer must be as thin as possible to avoid the formation of intermetallic compounds which can increase the resistivity significantly and thus lower the electrical performance. The application of thin sputter coating layers or organic Self-Assembled Monolayer (SAM) are promising methods, but still further research for the nanoscale characterization of the local surface modification and temperature stability is needed. Evaluation tools with convenient handling are needed for practical applications to characterize the passivation layers in the nanoscale. Especially for the investigation of SAM films, more advanced techniques with reduced lateral and vertical forces are required.

The measurement environment in which AFM based techniques are operated can influence the results obtained. Beside the ambient air environment, the use of a liquid environment improves the sensitivity for measuring interaction forces between AFM probe tip and sample surface. However, this measuring environment can cause an increased force acting on the AFM probe during its movement. Different influencing factors such as the cantilever geometry, parameter setup and the fluid conditions must be evaluated. For this reason, a simulation model must be developed to research the hydrodynamic drag forces which can be used to determine the best configuration for the measurement setup.

The electric flame-off (EFO) is the first step in the thermosonic wire bonding process cycle and is used to form the free air ball (FAB). Since the Cu wire tail is melted by a plasma discharge for the FAB formation, the FAB structure is influenced significantly. The objective of the research work was to

provide influencing factors of EFO process parameters on the oxidation, crystal structure of the FAB and on the strain within the microstructure.

In the previous initial section, the advantages of Cu as metallization material as well as interconnection material in semiconductor manufacturing are presented. Challenges/Limitations for Cu-Cu connections and the thermosonic wire bonding process are introduced and the evolution of the research in the field of Cu oxidation kinetic and the oxidation protection of Cu surfaces is presented. Furthermore, characterization techniques predominantly used in the literature are examined with respect to the general suitability and in particular, to the lateral resolution.

In chapter 3 the experimental details of the analytical methods used in this work are described. The elementary techniques of atomic force microscopy and scanning electron microscopy and particularly more advanced operated modes are explained and their benefits and limitations with respect to nanoscale characterization are discussed.

In chapter 4 characteristic contact potential difference values for the Cu oxides are introduced by combining PeakForce Kelvin Probe Force Microscopy (PF-KPFM) and X-ray as well as infrared spectroscopy. The nanoscale investigation of the Cu surface oxidation at the bonding temperature of 200 °C as well as the oxide grain growth in the initial five minutes are presented.

Chapter 5 introduces a numerical integrated model that enables the accurate prediction of hydrodynamic drag forces present in AFM fluid imaging applications. Triangular and rectangular cantilever geometries are analyzed as well as influencing factors related to liquid properties such as ethanol content or liquid temperature.

Chapter 6 is devoted to the nanoscale characterization of CH_3-terminated self-assembled monolayer protecting Cu surfaces from oxidation. The temperature induced degradation of the SAM films is analyzed in the nanoscale by applying characterization techniques with reduced lateral and vertical forces.

In chapter 7, the protective effect of platinum and carbon based nanometer films deposited onto Cu surfaces subject to pre-bonding temperature stress is analyzed. The degradation of the protective films with various thicknesses is studied in the nanoscale by combined non-destructive SEM techniques and PF-KPFM

In chapter 8 the Cu free air ball (FAB) formed by the electric flame-off (EFO) process in standard air environment is explored with respect to oxidation and recrystallization. Topographical variations and oxidation of FAB surfaces as well as oxidation, grain structure and strain of the internal of FABs are studied.

Finally, the main conclusions are summarized.

3. Experimental

In the experimental part the fundamentals of the different analytical methods used in this work are explained. Benefits and limitations are discussed with respect to nanoscale characterization of Cu surfaces or Cu based structures. The next sections are devoted to the elementary techniques of atomic force microscopy and scanning electron microscopy and particularly to more advanced operation modes, which were important for this work.

3.1 Atomic Force Microscopy

The atomic force microscopy (AFM) has its origin in the scanning tunneling microscope (STM) invented in 1981 by Heinrich Rohrer and Gerd Binnig. A STM consists of an electrical conductive probe which moves in a very low distance of a few nanometers over an electrical conductive sample. At an applied voltage between probe tip and sample a distance dependent measurable tunneling current flows. This tunneling current is held constant by controlling the distance between tip and sample. By evaluating these distance values, the surface topography can be reconstructed. The AFM invented in 1986 by Binnig et al. [95] is the further development of the STM. In contrast to a STM system, the AFM enables the investigation of both conductors and insulators on an atomic scale without the need of a vacuum measurement environment. The basic principle of any AFM-based techniques is shown in Fig. 3.1.

The AFM system uses the force interaction of an atomic sharp tip with a specimen surface. The atomic sharp tip is located on the end of a cantilever which bends due to the interaction force between probe tip and sample. In its easiest form, this normal interaction force can be calculated by Hooke's law,

$$\Delta F = k_{Tip} \cdot \Delta z \quad (3.1)$$

in which the force F is directly proportional to the deflection z. The factor k_{Tip} is the spring constant of the cantilever. It is important to note that this force applied to the tip calculated by Eq. 3.1 is only valid for samples that have very small adhesion with the tip. If the adhesive force between the sample and the tip is large, it should be included in the normal force calculation [96]. However, for the introduction of the basic principle of AFM-based techniques, only the normal interaction force is considered.

As schematized in Fig. 3.1, the micro-machined cantilever with the sharp tip is mounted on a piezo actuator incorporated into a tip holder. A laser beam is reflected by the backside of the cantilever and is guided by a mirror system to an array of photo diodes (Z-Detector). This two-dimensional detector can sense the deflection in vertical as well as in horizontal direction and provides the cantilever deflection

feedback signal. The backside of the cantilever can be coated with a highly reflective aluminum layer to minimize disturbances caused by a reflection of the laser beam from a reflective sample surface.

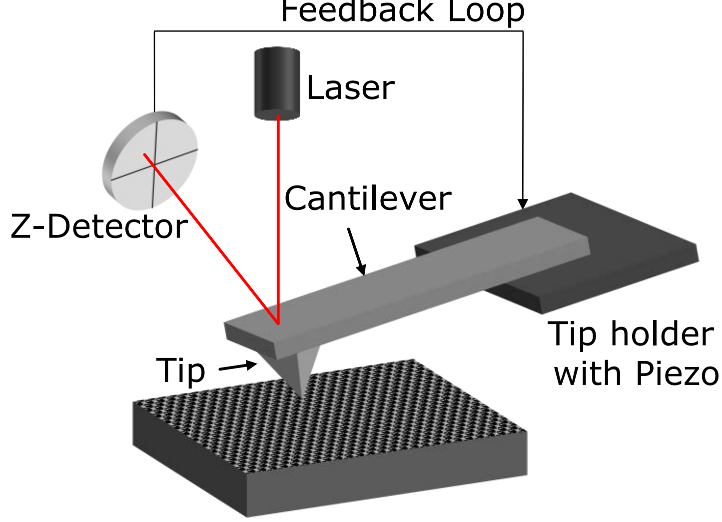

Figure 3.1. Basic principle of AFM-based techniques.

Fundamentally, AFM-based techniques may be divided into three most common categories indicating the mode of operation: contact mode (Cont-AFM), intermittent contact mode (IC-AFM) and non-contact mode (NC-AFM). These three operation modes are illustrated in Fig. 3.2.

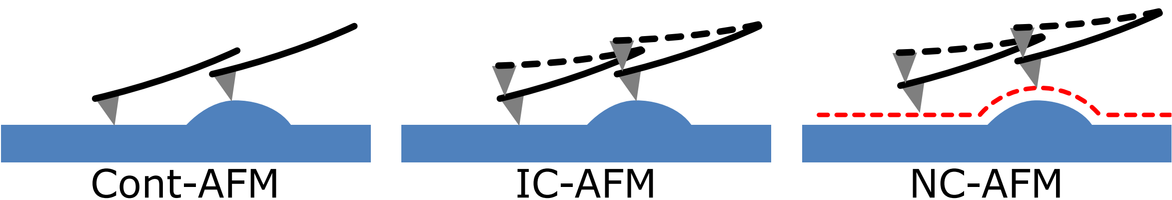

Figure 3.2. Schematic of the most common AFM operation modes.

In contact mode, the AFM tip is in physical contact with the sample. The topography image is generated by the deflection of the cantilever tip system. The cantilever deflection is maintained constant by a feedback circuit and therefore the mechanical force applied to the sample is held constant. In addition, this direct contact of the AFM tip with the sample can be used to map the current distribution of the surface. For this purpose, an additional current sensor has to be attached to the setup and the AFM tip has to be electrical conductive. Although the contact mode itself and the possible electrical characterization could be very useful for some materials, the mechanical forces applied to the sample can be harmful for many applications dealing with delicate materials which can be damaged by these forces. Beside the damage or the contamination of the sample surface, the forces applied by the contact

mode are the cause of tip wear and the loss of spatial resolution. Therefore, the contact mode is restricted to the imaging of only comparatively hard surfaces.

In non-contact mode, the AFM operates with a tip-sample distance in the range of 5 -15 nm. The non-contact mode may basically be performed with a static or a vibrating cantilever. The techniques using a vibrating cantilever belong to the dynamic AFM techniques and are predominately in use because of a better signal-to-noise ratio compared to static techniques. In the dynamic non-contact mode, the system may monitor either the change of the amplitude, amplitude modulation (AM-AFM) or the change of the resonant frequency, frequency modulation (FM-AFM), of the vibrating cantilever. Indeed, the non-contact mode does not suffer from tip or sample degradation effects, but the missing tip-sample contact limits the use in ambient environment due to monolayers of absorbed fluid present on the sample surface in air [97]. Contact-mode applications can penetrate the liquid layer and the surface topography can be imaged reliably.

The intermittent-contact mode is similar to the non-contact mode and also belongs to the field of dynamic AFM modes. The vibrating cantilever tip is brought closer to the sample, so that it just barely hits, or "taps", the sample at the bottom of its travel. Therefore, it is frequently called tapping mode. The cantilever-tip system oscillates at or near its resonant frequency. The topography imaging can be achieved by detecting the change of the amplitude of the cantilever's oscillation which is based on interaction forces such as Van-der-Waals forces acting on the probe tip. Generally, the damage done to the surface by IC-AFM is lessened compared to contact mode because lateral forces are almost eliminated. However, compared to the contact mode the vertical peak forces applied can be much higher and cannot be controlled exactly. Even so, topography imaging of soft sample surfaces is feasible by using IC-AFM.

In the next sections, the advanced AFM-based operation modes used in this work are explained in detail.

3.1.1 PeakForce Tapping (Pulsed Force Mode)

PeakForce Tapping (PFT) [98] or Pulsed Force Mode (PFM) [99] is an imaging mode utilizing force-distance curves recorded on each measurement point. In this operation mode, the AFM probe tip oscillates in a sinusoidal z-movement driven by the piezo incorporated into the tip holder (Fig. 3.1). In contrast to IC-AFM, PFT usually is operated at an oscillation frequency of 1 kHz or 2 kHz, which is far below the resonance frequency of the cantilever-tip system. The movement of the AFM probe tip can be precisely controlled and monitored.

The turning point of the oscillation is at the maximum force, the so-called peak force which constitutes the imaging feedback. In Fig. 3.3 the tip trajectory over time at one measurement point is presented. In "A", the tip is far away from the surface and approaches to the sample until the contact point "B" is reached. Afterwards the tip indents into the sample reaching the peak force at point "C". At the peak

force the approach process ends and the tip is withdrawn. "D" represents the maximum adhesion force between tip and sample surface during the pull-off. Finally, the tip recovers back to its original position ("E").

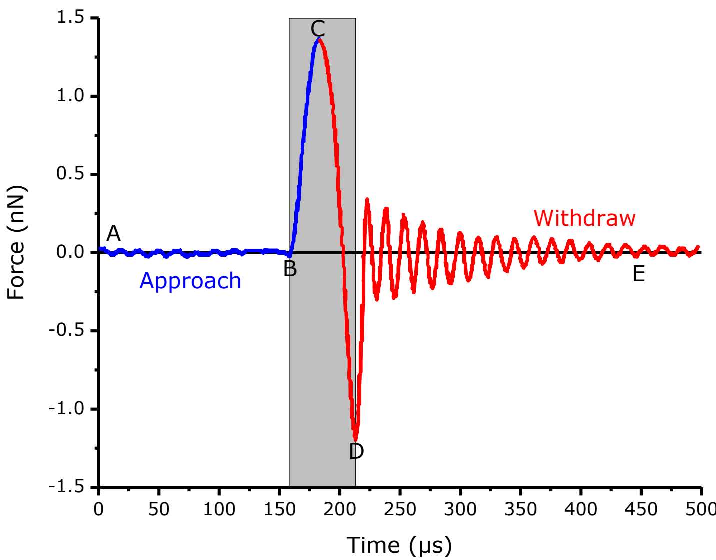

Figure 3.3. Principle of the PFT operation highlighting the force versus time during the cantilever oscillation [98]. This interaction force is evaluated by the background subtraction algorithm [100].

The typical amplitude of the oscillation is 150 nm. In some special cases, if the adhesion force is comparatively high, the amplitude must be increased to ensure that the tip is lifted from the surface. Based on the force-distance curves performed at each measurement point, several information such as the deformation, the elastic modulus or the adhesion force can be simultaneously extracted [98,101]. With respect to force control, tip wear and sample damage, PFT combines the advantages of the standard AFM modes. The vertical force applied to the sample can be controlled by adjusting or minimizing the peak force while eliminating the lateral forces as during force measurement the tip does not move laterally.

Fig. 3.4 details the background subtraction algorithm used by the PeakForce Tapping method. The z-movement creates a sinusoidal background. The peak force point in the repulsive interaction is the control parameter for the feedback loop. By subtracting the interpolated background from the total force, interaction forces in the range of some tens of pico-Newtons can be extracted. This method enables a dramatical increase of the signal-to-noise ratio and significantly improves the sensitivity for detecting even very low peak forces of a few pico-Newtons [98,100].

Consequently, tip wear and sample damage even of soft surfaces can be reduced significantly or even eliminated. These improvements compared to the standard AFM modes make PFT the proper method for high resolution topography imaging on any kind of sample surface by extracting the peak forces.

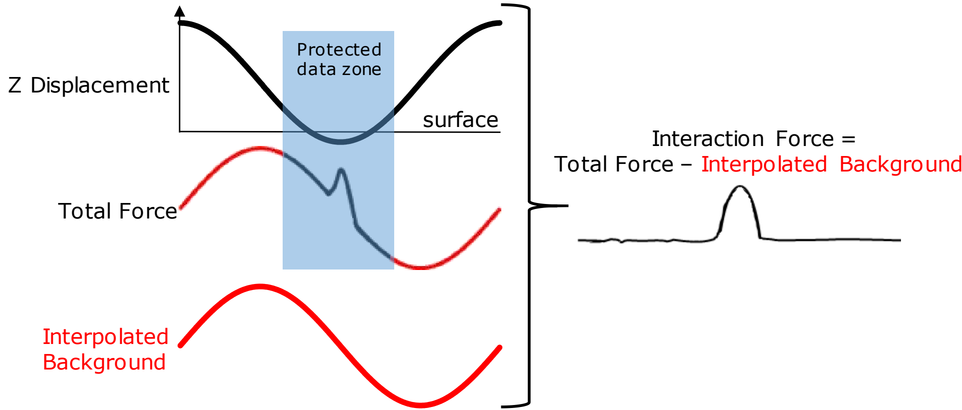

Figure 3.4. Scheme of the background subtraction algorithm. The sinusoidal Z modulation creates a sinusoidal background. Subtracting the interpolated background from the total force restores the interaction force [98,100].

3.1.2 Kelvin Probe Force Microscopy

Kelvin probe Force Microscopy (KPFM) was developed by Nonnemacher in 1991 [102] and measures the contact potential difference (CPD) between a conducting AFM probe tip and a sample. Traditionally, KPFM measurements are performed in a two-pass technique, which means that each line is scanned twice. The first scan detects the topographic structure and the second scan measures the CPD at a distinct surface distance controlled by the topography information from the first scan. This two-pass technique enables the detection of the contact potential difference unaffected by the topography.

The CPD (V_{CPD}) between the probe tip and the sample is defined as:

$$V_{CPD} = \frac{\phi_{tip} - \phi_{sample}}{-e} \tag{3.2}$$

where ϕ_{sample} and ϕ_{tip} are the work functions of the sample and the AFM probe tip and e is the electronic charge. Assuming that the tip-sample system is equivalent to a nanocapacitor, the resulting electrostatic force F_{es} between the AFM tip and the sample is given by:

$$F_{es}(z) = -\frac{1}{2}\frac{\partial C}{\partial z}\Delta V^2 \tag{3.3}$$

In this equation ΔV is the potential difference between V_{CPD} and the voltage applied to the AFM tip. For the CPD detection, the AFM probe tip is biased with a voltage V_{Tip} containing an AC (V_{AC}) and a DC (V_{DC}) component. Consequently, the potential difference ΔV will be:

$$\Delta V = V_{Tip} \pm V_{CPD} = (V_{DC} \pm V_{CPD}) + V_{AC}\sin(\omega t) \tag{3.4}$$

The $\pm$ sign in Eq. 3.4 depends whether the voltage V_{DC} is applied to the sample (+) or to the AFM probe tip (-) [103]. Substituting Eq. 3.4 into Eq. 3.3 the electrostatic force is defined as:

$$F_{es}(z,t) = -\frac{1}{2}\frac{\partial C}{\partial z}[(V_{DC} \pm V_{CPD}) + V_{AC}\sin(\omega t)]^2 \quad (3.5)$$

This equation can be divided into three parts resulting in one constant component and two frequency dependent components. The constant component F_{DC} (Eq. 3.6) results in a static deflection of the AFM tip. The component F_{ω} with the angular frequency ω (Eq. 3.7) can be used to measure the CPD voltage V_{CPD}. The $F_{2\omega}$ component (Eq. 3.8) can be used for capacitance microscopy [86], but it is neglected for the CPD detection because it does not contain any information regarding the CPD voltage.

$$F_{DC} = -\frac{1}{2}\frac{\partial C}{\partial z}(V_{DC} \pm V_{CPD})^2 \quad (3.6)$$

$$F_{\omega} = -\frac{\partial C}{\partial z}(V_{DC} \pm V_{CPD})V_{AC}\sin(\omega t) \quad (3.7)$$

$$F_{2\omega} = -\frac{1}{4}\frac{\partial C}{\partial z}V_{AC}^2[1 - \cos(2\omega t)] \quad (3.8)$$

The applied electrostatic forces to the probe tip causes a superimposition of these additional oscillating components to the mechanical oscillation of the tip. By using a Lock-in amplifier, the amplitude of the cantilever oscillation at ω is detected. According to Eq. 3.7, the V_{CPD} can be measured by applying a voltage V_{DC} in order to nullify the amplitude of the cantilever oscillation at ω and with it the component F_{ω} (Eq. 3.7) equals zero. This KPFM mode based on nullifying the measured amplitude is called amplitude modulation KPFM (AM-KPFM).

Besides AM-KPFM, the CPD can also be detected by frequency modulation KPFM (FM-KPFM). In this mode, the applied voltage V_{Tip} induces a modulation of the electrostatic force which is detected by a frequency shift at ω. In this case, V_{DC} is applied to nullify the frequency shift, thereby measuring V_{CPD}. In contrast to AM-KPFM, the changes in oscillation frequency are dependent on the electrostatic force gradient. Deduced from Eq. 3.3 and 3.7 the contribution for the FM-mode is:

$$\frac{\partial F_{\omega}}{\partial z} = -\frac{\partial^2 C}{\partial z^2}(V_{DC} \pm V_{CPD})V_{AC}\sin(\omega t) \quad (3.9)$$

Since FM-KPFM detects the electrostatic force gradient, the spatial resolution is approximately equal to the tip apex [86,104]. In AM-KPFM the electrostatic interaction includes both, the tip and the cantilever. This difference in signal detection of FM-KPFM and AM-KPFM is schematized in Fig. 3.5. As can be seen, the AM-KPFM signal detection leads to an averaging effect between the tip and the cantilever which limits the lateral resolution significantly [86,88,104]. Therefore, FM-KPFM is preferable for the nanoscale characterization of material surfaces. However, the detection sensitivity of FM-KPFM is very limited in ambient air environment because of a damping effect to the cantilever oscillation reducing the sensitivity.

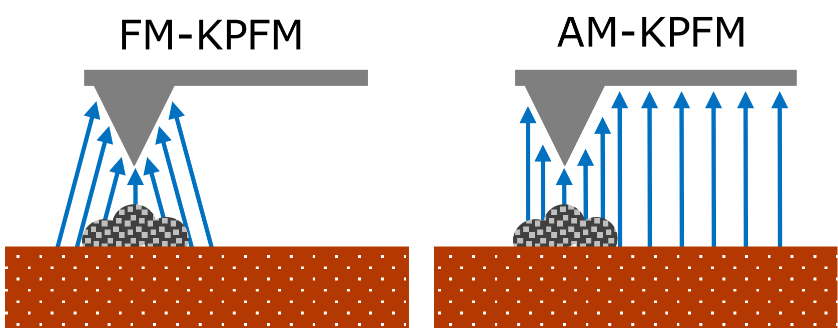

Figure 3.5. Signal distribution of FM-KPFM and AM-KPFM

The KPFM sensitivity which mainly depends on the quality factor Q of the probe oscillation and the spring constant k is defined as:

$$KPFM\ sensitivity \propto \frac{Q}{k}. \tag{3.10}$$

The quality factor relates the energy loss to the stored energy of the oscillator. A lower energy loss during probe oscillation because of a lower damping consequently results in higher KPFM sensitivity. Therefore, FM-KPFM was first realized under ultrahigh vacuum (UHV) [105] because the Q-factor of the AFM probe can be hundreds of times larger than in air.

The PeakForce Kelvin Probe Force Microscopy (PF-KPFM) is a further development of the FM-KPFM technique with improved sensitivity and repeatability in ambient air [106]. The advantages of PF-KPFM are closely linked to appropriate AFM probe tips with higher quality factor and lower spring constant providing higher KPFM sensitivity according to Eq. 3.10. The use of such probes is enabled by the combination of PFT and FM-KPFM. In a two-pass scan, at first the topographic structure is obtained by PFT and subsequent the CPD is detected by FM-KPFM at a distinct surface distance.

Additionally, it is important to note that in ambient air environment usually a water layer is present on top of the sample surface and that this water layer influences the CPD result significantly [91,104]. Referred to Eq. 3.2, a direct characterization of the sample's work function requires the prior identification of the work function of the AFM probe tip. This could be acquired by measuring the CPD of a sample surface with a known work function. However, quantitative results can only be obtained in ultrahigh vacuum conditions because, besides the potential shielding by the surface water layer [91], the work function is very sensitive to adsorbates [107] or oxidation [104].

Due to the advantages of PF-KPFM related to the improved lateral resolution of FM-KPFM and the better sensitivity compared to conventional FM-KPFM in ambient air, PF-KPFM was taken as preferred tool to investigate CPD variations on sample surfaces in the nanoscale.

3.1.3 Dynamic Chemical Force Microscopy

The dynamic Chemical Force Microscopy (dCFM) [108,109] is a further development of the conventional Chemical Force Microscopy (CFM) which is an advanced measurement method based on the atomic force microscopy for the chemical imaging of a material surface [110,111]. dCFM as well as the conventional CFM use chemical functionalized AFM probe tips interacting with the sample surface to achieve a chemical contrast on the surface. Chemical mappings achieved by CFM are based on lateral force microscopy (LFM) [111]. LFM is very similar to the standard contact mode because the AFM probe tip is also in physical contact with the surface. The difference of both techniques is the analysis of the signals. As contact mode evaluates the vertical deflection of the AFM probe tip for topography imaging, lateral force mode utilizes the torsional deflection of the AFM tip. A tip-sample interaction influenced by the chemical tip functionalization causes a torsional deflection of the tip depending on chemically induced interaction forces. As a consequence, the chemical functionalized AFM probe tip can map chemically different regions on the sample [112]. However, topography features can also cause such a torsional deflection. Therefore, CFM by using LFM is only reasonable on very flat surfaces [111,112]. Beside using LFM, individual points with chemical information can be achieved by performing force-distance curves [113]. The functionalized AFM probe tip is brought in contact with the surface and afterwards retracted. During the retraction, the adhesion force $F_{Adhesion}$ between functionalized probe tip and sample surface is detected. A strong chemical interaction is a measure for a high adhesion force [111,113].

The further development of the dynamic Chemical Force Microscopy is based on force-distance curves which are applied at multiple measurement points [108,109]. The AFM operates in the sinusoidal z-movement as mentioned for the PeakForce Tapping mode [98] which was already introduced in section 3.1.1. The principle of dCFM can be seen in Fig. 3.6. The turning point of the probe tip z-movement is defined by a maximal force F_{max}. Similar to the evaluation of individual force-distance curves, in dCFM the adhesion force $F_{Adhesion}$ is a measure for the molecular forces between the functionalized probe tip and the sample. As shown in Fig. 3.6 a chemically different sample surface results in a different adhesion force $F_{Adhesion}$. In dCFM the combination of the sinusoidal z-movement and the usage of functionalized probe tips enables the chemical imaging on a very local scale independent of the surface topography [108].

Since dCFM enables the chemical mapping of the sample surface without disturbances related to the topographic structure, this analysis technique was chosen as appropriate tool for further investigations of chemical nanoscale differences on the sample surface.

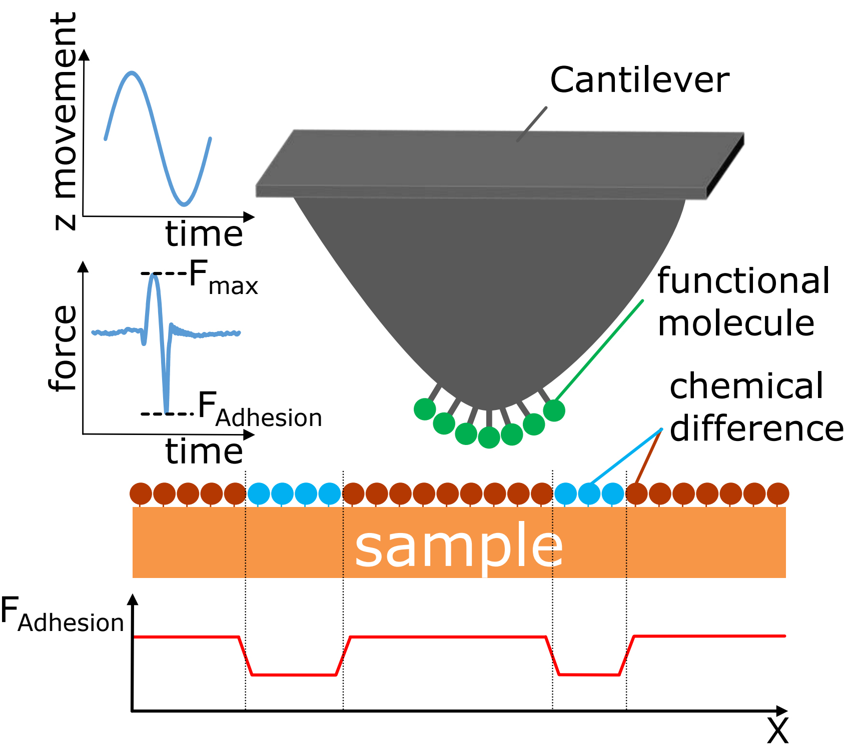

Figure 3.6. Principle of the dynamic Chemical Force Microscopy. By using a chemically functionalized probe tip, a chemical difference on the sample surface can be detected by the variation of the adhesion force. The functionalized tip operates in dynamic sinusoidal mode in z-direction and interacts with surface molecules. The maximal force F_{max} defines the turning point of the probe tip z-movement.

The environment for the chemical interaction based imaging is very important in determining the adhesion forces. dCFM measurements carried out in ambient air are more difficult to interpret since capillary forces are usually 1-2 orders of magnitude higher than specific chemical interactions [111] and obscure the chemical interaction between functionalized tip and sample. Such capillary forces are based on the water layer which is usually present on top of a sample surface in ambient air environment. Therefore, dCFM has to be performed with both, the functionalized probe tip and the sample surface, immersed in liquid. This liquid environment enables the detection of the exact adhesion force caused by the sample surface under investigation and the functionalized probe tip. However, besides the better chemical sensitivity due to the immersion in liquid, it has to be taken into account that the cantilever movement in fluid can be influenced by an additional deflection caused by the fluid resistance. For the exact determination of any influencing drag forces, a fluid dynamics simulation based on the finite element method (FEM) was performed and is introduced in chapter 5.

3.1.4 Torsional Resonance Tunneling Atomic Force Microscopy

Torsional Resonance Tunneling Atomic Force Microscopy (TR-TUNA) [114–116] is an advanced measurement technique for the electrical characterization of delicate samples. Beside the introduced standard operation modes, such as contact mode or intermittent contact mode, the torsional resonance (TR) operation mode is a contactless measurement technique which enables the electrical characterization without damaging neither the AFM tip nor the delicate sample surface. Fig. 3.7 shows a schematic illustration of the basic working principle of the TR operation mode. Two piezo actuator plates (red in Fig. 3.7) incorporated into the tip holder are used for the excitation of the torsional oscillation. In TR mode the feedback error is modulated by the TR amplitude change with respect to the tip-sample distance. The feedback loop controlled by the TR amplitude maintains the tip/surface relative position through lateral interaction.

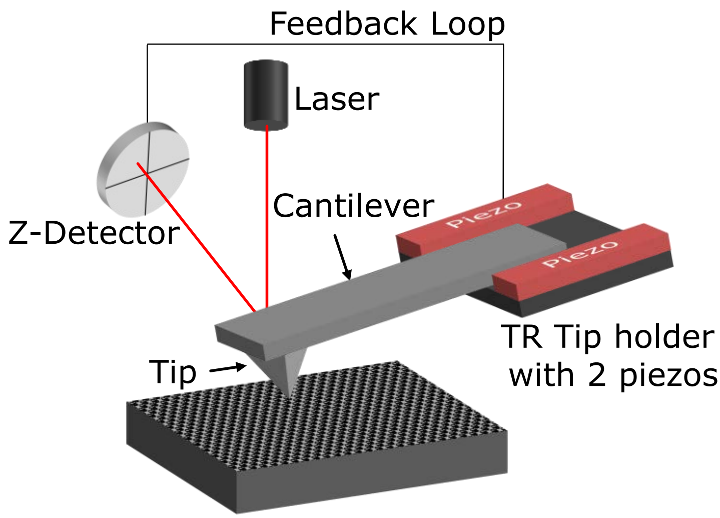

Figure 3.7. Basic working principle of the TR operation mode.

The topography imaging of very soft samples could also be performed by IC-AFM. However, the additional electrical characterization is not possible, which is obvious by comparing the AFM tip oscillation of IC-AFM and TR-AFM in Fig. 3.8. In IC-AFM the probe tip just taps the sample surface in a vertical movement and thus, the contact time, only 1% of the oscillation cycle, is too short for the current measurement [116].

In general, the standard operation mode for electrical measurements is the contact mode. The AFM tip is in physical contact with the sample surface and the current flow can be detected by a current sensor, provided that a conductive probe tip is used and an appropriate bias voltage is applied. However, as mentioned previously in the introductive part of section 3.1, the mechanical forces applied in the contact

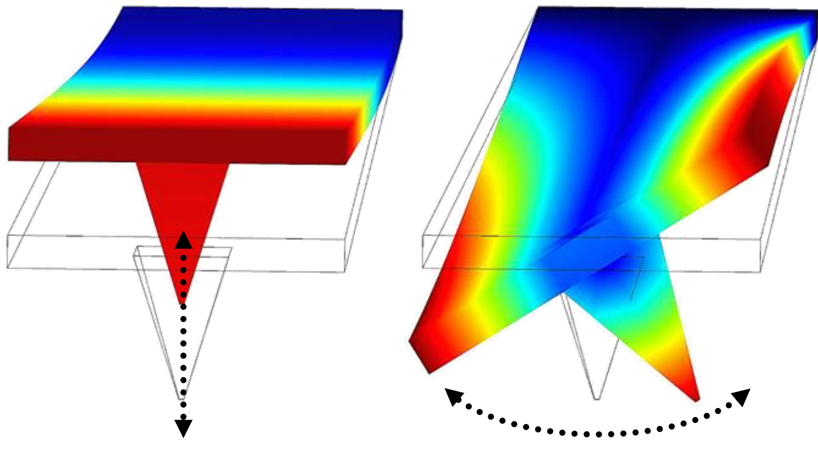

Figure 3.8. Comparison of AFM tip oscillation of IC-AFM (left) and TR-AFM (right)

mode can damage the sample surface. Thus, especially for the characterization of very delicate samples, the contact mode is not suitable.

By using the TR mode, the probe tip oscillates in torsional resonance in close proximity (typically 0.3-2 nm [117]) of the sample surface. This near field condition provokes that by applying an appropriate bias voltage the electrons can overcome the barrier between the conductive probe tip end and the sample surface and the tunneling current can be measured. Based on these near-field characteristics, the TR mode enables the ability to measure the current flow and simultaneously the topographic feedback is modulated by the TR amplitude.

3.2 Scanning Electron Microscopy

McMullan [118] presented the early history of the Scanning Electron Microscopy (SEM). In 1925 the German physicist Hans Busch developed the electron lens. He found out that a magnetic field can be used as a lens for electrons similar as a glass lens for a light beam. These results formed the background for the further development of the electron microscope. The first scanning electron microscope with a submicron probe was developed by the natural scientist Manfred von Ardenne in 1937. In today's scanning electron microscopes, the electron beam is generated by a thermionic field emission cathode, a so-called Schottky cathode. In this type of electron source a zirconium oxide (ZrO) reservoir combined with a mono-crystal tungsten tip is heated by a heating current up to 1800 K. By applying an additional electric field, the ZrO diffuses to the cathode tip and emits electrons. Besides the thermionic field emission, an alternative electron source consists mainly of a very sharp tungsten wire which is heated or to which an electric field is applied. The Schottky cathode combines both systems and has the advantage of comparatively higher beam intensities and improved image quality even at low acceleration voltages.

The electron beam is focused on the sample surface by using magnetic and electrostatic lenses and the area of interest is scanned line by line. The measurement is performed in a high vacuum chamber to prevent any disturbances of the electrons caused by any particles existing in an air environment. For the image formation in SEM operations, the primary electron beam interacting with the sample surface generates two fundamental electron types, the secondary electrons (SE) and the backscattered electrons (BSE). For the imaging of the topography, the low-energetic secondary electrons provide the topographic information. Their energy is in the range up to 50 eV. They are released by inelastic scattering of the primary electrons on the atomic core or on the electrons in the atomic orbitals. Due to its low energy, only the electrons near the surface are responsible for the image creation, because most of the energy is lost within a few nanometers. A more accurate view on the energy loss of the electrons provides a Monte Carlo simulation of electron trajectories. The simulation result in Fig. 3.9 shows that electrons with an energy of 100 eV lose most of their energy within 10 Å (1 nm) inside a silicon material. Even though the energy loss differs slightly for other materials, this confirms that only SE near the surface provide the topographic information because SE released in deeper regions are predominately absorbed in the material.

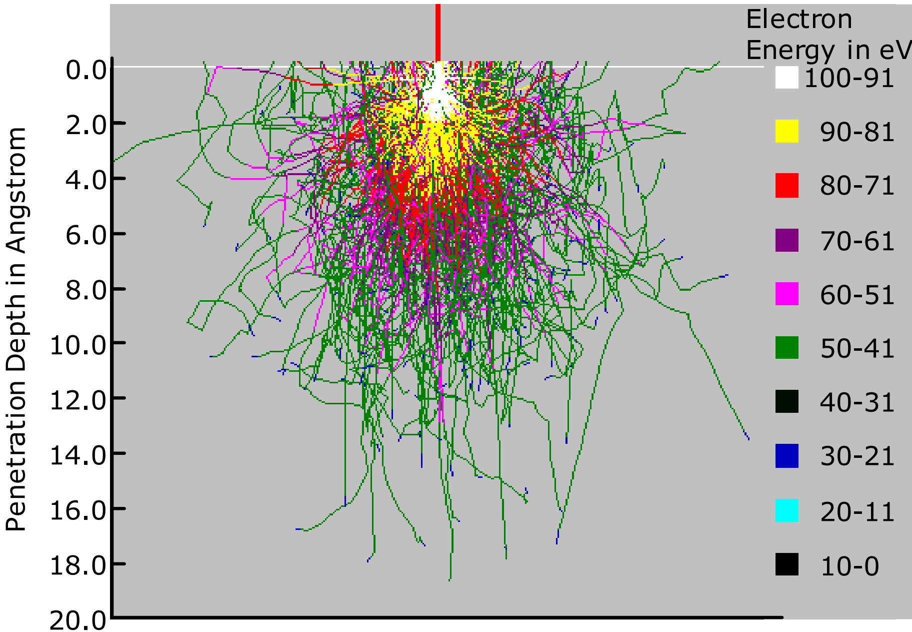

Figure 3.9. Monte Carlo simulation of electron trajectories presenting the energy loss of low-energetic electrons in silicon (Si).

The backscattered electrons are high energetic electrons interacting with the material by elastic scattering. They can have energies up to 100% of the primary electron's energy. Since they are created in a much deeper region of the excitation volume than the secondary electrons, they contain a depth information and provide a material contrast. Since materials with different densities or atomic numbers provide

different BSE energies, a resulting energy variation can be assigned to a material change. Additionally, it is worth noting that there is a clear correlation of material density and achieved BSE energy. Besides the material contrast, the detection of the BSE energies also achieves a crystal orientation contrast because different crystal orientations can also influence the electrons in different ways.

For the detection of SE or BSE different sensors are arranged inside the vacuum chamber which is depicted in Fig. 3.10. The SE2-detector, also known as Everhart-Thornley-detector, is arranged on the left side in the vacuum chamber and mainly detects secondary electrons for the topography imaging. Additionally, due to the geometrical arrangement, the SE2-detector also detects backscattered electrons. However, only 10% of the imaging signal are from BSE and thus, the resulting image represents the surface topography superimposed with a weakly visible material contrast.

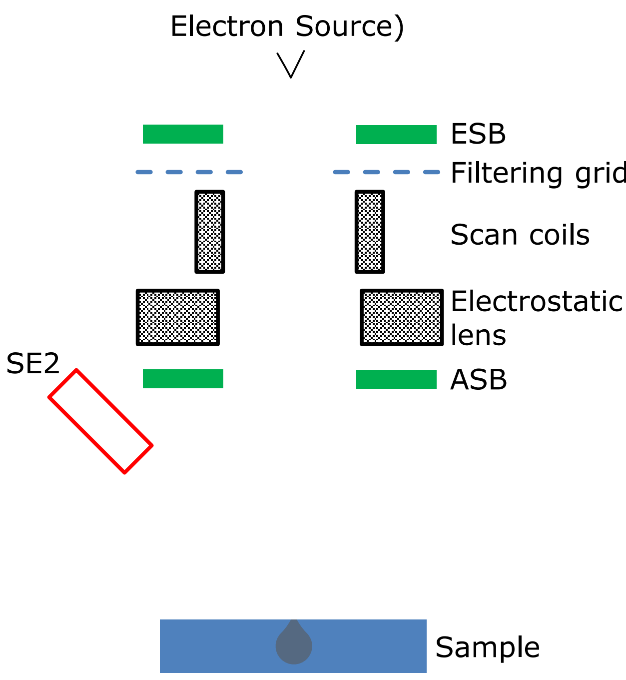

Figure 3.10. Schematic drawing of the geometrical arrangement of the detectors in the vacuum chamber and in relation to the beam control.

Further detectors presented in Fig. 3.10 are the angle selective backscatter (ASB) detector and the energy selective backscatter (ESB) detector. These both detectors are integrated for the detection of the backscattered electrons. Fig. 3.10 shows that they are arranged very near to the primary electron beam. The ASB-detector is mounted directly below the last electrostatic lens and detects mainly the low angle backscattered electrons which originate mostly from an area outside the beam spot center. Because of this signal origin, the identification of nanostructures is limited. Additionally, for applications related to low acceleration voltages below 3 kV, the ASB-detector is not suitable. For such applications, the ESB-detector is the appropriate choice because its geometrical arrangement directly in the beam path of the SEM system above a filtering grid (Fig. 3.10) enables the detection of high angle backscattered

electrons. This type of BSE originates from the very near of the spot center and hence offers an improved lateral resolution compared to the low angle backscattered electrons detected by the ASB-detector. Furthermore, the filtering grid ensures that only backscattered electrons with an energy higher than the desired energy are used for the image formation and secondary electrons can be discarded. For this reason, the ESB-detector can be used for imaging the material contrast structures or particles in the nanoscale by using low acceleration voltages (~1 kV) and low working distances smaller than 4 mm.

Besides the nanoscale imaging of the topography and the material contrast of the sample, the SEM offers additional techniques for material characterization. By using these advanced measurement techniques, it is able to investigate the element composition of the sample quantitatively as well as the crystal structure and the distribution of the grain size. These special methods are explained in detail in the next sections.

3.2.1 Energy Dispersive X-ray Spectroscopy

Energy Dispersive X-ray Spectroscopy (EDX) is an important measurement technique for material analysis and enables the determination of the element composition or the chemical characterization of a sample quantitatively. This can be done by detecting the X-ray characteristics of each element in the sample stimulated by an electron beam. The fundamental principle of the X-ray characteristics is shown in Fig. 3.11. Due to an external stimulation such as the electron beam, an electron from an inner shell e.g. the K-shell is kicked out. As this state is unstable, the remained vacancy is filled immediately by a higher energetic electron from a higher atomic orbital e.g. the L-shell. The energy difference between the higher energy shell and the lower energy shell is released in the form of X-ray radiation. The X-ray

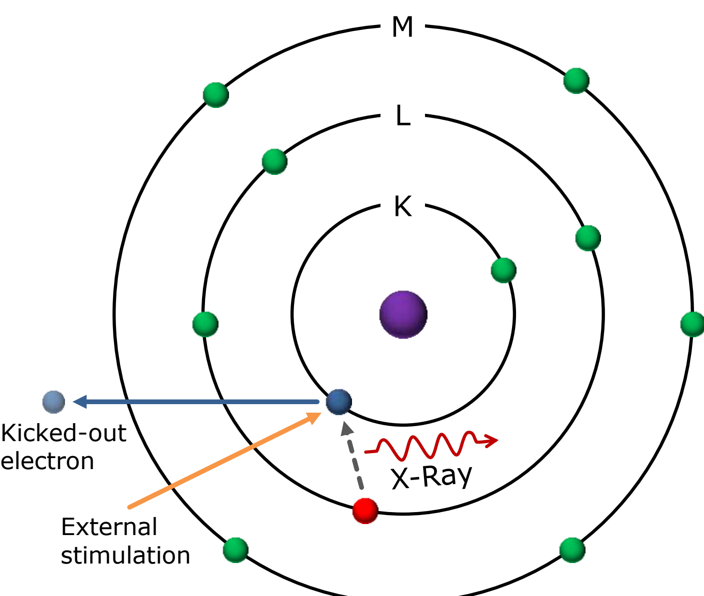

Figure 3.11. Fundamental principle of X-ray spectroscopy. An electron is kicked out from its shell by an external stimulation. An electron from a higher energy shell fills the vacancy and releases its energy in form of X-ray radiation.

energy strongly depends on the energy difference between the two shields and on the atomic structure of the element. For this reason, each element has its characteristic X-ray radiation and can be identified clearly by the EDX-detector.

The spatial resolution of EDX is limited by the beam interaction with the sample and the origin of the X-rays. In contrast to the SE and BSE electrons which are generated in the very near of the sample surface, the characteristic X-rays originate from a deeper region in the material. In Fig. 3.12 a schematic of an interaction volume generated by the electron beam excitation is depicted. The interaction volume is also often called excitation bulb because of its general form. Besides the characteristic X-ray radiation for the EDX analysis and the SE and BSE electrons for SEM image formation, there are also Auger electrons and the continuum X-ray radiation, also known as bremsstrahlung, in the interaction volume. The Auger electrons are another interaction product by the external stimulation and can be analyzed by Auger electron spectroscopy (AES). However, AES is not part of this work and thus, it is not explained further.

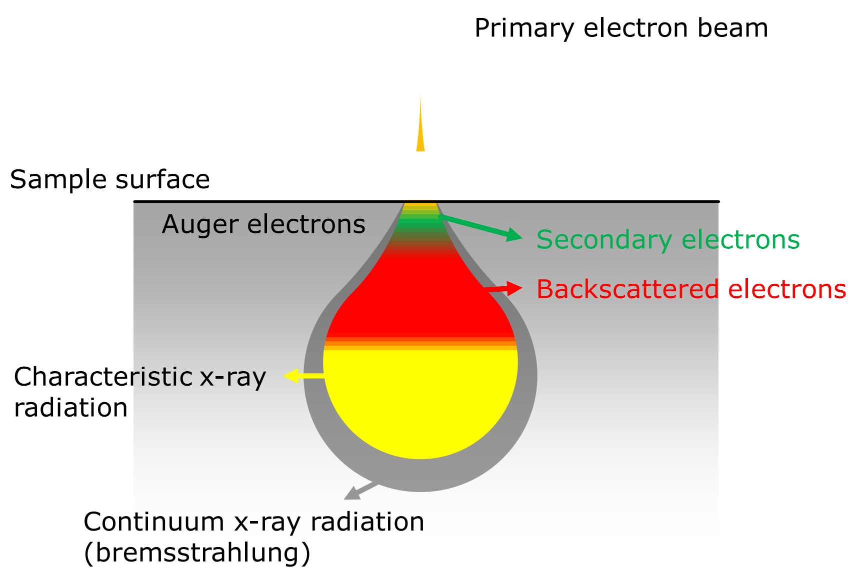

Figure 3.12. Interaction volume originated by an electron beam hitting the sample surface.

The continuum X-ray radiation is a by-product of the electron excitation. A part of the primary electrons is decelerated by the Coulomb fields of the atomic nuclei and the kinetic energy of the electrons is converted into electromagnetic radiation, the so-called bremsstrahlung. In case of the EDX analysis, this bremsstrahlung is an unwanted by-product which must be subtracted for quantitative characterization. The arrangement of the EDX-detector related to the remaining SEM system in Fig. 3.10 is depicted in Fig. 3.13.

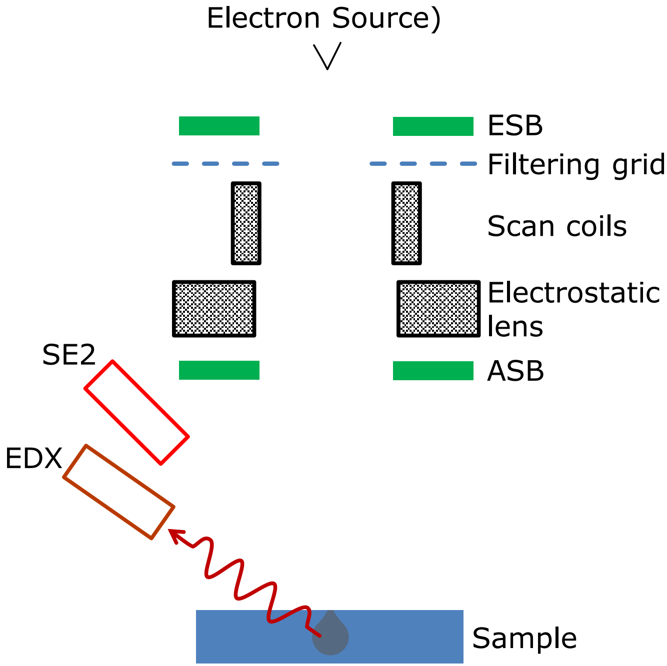

Figure 3.13. Schematic drawing of the geometrical arrangement of the EDX-detector in the vacuum chamber in relation to the remaining SEM system in Fig. 3.10.

3.2.2 Electron Backscatter Diffraction

Similar to EDX, the Electron Backscatter Diffraction (EBSD) is another advanced measurement technique in the field of material analysis. EBSD is able to determine the crystal structure, the orientation and the grain distribution of any crystalline or polycrystalline material. The fundamental principle of EBSD is based on the consecutive interference of waves, here associated with an incident electron beam, reflected by the crystalline lattice which forms the electron backscatter diffraction pattern on a phosphor screen. Such diffraction patterns was first reported by Nishikawa and Kikuchi in 1928 [119] and hence they are also known as Kikuchi patterns. In order to obtain high quality Kikuchi pattern, the geometrical arrangement of the measurement equipment shown in Fig. 3.14 is very important. The sample surface must be arranged in an angle of 20° to the incident electron beam. In general, this arrangement is performed by tilting the stage with the sample mounted for 70°. The EBSD-detector illustrated in Fig. 3.14 consists of a camera focused on the phosphor screen on which the Kikuchi patterns fluoresce.

The geometry of the Kikuchi patterns can be identified as the projection of the crystal lattice on the phosphor screen. The primary beam electrons with a wavelength comparable to the atomic spacing interact with the crystalline lattice and low energy loss backscattered electrons undergo constructive interference.

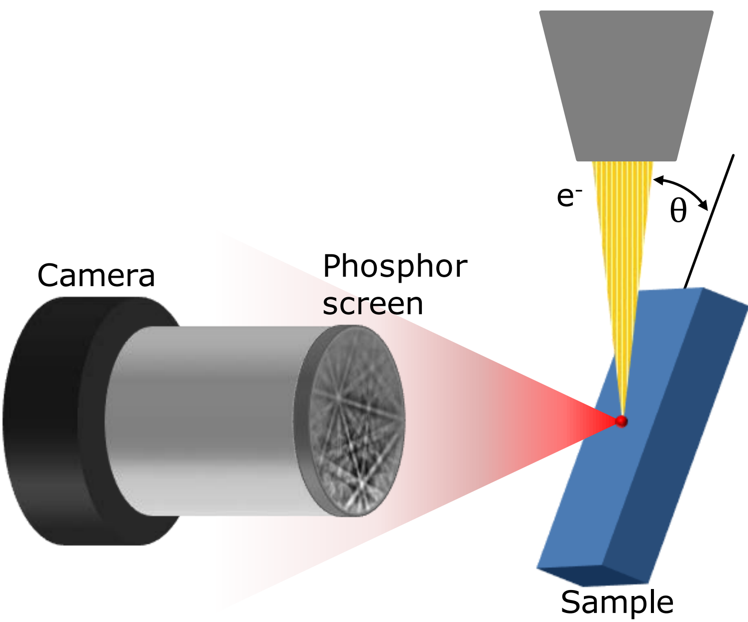

Figure 3.14. Schematic drawing of the EBSD-detector, consisting of a phosphor screen and the CCD camera, arranged in angle of 70° to the sample.

The condition for this constructive interference is called the Bragg condition and is defined as:

$$n\lambda = 2d\sin\theta \tag{3.11}$$

where n is a positive integer, λ is the wavelength, d represents the lattice constant and θ is the angle of incidence. Two waves are subject to constructive interference if the path difference given by $2d \cdot \sin\theta$ is equal to the integer multiple of the wavelength λ. A further explanation of the Bragg condition yields Fig. 3.15. The red lines are waves hitting parallel lattice planes with the atomic spacing d. If the difference of the path length of the two waves is equal to $2d\sin\theta$, they remain in phase and interfere constructively. At an angle Θ of 20° of the incident wave to the atomic lattice, the constructive

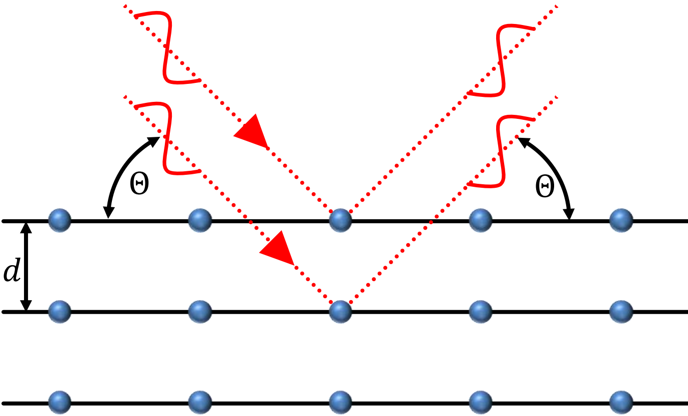

Figure 3.15. Bragg condition fundamental for the EBSD measurement. Two waves (red dotted) interfere constructively if the path length 2d sinθ is equal to the integer multiple of the wavelength nλ

interference is strongest and thus, the Kikuchi pattern exhibits the best contrast. Therefore, the EBSD-detector must be arranged as shown in Fig. 3.14.

The spatial resolution of EBSD is strongly related to SEM conditions such as electron beam spot size and acceleration voltage [120–122]. Based on these influencing factors and the mentioned literature, the approximately range of the spatial resolution can be estimated to be 20 to 60 nm. Additionally, Chen et al. [122] reported that the depth resolution depends on the crystal structure of the material and the acceleration voltage of the SEM. Especially for copper, they indicated that the depth resolution for Cu ranges from 3.98 nm at an acceleration voltage of 20 kV and a probe current of 40 nA to 7.87 nm at 30 kV and also 40 nA. Consequently, these values with respect to the spatial and depth resolution shows that EBSD analysis of Cu surfaces are able to map crystallographic differences of nanoscale structures.

3.3 Fourier Transform Infrared Spectroscopy

The Fourier Transform Infrared Spectroscopy (FTIR) is a measurement technique belonging to the molecule spectroscopy and basically relies on the excitation of energy states of molecules by infrared radiation. In detail, FTIR measures the absorption of an infrared beam with a distinct wave length or wave number. The molecules of the sample absorb the infrared beam at specific wave numbers depended on their characteristic structure. This absorption is based on the vibration modes of the molecules. As an example, three characteristic vibration modes of a CH_2 molecule can be seen in Fig. 3.16. Each vibration mode results in an absorption of the incident infrared beam at specific wave numbers. Related to the example in Fig. 3.16, the symmetrical stretching of the CH_2 molecule offers an absorption band at 2850 cm^{-1}, the asymmetrical stretching at 2918 cm^{-1} and the rocking absorption at 718 cm^{-1}.

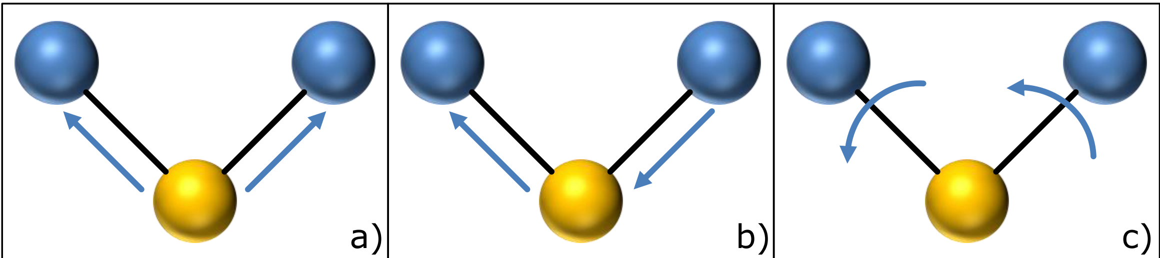

Figure 3.16. Three characteristic vibration modes of a CH_2 molecule. a) symmetrical stretching b) asymmetrical stretching c) rocking

The detection of such molecular vibrations can be performed by FTIR. Basically, a spectroscope consists of a Michelson Interferometer, which is a certain configuration of mirrors. The schematic drawing of a Michelson interferometer adapted for FTIR is presented in Fig. 3.17. The polychromatic infrared (IR) source is a black-body radiator. The light is collimated and directed to a beam splitter which splits up the beam towards a fixed mirror and a movable mirror.

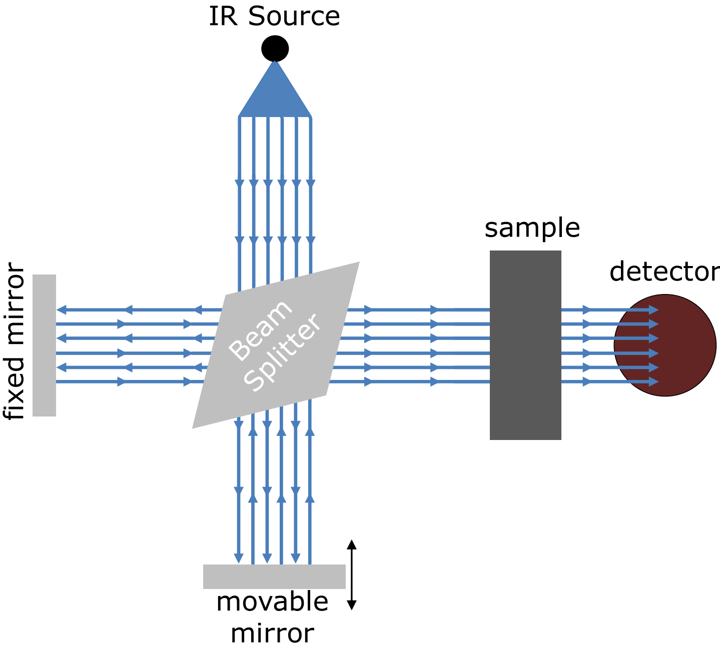

Figure 3.17. Schematic drawing of a Michelson interferometer adapted for FTIR. The reflected light from the two mirrors is directed to the sample and the transmitted beam after the interaction with the sample is analyzed by the detector.

Subsequently, the reflected light from the two mirrors is consolidated by the beam splitter again and directed to the sample. Depended on the frequencies contained in the IR beam and the position of the movable mirrors, the consolidating beams results in an interferogram as seen in the left image in Fig. 3.18. The maximum of this interferogram correlates with the position at which the length of path to the movable mirror is the same as to the fixed mirror. At this position, all the frequencies in the beam interfere constructively. By the usage of the Fourier transformation this interferogram can be converted into a single beam spectrum as shown in the right image in Fig. 3.18. This single beam spectrum in Fig. 3.18 corresponds to a measurement without a sample present. Therefore, this spectrum contains all environmental based influences and thus, it is called the background spectrum. For each measurement, this background spectrum must be subtracted to achieve the absorbance bands of the sample.

The schematic drawing in Fig. 3.17 represents the FTIR configured for the detection of the IR beam transmitted through the sample. Since in this work FTIR analysis are used for the characterization of Cu based structures, the transmittance configuration is not suitable because the IR beam is totally reflected from the Cu surface.

Therefore, the FTIR must be adapted for the analysis of the reflectance of the sample surface. In Fig. 3.19, the schematic drawings of two configuration setups suitable for reflectance FTIR are depicted. In both techniques, the IR beam interacts with surface layers such as oxide films or any other additional layer under investigation and is then reflected to the detector. In the specular reflectance FTIR, the IR beam is guided in an angle of 20° to the sample surface and is reflected to the detector after the

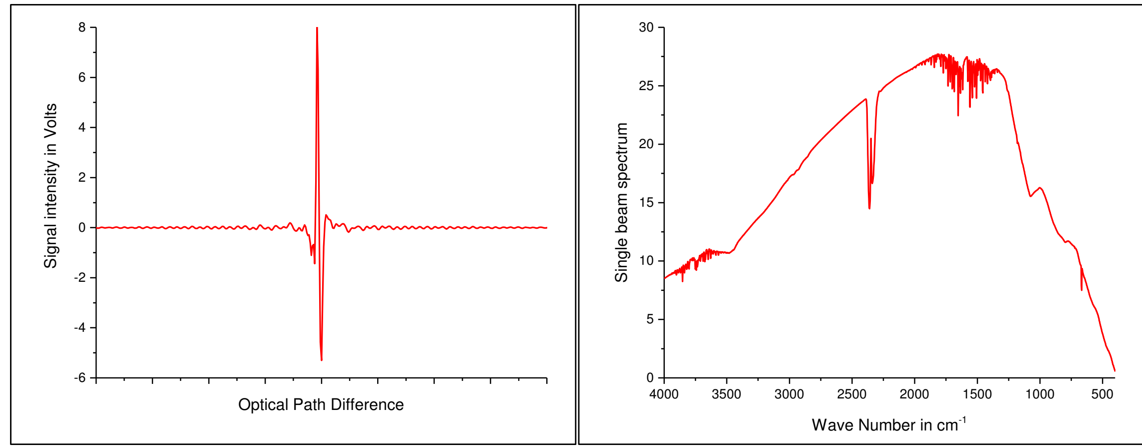

Figure 3.18. Interferogram (left) and Fourier transformed spectrum (right).

interaction. In contrast, the Attenuated Total Reflectance (ATR) FTIR uses a special ATR-diamond which is in contact with the sample surface and the IR beam is guided through this diamond to the sample and reflected after the interaction to the detector. Since the IR beam run through the surface layer under investigation twice, the interaction volume for the analysis is doubled, too.

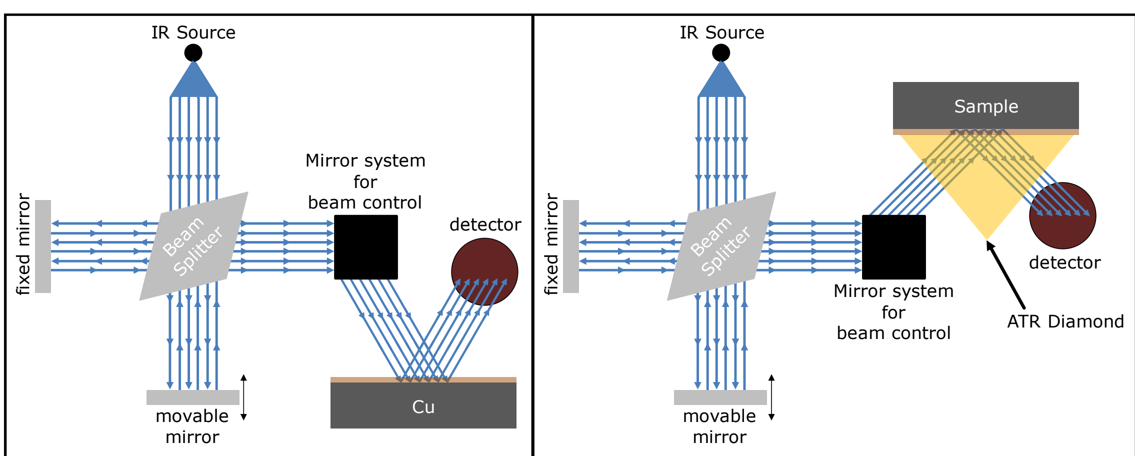

Figure 3.19. Schematic drawing of the FTIR configured for specular reflectance FTIR (left) or Attenuated Total Reflectance FTIR (right)

It is evident that both methods can be appropriate tools to characterize even very thin surface layers. However, as can already be assumed from Fig. 3.19, the lateral resolution is very limited because of the diameter of the IR beam exciting the sample surface. In this work, the equipment used provides an IR beam diameter of approximately 1 mm. Therefore, FTIR is rather stated to be a macroscopic measurement technique. Nevertheless, it can be very suitable as an additional analysis method to the microscopic measurement techniques, because it can reliably detect molecules such as Cu_2O or CuO and does not need any specific sample preparation.

4. Nanoscale characterization of copper oxide by KPFM

Copper (Cu) has become an important metallization material in semiconductor manufacturing. Notwithstanding the importance of Cu metallization, wire bonds are still predominantly made of gold wires due to their key advantages such as flexibility and reliability [8]. In comparison to gold, copper is cheaper and it possesses an increased thermal and electrical conductivity. However, one of the main drawbacks of Cu is that the surface is subject to oxidation, even at room temperature. Chuang et al. [28] demonstrated that the oxidation of the Cu bond pad influences the quality and the reliability of the bond contact. Ho et al. [29] observed that, even within the same lot of identically processed wafers, some contact structures are bondable, whereas others are not and associated their observation to the oxidation behavior of the Cu bond pad. Few researchers have addressed the problem of the Cu oxidation by coating the copper surface with an additional metal layer or a thin organic self-assembled monolayer (SAM) in order to prevent the oxidation [29,123–125]. However, due to the elevated bonding temperature the surface oxidation cannot simply be neglected and has to be taken into account. For manufacturing of reliable and predictable copper wire bonds and the development of respective industrial processes additional research is necessary to analyze the oxidation behavior of the bond pad and the role of possible other contaminations.

The characterization methods predominantly used in recent studies have been X-ray Diffraction (XRD) and X-ray Photoelectron Spectroscopy (XPS) [28,126,127]. Even though these methods are suitable for detecting the oxidation states of the Cu pad, they allow only limited lateral resolution due to the excitation by an X-ray beam and therewith a correlation between small topography features and oxidation state remains unstudied. PeakForce Kelvin Probe Force Microscopy (PF-KPFM) [106] has the potential to address these needs. PF-KPFM is a modification of the common Kelvin Probe Force Microscopy (KPFM) [86–88] and enables the measurement of the Contact Potential Difference (CPD) of material surfaces with high lateral resolution at ambient environment. The CPD value is related to the work function of the surface. However, a direct characterization of the oxidation state by comparing a theoretical CPD value of the Cu oxide with the measured CPD value was not possible. Local variations of surface properties and related work function values and, as reported by Sugimura et al. [91], the presence of a surface water layer in ambient environment, which shields the CPD value, are reasons for this observation. Therefore, I used Energy Dispersive X-ray Spectroscopy (EDX) and Fourier Transform Infrared Spectroscopy (FTIR) as reference measurements and correlated the CPD values achieved by PF-KPFM with the corresponding Cu oxide state detected by EDX and FTIR. As a result, PF-KPFM measurements in air enabled to distinguish between the different types of Cu oxide with nanometer resolution and to correlate the oxidation states to local topography features. In this work, I show that the combination of different measurement techniques facilitates the advanced characterization

of the oxidation behavior of the Cu surfaces, the investigation of thin oxide films and the correlation of local topography changes to the corresponding oxidation state.

4.1 Experimental

In this work the key method used for the characterization of thermally grown Cu oxides is PF-KPFM. However, as PF-KPFM performed in air environment is subject to diverse disturbances, it is important to validate the data achieved. For this reason, EDX and FTIR are employed and specific details are introduced in this section. The basic principle of EDX and FTIR were explained in section 3.2.1 and 3.3, respectively. Fig. 4.1 shows the schematic cross-section of the Cu test samples used in this study.

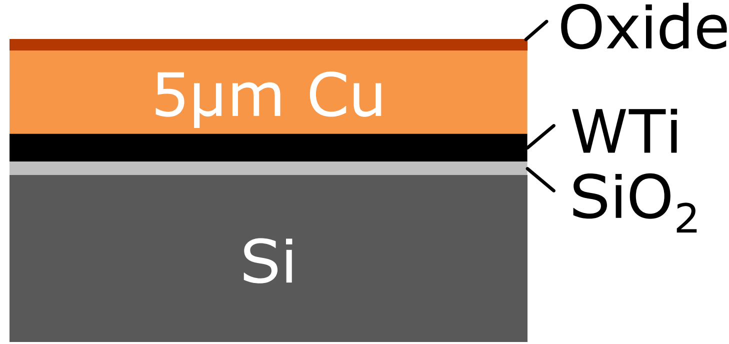

Figure 4.1. Schematic cross-section of test samples consisting of a 5 µm PVD copper layer on top of a Si base separated by a thin SiO_2 film and a WTi liner.

The 5 µm thick Cu layer was deposited by plasma vapour deposition (PVD) sputtering on top of a supporting sample structure consisting of a tungsten titanium (WTi) liner on a silicon (Si) base with a thin silicon dioxide (SiO_2) film. The PVD sputtered 5 µm Cu shows a well-defined surface structure (Fig. 4.2). Individual grains and grain boundaries may clearly be identified and the grains offer a uniform grain orientation Cu(111) measured by Electron Backscatter Diffraction (EBSD). In order to achieve sufficient thick cupric oxide CuO and cuprous oxide Cu_2O for the EDX and the FTIR investigations the Cu samples were oxidized, according to the literature [46,128], on a heater in ambient air for two hours at 300 °C and for 24 h at 120 °C, respectively. Comparatively thin oxide films were generated by oxidizing for two and five minutes at 200 °C, which is based on real bonding conditions [19]. Prior to oxidation, the samples were chemically cleaned with an aqueous solution of 10% sulfuric acid to remove the native oxide and contaminations and subsequently rinsed with a 1:1 solution of ultrapure water and isopropanol. Except for the measurements, the samples were constantly stored in a dry air environment (~23°C, 0% humidity) to prevent surface contamination and to reduce the influence of a water layer on the sample surface.

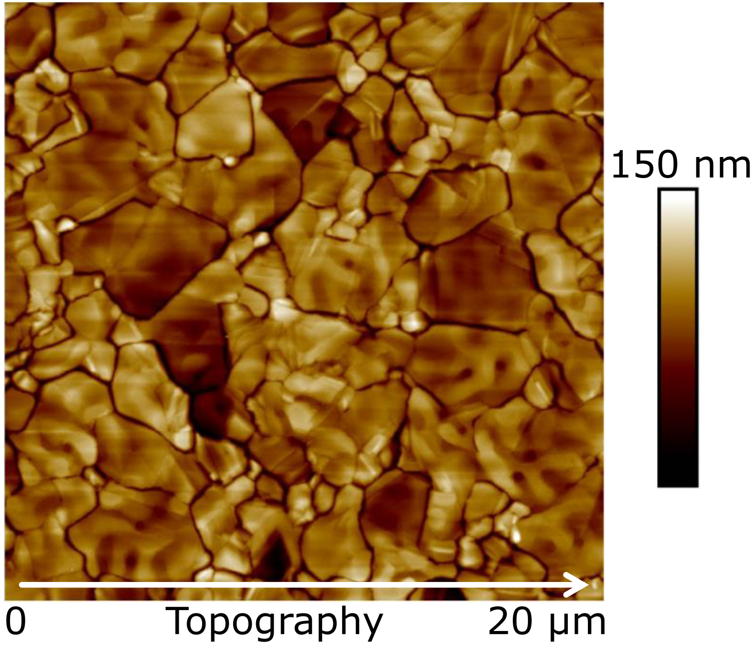

Figure 4.2. AFM topography image of the copper surface.

In this experiment, a Zeiss Ultra 55 scanning electron microscope equipped with the EDAX Trident system and an Energy Selective Backscatter Detector (ESB) was used to perform EDX, EBSD and Backscattered Electron (BSE) imaging. EDX is able to measure the element content quantitatively and was employed to identify the oxidation state by the ratio of the atomic weight of Cu to oxygen (O). However, this is only applicable for comparatively thick oxides, which were grown purposely for these experiments. For thin oxide layers and small oxide particles in the nm range the capabilities of EDX are limited because of the penetration depth caused by the electron beam. The acceleration voltage used was 3 kV. Based on the SEM parameters I performed a Monte Carlo simulation of electron trajectories using the software tool electron flight simulator (EFS). EFS simulates the electron beam penetration by the energy loss resulting from inelastic collisions in-between individual elastic scattering events [80].

In Fig. 4.3 the result of the Monte Carlo simulation can be seen. I computed a penetration depth at 3 kV of approximately 60-70 nm for bulk Cu_2O with a density of 6.0 g/cm^3 and a depth of about 50-60 nm for bulk CuO with a density of 6.32 g/cm^3. For comparison, the derived values can be evaluated by calculating the X-ray generation depth with the formula of Castaing [129]. The formula is given by

$$z_m = 0.033(E_0^{1.7} - E_C^{1.7})\frac{A}{\rho Z} \qquad (4.1)$$

where z_m denotes the X-ray generation depth or analytical depth, E_0 is the acceleration voltage in keV, E_C denotes the minimum emission voltage in keV for the bulk element, A denotes the atomic mass in g/mol of the bulk element, ρ denotes the density in kg/m^3, and Z denotes the atomic number of the bulk element. Since in this study the Cu oxide compounds are investigated, the necessary parameters of

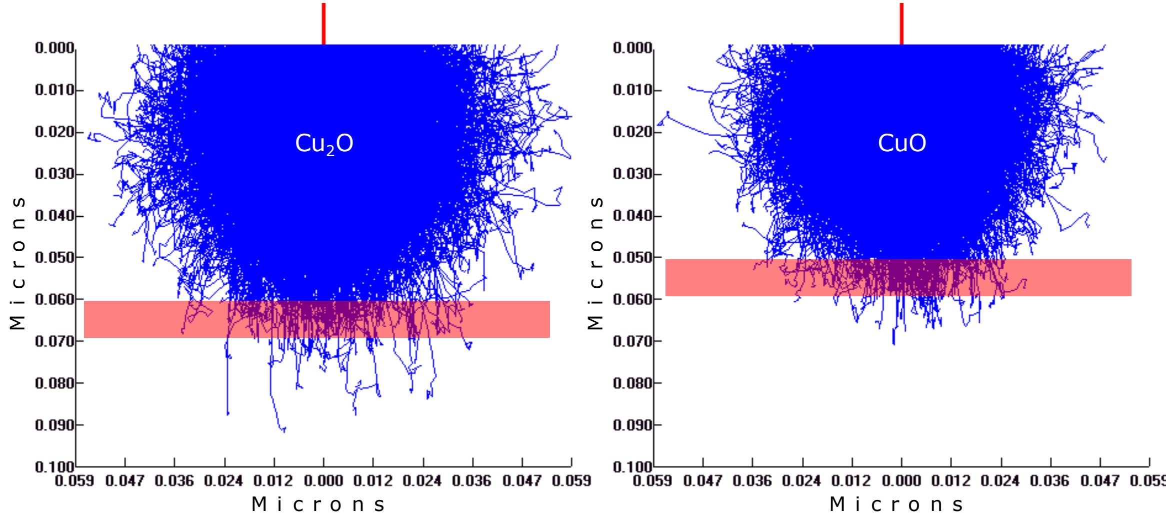

Figure 4.3. Monte Carlo simulation of electron trajectories for Cu_2O (left) and CuO (right). The estimated penetration depth for the respective material, 60-70 nm for Cu_2O and 50-60 nm for CuO, is marked by the reddish rectangle in both graphs.

the compound for the Eq. 4.1 must be evaluated. The density ρ for both materials is known and is 6.0 g/cm³ for CuO and 6.32 g/cm³ for Cu_2O. For the evaluation of the analytic depth the mean atomic mass A_{mean} and the mean atomic number Z_{mean} must be calculated. A_{mean} is defined by

$$A_{mean} = \frac{N_{Cu}}{N_{total}} \cdot A_{Cu} + \frac{N_O}{N_{total}} \cdot A_O \qquad (4.2)$$

where N_{Cu} denotes the number of copper atoms, N_0 denotes the number of oxygen atoms and N_{total} the total number of atoms in the molecule. The atomic number corresponds to the atomic mass of the element. For this reason, the theoretical mean atomic number for CuO and Cu_2O must correspond to the molecular weight ratio of the compounds. Based on that, Z_{mean} is defined by

$$Z_{mean} = \frac{N_{Cu} \cdot A_{Cu}}{M} \cdot Z_{Cu} + \frac{N_O \cdot A_O}{M} \cdot Z_0 \qquad (4.3)$$

where M denotes the molecular mass of CuO and Cu_2O, respectively. As can be seen in Table 4.1, the emission voltage E_C for the compounds was defined to be the value for Cu, because the remaining energy of the electron must be high enough for the excitation of the Cu X-ray quantum.

Table 4.1. Material parameters for Eq. 4.1 of Cu and O and the corresponding values for the molecules Cu_2O and CuO. [1]Calculated values according to the equations 4.2 and 4.3.

	Cu	O	Cu_2O	CuO
E_0 (keV)	3	3	3	3
E_c (keV)	0.930	0.523	0.930	0.930
A (g/mol)	63.55	16.00	47.70[1]	39.78[1]
M (g/mol)	-	-	143.1	79.55
ρ (kg/m³)	8.93	1.57	6	6.32
Z	29	8	26.65[1]	24.78[1]

As a result, the calculation of the analytical depth with the data from Table 4.1 inserted in the Eq. 4.1 provides that the values for Cu_2O and CuO are 55.0 nm and 46.8 nm, respectively. The comparison of the calculated analytic depth and the computed penetration depth of the electrons is illustrated in Fig. 4.4. It is obvious that the compared results in Fig. 4.4 are slightly different. As an explanation, it must be considered that the electrons lose energy the deeper they penetrate the material. For the characterization of the Cu oxides, the electron energy must be suitable for the excitation of the Cu X-ray quant at 930 eV. Consequently, it can be concluded that the electron energy below the calculated analytic depth in Fig. 4.4

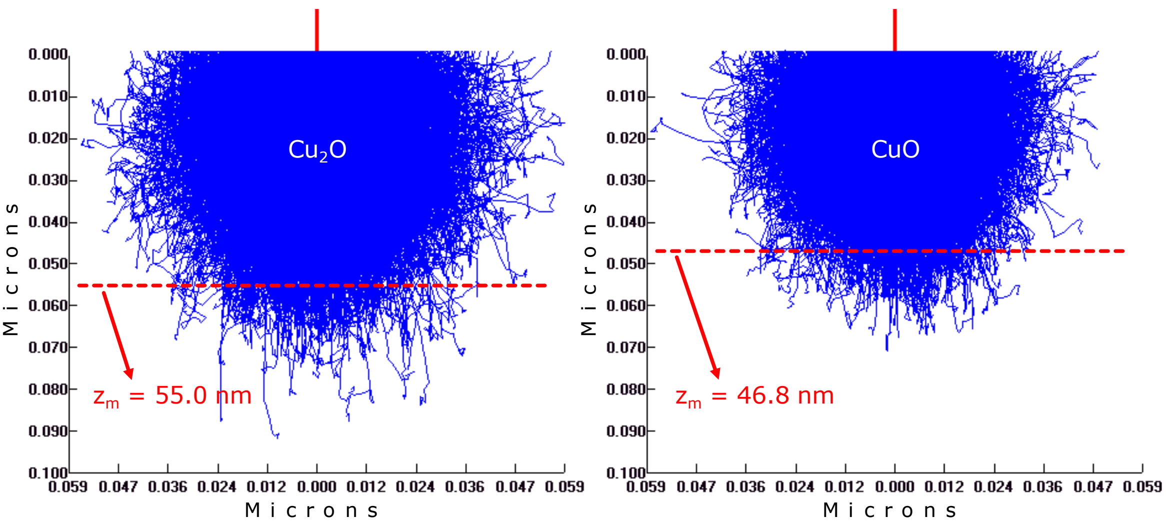

Figure 4.4. Comparison of Monte Carlo simulation of electron trajectories for Cu_2O (left) and CuO (right) and the calculated analytical depth for the respective material, 55 nm for Cu_2O and 46.8 nm for CuO, marked by the red dashed line in both graphs.

is too low for the X-ray generation. Therefore, it can be summarized that the computation and the simulation are in good agreement. It is worth noting that the calculated X-ray generation depth and the appropriate propagation characteristics estimated by the Monte Carlo simulation of electron trajectories define the measurement depth for the EDX characterization.

For analyzing oxide layers or oxide particles smaller than the calculated penetration depth, the ESB detector was chosen. This detector provides a relative material contrast by BSE imaging and was applied to validate the PF-KPFM results of the comparatively thin oxide layers. EBSD was used to identify the grain orientation of the Cu layer. As the EBSD measurement displayed an amorphous structure of the grown oxides, a discrimination of the Cu oxides by using EBSD was not possible.

In addition to the SEM techniques an additional chemical characterization was performed by reflectance FTIR with a Thermo Nicolet Nexus 470 spectrometer in dry air environment (~23 °C, 0% humidity). The detector is sensitive in the wave number range of 4000 cm^{-1} to 400 cm^{-1} and the incidence angle of the IR beam to the sample was 20°. Since CuO and Cu_2O show different vibration modes [130], they can be distinguished by FTIR. Thin oxide layers have still a highly reflective surface and therefore the absorption area of the IR beam is very low. That limits the usability for detecting thin oxide layers. FTIR was used as an additional validation of the EDX and the PF-KPFM results.

The Atomic Force Microscopy (AFM) measurements were performed with a Bruker Dimension Icon AFM. Beside various standard operation AFM modes, the AFM employed offers the PF-KPFM [106] operation mode, which is able to measure the CPD value. The CPD value constitutes the difference of the work function of the AFM probe tip and the sample. In my setup, the measured CPD is defined by the work function of the AFM probe tip Φ_{tip} minus the work function of the sample Φ_{sample}. Thus, a Φ_{sample} higher than the Φ_{tip} yields negative CPD values and vice versa. However, a direct characterization of the oxidation state by comparing theoretical and measured CPD values is not possible because the work function of materials shows some variations which are dependent on e.g. crystal structure or surface states and may not be assigned to a single value. Moreover, as the measurements were performed under ambient conditions (~25 °C, 50% humidity), it needs to be taken into account that a water layer may be present on top of the oxide surface and that this water layer influences the CPD value [91].

PF-KPFM reveals additional mechanical properties such as adhesion and elastic modulus [101] and, most important here, it provides the CPD values with improved sensitivity and repeatability in ambient air [106]. The advantages of PF-KPFM are closely linked to appropriate AFM probe tips with higher quality factor Q and lower spring constant k. I used uncoated silicon probe tips (PFQNE-AL from Bruker AXS) with a nominal spring constant of 0.8 N/m and a resonance frequency of 300 kHz, which are especially designed for PF-KPFM. The lateral resolution of PF-KPFM is closely linked to the shape of the AFM probe used and the working distance of the AFM probe tip over the sample [106]. For the identification

of particles in the nanometer range the adjustable working distance must be chosen in an accurate manner. The impact of the working distance on the CPD signal is depicted in Fig. 4.5. By identifying structures in the nanometer range, the CPD signal is influenced by the work function of the surrounding material. As can be seen in Fig.4.5 the larger the distance between AFM probe tip and sample the greater the influence of the surrounding material on the CPD signal. Therefore, it should be noted, that for the most accurate CPD result of nanoscale particles the working distance has to be adjusted as low as possible to minimize such influences and at the same moment the distance must be large enough to avoid any disturbances caused by a direct tip-sample contact.

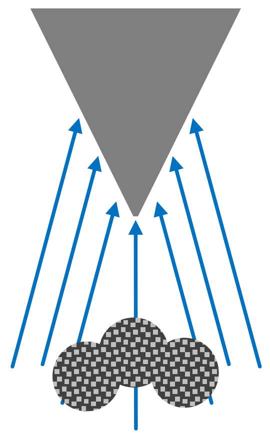

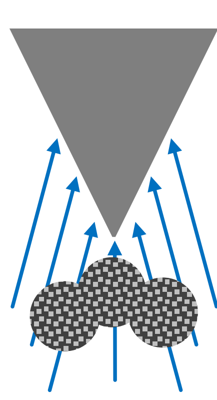

Figure 4.5. Influence of the working distance of the AFM probe tip during the scan on the area responsible for the CPD signal.

In order to enhance the reliability of the results and to prevent artifacts due to contaminated or damaged probe tips the measurements were repeated with different probe tips of the same type. The CPD values obtained for thick oxides by PF-KPFM in association with the corresponding validation by EDX and FTIR were taken as basis for the measurements of comparatively thin oxides obtained by the oxidation step at 200 °C.

4.2 Evaluation of PeakForce Kelvin Probe Force Microscopy

In this study, PF-KPFM was used to characterize the oxidation state of thermally grown copper oxide by using EDX and FTIR as reference. The 300 °C oxidized Cu sample exhibited a black surface which indicates that the layer consists of cupric oxide CuO [38]. The copper layer oxidized at 120 °C exhibited a reddish surface which suggests that the oxide layer consists of Cu_2O [38]. Both observations are in accordance with results obtained by other researcher [46,128].

EDX and FTIR were used to confirm this assumption. In Fig. 4.6 the EDX and the FTIR results of the samples oxidized at 300 °C (Fig. 4.6a+b) or at 120 °C (Fig. 4.6c+d) are presented. The EDX characterization of the sample oxidized at 300 °C (Fig. 4.6a) revealed a ratio of the atomic weight of

Cu:O of 1.17:1, which is near the theoretical ratio of 1:1 of cupric oxide CuO. Compared to the theoretical ratio, the slightly increased Cu value can be explained by the penetration depth of the electron beam, which may exceed the CuO film thickness and intrudes into a subjacent Cu_2O layer or into the Cu substrate. Based on the previously simulated penetration depth the CuO layer seemed to be slightly thinner than 47 nm. The EDX characterization of the sample oxidized at 120 °C (Fig. 4.6c) yielded a ratio of the atomic weight of Cu:O of 2.40:1, which is near the theoretical ratio of Cu_2O of 2:1. Again, the electron beam may penetrate the Cu_2O layer and intrudes into the Cu substrate. Based on the previously computed X-ray generation depth of approximately 55 nm, the increased Cu content suggests a Cu_2O layer thinner than the mentioned depth. The small carbon (C) peak visible in the EDX results in Fig. 4.6a+c suggests a carbon contamination of the oxidized copper samples. However, the carbon peak for both samples oxidized at very different setups was observed to be very similar and I observed a similar amount of C by using the same measurement setup on a plasma cleaned copper sample and even on a plasma cleaned gold sample. Therefore, I interpreted the carbon peak as a general carbon contamination of the SEM vacuum chamber. Even though the peak may be classified as a measurement artifact, a carbon contamination of the oxide layer cannot be excluded completely.

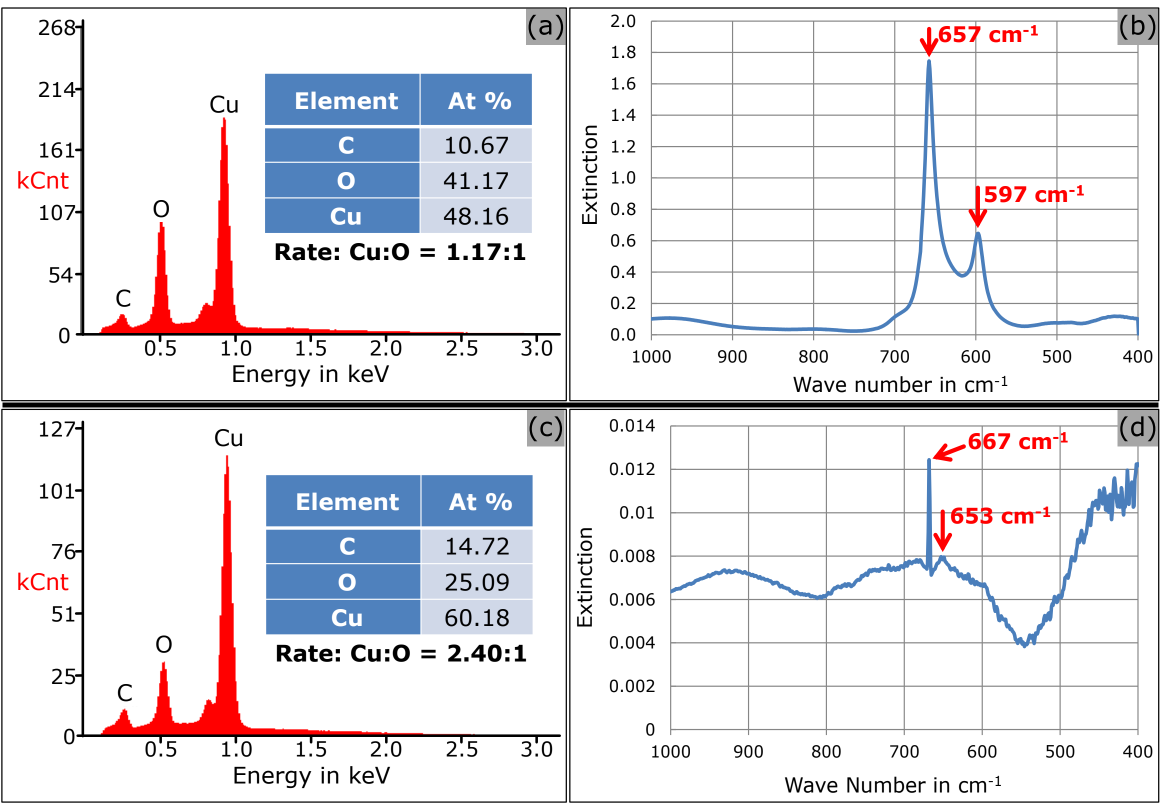

Figure 4.6. EDX (a+c) and FTIR (b+d) results of copper samples oxidized at 300 °C (a+b) and 120 °C (c+d), respectively. The ratio of 1.17:1 for copper to oxygen (a) indicates a top CuO layer which is congruent with the absorbance peak at 597 cm^{-1} in the FTIR results (b). The ratio of 2.40:1 for copper to oxygen (c) indicates a Cu_2O layer which is congruent with the absorbance peak at 653 cm^{-1} in the FTIR result (d).

The FTIR result of the sample oxidized at 300 °C (Fig. 4.6b) indicates two absorbance peaks at wave numbers of 657 cm^{-1} and 597 cm^{-1}. Lefez et al. [130] mentioned the longitudinal optical vibration mode of CuO at 600 cm^{-1} and of Cu_2O at 650-660 cm^{-1}. Thus, the absorbance peaks at 597 cm^{-1} and at 657 cm^{-1} observed in Fig. 3b can be assigned to CuO and Cu_2O, respectively. The FTIR result is in good agreement with the EDX result (Fig. 4.6a). Both methods identify the top oxide layer to consist of CuO. The FTIR result of the sample oxidized at 120 °C (Fig. 4.6d) displays two main absorbance peaks at wave numbers of 667 cm-1 and 653 cm^{-1}. The band at 667 cm^{-1} is a main band of carbon dioxide in the surrounding atmosphere and also visible without any sample present. The low absorbance band at 653 cm^{-1} is in the range of the longitudinal optical vibration mode of Cu_2O [130]. In contrast to CuO (Fig. 4.6b), the absorbance peak is very low because of the high reflectivity of the surface. Notwithstanding the comparatively small FTIR signal, in combination with the EDX investigation and the observed reddish surface, the grown oxide can be identified as Cu_2O. The FTIR results of both samples are in good agreement with the EDX results and the top oxide layers are identified as CuO and Cu_2O, respectively.

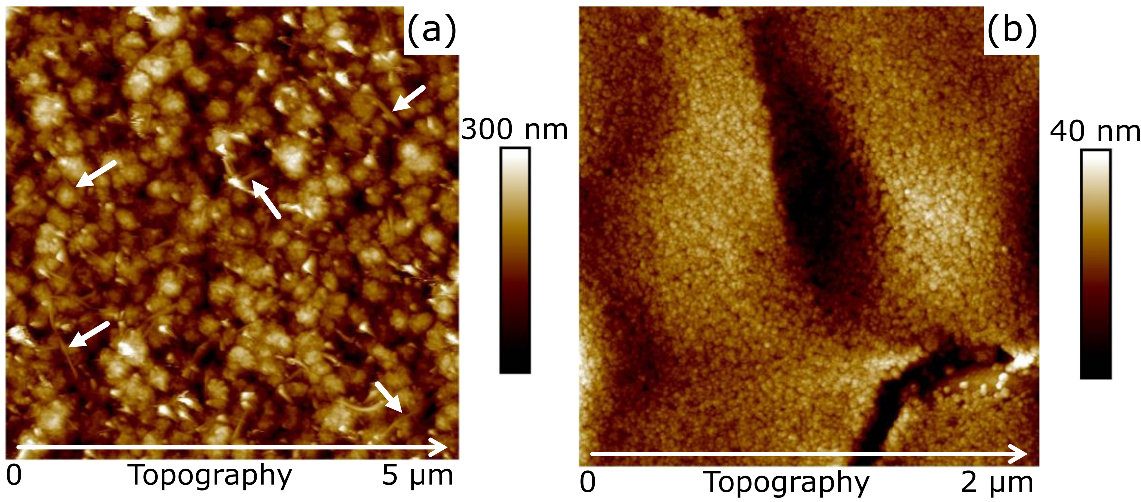

Figure 4.7. AFM topography images of (a) the cupric oxide CuO grown at 300 °C and of (b) the cuprous oxide Cu_2O grown at 120 °C. The arrows in (a) highlight some nanowires.

Fig. 4.7 shows the surface morphology of both oxidized samples. The surface of the CuO layer (Fig. 4.7a) differs significantly from the original Cu surface (Fig. 4.2). Comparatively large oxide grains and nanowires can be seen on the CuO surface and the original Cu grain structure vanished. The topography image of the Cu_2O surface (Fig.4.7b) shows very small oxide grains covering the surface. The Cu_2O surface (Fig. 4.7b) is very different compared to the CuO surface (Fig. 4.7a) because the grain size of CuO is much larger than the grain size of Cu_2O. The surface morphology observed for CuO and Cu_2O is in agreement with the observations of other researchers [43] and confirms the EDX and the FTIR results of this study.

For the corresponding PF-KPFM characterization, I performed 40 measurements on each sample at different random positions. Fig. 4.8 displays the results. For the oxide previously identified as CuO, I observed a CPD mean value of -802 ± 33.3 mV and min/max values of -859 mV/-709 mV. For the oxide previously identified as Cu_2O, I observed a CPD mean value of -575 ± 28.6 mV and min/max values of -635 mV/-524 mV. As the oxides were identified by different other methods to be CuO and Cu_2O, respectively, and as the respective CPD values obtained (Fig. 4.8) are well separated, I draw an important conclusion: CuO and Cu_2O can be identified with PF-KPFM in ambient environment by a corresponding characteristic CPD value range. The variations of the CPD values (Fig. 4.8) can be explained either by an inconsistence of the thermally grown oxide caused by impurities or by the influence of the ambient environment. The negative CPD values indicated that the work functions of CuO and Cu_2O are higher than the work function of the AFM probe tip which is made of Si. In addition, the results indicated that the work function of CuO is higher than the work function of Cu_2O, which is in agreement with other researchers [131,132].

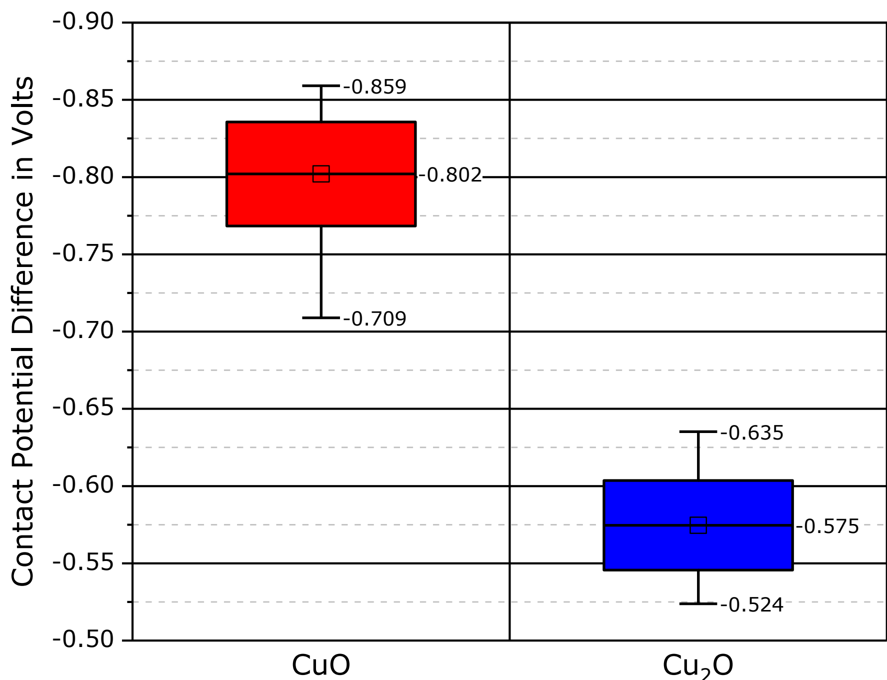

Figure 4.8. CPD value distribution with standard deviation from the mean value and minimum and maximum values of CuO and Cu_2O according to the topography images in Fig. 4.7. Each single value was obtained by 40 PF-KPFM measurements on a separate location with different probes of the same type.

4.3 Correlation of topographic features and oxide type at the nanoscale

Based on my conclusion that the Cu oxide type can be identified by a characteristic CPD value range, I employed PF-KPFM to investigate the surface change due to oxidation at a temperature of 200 °C after two and five minutes. In contrast to the comparatively thick oxides characterized before, here, the oxides

were grown near real bonding conditions and were much thinner. Fig. 4.9 shows the respective topographies and the corresponding PF-KPFM images. The topography image after two minutes of oxidation (Fig. 4.9a1) displays many small grains covering the surface, which is similar to the structure of the Cu_2O surface observed in Fig. 4.7b. However, the CPD values of the PF-KPFM image (Fig. 4.9a2) show a range of -730 mV to -620 mV, which exceeds the range of -635 mV to -524 mV previously assigned to Cu_2O (Fig. 4.8).

The extreme CPD values in the areas marked by dashed lines in Fig. 4.9a2 could be associated to topographic artifacts (Fig. 4.9a1) because they solely appeared at edges, ascending slopes of grains or directly next to such topographic effects. These artifacts, which comprise only 2.6 % of the overall number of CPD values, were excluded for further analysis and their extreme values are outside the evaluated scale bar values of Fig. 4.9a2.

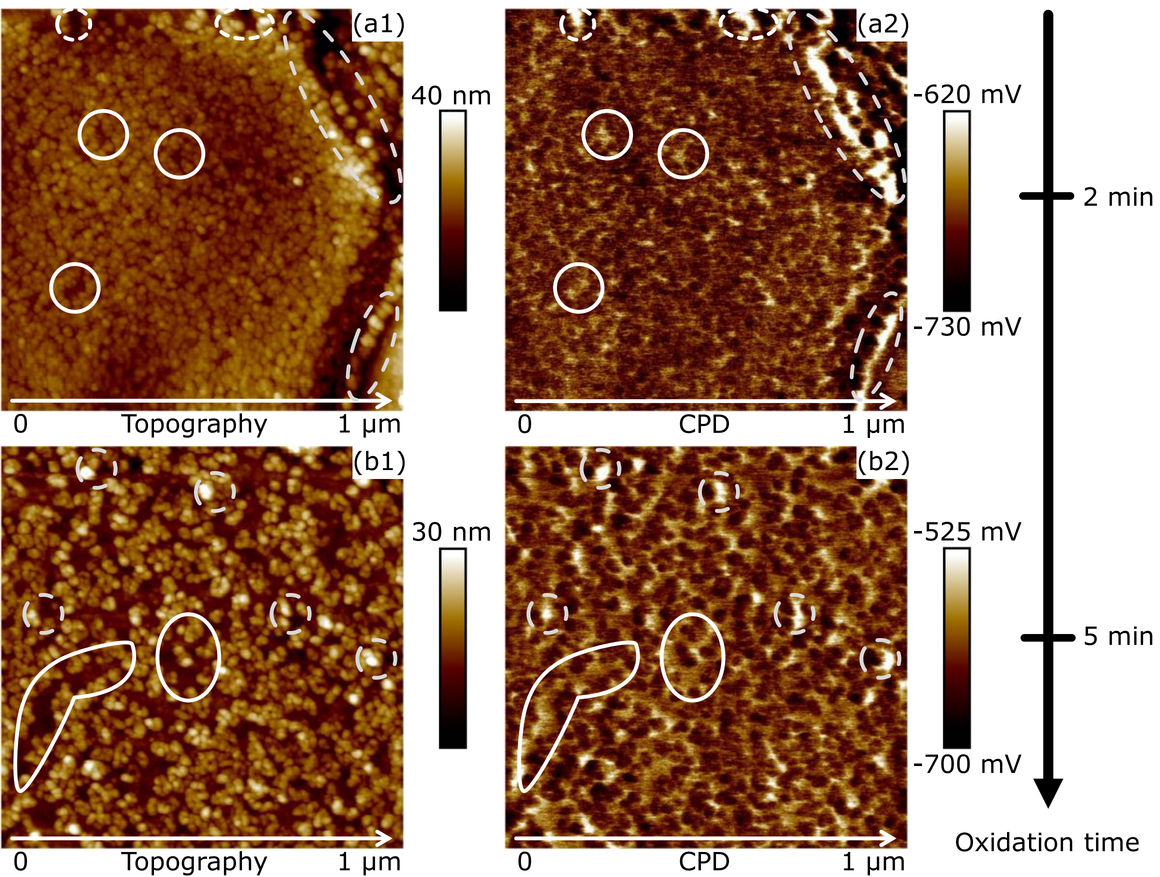

Figure 4.9. AFM topography (a1, b1) and PF-KPFM (a2, b2) images of a Cu surface oxidized at 200 °C in ambient air after two (a) and after five (b) minutes. The areas marked by dashed lines highlight extreme CPD values outside the scale bar values data regions of special topographic artifacts such as edges of grains. The areas marked by solid lines illustrate the correlation of topography (a1, b1) and PF-KPFM result (a2, b2).

In the evaluated range of -730 mV to -620 mV the lower CPD values match the range of -859 mV to -709 mV previously assigned to CuO (Fig. 4.8) while the higher values are in the region of -635 mV

to -524 mV previously assigned to Cu_2O (Fig. 4.8). By inspecting the PF-KPFM image (Fig. 4.9a2) it may be observed that the higher CPD values appear at the spacing between the grains whereas the lower CPD values appear right at the grains. This important observation indicates that the visible small grains consist of CuO and that the subjacent layer consists of Cu_2O.

In order to interpret the CPD values correctly, some aspects with respect to resolution and selectivity need to be noted. The lateral resolution of PF-KPFM is closely linked to the shape of the AFM probe used [106]. Therefore, in case of nanoscale grains or interspaces close to the size of the AFM probe tip as imaged in Fig. 4.10, the CPD values of grains and interspaces are influenced by each other.

As the grains and particularly the interspaces are comparatively small, the respective CPD values detected by the AFM probe may interfere to some extent, which poses an averaging effect. Nevertheless, the results show that PF-KPFM is able to distinguish the oxides precisely and that even after two minutes at a temperature of 200 °C a CuO layer on top of a Cu_2O layer may be observed.

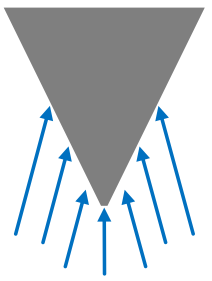

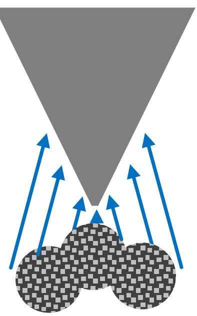

Figure 4.10. Averaging effect of the CPD signal by measuring nanoscale grains and interspaces.

After five minutes of oxidation at 200 °C the topography (Fig. 4.9b1) changed significantly. Compared with Fig. 4.9a1 the topography in Fig. 4.9b1 indicates that oxide grains merged and interspaces increased considerably. Again, the PF-KPFM image (Fig. 4.9b2) shows lower CPD values for the grains and higher CPD values for the gaps, which is an indication for CuO grains on top of a Cu_2O layer. As before, the CPD values at edges or ascending slopes of grains were allocated to topographic artifacts (Fig. 4.9b, dashed lines) and were excluded (~0.5%). The CPD values evaluated range from -700 mV to -525 mV. The lower CPD values correlate with the grains (Fig. 4.9b) and the higher CPD values correlate with the gaps. The higher values of the gaps match the range observed for Cu_2O (Fig. 4.8) while the lower values are slightly below the range observed for CuO (Fig. 4.8). Since the gaps in this case are much wider than before, they could increase the overall level of CPD values measured toward the Cu_2O range (Fig. 4.8) as a result of the averaging effect posed by the AFM probe addressed in Fig. 4.10.

To validate my assumption that CuO grains sit on top of a Cu_2O sub-layer, the distribution of the elastic modulus was investigated (Fig. 4.11a). Fig. 4.11a is scaled in arbitrary units and provides relative

information rather than absolute values. Nonetheless, the results show that the grains and the structure beneath have different elastic moduli and can clearly be assigned to different materials. An additional BSE image (Fig. 4.11b) supports this result because it displays a material contrast between the grains and the underlying structure. Therefore, I allocate the grains with the lower CPD values to CuO and the interspaces with higher CPD values to Cu_2O indicating a Cu_2O sub-layer. The PF-KPFM measurements show that, after the increased oxidation time from two to five minutes, the small CuO grains apparently merged thereby increasing the CuO grain size and the interspace width rather than building a more homogeneous, compact oxide film.

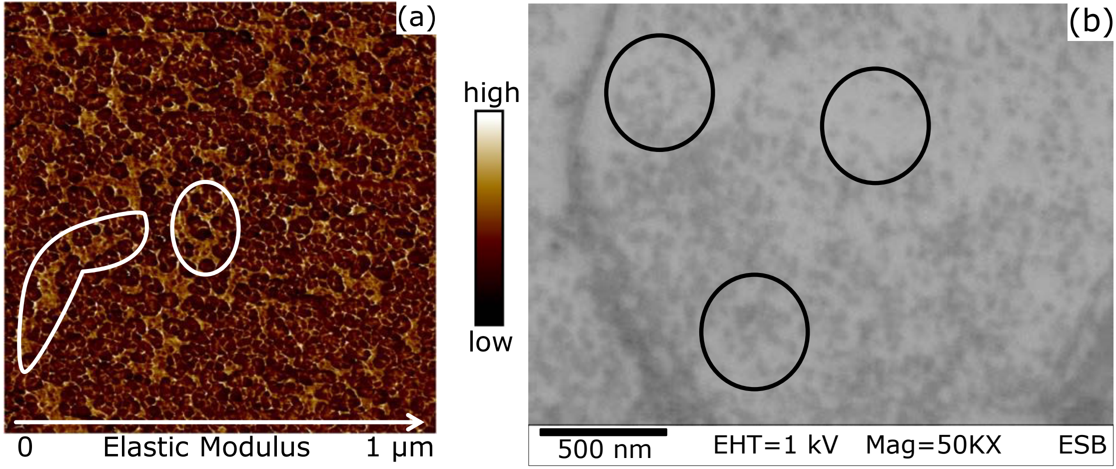

Figure 4.11. The distribution of the elastic modulus (a) indicates different elastic moduli corresponding to Fig. 4.9b1 and 4.9b2 illustrated by the solid lines. The BSE image (b) of the same sample in Fig. 4.9b1 at another position reveals a material contrast between the grains and the underlying structure highlighted by the circles. Both images, (a) and (b), discriminate different surface materials.

On the foundation of my EDX and FTIR analyses of thick Cu oxide films, I found characteristic CPD values for CuO and Cu_2O, respectively, by PF-KPFM measurements at ambient conditions (Fig. 4.8). Employing PF-KPFM in air along with the associated characteristic CPD values, it was possible to determine the local oxidation state of thin oxide layers and local surface structures grown by short time thermal oxidation near bonding conditions. As an important consequence, therewith, the method allows the correlation of topography and oxidation state with spatial resolution in the nanometer scale. For the development of a reliable bonding process the interplay of topography and local oxidation state may be important but is still widely unknown. A homogenous, compact oxide layer as seen in Fig. 4.7b or 4.9a1 could influence the bonding result differently than comparatively separated oxide grains on an oxide sub-layer as seen in Fig. 4.9b1. Therefore, PF-KPFM in air is a valuable tool for root cause analysis and further research toward increased Cu bond quality.

4.4 Summary

Different copper oxides, cupric oxide CuO and cuprous oxide Cu_2O, may clearly be distinguished by the CPD value measured by PF-KPFM at ambient conditions. The PF-KPFM results were validated by EDX and FTIR measurements. The statistical evaluation of the measured CPD values demonstrated that even the maximum and minimum values do not overlap, and therefore the Cu oxides may clearly be distinguished solely by PF-KPFM. For CuO PF-KPFM yields CPD values in the range of -859 mV to -709 mV and for Cu_2O in the range of -635 mV to -524 mV. Based on those results, the investigation of the oxidation at the bonding temperature of 200 °C yields that already after two minutes CuO has grown on top of a Cu_2O layer. The small CuO grains cover almost the whole surface. At five minutes of oxidation the small CuO grains apparently merged and build up larger grains. Additionally, the gap between the CuO grains increased and can clearly be identified to consist of Cu_2O indicating a Cu_2O sub-layer.

5. Numerical study of hydrodynamic forces for AFM operations in liquid

Since the invention by Binnig in 1986 [95], the atomic force microscopy (AFM) is finding increasing use in the characterization of chemical surface modifications [133,113] to achieve a chemical mapping of the surface in the nanoscale. This advanced method is called Chemical Force Microscopy (CFM) [113,110] and is based on sensing the interaction forces between a chemical modified AFM probe tip and the sample surface. The measurement environment plays an important role for the performance of CFM because any attractive or repulsive forces influenced by the measurement environment could obscure the molecular forces. In general, AFM experiments are carried out in ambient atmosphere similar to the schematic depicted in Fig. 5.1a. Under these conditions, a water layer usually covers both tip and sample.

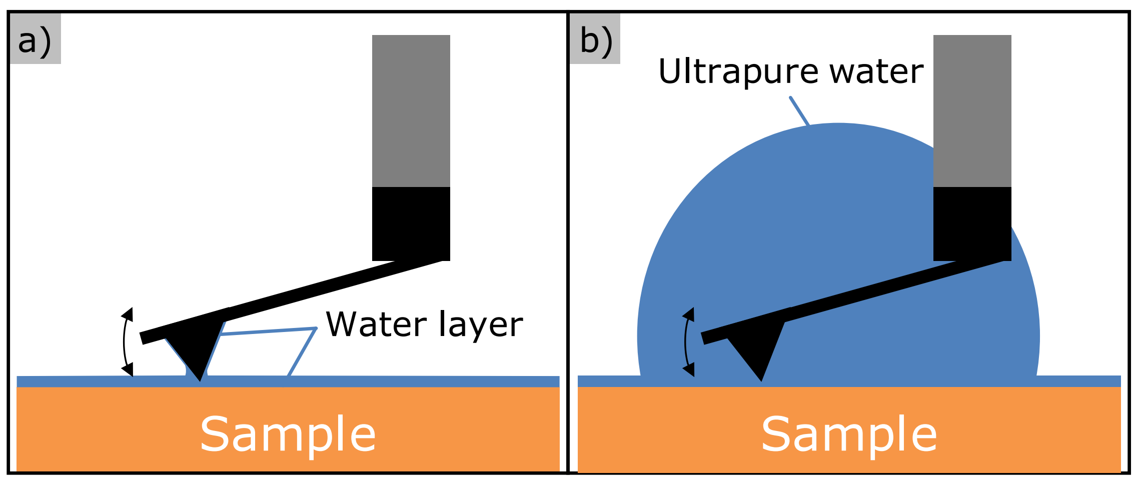

Figure 5.1. Schematic of AFM operation in air a) or in liquid b) environment.

Such a thin film of water gives rise to capillary forces between AFM probe tip and sample surface having a strong impact on the force-distance curves [134]. Fig. 5.2 displays the comparison of the tip sample interaction influenced by the measurement environment in detail. The water meniscus due to the water layer present in the pull-off forces obscure the molecular adhesion forces under surveillance between the modified tip and the sample surface as they are two to three magnitudes larger [134,111]. Therefore, the air environment is not suitable for the reliable measurement of molecular adhesion forces. For CFM experiments the adhesion force evaluated from the force-distance curves should reflect the interplay between the chemical modified tip and the sample surface. A liquid environment (Fig. 5.1b and Fig. 5.2) can eliminate the capillary effect and thus the detrimental effect of the pull-off forces and hence, enables the measurement of molecular adhesion forces one or two orders of magnitude less than is possible in air [111,135].

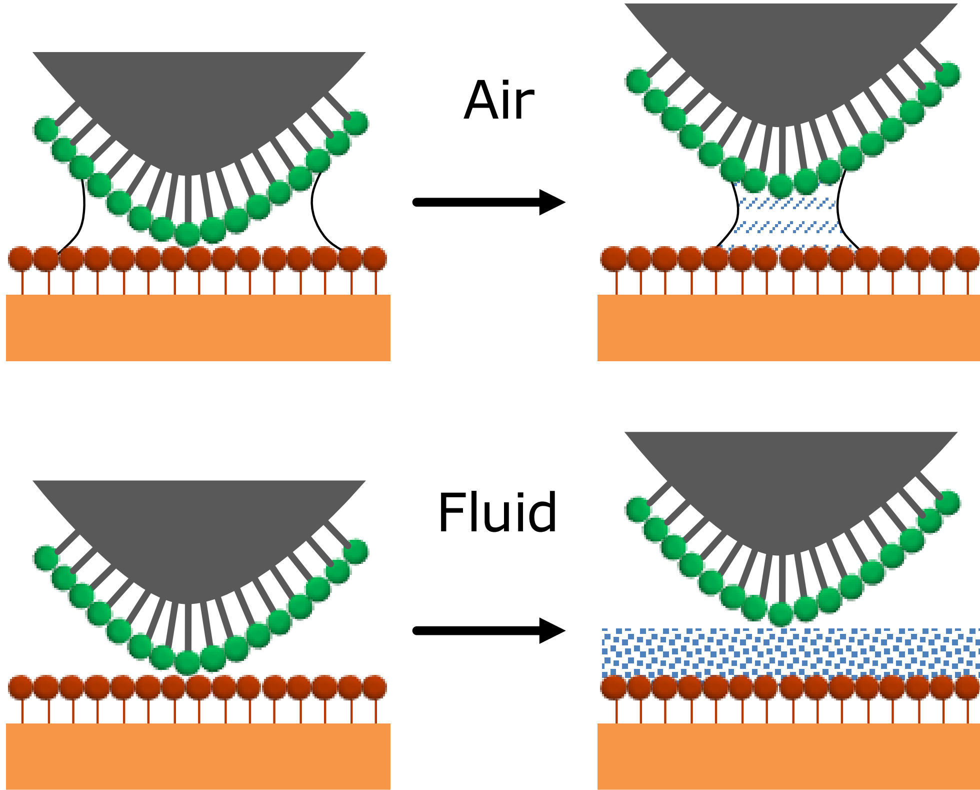

Figure 5.2. Comparison of the tip-sample interaction during separation in air and in liquid environment.

Beside the increased sensitivity for detecting adhesive forces, the liquid environment also improves the investigation of very soft sample surfaces by applying very low forces. Therefore, in recent literature AFM measurements of biological samples were undertaken in liquid environment [136–138].

The mechanical behavior of the moving AFM cantilever depends on density and viscosity of the ambient medium. A liquid, such as ultrapure water, possesses substantially different values of density and viscosity than air. At standard environmental conditions of 293 K and 1013 hPa, the density of air ρ_{air} is $1.2044\ \frac{\mathrm{kg}}{\mathrm{m}^3}$ and the dynamic viscosity μ_{air} is $1.8140 \cdot 10^{-5}$ Pa·s. The density ρ_{water} of ultrapure water is $999.615\ \frac{\mathrm{kg}}{\mathrm{m}^3}$ and the dynamic viscosity μ_{water} is $1.009347 \cdot 10^{-3}$ Pa·s. The much higher density and viscosity of the liquid affects the force measurements by hydrodynamic drag forces [138–140]. Various researcher stated that the influence of this effect is already more significant for cantilever tip velocities above a few µm/s [138–142]. In their study, Mendez-Mendez et al. [138] introduced a numerical model to predict the hydrodynamic forces for tip velocities up to 105 µm/s. They show that the usage of different fluids significantly influences the drag force acting on the cantilever and confirm that the drag force dependence on tip speed is essentially linear in nature.

In recent literature, for the investigation of very soft samples or especially organic samples, the PeakForce Tapping (PFT) mode [98] was introduced to control vertical forces in the range of some tens of pico-Newtons [137,100]. Additionally, PFT enables the mapping of nano-mechanical properties

[98,143]. This advanced characterization technique also provides advantages for the investigation of chemical modifications by CFM because this dynamic operation mode enables a complete chemical mapping of the surface [109,108] and is not just limited to applying individual force-distance curves at distinct measurement points. The combination of PFT and CFM is defined as dynamic Chemical Force Microscopy (dCFM).

In contrast to the hydrodynamic drag forces for tip velocities up to 105 μm/s researched by Mendez-Mendez et al. [138], for PFT performed in an aqueous solution, the cantilever tip is operated in a sinusoidal z-movement with an oscillation frequency of usually 1 kHz and oscillation amplitudes ranging from 50 nm to 300 nm. Based on these parameters, the maximum cantilever tip velocity in the fluid can vary from 314 μm/s to even 1885 μm/s. Therefore, other researchers stated that the hydrodynamic forces in a fluidic environment can be as high as 10-20 nN [100]. The measurement principle of PFT was explained in detail in section 3.1.1.

This magnitude of parasitic hydrodynamic forces may distort the outcomes and could limit the control of the vertical forces significantly. Consequently, further research is necessary to investigate the hydrodynamic drag forces acting on the cantilever during the PFT operation in liquid environment. The present work addresses these needs and provides a numerical model to investigate the hydrodynamic drag forces for different cantilever geometries and varying fluid conditions for tip speeds associated with PFT measurements. Therewith, the measurement setup can be optimized by minimizing parasitic drag forces and by reducing experimental uncertainties for a more precise force control regarding studies of soft samples in liquids.

5.1 Numerical Model

In this study, a fluid dynamics simulation based on the finite element method (FEM) was performed. FEM divides a complex problem in many finite small elements. By using a finite number of parameters, a set of partial differential equations with some boundary conditions can be solved. In the case of the AFM probe movement in the fluidic environment, the FEM simulation is based on the Navier-Stokes equations for fluid dynamics which describe the motion of viscous fluids. The terms of the equations correspond to the inertial forces $F_{inertial}$, the pressure forces $F_{pressure}$, the viscous forces $F_{viscous}$ and the external forces F_{ext} applied to the fluid. The different terms are related as follows:

$$F_{inertial} = F_{pressure} + F_{viscous} + F_{ext}. \qquad (5.1)$$

The different forces can be described as:

$$F_{inertial} = \rho\left(\frac{\partial u}{\partial t} + u \cdot \nabla u\right) \quad (5.2)$$

$$F_{pressure} = -\nabla p \quad (5.3)$$

$$F_{viscous} = \nabla \cdot \left(\mu(\nabla u + (\nabla u)^T) - \frac{2}{3}\mu(\nabla u)I\right) \quad (5.4)$$

where u represent the fluid velocity, p is the fluid pressure, ρ and μ are the fluid density and the fluid dynamic viscosity, respectively. I is the identity matrix and T is defined to be the notation for a transposition. Combined the terms denote the Navier-Stokes equations for a compressible Newtonian fluid:

$$\rho\left(\frac{\partial u}{\partial t} + u \cdot \nabla u\right) = -\nabla p + \nabla\left(\mu(\nabla u + (\nabla u)^T) - \frac{2}{3}\mu(\nabla u)I\right) + F_{ext}. \quad (5.5)$$

These equations represent the conservation of momentum and are always solved together with the continuity equation described as:

$$\frac{\partial \rho}{\partial t} + \nabla(\rho u) = 0. \quad (5.6)$$

The continuity equation represents the conservation of mass, whereas the Navier-Stokes equations symbolize the conservation of momentum. By using these general equations, the fluid velocity and the pressure in a given geometry can be calculated. For the best and fastest solution, the equations have to be adapted to the real conditions. As mentioned before, the Eq. 5.5 and 5.6 represent the Navier-Stokes and the continuity equations, respectively, for a compressible Newtonian fluid. However, for the model of the AFM probe movement the fluids of interest are liquids such as ultrapure water which are known to be incompressible Newtonian fluids. The fundamental statement for an incompressible fluid is that the density ρ is constant over the whole volume. Based on this assumption, the continuity equation can be simplified to:

$$\rho \nabla u = 0 \quad (5.7)$$

The continuity equation for an incompressible fluid states that the divergence of the velocity is equal to zero. Applied to the Navier-Stokes equations from Eq. 5.5 the viscous force term simplifies to:

$$\rho\left(\frac{\partial u}{\partial t} + u \cdot \nabla u\right) = -\nabla p + \nabla \cdot \left(\mu(\nabla u + (\nabla u)^T)\right) \quad (5.8)$$

Additionally, external forces F_{ext} such as gravitational forces are very small and can be neglected as well for the model.

For the simulation of the hydrodynamic effect, the cantilever movement in the fluidic environment is interpreted as a fixed body flowed by a fluid. This principle, schematized in Fig. 5.3, assumes that the

cantilever movement in the fluidic environment is identical to a fluid circulating around a fixed cantilever. Since the relative velocity from the cantilever to the liquid is the same, both approaches are valid for the simulation of the hydrodynamic force. Fig. 5.3 shows two different flow effects. Laminar flow occurs if the fluid passes the cantilever without turbulences and accordingly turbulent flow is described as a stream subject to disturbances.

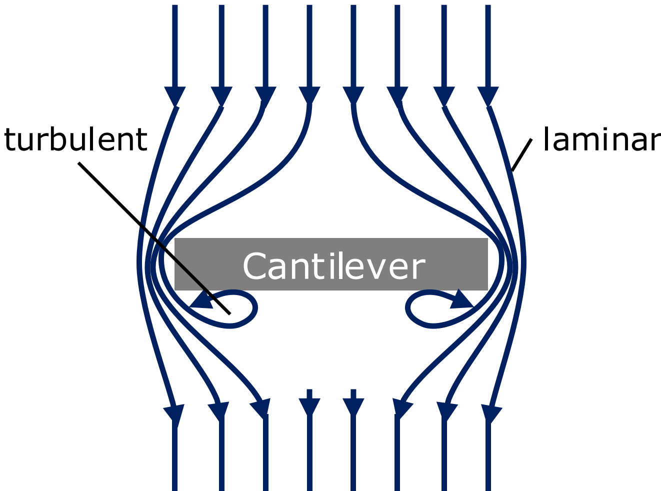

Figure 5.3. Principle of the fixed cantilever flowed by a fluid. Laminar and turbulent fluid flow effects are marked.

The laminar as well as the turbulent flow could affect the parasitic force acting on the AFM cantilever during its movement and therefore, both must be considered in the numerical model. Simulations of turbulent flow models are usually computationally expensive because such models are often transient in nature and therefore, they need a high resolution to match the needs in both, the time and space domain. In this study, the simulation was performed by using the Comsol CFD (Computational Fluid Dynamics) model which is based on the Reynolds-Averaged Navier Stokes (RANS) formulation for incompressible fluids. Since in most applications the average quantities are of interest, the RANS formulation of the Navier Stokes equations averages for the modeling of turbulent flows the velocity and pressure fields in time [138,144]. The RANS formulation is as follows:

$$\rho(U \cdot \nabla U) = -\nabla P + \nabla\left(\mu(\nabla U + (\nabla U)^T)\right) - \nabla \rho R_{stress} \tag{5.9}$$

where U and P are the time-averaged velocity and pressure, respectively. The term ρR_{stress} is called Reynolds stress and represents the components of the total stress in a fluid obtained from the averaging operation used for the RANS formulation to account for the turbulent fluctuations in fluid momentum.

According to the Boussinesq hypothesis introduced in 1877 the Reynolds stress term can be expressed as:

$$\rho R_{stress} = -\mu_T(\mathrm{U} + (\nabla U)^T) + \frac{2}{3}\rho K_t \tag{5.10}$$

where μ_T represents the turbulent viscosity and K_t is the turbulent kinetic energy. Combined with Eq. 5.9 the RANS formulation is:

$$\rho\left(\frac{\partial u}{\partial t} + u \cdot \nabla u\right) = -\nabla p + \nabla\big(\mu(\nabla u + (\nabla u)^T)\big) + \nabla\big(\mu_T(\nabla u + (\nabla u)^T)\big) - \frac{2}{3}\rho K_t \tag{5.11}$$

For the evaluation of the turbulent viscosity μ_T an additional transport model must be introduced. A very versatile model is the K-epsilon (K-ε) turbulence model [145,146]. This model calculates μ_T by solving two additional equations for the transport of turbulent kinetic energy K_t and the turbulent dissipation ϵ.

The turbulent viscosity μ_T is modeled as:

$$\mu_T = \rho C_\mu \frac{K_t^2}{\epsilon} \tag{5.12}$$

The model constant C_μ is an empirical constant as mentioned in literature [145,146]. The RANS equations combined with the introduced K-ε turbulence model can be used to simulate both, laminar and turbulent flow effects during the cantilever movement in the fluidic environment.

5.2 Cantilever Model

In this study, commercially available cantilever types with chemically modified tips (ST-PNP from Nanoandmore GmbH and Nanocraft Coating GmbH) are considered. All cantilevers are made of silicon nitride (Si_3N_4). The shape is either triangular or rectangular. Fig. 5.4 shows the geometrical dimensions of the different cantilevers including the supporting chip.

Beside the geometry of the cantilever material, parameters such as the Young's modulus E are very important because they strongly influence the stiffness k and the deflection of the cantilever. In case of the Young's modulus E an exact value for the cantilever material is not specified. In contrast, the average stiffness or spring constant k of the cantilevers are provided by the manufacturer. Accordingly, the triangular cantilevers possess spring constants of 0.08 N/m and 0.32 N/m and the rectangular cantilevers of 0.06 N/m and 0.48 N/m for 200 μm and 100 μm cantilevers length, respectively. An overview of all cantilever dimensions and their averaged spring constants provided by the manufacturers is summarized in Table 5.1.

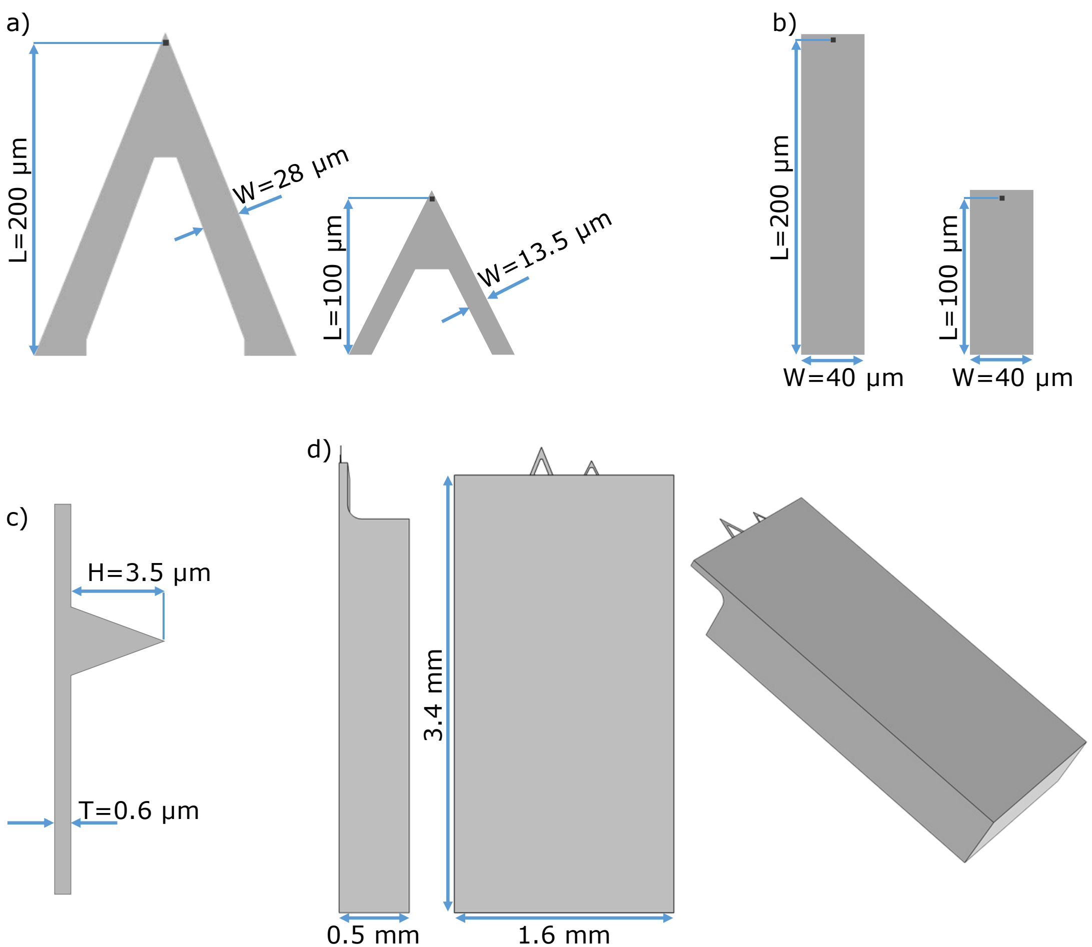

Figure 5.4. (a) Triangularly shaped cantilever with a length L of 200 µm and 100 µm; (b) 200 µm and 100 µm long rectangularly shaped cantilever; (c) Cantilever thickness and AFM tip geometry identical for all geometries; (d) Main components considered for the cantilever model consisting of the support chip which carries the Si_3N_4 cantilever.

However, these values may vary due to some manufacturing tolerances. For the fluid dynamics, the effective values for k as well as for the Young's modulus E are very important because based on Hooke's law,

$$F = k \cdot \Delta z, \tag{5.13}$$

the force F acting on the cantilever is directly dependent on the effective spring constant k and the corresponding cantilever deflection Δz. Adopting this assumption means that a methodology for calculating an effective value for the Young's modulus E and the spring constant k of the cantilever is required. The three-dimensional model of the triangular cantilever based on the geometrical data in Table 5.1 is shown in Fig. 5.4d.

Table 5.1. Summary of the geometrical dimensions of the cantilevers introduced in Fig. 5.4 and their spring constant k

Cantilever Shape				
Length L [μm]	100	200	100	200
Width W [μm]	40	40	13.5	28
Thickness T [μm]	0.6	0.6	0.6	0.6
Tip Height H [μm]	3.5	3.5	3.5	3.5
Spring constant k [N/m]	0.48	0.06	0.32	0.08

The values for the lateral dimensions of the pyrex support chip are provided by the manufacturer. The pyrex chip as well as the positioning of the cantilever in Fig. 5.4d are identical for the rectangular cantilever shape. For these model geometries, the exact spring constant and the effective value for the Young's modulus E of the cantilevers have to be evaluated.

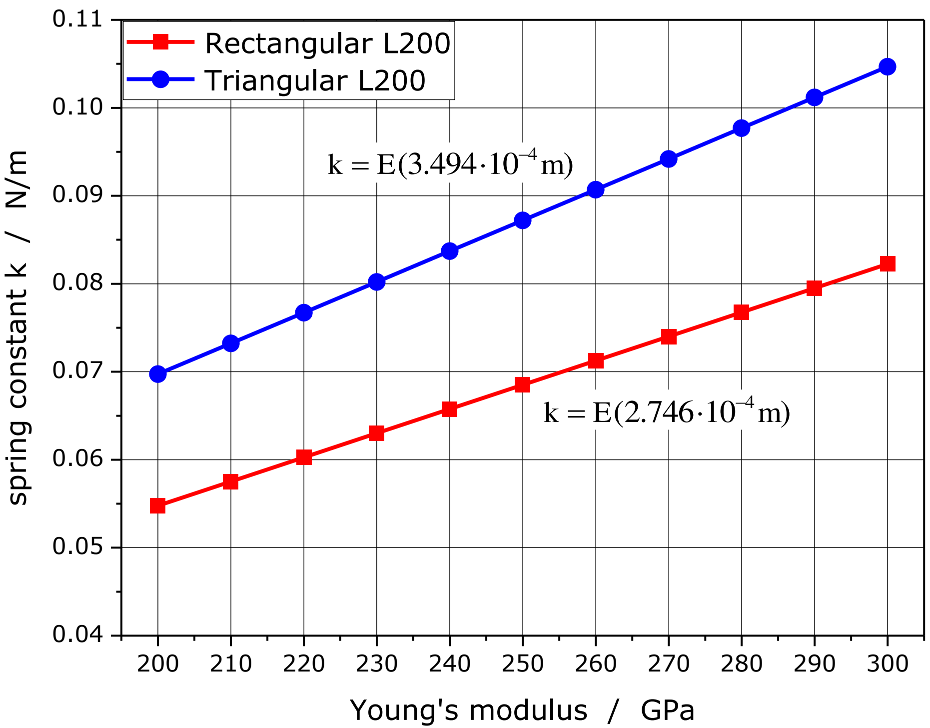

Figure 5.5. Relationship between spring constant k and Young's modulus E for the rectangular and triangular cantilever with a length L of 200 μm

For the calculation, the ends of the cantilevers were fixed and a force in the range of 1 nN was applied to the tip. The Young's modulus E was varied in the range of 200–300 GPa. A deflection of the cantilever was achieved by the applied force to the probe tip and the corresponding spring constant k was

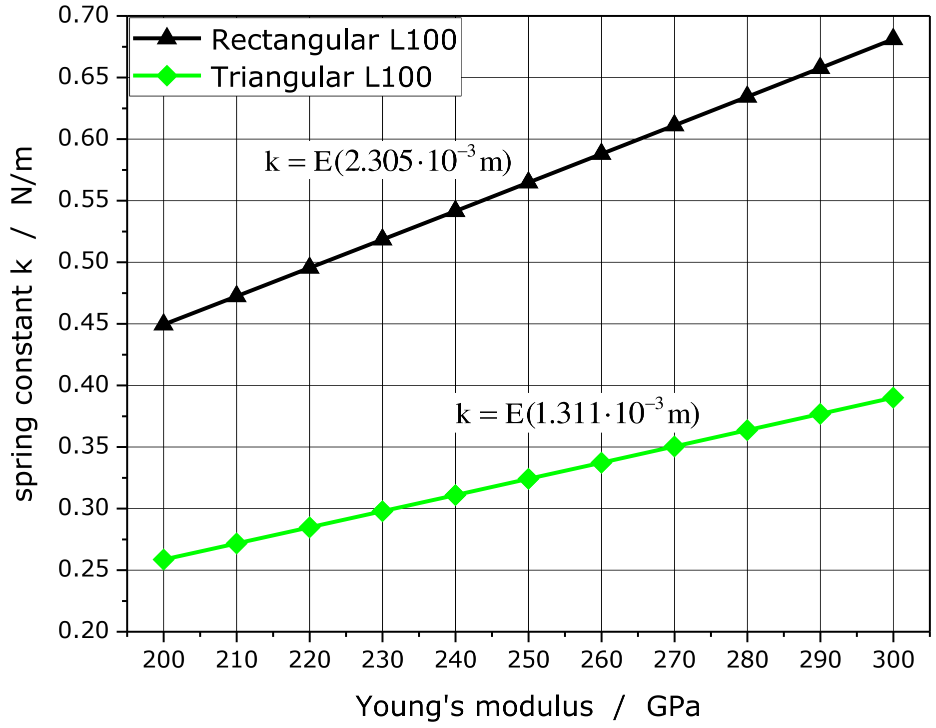

Figure 5.6. Relationship between spring constant k and Young's modulus E for the rectangular and triangular cantilever with a length L of 100 µm

calculated using Eq. 5.13. The Fig. 5.5 and 5.6 illustrate the computed values in a diagram with k as a function of E. For all cantilevers the results yield a linear relationship between k and E. Compared with the spring constant values supplied from the manufacturer the corresponding Young's modulus E would be different for each cantilever type. As the material for all cantilevers is the same, the material properties specified in the simulation model should be kept constant, too. By this reason, the Young's modulus E for Si_3N_4 used as cantilever material is defined to be 250 GPa and the corresponding spring constant k is evaluated based on the outlined results in Fig. 5.5 and 5.6. In Table 5.2 the relations for k as a function of E extracted from the plotted curves in Fig. 5.5 and 5.6 and the calculated spring constant k for a Young's modulus E of 250 GPa are stated. By comparing the spring constants of the cantilevers provided

Table 5.2. Evaluated spring constant k of the cantilevers for a Young's modulus E of 250 GPa.

Cantilever shape	Length L in µm	Relation k = f(E)	spring constant k in N/m
Rectangular	200	$k = E \cdot (2.746 \cdot 10^{-4} m)$	0.0687
Triangular	200	$k = E \cdot (3.494 \cdot 10^{-4} m)$	0.0874
Rectangular	100	$k = E \cdot (2.305 \cdot 10^{-3} m)$	0.5763
Triangular	100	$k = E \cdot (1.311 \cdot 10^{-3} m)$	0.3278

by the manufacturer summarized in Table 5.1 and the calculated spring constants in Table 5.2, it can be noticed that in most cases the k values are very similar. Only the computed spring constant of 0.5763 N/m for the rectangular cantilever with a length L of 100 µm is significantly higher than the k value provided by the manufacturer.

5.3 Fluid Model

In the introductive part of this section the importance of the fluidic environment for the measurement of the interaction forces by dCFM was outlined. In this respect, the focus was on water or ultrapure water, but alternative solvents may also be useful to improve interaction forces and thus to increase measurement accuracy. Investigations of different researchers have handled the influence of various solvents on the interaction force between chemical modified probe tips and sample surfaces [113,147,148]. Thereby, the ethanol-water mixture has proven to be a promising solvent for measuring interaction forces. Kokkoli and Zukoski [147] as well as Yaacobi and Ben-Naim [148] have shown in their studies that mole fractions of ethanol (EtOH) up to 0.2 can increase the strength of hydrophobic interaction forces. Additionally, they stated that a higher ethanol mole fraction in the ethanol-water mixture results in a significant lowering of the interaction forces. Besides the strengthening of the interaction forces by the EtOH content, a possible side effect could be a prevention of the chemical modified tip and the sample surface from organic contaminations. In the long term the probe tip stability can be improved.

Though, by mixing ethanol with water fluid properties such as the density ρ and the dynamic viscosity μ may be changed significantly. As these variables are fundamental for the drag forces acting on the cantilever during the movement in the solvent, any deviation caused by an increase or decrease of the density and viscosity of the medium must be considered in the simulation model.

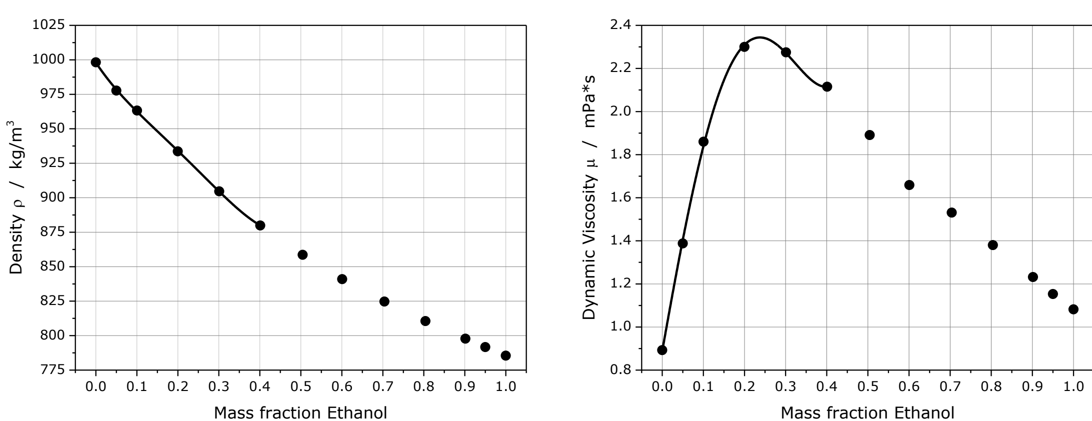

Figure 5.7. Change of the density ρ and the dynamic viscosity μ in relation to the mass fraction of ethanol in an ethanol-water mixture at a temperature of 25 °C (298.15 K) based on [149]. The solid line indicates the fitted values derived by Eq. 5.14 and 5.15 up to an ethanol concentration of 40%.

The diagrams in Fig. 5.7 relate the mass fraction of ethanol in an ethanol-water mixture to the density ρ and the dynamic viscosity μ of the resulting solvent at a temperature of 25 °C. The plotted values were measured by Gonzales et al. [149].

Adapted from these values the mathematical description of the diagrams can be derived. Based on the assumption that small quantities of ethanol could cause a strengthening of the interaction forces [147,148], the formulaic description only was derived for an EtOH mass fraction x_{etoh} in the range of 0 to 0.4.

$$\rho = a_0 + a_1 \cdot x_{etoh} + a_2 \cdot x_{etoh}^2 + a_3 \cdot x_{etoh}^3 + a_4 \cdot x_{etoh}^4 \quad for \quad 0 \leq x_{etoh} \leq 0.4 \tag{5.14}$$

$$\mu = b_0 + b_1 \cdot x_{etoh} + b_2 \cdot x_{etoh}^2 + b_3 \cdot x_{etoh}^3 + b_4 \cdot x_{etoh}^4 \quad for \quad 0 \leq x_{etoh} \leq 0.4 \tag{5.15}$$

The values of the variables can be seen in Table 5.3. The coefficient of determination R^2 for the fitted values in Fig. 5.7 is 99.9 %, which emphasizes that the derived equations are suitable for describing the dependence of the mass fraction of ethanol in the ethanol-water mixture on the density ρ and the dynamic viscosity μ.

Table 5.3. Derived values of the variables for the formulaic description in Eq. 5.14 and 5.15.

a_0	a_1	a_2	a_3	a_4
999.397	-448.709	1509.0	-5302.06	6338.21
b_0	b_1	b_2	b_3	b_4
0.999606	14.5865	-23.2774	-56.7031	117.223

Obviously, adding ethanol to an ethanol-water mixture causes a very opposed trend for the density and the viscosity of the mixture. Especially, for the interesting range below a fraction of 0.2, Fig. 5.7 shows that the density is reduced slightly, but the dynamic viscosity is increased very strongly in this area. By using the derived fluid properties of the ethanol-water mixture calculated by the equations 5.14 and 5.15, the fluidic environment in the simulation model can be defined to be either ultrapure water or an ethanol-water mixture.

For the AFM measurement, a special cantilever holder for fluid operations is used. Fig. 5.8 presents the geometrical model developed for the simulation of the fluid dynamics according to the cantilever model DECAFMCH from Bruker AXS. The geometry in Fig. 5.8 is modeled for realistic conditions during the AFM scan in fluid. The colors mark the different parts such as cantilever chip holder, cantilever chip, fluid and sample. The probe tip is completely immersed in the liquid, which completely covers the sample surface at the area of interest.

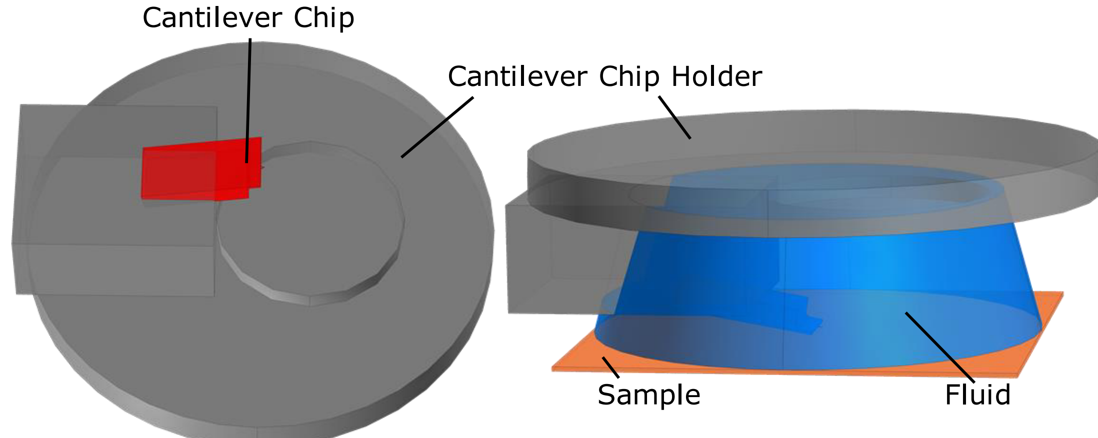

Figure 5.8. Geometrical model of the cantilever holder (DECAFMCH from Bruker AXS) with a mounted AFM probe (Fig. 5.4) (left) and probe holder with mounted probe immersed in a fluid on top of a sample surface (right).

For the simulation model the different parts of the probe holder were eliminated. As a result, Fig. 5.9 illustrates the shape of the fluid medium on top of the sample surface. The outer limitations of the liquid medium were defined as boundary conditions. As an additional precondition the AFM cantilever immersed in the fluid was specified to be fixed at the base and is freely suspended at its end, where the tip is located.

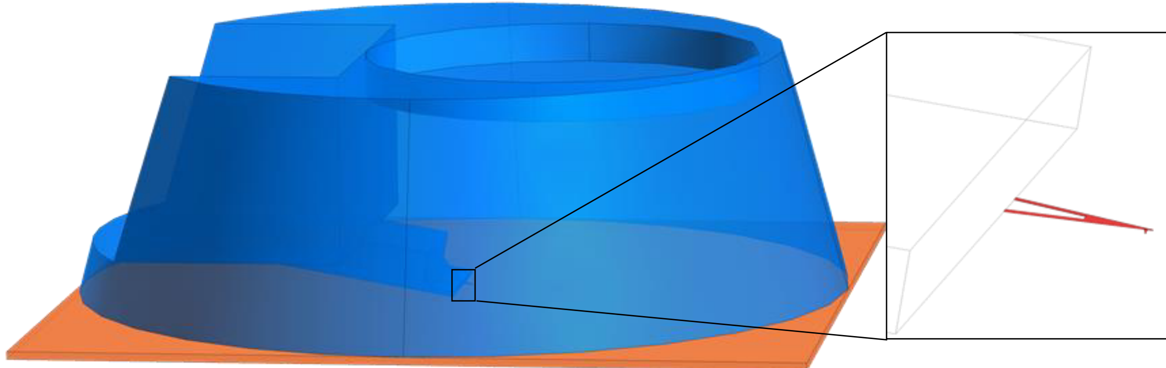

Figure 5.9. Fluid medium shape and AFM cantilever on top of the sample surface in the AFM experimentation based on the sketch in Fig. 5.8.

The relation between the real cantilever movement and the fluid flow direction for the simulation can be described as indirect proportional. The correlation is also pointed in Fig. 5.10. As a result, the z-movement of the cantilever in the fluid during the approaching to or withdrawing from the sample surface is equivalent to a fixed cantilever flowed by the fluid in the opposite direction.

The sinusoidal movement of the AFM cantilever in the fluid can be described as:

$$z(t) = z_{max} \cdot \sin(2\pi f \cdot t) \tag{5.16}$$

where z_{max} represents the amplitude maximum of the sinusoidal cantilever movement, f is the oscillation frequency and t is the time. z_{max} can be varied from 50 nm up to 300 nm. The velocity can be calculated by differentiation:

$$v(t) = \frac{d}{dt} z(t) = z_{max} \cdot 2\pi f \cdot \cos(2\pi f \cdot t). \tag{5.17}$$

The highest drag forces may be expected for the maximum relative velocity of cantilever and fluid. This is independent whether the model of Fig. 5.3, resting cantilever and moving fluid, with which the force calculations are performed, or real measurement conditions, resting liquid and moving cantilever, is considered. This correlation is also shown in Fig. 5.10. The maximal cantilever velocity v_{max} for the model can be deduced from real measurement conditions by:

$$v_{max} = z_{max} \cdot 2\pi f. \tag{5.18}$$

Transferred to the simulation model, the force deflecting the cantilever induced by the movement in the liquid medium can be calculated according to Eq. 5.18.

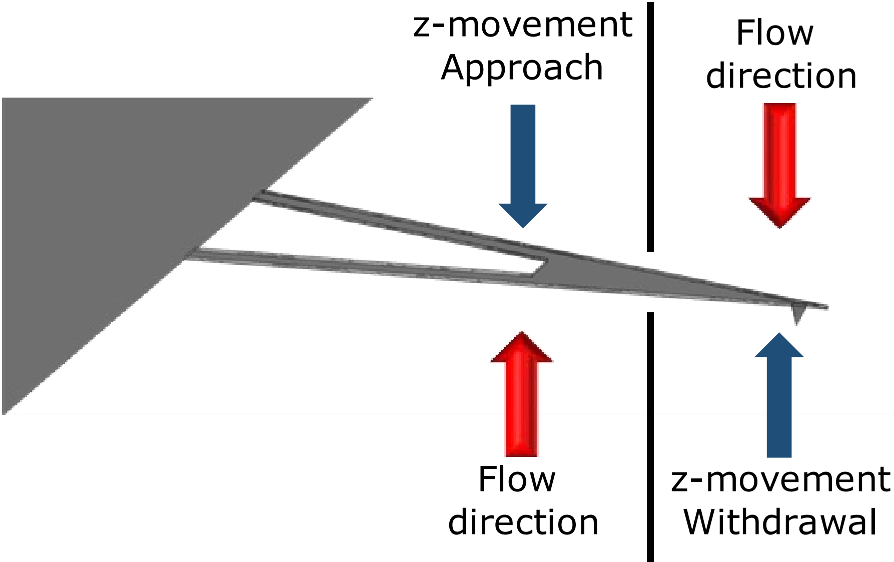

Figure 5.10. The fluid flow direction chosen in the simulation model related to the cantilever's z-movement in real. The movement of a body in the fluid is equivalent to a fixed body flowed by the fluid.

5.4 Results and Discussion

The introduced simulation model can evaluate the deflection of the cantilever caused by the liquid environment. The 3D plot in Fig. 5.11 images the achieved result of the simulation. The plot contains two different information which are illustrated by the color scales, the flow velocity of the fluid medium and the displacement of the cantilever as well as of the Cu substrate. It can be seen, that the fluid flow in the outer area is zero and that the displacement of the Cu substrate caused by the fluid flow is zero. Much more interesting is the area around the cantilever which is also shown in Fig. 5.11. The cantilever shape colored with respect to the displacement as well as the streamlines illustrating the fluid flow around the cantilever can be roughly seen.

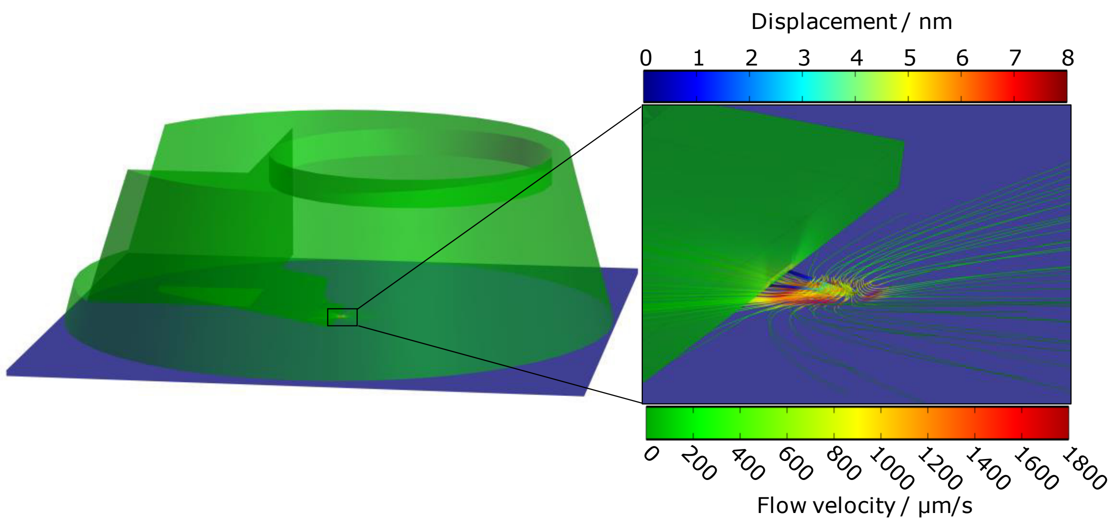

Figure 5.11. Simulation result and zoomed region of interest of the cantilever. The area of the fluid medium as well as the streamlines around the cantilever are highlighted corresponding to the color range of the flow velocity. The colors of the cantilever and the Cu substrate correspond to the color scale of the displacement caused by the fluid flow.

Consequently, the interesting area around the cantilever is illustrated in more detail in Fig. 5.12. In this figure the cantilever can be seen more clearly. The colors of the cantilever shape illustrate the respective deflection of the cantilever according to the displacement color scale. It is obvious that the tip end of the cantilever experiences the highest bending. The streamlines depicted in Fig. 5.12a represent the fluid flow around the cantilever. The associated flow velocity of the streamlines is indicated by the respective color scale. It can be concluded that the resulted velocity variation is induced by the resistance to flow

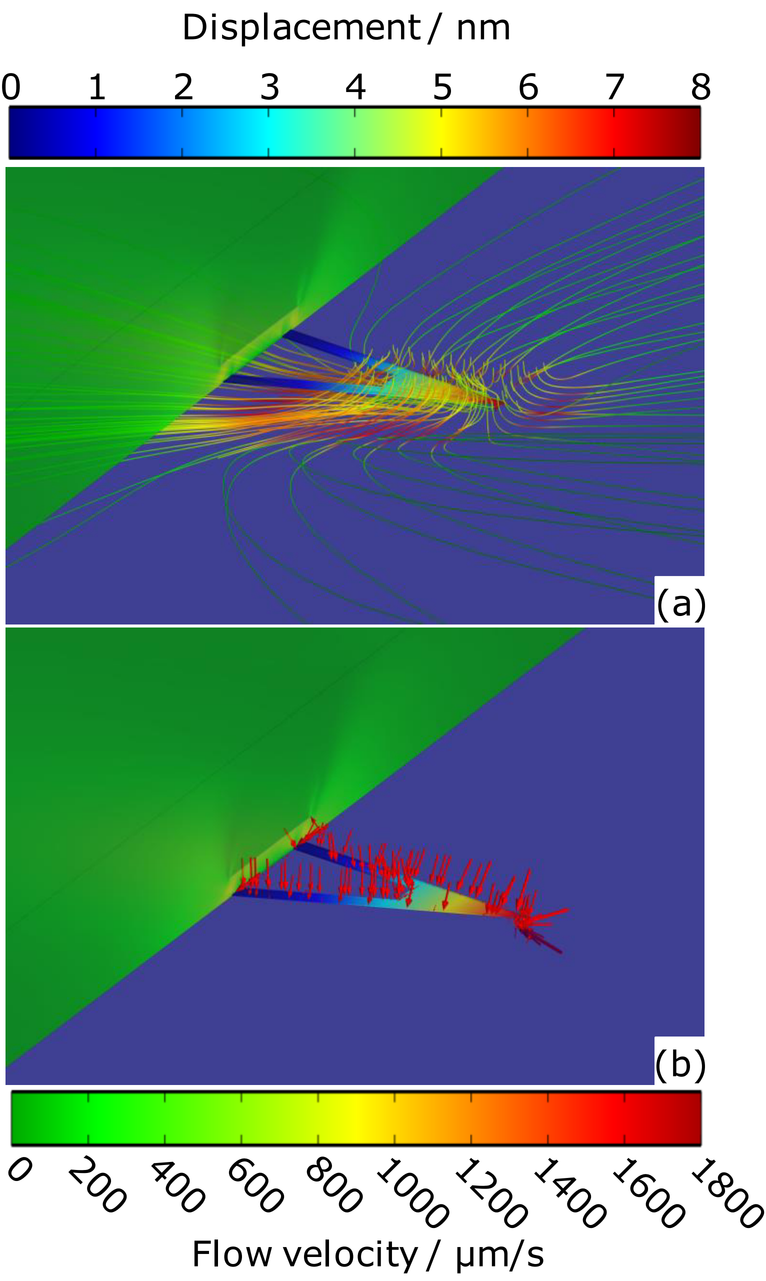

Figure 5.12. Simulation result around the cantilever area showing in (a) the flow velocity around the cantilever by streamlines as well as the deflection of the cantilever and in (b) also the deflection of the cantilever as well the pressure acting on the cantilever because of the fluid flow highlighted by red arrows.

of the cantilever. Due to this resistance, the liquid flow results in pressure acting on the cantilever which is highlighted by the red arrows in the Fig. 5.12b and this pressure causes the deflection of the cantilever. Upon these results, the drag force can be calculated by using the spring constant which was evaluated in section 5.2.

For a reliable simulation model, the calculated results must be hedged by comparing with own measurement results or with published data from other researchers. In the experimental part regarding the PeakForce Tapping [98] method the background subtraction algorithm was already introduced. This algorithm dramatically gains the signal-to-noise ratio and enables the application of very low peak forces in the range of some tens of pico-Newtons which is essential for the measurement of very soft sample surfaces [100,137]. However, this background subtraction limits the investigation of the real hydrodynamic forces. Consequently, the evaluation of the simulation model was realized by comparing the simulated results with published data of other researchers.

5.4.1 Evaluation of the sensor dynamics simulation model

The simulation model was developed to estimate the influence of the liquid medium on the cantilever deflection during the PFT operation mode. For an evaluation of the present model appropriate for PFT operations presented in this work, the studies of other researchers were used. Janovjak et al. [139] quantified hydrodynamic drag forces as a function of pulling speed using the scaled spherical model of Alcaraz et al. [140]. Mendez et al. [138] introduced a numerical model to predict the hydrodynamic drag force in measurements undertaken in fluids and already compared their model with the results derived in the study of Janovjak et al. [139]. In both works, the hydrodynamic drag force obtained for a small OTR4 Olympus V-shaped cantilever in water was presented. Fig. 5.13 shows the respective cantilever model with exact geometrical dimensions.

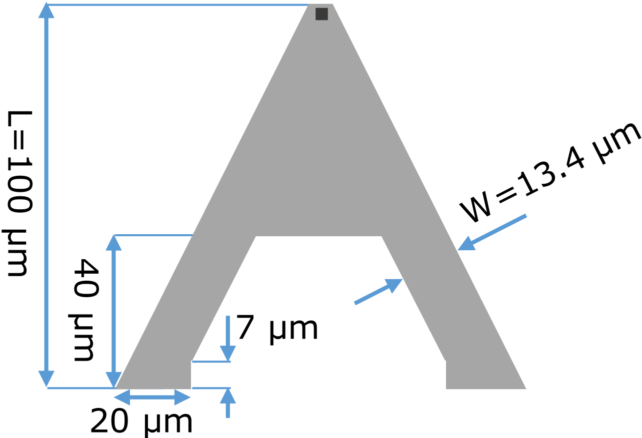

Figure 5.13. Cantilever model OTR4 Olympus with a thickness of 0.4 µm according to the data in [138] and [139].

To compare the results of both studies with the model developed in this work, the methodology described in section 5.2 to calculate the effective spring constant for a Young's modulus E of 250 GPa at a temperature of 25 °C was used. The value of the effective spring constant calculated for the cantilever shown in Fig. 5.13 was $0.1402\ \frac{\mathrm{N}}{\mathrm{m}}$. Fig. 5.14 compares the results of the present model with the results of the other studies. The predictions of the present model are in good agreement with the results of the other researchers. The linear dependence of drag force and tip velocity is clearly visible. Especially the results of Mendez et al. [138] accord very well with the numerical predictions of the present model. Based on these outcomes it must be noted that the introduced model is very well suited to predict the drag force caused by the AFM probe tip movement in a liquid measurement environment.

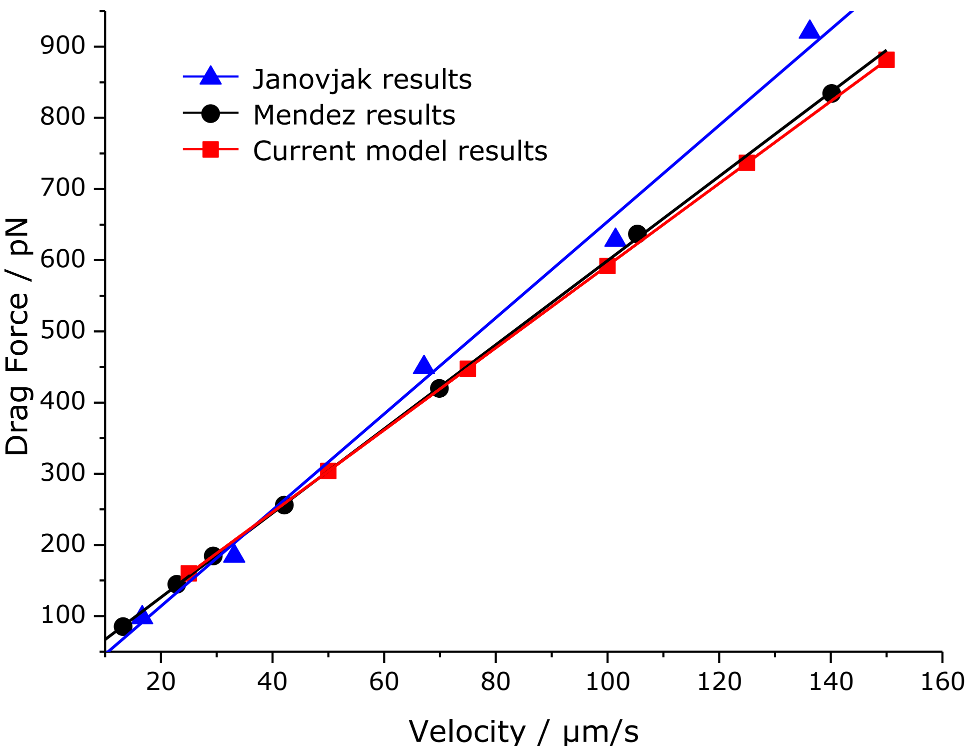

Figure 5.14. Comparison of the FEM simulation results with the numerical predictions published by Mendez et al. [138] and Janovjak et al. [139].

5.4.2 Sensor dynamics in ultrapure water

For AFM fluid imaging application in general and dCFM measurements in particular, the frequency for the probe tip movement was fixed to 1 kHz. The amplitude of the cantilever oscillation can be changed in the range of 50 nm up to 300 nm. Therefore, the flow velocity in the simulation model was varied within this amplitude range with respect to Eq. 5.18.

Fig. 5.15 presents the hydrodynamic drag force in relation to the oscillation amplitude for the different cantilevers under investigation. The drag force acting on the cantilevers changes significantly with the amplitude and displays a linear behavior. The maximum drag force for the triangular cantilever is much smaller than for the rectangular cantilever geometry. This may be interpreted that triangular cantilevers provide an improved flow behavior. Shorter cantilevers cause smaller drag forces than longer cantilevers. This can be explained by the fact, that with cantilever length the effective area presented to the liquid is increased which causes increased drag forces and vice versa. As can be seen in Fig. 5.15, the cantilevers are subject to different drag forces for approach and withdrawal movement. These differences vary from 0.28% and 0.79% for the 100 µm triangular cantilever and the 100 µm rectangular cantilever to 6.09% and even 12.80% for the 200 µm triangular cantilever and the 200 µm rectangular cantilever, respectively. The general difference can be explained by the tip geometry increasing the drag force during the approach movement. As an important outcome, it is worth noting that the 200 µm long cantilevers provide a much lower relative difference in drag force for triangular versus rectangular geometries

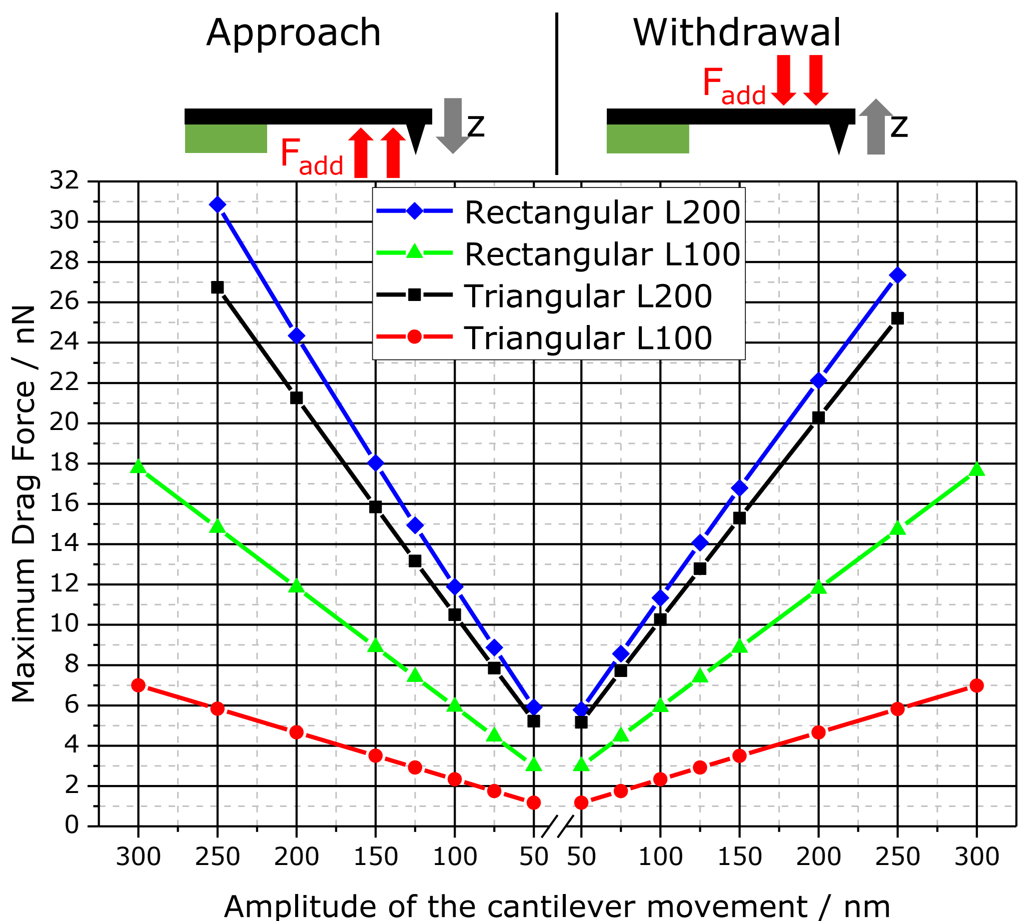

Figure 5.15. The maximum drag force versus the oscillation amplitude for different AFM cantilevers in water at 25 °C for a tip-sample distance of 500 nm. Both the values for the approach and the withdrawal are plotted.

compared to 100 μm long cantilevers. Overall it is obvious that the triangular cantilever with a length of 100 μm features the lowest drag force during the approach movement as well as during the withdrawal.

The computed drag forces are much higher than the values calculated for the evaluation of the simulation model in Fig. 5.14. The tip speed during the PFT operation ranges from 1885 μm/s for an amplitude of 300 nm to 314 μm/s for an amplitude of 50 nm and these values are much higher than the velocities considered in Fig. 5.14. For this reason, the drag forces achieved for the dCFM conditions are much higher. Compared to that results, Schillers et al. [100] also mentioned that the hydrodynamic forces can be as high as 10-20 nN. As can be seen in Fig. 5.15, it can be confirmed that such force values are in the scope of this work depending on cantilever type and length as well as amplitude of cantilever movement. As an important conclusion, for dCFM operations in the liquid environment triangular cantilever geometry and short cantilevers are recommended. Consequently, for the further examinations presented in this study the triangular cantilever with a length of 100 μm were considered.

The outcomes in Fig. 5.15 were achieved for operations in ultrapure water at 25 °C. These conditions are close to normal ambient air. However, during operation the AFM equipment and thus the liquid environment becomes warmer due to energy dissipation of the equipment. The main parameters of the fluid influencing the hydrodynamic forces are the density ρ and the dynamic viscosity μ. The relationship between temperature and density as well as temperature and dynamic viscosity is indicated in Fig. 5.16. The temperature dependence of the fluid properties were derived from the Comsol built-in material library and were also confirmed in literature [150]. Both curves exhibit that the density as well as the dynamic viscosity decrease significantly at higher temperatures.

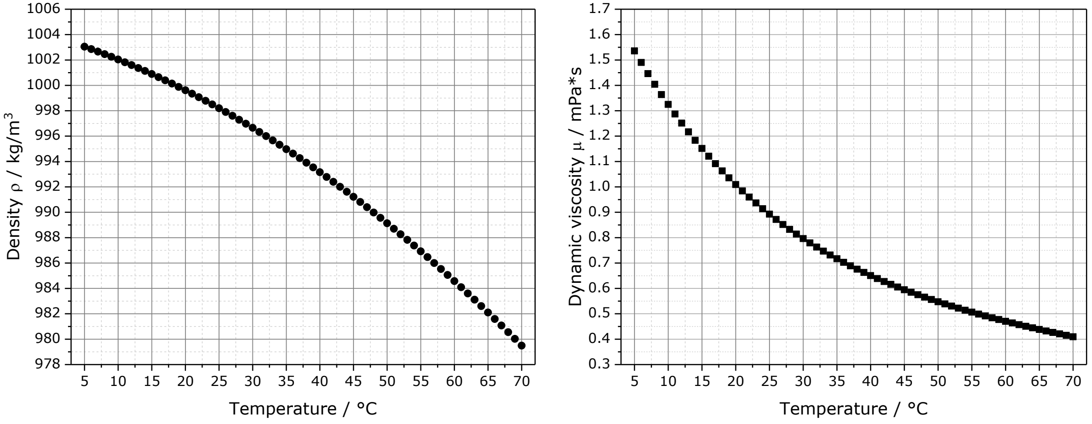

Figure 5.16. Temperature versus density ρ (left) and dynamic viscosity μ (right) of water derived from the Comsol built-in material library and [150].

Transferred to the simulation model the influence of the fluid temperature on the drag force can be investigated. Based on the previous evaluation of the different cantilever types in Fig. 5.15, the influence of the fluid temperature was examined for the 100 µm long triangular cantilever. The variation of the drag force influenced by the temperature is shown in Fig. 5.17. As expected from the data depicted in Fig. 5.16, an increase of the fluid temperature to 35 °C lowers the drag force significantly.

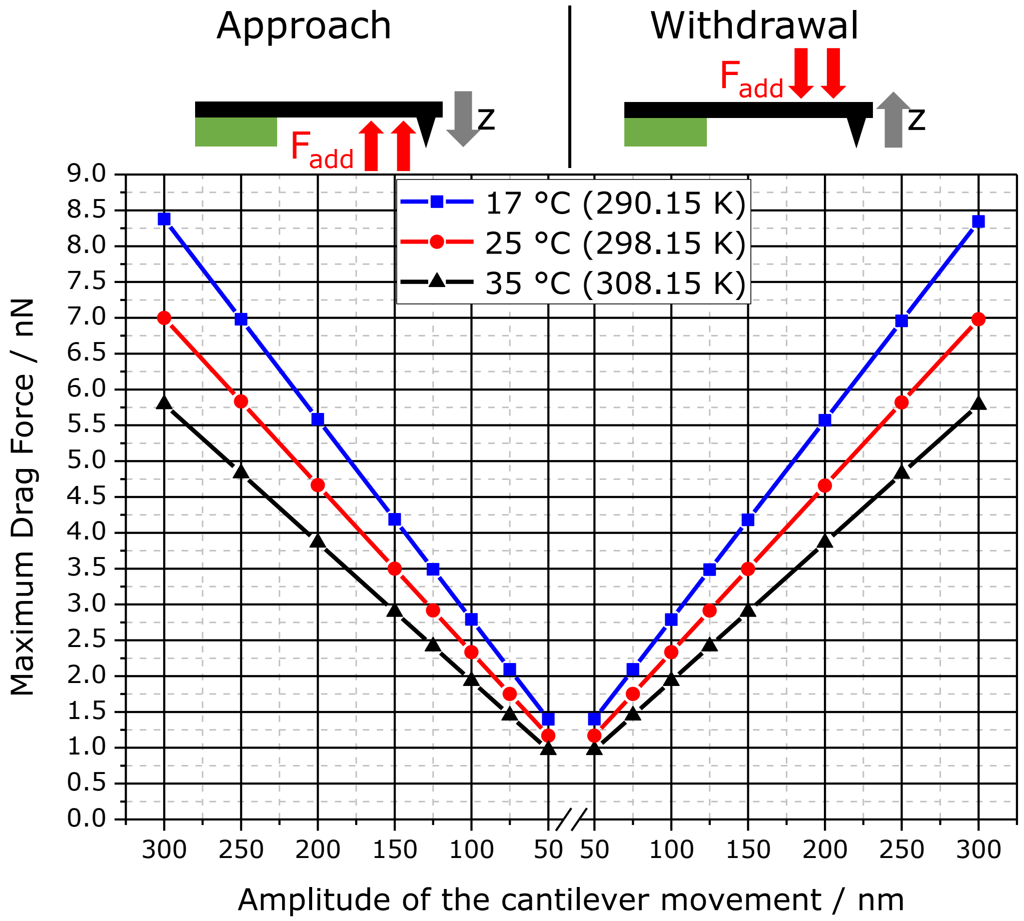

Figure 5.17. The maximum drag force versus the oscillation amplitude of the 100 µm long triangular cantilever at various temperatures of the water for a tip-sample distance of 500 nm. Both the values for the approach and the withdrawal are plotted.

For a more detailed investigation of the temperature influence, the simulation should be performed for an extended temperature range. By examining the results in Fig. 5.17, I could figure out that the relative variation induced by temperature change is identical for each amplitude value. The rise of the temperature from 17 °C to 35 °C leads to a reduction of the drag force by approximately 31%. The variation from 25 °C to 35 °C still results in 17% lower drag forces. The finding that the relative variation induced by temperature change is identical for each amplitude value is very important. It means that for the further investigation of the temperature influence on the drag force it is sufficient that the

temperature change is calculated at a single amplitude value. This procedure is essential time- and resource-saving.

Fig. 5.18 presents the drag force over the fluid temperature for ultrapure water and a 100 µm long triangular cantilever operated at an oscillation amplitude of 100 nm. As expected from Fig. 5.16, the increasing fluid temperature lowers the drag force significantly. The labels of the data points represent the percentage change with respect to the force at a temperature of 25 °C. An increase from 25 °C to 30 °C reduces the drag force by 9.4% and a further increase to 35 °C decreases the drag force by 17.2%. It clearly illustrates that the fluid temperature influences the drag force significantly.

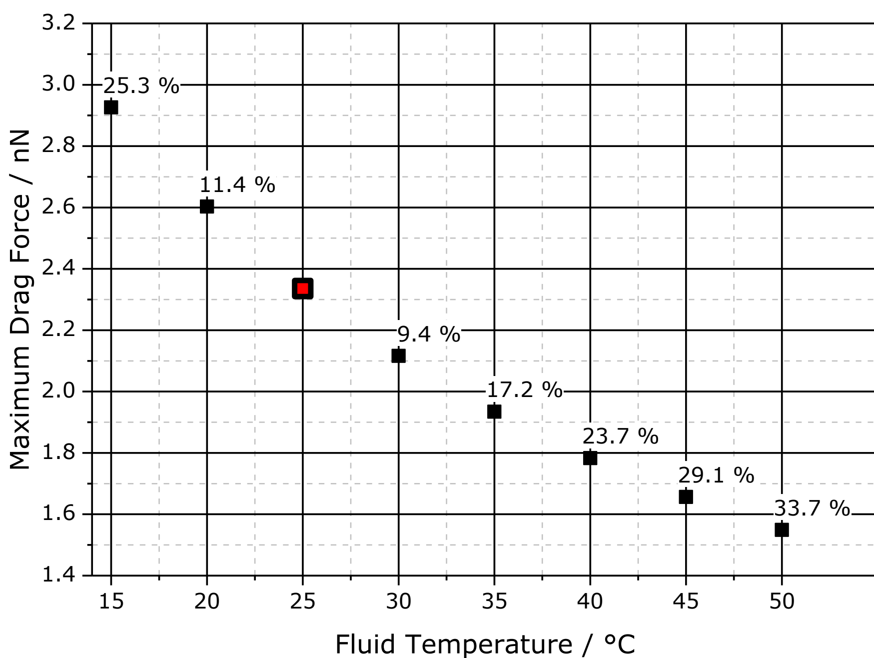

Figure 5.18. The maximum drag force versus the temperature of the surrounding ultrapure water during the operation of the 100 µm triangular cantilever at an oscillation amplitude of 100 nm. The labeling of the data points is the percentage change based on the drag force at a temperature of 25 °C

As mentioned previously, the percentage change of the drag force at a single oscillation amplitude can be transferred to the remaining amplitude values. Pinpointed in Fig. 5.19 the outcomes of the calculated values based on the percentage change derived in Fig. 5.18 can be seen. Fig. 5.19 represents in more detail the significant influence of the fluid temperature on the drag force over an extended temperature range. Due to Fig. 5.18 and 5.19, it can be concluded that a slight temperature increase reduces the drag force significantly and may thus influence AFM measurement results. Therefore, it is recommended to start AFM fluid imaging procedures after equipment and cantilever holder including the respective liquid have reached thermal equilibrium, which is for normal AFM measurements in liquid in the range of 25 °C to 35 °C. The corresponding forces were calculated up to a temperature of 50 °C (Fig. 5.19). Such

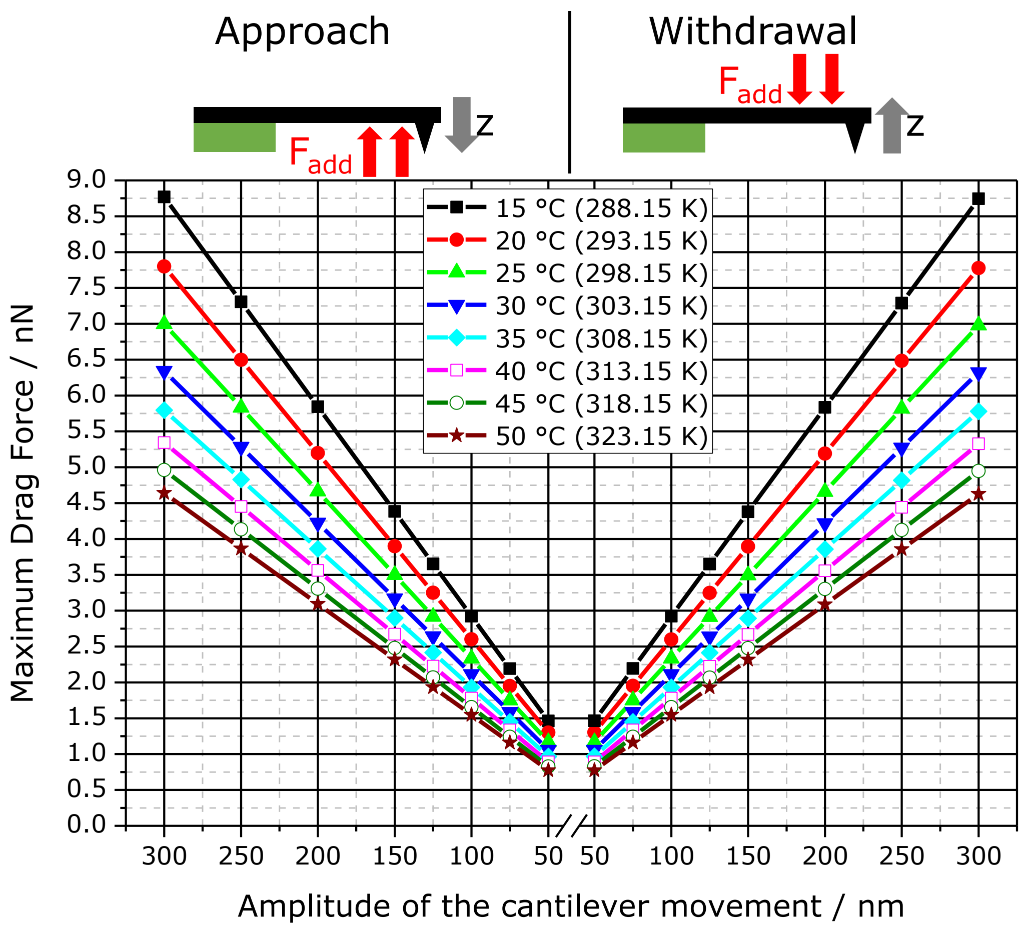

Figure 5.19. Maximum drag force versus the oscillation amplitude of the 100 μm triangular cantilever at various fluid temperatures based on Fig. 5.18. Both the values for the approach and the withdrawal are plotted.

temperature ranges could be reached by purposely applied additional sample heating. In this case, it must be considered, that the evaporation rate of the liquid is increased and the liquid content of the cantilever holder must be controlled frequently to ensure stable measurement conditions.

5.4.3 Sensor dynamics in an ethanol-water mixture

The results presented so far were achieved for ultrapure water as fluid medium. In the previous section 5.3 introducing the fluid model an ethanol-water mixture was already mentioned as alternative medium and potential advantages by strengthening of interaction forces were presented by experiments of other researchers [147,148]. Based on the derived values of the density ρ and the dynamic viscosity μ in relation to the ethanol concentration previously introduced and imaged in Fig. 5.7, the fluid properties could be defined accurately for the simulation. The drag forces for the 100 μm long triangular cantilever and varying ethanol content over the amplitude of cantilever movement are represented in Fig. 5.20. It is obvious that an increased ethanol concentration increases the resulted drag forces significantly. Even a comparatively low ethanol concentration of 10% doubles the hydrodynamic forces.

In their experimental investigation, Yaacobi et al. [148] mentioned that the molecular interaction forces are amplified for an ethanol concentration in the range from 3% to 20%. In addition, the experimental data of Kokkoli et al. [147] show a strengthening of the attraction and adhesion of two hydrophobic surfaces for an ethanol concentration $x_{EtOH} \leq 0.05$. Since both research articles [147,148] provide recommended EtOH concentrations in the range of 5% or even lower to amplify interaction forces and since low EtOH fractions and thus reduced hydrodynamic drag forces are preferable, this range is considered for further investigations. The detailed examination of this EtOH range in Fig. 5.20 shows that 1% EtOH increases the drag forces by approximately 11.6%, the rise for 2.5% EtOH can be estimated at 29.3% and 5% EtOH even provides 57.5% higher drag forces.

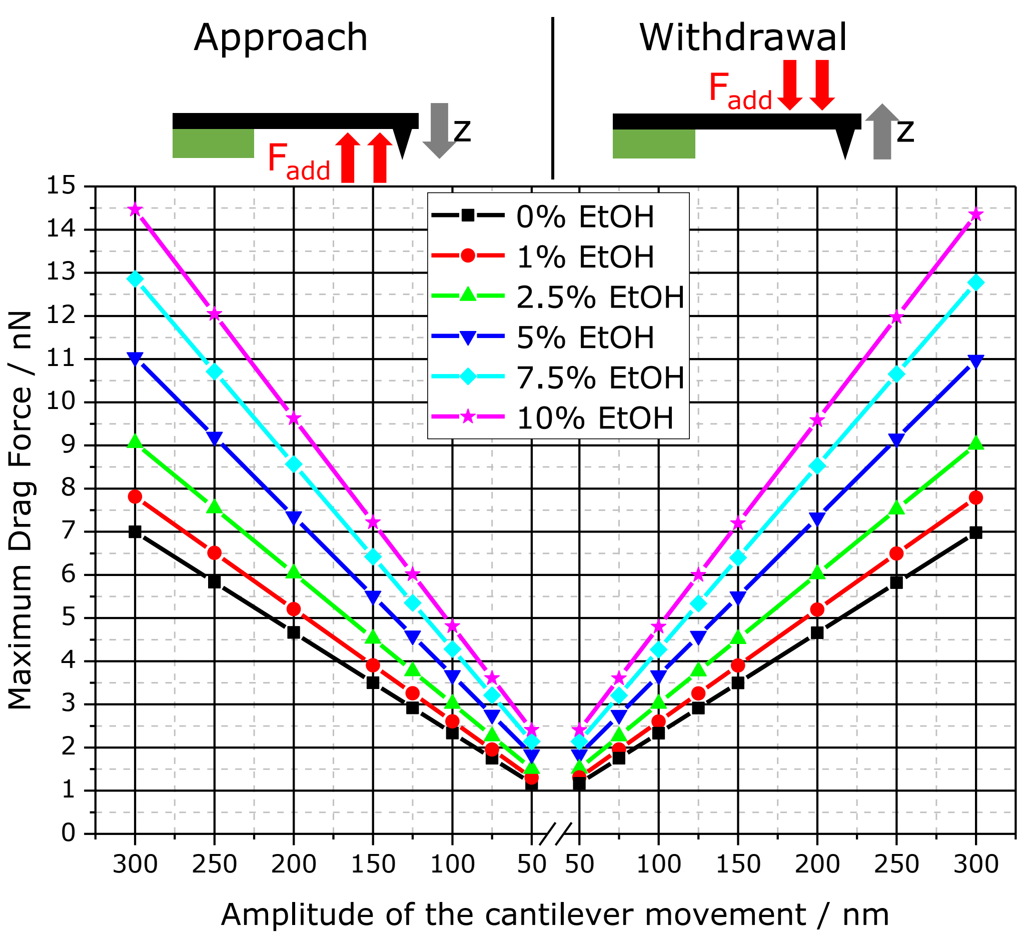

Figure 5.20. Maximum drag forces derived for the 100 µm long triangular cantilever operated in an ethanol-water mixture at 25 °C (298.15 K) with a varying ethanol concentration up to 10%.

Since the values in Fig. 5.20 are related to environmental conditions of 25 °C, analogous to the application of pure water, the temperature impact was analyzed for the ethanol-water mixture used as sensor fluid. The temperature dependence of the density as well as of the dynamic viscosity must be considered for each individual mass fraction of ethanol. The variation of the fluid properties can be

observed in Fig. 5.21. While the temperature dependence of the density ρ is comparatively low, the dynamic viscosity μ changes significantly with temperature. For studying the temperature influence for each ethanol concentration and oscillation amplitude, the simulation with that many parameters would be very time-consuming. In the section 5.4.2 regarding the sensor dynamics in ultrapure water, this problem was solved by the finding that the relative variation induced by the temperature is identical for each amplitude value. Transferred to the ethanol-water mixture, the same observation can be made for each individual ethanol concentration.

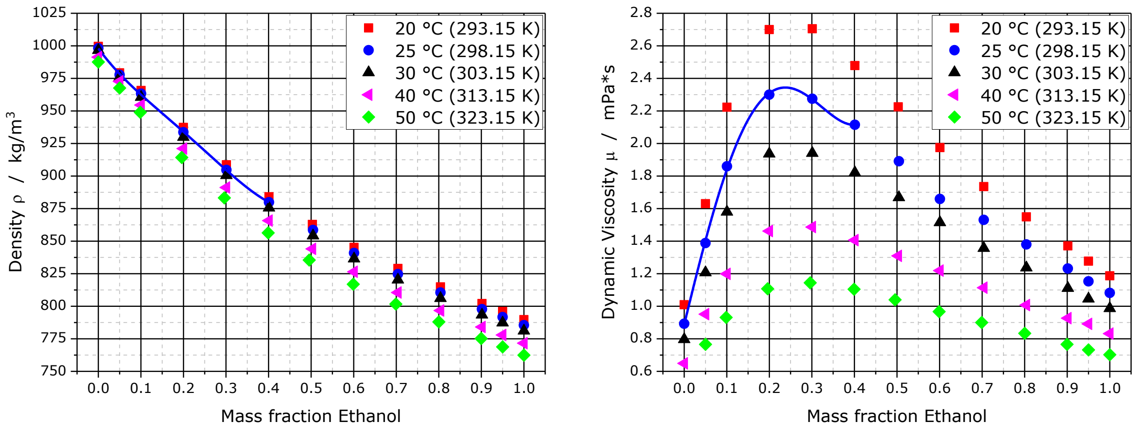

Figure 5.21. Change of the density ρ (left) and the dynamic viscosity μ (right) in relation to the mass fraction of ethanol in an ethanol-water mixture at different temperatures based on [149,151]. The solid line indicates the fitted values for 25 °C (298.15 K) which were used for calculating the results in Fig. 5.20.

Consequently, the more precise study of the drag force variation influenced by different fluid temperatures at an oscillation amplitude of 200 nm operated in an ethanol-water mixture with varying ethanol concentration is shown in Fig. 5.22. The fixed-point for the labeling of the percentage change is the value for 25 °C. Even a slight increase to 30 °C lowers the hydrodynamic force by 11.1% for 1% EtOH, by 12.9% for 2.5% EtOH and by 13.5% for 5% EtOH. These derived values were taken to calculate the drag forces for the different oscillation amplitudes in a temperature range beginning from 15 °C up to 50 °C. This allows the precise examination of the temperature dependence of the hydrodynamic drag forces during the cantilever oscillation in the ethanol water mixture.

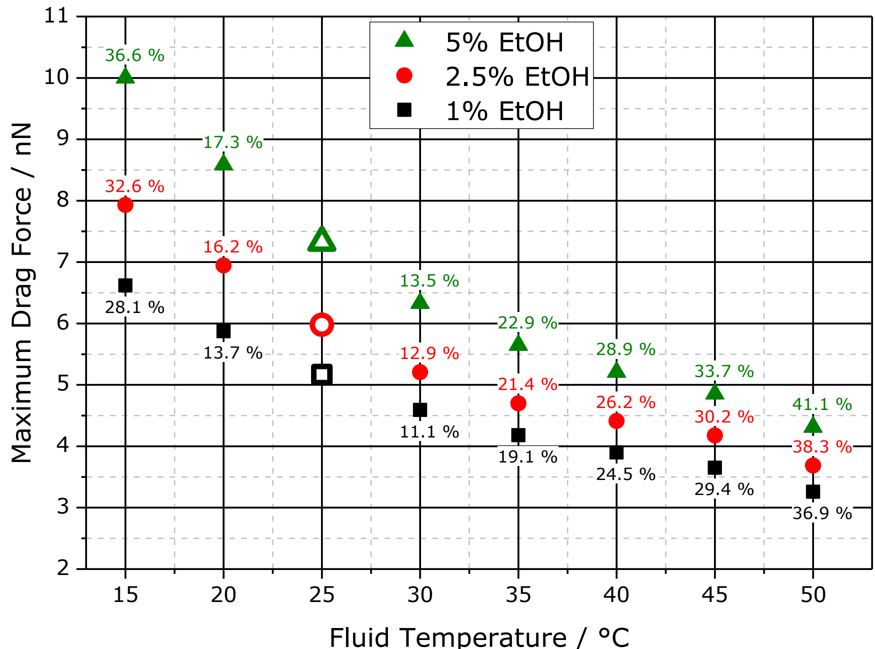

Figure 5.22. Maximum drag force versus temperature of the surrounding ethanol-water mixture with varying ethanol concentrations during operation of the 100 µm long triangular cantilever at an oscillation amplitude of 200 nm. The labeling of the data points is the percentage change based on the drag force at a temperature of 25 °C

In Fig. 5.23 the detailed results related to 5% EtOH are summarized. Like the observations of the ultrapure water and as already expected from Fig. 5.22, the significant decrease of the drag force caused by elevated temperatures is evident. The corresponding drag forces were calculated up to a temperature of 50 °C (Fig. 5.23), which is above the temperature range reachable by the self-heating of the equipment.

Such temperature ranges could be reached by a purposely applied additional sample heating. In this case, it must be considered, that the evaporation rate of the liquid is increased and the amount of liquid must be controlled frequently to ensure stable measurement conditions. Without an additional heat source, the temperature range related to the energy dissipation of the equipment was defined in the range from 25 °C to 35 °C.

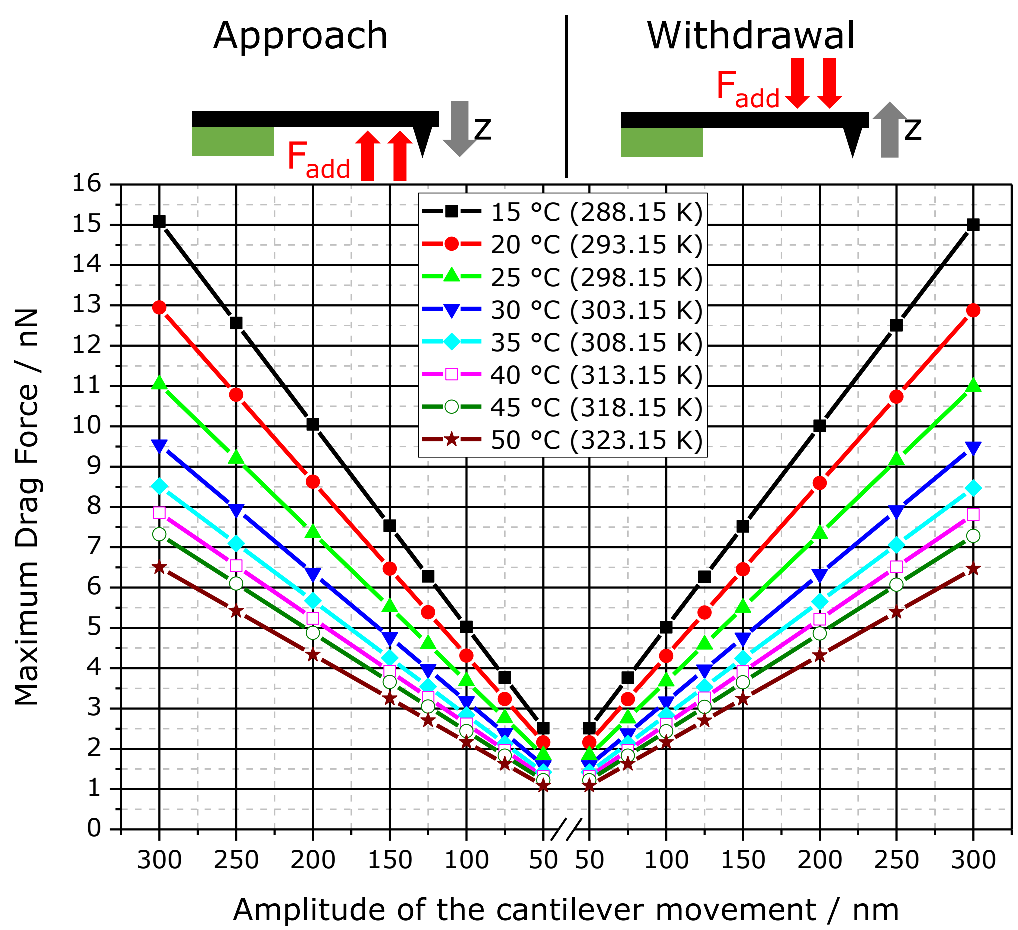

Figure 5.23. Maximum drag force versus the oscillation amplitude of the 100 μm triangular cantilever operated in an 5% ethanol-water mixture at various fluid temperatures based on Fig. 5.22. Both the values for the approach and the withdrawal are plotted.

Fig. 5.23 shows the temperature influence in the extended range from 15 °C to 50 °C. The calculated values considered in this diagram are only related to an ethanol-water mixture with an ethanol concentration of 5%. However, in Fig. 5.22 the temperature dependence of various ethanol concentrations is displayed. Based on these values, the temperature influence on the hydrodynamic drag force acting on the 100 μm long triangular cantilever operating in an ethanol-water mixture with different ethanol concentrations is plotted in Fig. 5.24.

The temperature range in this diagram can be related to the self-heating of the equipment. The different colors are allocated to the corresponding ethanol concentrations. The areas related to the ethanol concentrations overlap for some temperature values. This final diagram completes the investigation of the sensor dynamics in the ethanol-water mixture. The presented results clarify that the hydrodynamic drag forces can be determined exactly for each individual measurement setup used for the dCFM analysis.

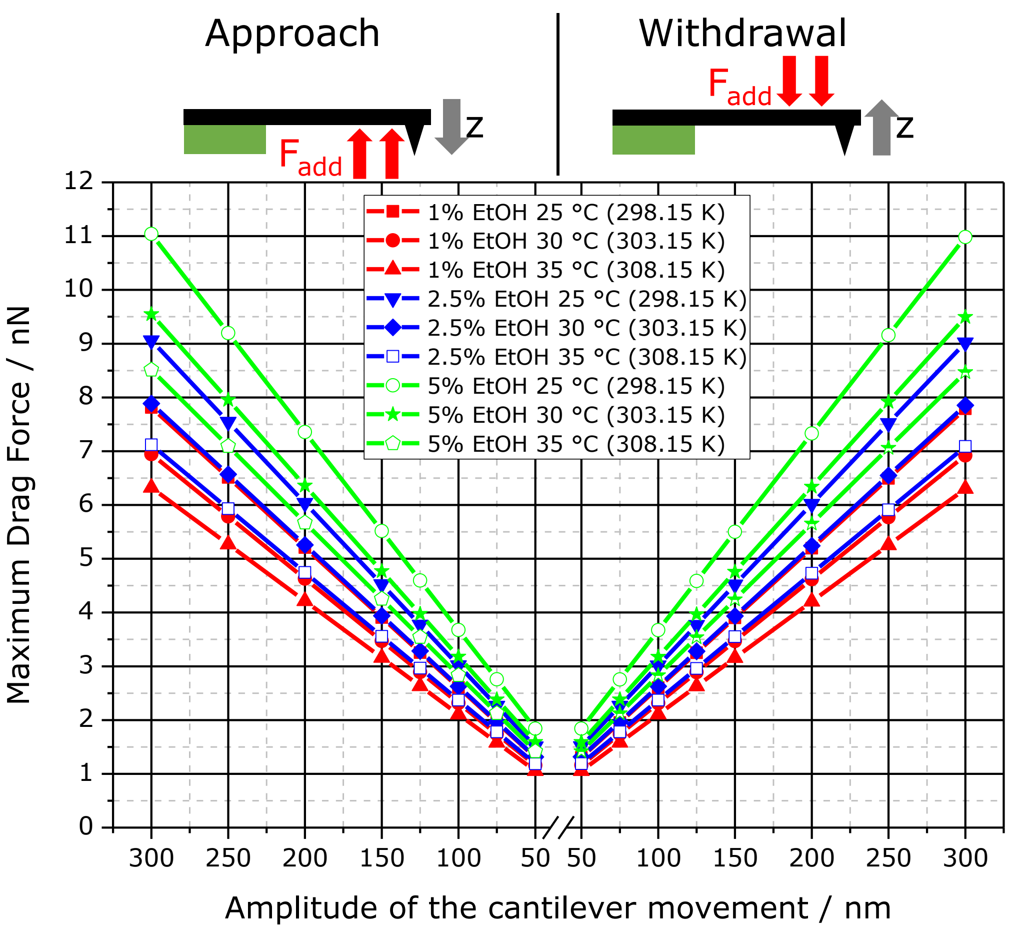

Figure 5.24. Maximum drag force versus oscillation amplitude of the 100 µm triangular cantilever operated in an ethanol-water mixture with 1%, 2.5% and 5% ethanol concentrations with fluid temperatures ranging from 25 °C to 35 °C.

5.5 Summary

In this study a numerical integrated model was presented that is able to provide accurate predictions of the hydrodynamic drag forces present in AFM fluid imaging applications in general and in chemical force measurements in particular. The results include a wide range of cantilever types, cantilever oscillation amplitudes, fluid types and fluid temperatures. The numerical 3D model employed was verified by comparing the predicted drag forces with published results of other researchers and good agreement was observed. The findings of this study confirmed that drag force dependence on tip speed is essentially linear in nature.

The numerical results could show that the triangular cantilever geometry is preferable for AFM measurements in liquid because it provides significantly lower drag forces than the rectangular cantilever geometry. Beside the examination of different cantilevers and their oscillation amplitudes, the influence of the used fluid medium such as ultrapure water or an ethanol-water mixture could be demonstrated.

The results showed that ultrapure water provides the lowest drag forces, whereas with increasing ethanol concentration the drag forces increase. In addition, the presented fluid temperature dependence on the drag force clarified that besides the self-heating of the equipment, an additional heat source could be used for a further improvement of the parasitic hydrodynamic drag forces. By operating the 100 µm long triangular cantilever with standard parameters (frequency = 1 kHz and oscillation amplitude = 100 nm) in ultrapure water at a temperature of 35 °C, the hydrodynamic drag force can be stated to be 1.93 nN.

6. Nanoscale characterization of Self-Assembled Monolayer on Cu

Copper (Cu) has become an important material to replace gold and aluminum [29] in microelectronic packaging. Advantages of Cu are high electrical and thermal conductivities plus low cost and easy fabrication. However, one of the main drawbacks of Cu is that the surface is subject to oxidation, even at room temperature. In contrast to aluminum, Cu oxide does not form a self-passivation layer to prevent the underlying Cu surface from further corrosion. As a consequence, Cu oxidation is the reason for reliability concerns [28] in one of the key processes, the thermosonic wire bonding. Therefore, protection of copper against oxidation is a promising approach to bypass any oxidation-related problems.

Studies show that thin organic Self-Assembled Monolayer (SAM) act as effective barrier to protect metal, in general, and Cu, in particular, from corrosion [29,33,68–71]. As copper is exposed to elevated temperatures during the bonding process, integrity, degradation and temperature stability of the protective layers are critical issues.

The methods predominantly used to characterize SAM films in recent studies were X-ray Photoelectron Spectroscopy (XPS) [33,68–70] and contact angle measurements (CAM) [33,70]. Whelan et al. [33] and Rao [70] showed that high hydrophobicity detected by CAM correlates with high quality SAM films.

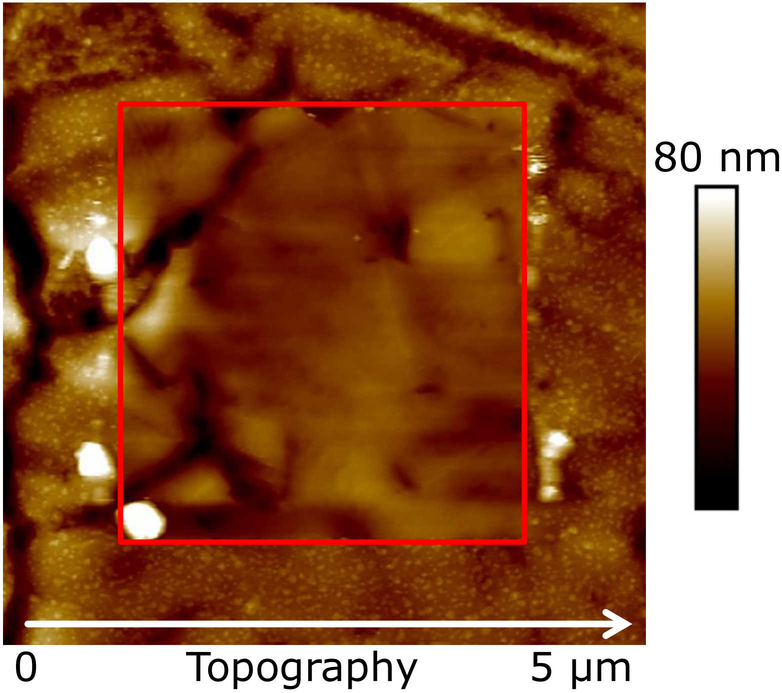

Figure 6.1. AFM topography image achieved by intermittent contact mode of a SAM modified Cu surface damaged by a previously performed contact mode measurement marked by the red rectangle. The significant wear marks indicate a clear surface damage by contact mode operation.

Even though XPS and CAM may provide valuable information about chemical composition and hydrophobicity of the films, respectively, they are not able to achieve very local information. AFM based techniques are able to monitor properties in the nanometer scale and were already employed to investigate SAM films. Rao [70] used AFM based techniques solely for topography imaging. Chintala et al. [92] employed conductive-AFM (C-AFM) to investigate the electrical properties of SAM films on silicon substrate. They observed that SAM films are isolating and that film homogeneity may be monitored by local tunneling current measurements.

However, as shown in Fig. 6.1, in preliminary experiments I frequently observed significant wear marks of the SAM film on Cu after C-AFM measurements. Due to the obvious surface change in Fig. 6.1, I stated that the comparatively high lateral and vertical forces applied by the probe tip during the contact mode measurement damages the SAM film clearly. Therefore, I concluded that contact mode AFM applications are not appropriate for my study.

In the present work, I used Torsional Resonance Tunneling AFM (TR-TUNA) and dynamic Chemical Force Microscopy (dCFM) to characterize SAM films with CH_3 end-group molecules on Cu. TR-TUNA enables the electrical characterization by measuring local tunneling current variations, while dCFM is able to assess local hydrophobicity by measuring chemical forces between probe tip and sample. In both methods lateral and vertical forces are dramatically reduced compared to standard contact mode applications. I stressed the SAM films at 100 °C and 150 °C, respectively and compared the electrical and chemical characteristic with new and unstressed films. Attenuated Total Reflectance Fourier Transform Infrared Spectroscopy (ATR-FTIR) was used to assess the chemical properties of the SAM films on macroscopic scale. I combined ATR-FTIR, TR-TUNA and dCFM measurements in order to validate the individual results and to improve the significance of my conclusions.

6.1 Experimental

The sample structure can be seen in Fig. 6.2 as part of the schematic drawing of the TR-TUNA measurement setup. The SAM films were deposited on a 5 μm thick Cu layer on top of a supporting sample structure consisting of a tungsten titanium (WTi) liner on a silicon (Si) base with a thin silicon dioxide (SiO_2) film. Before SAM deposition, the Cu surface was cleaned chemically by an aqueous solution of 1 % hydrochloric acid and, subsequently, physically by an argon ion beam for 2 min at an acceleration voltage of 2 kV. The cleaning procedure removes contaminations and native oxides and ensures high quality SAM films.

For the SAM coating a nano-polymer solution from Nanocraft Coating GmbH was used [152]. The cleaned Cu surface was kept immersed in an aqueous nano-polymer solution in a temperature range of 60-65 °C for 5 min. By this means, a homogenous SAM film was built on the surface with CH_3-molecules as end-groups. The CH_3-molecules are responsible for the hydrophobic character of the resultant sample

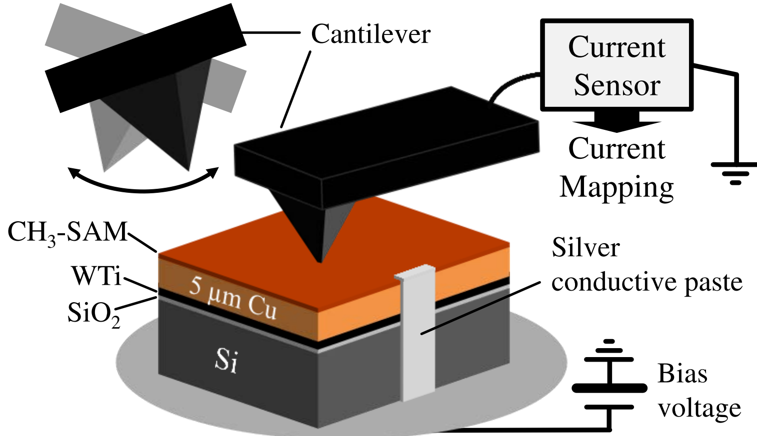

Figure 6.2. Structure of the test sample and schematic drawing of the TR-TUNA measurement setup. The conductive tip is oscillating in torsional resonance very close to the surface and tunneling current is detected. Silver conductive paste improves the conductivity of the copper layer to the measurement chuck.

surface. After deposition, in a first step, the samples were rinsed in ultrapure water and dried in a nitrogen jet. In a second step, the samples were rinsed in a sequence of ethanol and ultrapure water and dried with a nitrogen jet in order to remove disengaged molecules and particles from the surface. The second step was frequently repeated before measurements. Except during the measurements, the samples were continually stored in dry air environment (23 °C, 0% humidity). For the investigation of the temperature stability the SAM films were stressed according to literature [33] at 100 °C and 150 °C, respectively. The temperature stress was applied for 30 min which was a suitable time window related to the bonding process.

The chemical properties of the SAM film were characterized by Attenuated Total Reflectance Fourier Transform Infrared Spectroscopy (ATR-FTIR) with a Thermo Nicolet Nexus 470 spectrometer in dry air environment (~23 °C, 0% humidity). The detector is sensitive in the wave number range of 4000-400 cm^{-1}.

The Atomic Force Microscopy (AFM) measurements were performed with a Bruker Dimension Icon AFM. In preliminary experiments, I used the AFM in contact mode and noticed severe damage of the comparatively soft SAM film surface. Therefore, I discarded contact mode applications of the AFM for the present research and employed advanced AFM techniques with reduced lateral and vertical forces between probe tip and sample.

For the electrical characterization of the SAM films Torsional Resonance Tunneling Atomic Force Microscopy (TR-TUNA) [114,115] was used. The schematic measurement setup is depicted in Fig. 6.2. TR-TUNA is a contactless measurement technique. The AFM cantilever probe tip oscillates in torsional resonance in close proximity (~1-2 nm) of the sample surface. Since the probe tip is close to the sample, a tunneling current can be detected by the current sensor provided that a conductive probe tip is used

and an appropriate bias voltage is applied. As a result, this method generates a two-dimensional map of the electrical conductivity of the area under surveillance. The measurements were performed under ambient conditions (25 °C, 50% humidity). I used platinum-iridium coated probe tips (SCM-PIT from Bruker AXS) biased with a voltage of 100 mV to achieve a current flow directed from the probe tip into the sample. The resonant frequency of torsional oscillations was around 800 kHz. The Cu layer was connected electrically to the stage by a conductive paste (Fig. 6.2). In order to enhance the reliability of the results and to prevent artifacts due to erroneous or damaged probe tips, I repeated the measurements with different probe tips of the same type.

Dynamic Chemical Force Microscopy (dCFM) was employed to study the local hydrophobicity of the SAM films. The measurement principle of dCFM was explained in detail in section 3.1.3. I used CH_3-modified probe tips from Nanocraft Coating GmbH [152]. The modification by functional CH_3-molecules gives the tip a hydrophobic character and acts as agent between tip and sample. In dCFM the AFM operates in the PFT mode which was explained in detail in section 3.1.1. In PFT the turning point of the probe tip z-movement is defined by a maximal force F_{max}. The adhesion force $F_{Adhesion}$ acting between probe tip and sample surface is a measure for the hydrophobicity of the surface. For CH_3-terminated probe tips $F_{Adhesion}$ increases with the grade of hydrophobicity and vice versa.

With respect to the evaluated hydrodynamic drag force in chapter 5, the 100 µm long triangular cantilever with a nominal spring constant of 0.32 N/m was chosen. To achieve lowest drag forces and improved sensitivity, the measurements were performed in ultrapure water preheated up to 35 °C by the energy dissipation of the AFM equipment. The measurement parameter for the sinusoidal z-movement was set to 1 kHz for the frequency and 100 nm for the oscillation amplitude.

This setup ensures low drag forces and the exact control of the peak force by the background subtraction algorithm. Altogether with minimized lateral forces, dCFM enables the nondestructive characterization of the SAM film.

For reliable measurements, the integrity of the CH_3-modification of the probe tip is critical. A damaged or defective tip modification would lead to a comparatively low adhesion force, even at high hydrophobic areas. For this reason, I frequently reviewed the integrity of the CH_3 probe tip modification between measurements using new and highly hydrophobic SAM films as reference.

6.2 Characterization of virgin SAM film on Cu

First, I investigated a new and unstressed SAM film. Fig. 6.3 presents the respective ATR-FTIR spectrum. In the wave number range of 3100-2700 cm^{-1} four sharp and intense bands are visible that represent the asymmetric and symmetric CH_3 (CH_{3asym} at 2955 cm^{-1}, CH_{3sym} at 2872 cm^{-1}) and CH_2 stretching vibration bands (CH_{2asym} at 2918 cm^{-1}, CH_{2sym} at 2850 cm^{-1}), respectively [153,154]. The

vibration band at 718 cm^{-1} corresponds to the CH_2 rocking absorption and indicates that the SAM film has a chain length from at least 4 up to about 10 CH_2 molecules in a row. For longer chains this absorption splits into two bands. The ATR-FTIR results prove the formation of a SAM film with CH_3 molecules as end-groups and a chain length of at least 4 molecules on the Cu surface.

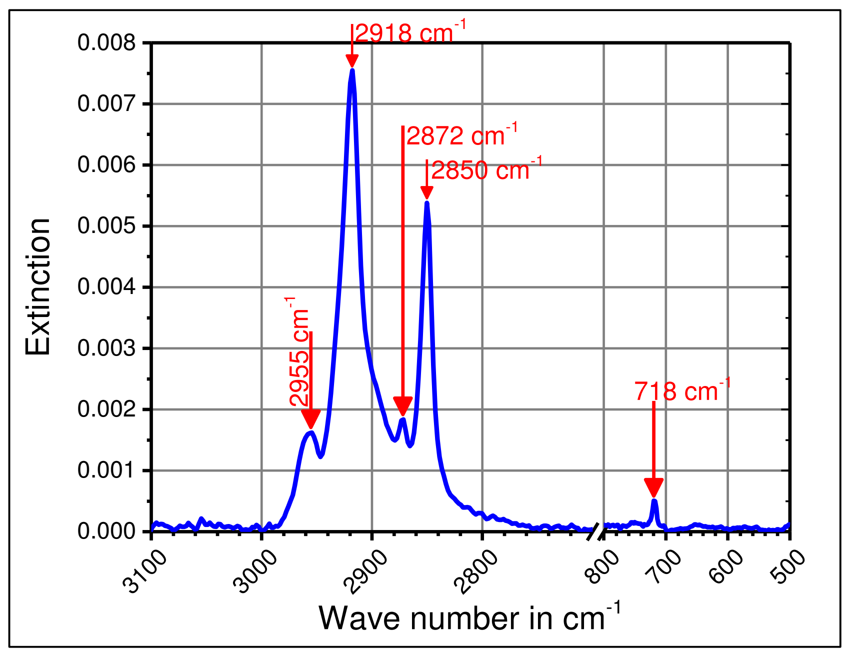

Figure 6.3. ATR-FTIR result of a new and unstressed SAM film with asymmetric and symmetric CH_3 (CH_{3asym} at 2955 cm^{-1}, CH_{3sym} at 2872 cm^{-1}) and CH_2 (CH_{2asym} at 2918 cm^{-1}, CH_{2sym} at 2850 cm^{-1}) stretching vibration bands. CH_2 rocking absorption (CH_{2rock} at 718 cm^{-1}) indicates a chain length from at least 4 up to about 10 CH_2 molecules in a row.

Fig. 6.4a1 depicts the topography of the unstressed SAM film. The loops illustrate parasitic particles on top of the surface (dotted) and a small pit (solid). The topography image itself is not able to indicate the quality of the SAM film. Fig. 6.4a2 shows the corresponding dCFM result. The overall mean value of the adhesion forces measured was 8.76 nN with peak values of 13 nN. These comparatively high values illustrate the hydrophobic character of the virgin SAM film. The peak values observed are congruent with adhesion forces between a CH_3-terminated probe tip and a CH_3-terminated sample presented in literature [113]. The protrusions highlighted in Fig. 6.4a1 (dotted circles) exhibit lower adhesion force values (Fig. 6.4a2) and represent particles on top of the SAM film and not film inherent defects. In contrast, the pit in Fig. 6.4a1 (solid circle) with an adhesion force of only 2 nN (Fig. 6.4a2) indicates a defect of about 50 nm diameter in the SAM film.

Fig. 6.4b1 and b2 displays the topography and the corresponding tunneling current map, respectively, of a fresh and unstressed SAM film. The data were recorded simultaneously by TR-TUNA. The current mapping (Fig. 6.4b2) appears quite homogenous all over the sample. However, the current values showed that no significant tunneling current through the SAM film could be detected (noise level

of ± 0.25 pA) which indicates that the surface is completely covered by the isolating virgin SAM film. These observations agreed with C-AFM studies of Chintala et al. [92].

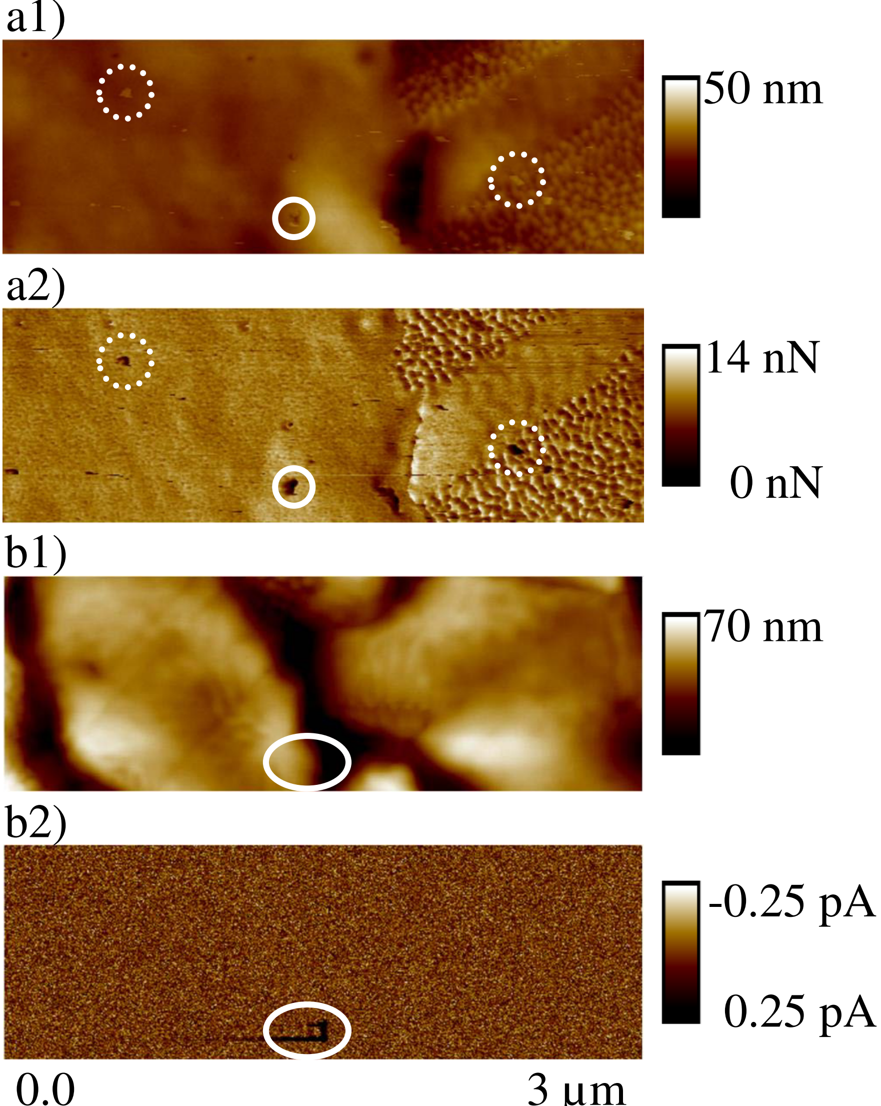

Figure 6.4. Topography (a1) and corresponding dCFM image (a2) of the unstressed SAM film and, at different scan position, topography (b1) and corresponding TR-TUNA image (b2). The dotted circles in (a1) and (a2) highlight some parasitic particles on top of the surface. A defect hole in the SAM film is marked by the solid circle in (a1) and (a2). The current spot in (b2) caused by the topography in (b1) is highlighted by the solid circle.

The high current spot (Fig. 6.4b2, solid circle) was discarded because it may be attributed to a disturbance of the measurement and not to SAM film properties. The probe tip was not able to follow the topography edge (Fig. 6.4b1, solid circle) immediately and penetrated the SAM film causing a current peak value of 12 pA. It needs to be noted that the measurement locations of Fig. 6.4a1, a2 and b1, b2, respectively, are different. TR-TUNA and dCFM require completely different measurement setups and, therefore, it was

not possible to measure with both methods at a single site. Nonetheless, as the results observed for different sites and different samples were consistent all over my research, the fundamental conclusions drawn are sound.

Overall, the results confirm that virgin SAM films cover the Cu surface homogeneously. The films exhibit comparatively high hydrophobicity indicated by a high adhesion force (Fig. 6.4a2) and a comparative isolating character indicated by a non-detectable tunneling current through the SAM film (Fig. 6.4b2).

6.3 Advanced investigation of the SAM film degradation

In a next step, I studied degradation and temperature stability of the SAM films. The ATR-FTIR spectra in Fig. 6.5 provide a macroscopic overview of the surface chemistry after temperature stress. Compared to the spectrum of the virgin film (Fig. 6.3) the SAM film after 100 °C temperature stress (Fig. 6.5a) exhibits a reduced intensity of the CH_3 and the CH_2 vibration bands. In addition, a vibration band at 645 cm^{-1} occurred, which can be assigned to cuprous oxide (Cu_2O) [130]. The reduced excitation of the CH_3 and the CH_2 bands as well as the appearance of Cu_2O suggests a degradation of the SAM film and a loss of film integrity. In the ATR-FTIR result for the SAM film exposed to 150 °C temperature stress (Fig. 6.5b) the typical vibration bands vanished completely and the intensity of the Cu_2O vibration band increased. These observations indicate a decomposition of the SAM film and a propagation of surface oxidation. The correlation of decomposition state and temperature stress is in good agreement with former observations of other types of SAM on Cu [33].

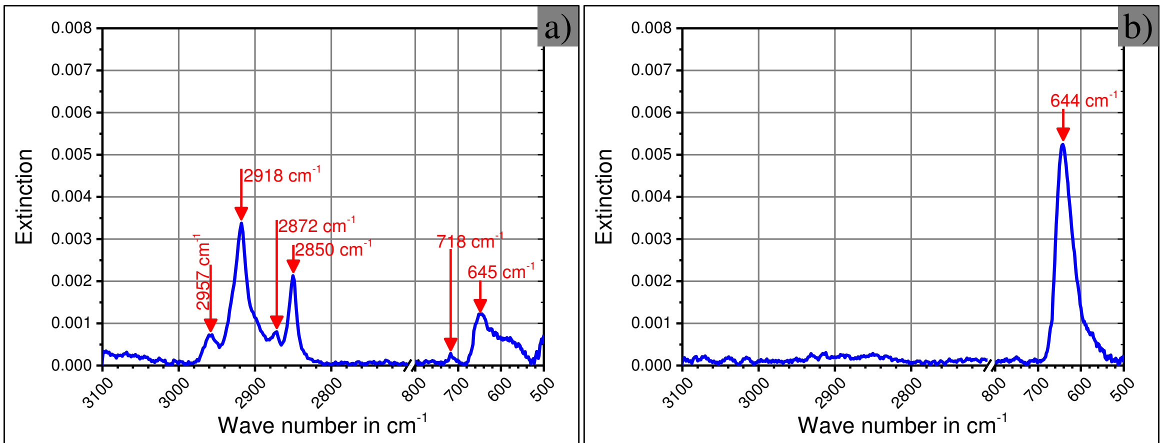

Figure 6.5. ATR-FTIR result for SAM films stressed at (a) 100 °C and (b) 150 °C, respectively. The asymmetric and symmetric CH_3 (CH_{3asym} at 2955 cm^{-1}, CH_{3sym} at 2872 cm^{-1}) and CH_2 (CH_{2asym} at 2918 cm^{-1}, CH_{2sym} at 2850 cm^{-1}) stretching vibration bands and the CH_2 rocking absorption (CH_{2rock} at 718 cm^{-1}) indicate a still existing SAM film (a). The Cu_2O vibration band (Cu_2O at 645 cm^{-1}) in (a) indicates surface oxidation. In (b) the absence of the CH_3 and the CH_2 bands and the increased Cu_2O peak suggest a decomposition of the SAM film and further surface oxidation.

Fig. 6.6 displays topography and adhesion force achieved for SAM films stressed at 100 °C and 150 °C, respectively. The topography for 100 °C temperature stress (Fig. 6.6a1) displays many tiny particles with heights up to 5 nm, which are illustrated in more detail by the insert. Moreover, the white loops indicate that at some locations the particles are ordered in a line or arranged around particle free areas, while at other locations the particles are distributed randomly.

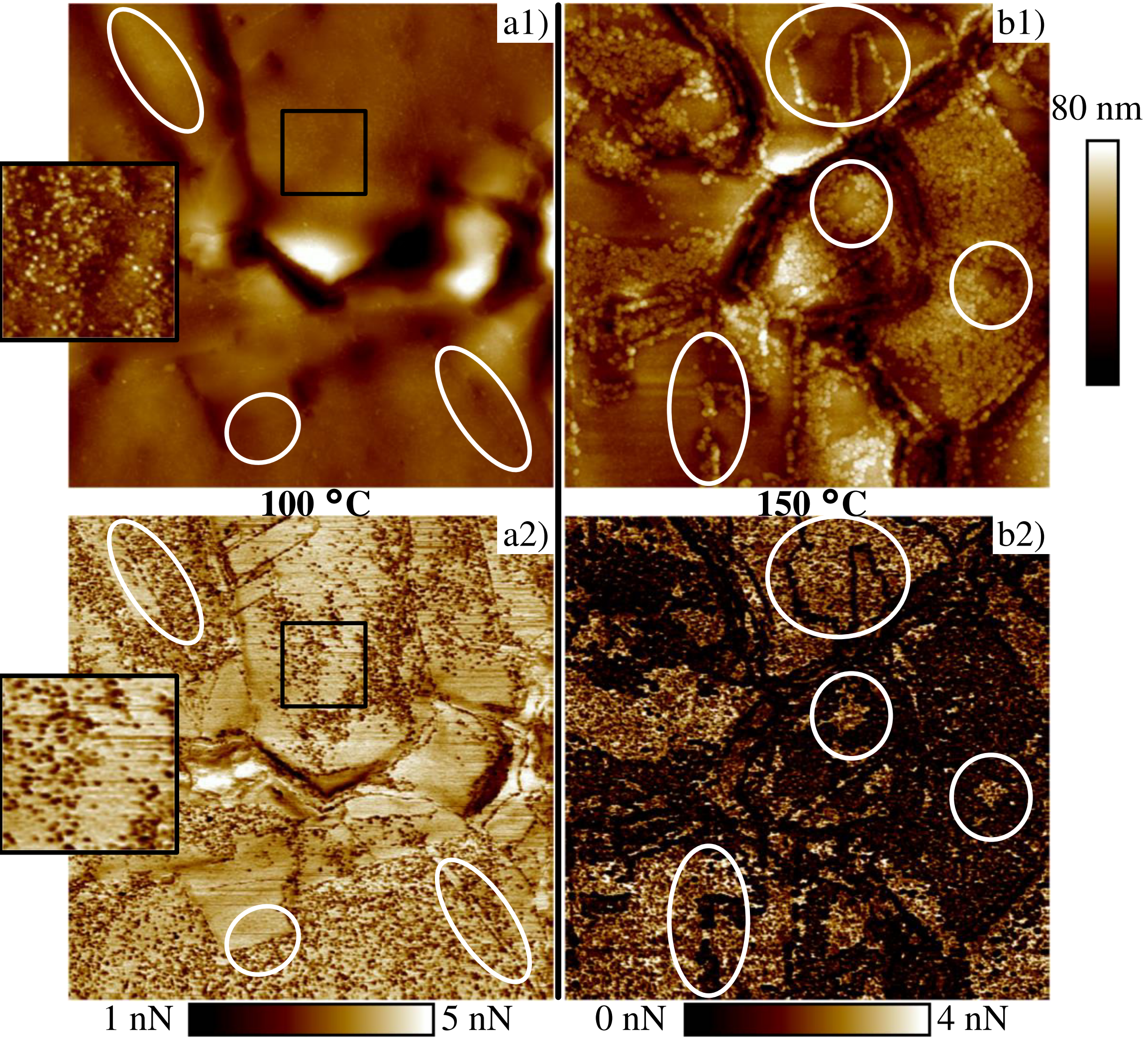

Figure 6.6. Topography (a1+b1) and dCFM result (a2+b2) for SAM films stressed at 100 °C (a1+a2) and 150 °C (b1+b2), respectively. The scan size was 3 × 3 µm². The white solid circles indicate characteristic surface features in (a1) and (b1) and correlation to hydrophobic minima in (a2) and (b2). The insets in (a1) and (a2) facilitate the correlation of surface particles and hydrophobic minima. They constitute magnified regions marked by the respective black box.

Fig. 6.6a2 shows the corresponding dCFM result. The overall mean value of the adhesion force was 3.7 nN with peak values of 5 nN. Overall mean value and peak values were well below the respective adhesion force values (mean 8.8 nN, peak 13 nN) of the unstressed film and already indicate degradation. The particles observed on the surface exhibit a hydrophobic contrast with comparatively low adhesion forces below 3.5 nN. Fig. 6.7a presents the current map of the sample stressed at 100 °C. It may

immediately be observed that the very homogenous character of the current map of the unstressed sample (Fig. 6.4b2) vanished. High current spots depicted as dark regions, up to 800 pA, are visible and the overall mean value rose to 150 pA. In addition, the high current spots form characteristic surface structures. Intermediate areas show a significant lower current flow of about 20 pA. When compared to the dCFM image the pattern of the high current spots and the pattern of the hydrophobicity contrast are similar, even though the measurement locations are not identical. The equivalent geometrical arrangement suggests that features with increased current flow (Fig. 6.7a) correlate to the particles (Fig. 6.6a1) and to the spots of low adhesion force (Fig. 6.6a2). It is worth noting that the consistent TR-TUNA and dCFM results confirm the ATR-FTIR result (Fig. 6.5a) and indicate a degradation of the SAM film. Moreover, the Cu_2O vibration band in the ATR-FTIR spectrum combined with the nanoscale characterization of the reduced hydrophobicity and increased current flow at particle sites suggest that the particles are Cu_2O grains.

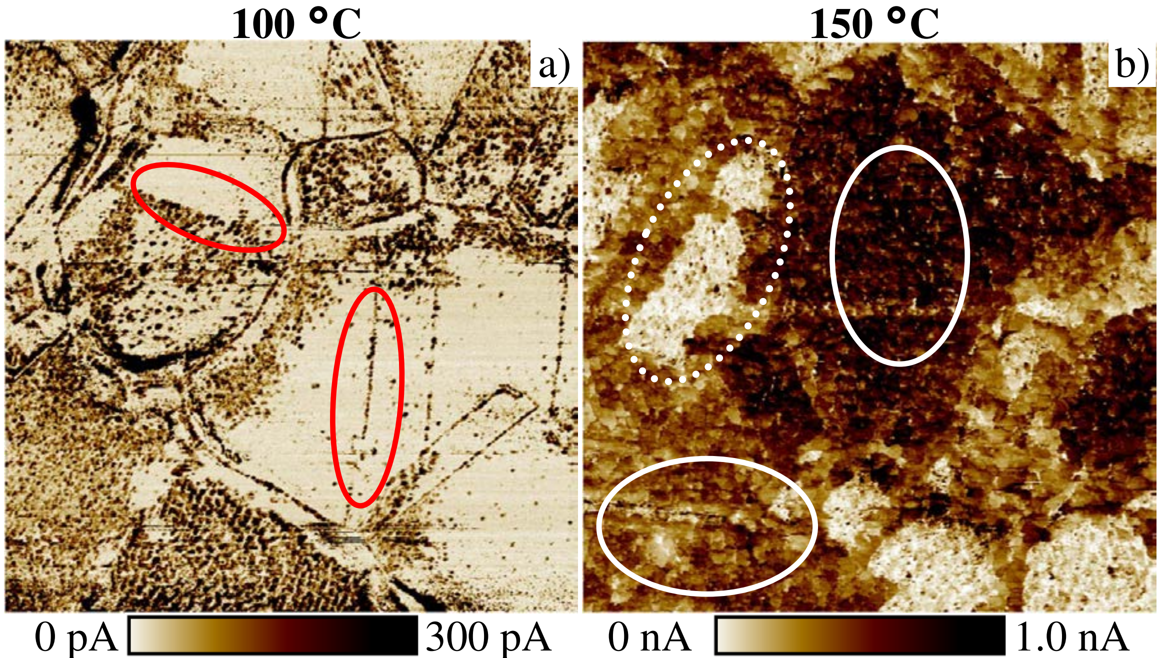

Figure 6.7. Typical TR-TUNA images of SAM films stressed at 100 °C (a) and 150 °C (b), respectively. The scan size was 3 × 3 μm². The red solid circles in (a) highlight characteristic arrangements of high current spots. The white solid circles and the white dotted circle in (b) discriminate characteristic areas with grain structures and significantly different tunneling current.

Fig. 6.6b1 shows the topography of the SAM film subject to 150 °C temperature stress. Compared to Fig. 6.6a1 and Fig. 6.4a1 the surface structure changed significantly and indicates an increased degradation. While after 100 °C temperature stress (Fig. 6.6a1+a2) only comparatively small particles were visible, after 150 °C temperature stress (Fig. 6.6b1) the grain size increased up to a height of 20 nm.

The distribution of the grains is similar for 100 °C (Fig. 6.6a1) and 150 °C (Fig. 6.6b1). Some grains are distributed randomly while others are arranged in lines or around islands.

The corresponding dCFM result (Fig. 6.6b2) reports that the grains have a comparatively low hydrophobicity because the adhesion forces did not exceed 1.5 nN. The regions without grains exhibit adhesion force values from 1.5 nN to 4 nN. The average adhesion force value for 150 °C temperature stress (Fig. 6.6b2) was 1.1 nN, which is significantly lower than the respective value of 3.7 nN for 100 °C. The significant change of the surface structure and the increased grains with reduced hydrophobicity correlate with the absence of the CH_3 and the CH_2 vibration bands (Fig. 6.5b) and suggest a decomposition of the SAM film. In addition, the strong Cu_2O vibration band in the ATR-FTIR result (Fig. 6.5b) indicates that the grains observed consist mainly of Cu_2O.

The disintegration of the SAM film subject to 150 °C temperature stress is confirmed by the tunneling current image (Fig. 6.7b). In general, the tunneling current increased dramatically. Peak values were in the order of 1.1 nA and the overall mean value was 500 pA. Furthermore, the tunneling current distribution over the surface changed when compared to Fig. 6.7a. It rather shows high current clusters than pronounced current spots. Intermediate areas show a significant lower current flow of 150 pA when compared to 470 pA and 800 pA, respectively, at areas with grain structure. The pattern of low and high current values correlate with the pattern of low and high adhesion force values (Fig 6.6b2) indicating high and low hydrophobicity, respectively.

The gain of the Cu_2O vibration band in the ATR-FTIR results of the temperature treated samples (Fig. 6.5) indicates a further oxidation of the surface. In general, the further oxidation of a Cu surface goes along with an increase in resistivity [155]. However, I observed a rise of the tunneling current as can be seen in Fig. 6.7. This disagreement can be explained by the further disintegration of the isolating SAM film which may have a stronger impact on the conductivity than the grown Cu_2O. Beside the impact of the SAM film, the Cu_2O itself could have a lower resistivity caused by an annealing effect of the temperature treatment. Musa et al. [50] observed that annealed Cu_2O layers produced by thermal oxidation possessed a decreased resistivity.

It should be noted that, in Fig. 6.7b the tunneling current observed varies for regions with grains from 470 pA to 800 pA (white solid circles). The reason for this observation is not clear yet and may be addressed in a separate study. Probably, it may be attributed to different states of oxidation, local variations caused by SAM residuals or to different annealing effects.

From the experimental point of view, it is important to note that, compared to the AFM based techniques the ATR-FTIR is a macroscopic measurement method with a very limited spatial resolution in the millimeter range. Even though it is possible to detect the CH_3- and the CH_2-groups of the SAM film and to identify Cu_2O at the sample surface after degradation, it is not possible to allocate the results to specific surface features. The combination with advanced AFM techniques offers additional

characterization options on the nanometer scale. TR-TUNA and dCFM are valuable tools to explore properties and degradation of SAM films by monitoring local tunneling current and adhesion force, respectively. In contrast to contact mode applications, wear marks or other surface damage were not observed.

6.4 Summary

I found that, CH_3-terminated SAM films are able to protect copper from oxidation. Subject to temperature stress the films degrade and gradually lose their integrity. Torsional Resonance Tunneling AFM and dynamic Chemical Force Microscopy are appropriate tools to monitor film integrity and degradation on nanometer scale without damaging the film. High hydrophobicity and low tunneling current, respectively, correlate with intact film integrity and vice versa. By comparing my microscopic results with the macroscopic chemical film composition achieved by ATR-FTIR, I conclude that after 100 °C stress regions with high tunneling current and low hydrophobicity correlate with local SAM film disintegration and local oxidation of the copper surface. With stress temperatures up to 150 °C the grade of disintegration and oxidation increases and may finally lead to a complete decomposition of the SAM film. The film degradation observed is critical for the application of SAM films in wire bonding processes. For semiconductor manufacturing, in general and copper wire bonding, in particular, TR-TUNA and dCFM are valuable tools for further research, predominately when sensitive surface layers are involved.

7. Protective nanometer films on copper

The oxidation protection of copper surfaces is an important and advantageous procedure for many different applications to achieve reliable and stable surface conditions for subsequent process steps. This study focuses mainly on applications in the field of interconnection techniques in general and thermosonic wire bonding in particular. Previous studies of other researchers investigated different coating layers with thicknesses in the micrometer range for the usage in interconnection methods [22,26,24,25]. However, as already shown in the introducing section, the growth of intermetallic phases limits the electrical performance of such connections [22]. Therefore, protective layers with a thickness of a few nanometers must be introduced to avoid the growth of any parasitic interfaces with an increased transition resistance. Aoh et al. [30] reported that such thin passivation layers could provide excellent bondability because they can be removed using ultrasonic power during the thermosonic bonding process.

Graphene coatings provided promising results as very thin protective layer on copper surfaces [60–63]. Kirkland et al. [60] as well as Prasai et al. [63] introduced in their research that single layer graphene as well as multi-layer graphene e.g. graphite can serve as effective barriers to electrochemical corrosion. Additionally, the protective effect caused by the atomic graphene layer goes along with an improved mechanical stability of the protected surface. Various researchers published in their studies that a graphene layer effects an improved wear resistance of the coated surface [64,65]. Especially for further applications of any interconnection methods, the modified mechanical stability of the surface may limit significantly the ability for applying processes such as the thermosonic wire bonding.

Consequently, alternative coating materials or processes must be validated to deposit a thin protective layer on the Cu surface. In SEM experiments sputter coatings are well known to achieve very thin conductive layers and can be an interesting approach to address the needs of the protective layer. Former studies by Stokroos et al. [66] showed that structural details such as density and particle size are closely linked to the material and can influence a possible protective effect. Chromium (Cr) provides a very smooth coating film, but it is known that the Cr layer degrades in ambient environment and can oxidize rapidly. Noble metals such as gold (Au) or platinum (Pt) could yield a surface coating inert with the ambient environment. In detail, the Pt coatings tend to offer a much smaller grain size compared to an Au coating layer and in the initial stage the Au grows rather in clusters than in an uniform layer [156]. Beside protective metal films, carbon (C) coating layer can be an interesting alternative to achieve very thin and stable protection layers. Especially for depositing thin carbon layers Ion-beam sputtering deposition (IBSD [157]) techniques must be used because DC magnetron coaters tend to build up non-conductive diamond-like carbon (DLC) layers with improved mechanical stability [67].

In this study, I investigated the applicability of a few nanometers thick IBSD Pt or C coating layers to achieve reliable surface conditions. The degradation and temperature stability of the protective layer were investigated by combining non-destructive Scanning Electron Microscopy (SEM) and Atomic Force Microscopy (AFM) characterization techniques.

7.1 Experimental

The schematic cross-section of the Cu samples used in this study is shown in Fig. 7.1. The 5 μm Cu was deposited by an electroplating process which defines a surface structure as shown in Fig. 7.2. Prior to the deposition process of the protection layer, the Cu surfaces were cleaned by a chemical treatment with an aqueous solution of 10% sulfuric acid to remove the native oxide and any contaminations and

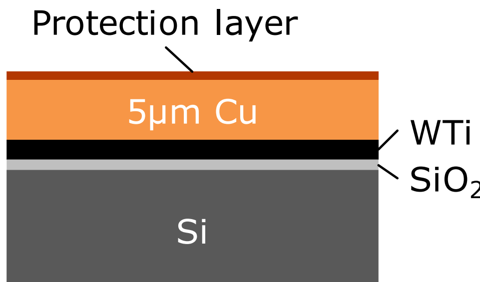

Figure 7.1. Schematic cross-section of the test samples consisting of a 5 μm copper layer on top of a Si base separated by a thin SiO_2 film and a WTi liner.

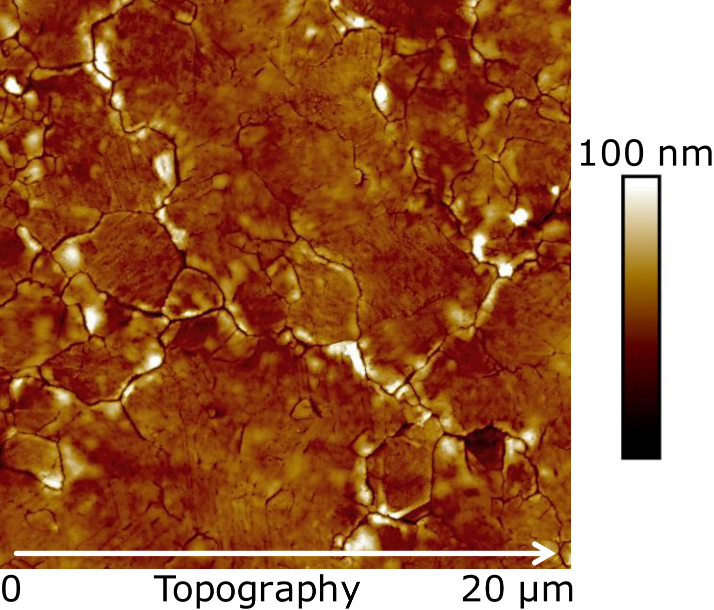

Figure 7.2. AFM topography image of the Cu surface deposited by an electroplating process

subsequently rinsed with a 1:1 solution of ultrapure water and isopropanol. After that cleaning process, the sample was stored in a vacuum chamber. The deposition process took place by using a Gatan 682 Precision Etching and Coating System (PECS). This system enables the sample cleaning by an argon ion (Ar^+) beam bombardment and the coating by Ion beam sputtering deposition [157] without the need of a sample transfer. Consequently, before the coating, the argon ion beam treatment with an acceleration voltage of 1.5 kV was performed for approximately one minute to remove any possible organic contaminations remained on the surface.

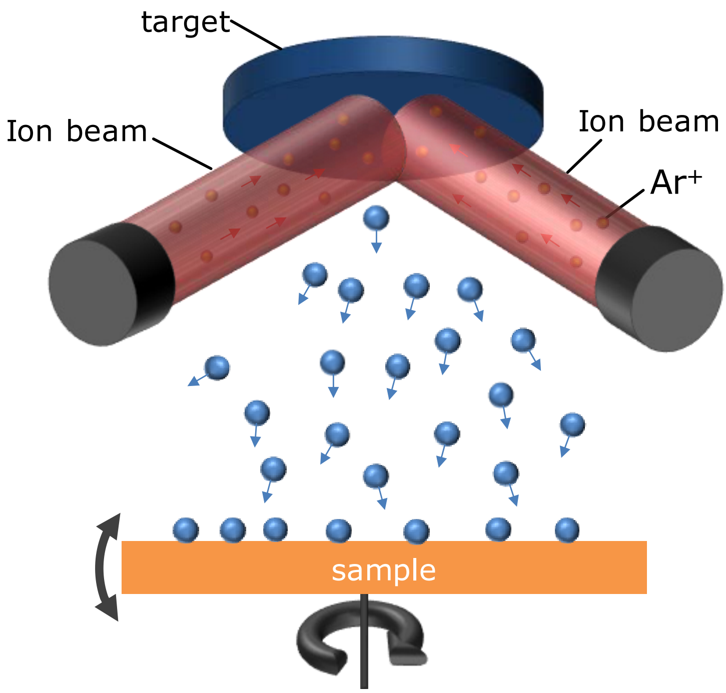

Figure 7.3. Basic principle of the surface modification based on Ion beam sputtering deposition [157]. The sample can be rotated and tilted.

The basic principle of the deposition process is imaged in Fig. 7.3. Two Penning Ion guns are used to accelerate the argon ions to the target material. The ions eject particles in the atomic scale from the target to form a thin film on the nearby sample surface [157]. As detailed in Fig. 7.3, the sample can be tilted and rotated during the deposition process which is important to avoid any edge effects based on topographic features and to achieve a constant layer thickness over the entire sample surface. The coating conditions were kept constant for all experiments and are summarized in Table 7.1.

Table 7.1. Coating conditions for the deposition process

Acceleration voltage	9 kV
Maximum tilt angle	15°
Rotation velocity	20 rpm
Rocking velocity	8°/sec

The thickness of the coating layer was validated in-situ during the coating process by using a quartz crystal oscillator. For the investigation of the temperature stability, the protective coatings were stressed on a heater in ambient air up to a temperature of 200 °C for 15 min related to real bonding conditions [19]. For the lower temperatures, 150 °C and 100 °C, the stress time was increased to 30 min.

In this experiment, a Zeiss Ultra 55 scanning electron microscope equipped with the EDAX Trident system and an Angular Selective Backscatter Detector (ASB) was used to perform topography and BSE imaging as well as an EDX analysis. The basic principles of these characterization techniques were introduced in the section 3.2. These SEM based methods enables the investigation of the surface topography, the material contrast imaging and the quantitative determination of the element distribution. The AFM measurements were performed with a Bruker Dimension Icon AFM. Beside various standard operation modes, the AFM employed offers the PeakForce Kelvin Probe Force Microscopy (PF-KPFM) [106] operation mode, which is able to measure the Contact Potential Difference (CPD) at the nanoscale. The AFM operation modes as well as the PF-KPFM method were described in detail in the experimental part in the sections 3.1.1 and 3.1.2, respectively.

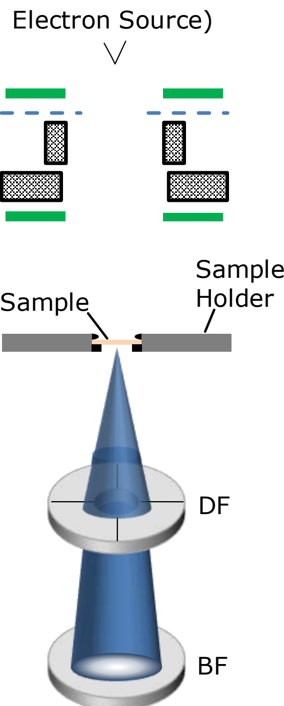

Figure 7.4. Basic principle of the Scanning Transmission Electron Microscopy (STEM) with the arrangement of the Dark-Field (DF) and the Bright-Field (BF) detector.

In addition, Scanning Transmission Electron Microscopy (STEM) was used to investigate the structural properties of the coating layer which are closely linked to the material [66]. A schematic of the measurement principle is displayed in Fig. 7.4. For the STEM analysis, the coating layer was deposited on a special grid. As detailed in Fig. 7.4, there are two detectors to collect the electrons interacted with

the sample layer. For the image generation, both, the scattered electrons (Dark Field) and the unscattered electrons (Bright Field) can be collected. For the analysis of the coating layer especially the bright field imaging was used to detect the interaction of the direct electron beam with the sample layer.

7.2 Structural and elemental analysis

First, I investigated the topography of the initial pure and of the coated Cu surface by performing SEM imaging. The resulted images can be seen in Fig. 7.5. It is obvious that the uncoated and coated Cu surfaces look very similar. A change caused by the protective film cannot be observed because the thickness of the coating layer is very thin and the particle size is obviously too small to be resolved by the electron beam in standard SEM operation. Consequently, STEM Bright Field imaging was used to represent the structural properties of the different protective coatings. The high-resolution images of the platinum and the carbon coating can be seen in Fig. 7.6. The fine structure of the coatings is very

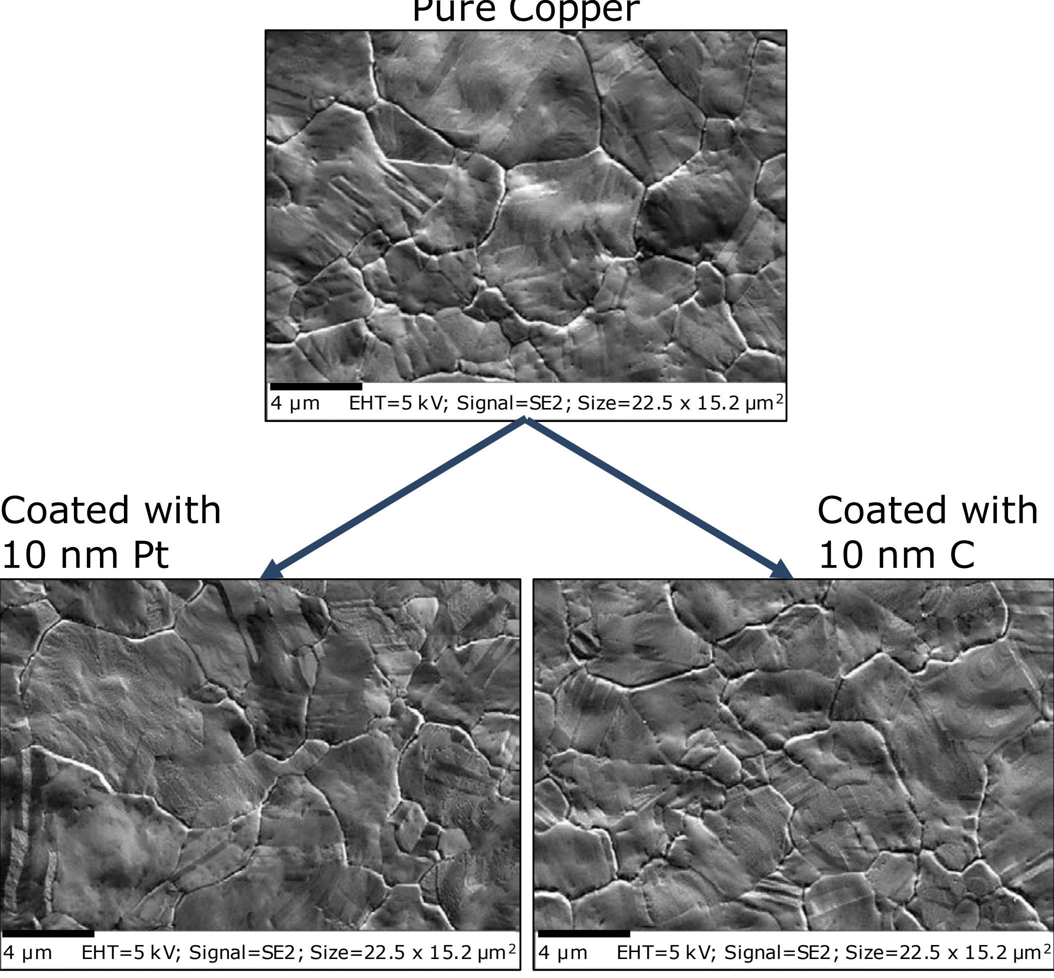

Figure 7.5. SEM images of the topography of an uncoated pure copper surface and of Cu surfaces coated by (left) a 10 nm thick Pt layer and (right) a 10 nm thick C layer.

different. The topology of the Pt coating suggests that the Pt grains arranged on the subjacent surface feature a closed layer. The fine structure of the C coating provides a much smoother surface. Related to the particle size of the Pt and C coating, the presented subsections in Fig. 7.6 indicate much different structures. Whereas the grains of the Pt layer can be expected by observing the subsections, the particle size of the carbon coating seems to be much smaller and cannot be identified in the STEM images. However, beside the different layer structures, both, the Pt as well as the C coating, feature a closed layer which should be suitable to protect any subjacent structure, at least for a specific time range and temperature.

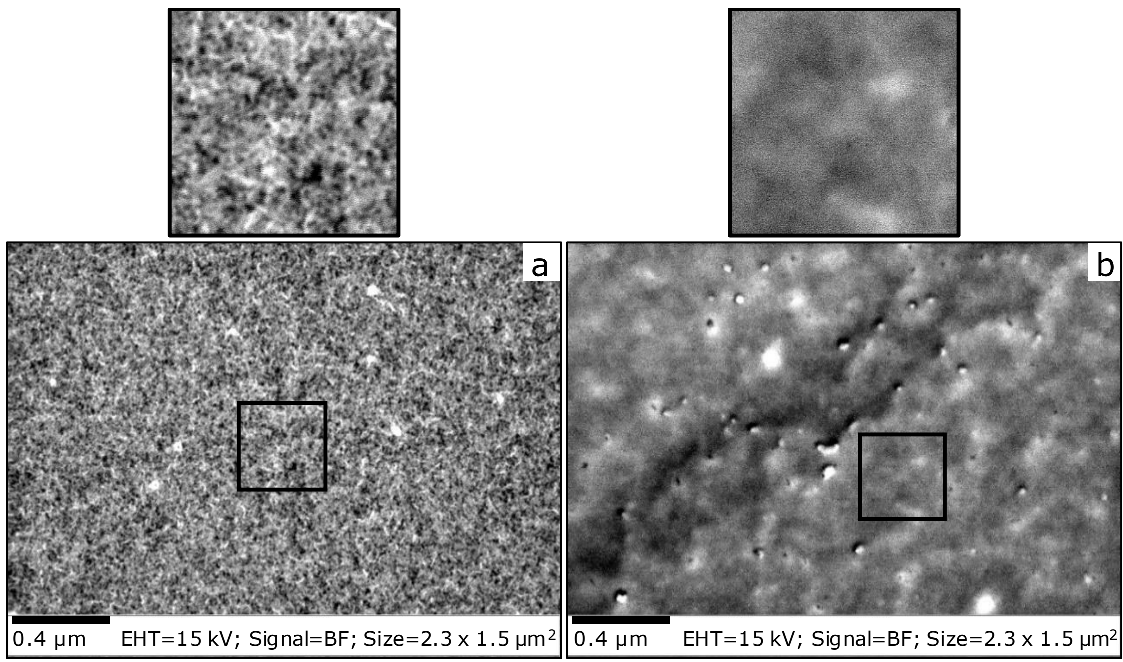

Figure 7.6. STEM Bright Field images at different magnifications of the Pt coating (a) and the C coating (b). The black squares (size = 357 nm) highlight magnified areas of the shown subsections.

Since the bonding process needs elevated temperatures up to 200 °C [19], the temperature stability of the protective coating is an important factor As an indicator for a possible degradation of the protective layer, the oxidation of the Cu surface was used. Therefore, the oxygen fraction indicating an oxidation was determined by performing an EDX analysis at five different surface regions before and after temperatures stress. The mean value and the corresponding standard deviations of the atomic weight of oxygen and of the remaining individual elements achieved by the measurements at the different positions are summarized in Fig. 7.7. It is obvious that the 10 nm Pt coating provides an increased oxygen content for elevated temperatures. As detailed in the inset, the oxygen values after the 150 °C stress vary a lot. This finding suggests that the oxidation differs at the various measurement regions. At 200 °C the mean value of oxygen is raised and the deviation is significant lower. This is evidence for a further oxidation and thus, for a further degradation of the surface. Additionally, the degradation influences the carbon

values which are slightly increased for 150 °C and 200 °C. Due to these observations, the conclusion can be drawn, that the Pt layer degrades significantly at these temperatures and does not protect the Cu surface anymore.

In contrast to this, the atomic weight of the elements in Fig. 7.7 identified for the carbon coating on the Cu surface exhibits only slightly variations of the oxygen weight or of the other elements for the temperature range up to 200 °C. Interestingly, the oxygen values deviate more for the untreated sample surface und seem to be more stable after the temperature treatment. These variations are in the range of 0.3% for the untreated sample and approximately 0.2% for the stressed samples. Since the variations are so low, they are assigned to the measurement accuracy. Consequently, it is worth noting that the carbon coating enables an effective protection of the subjacent structure even for elevated temperatures.

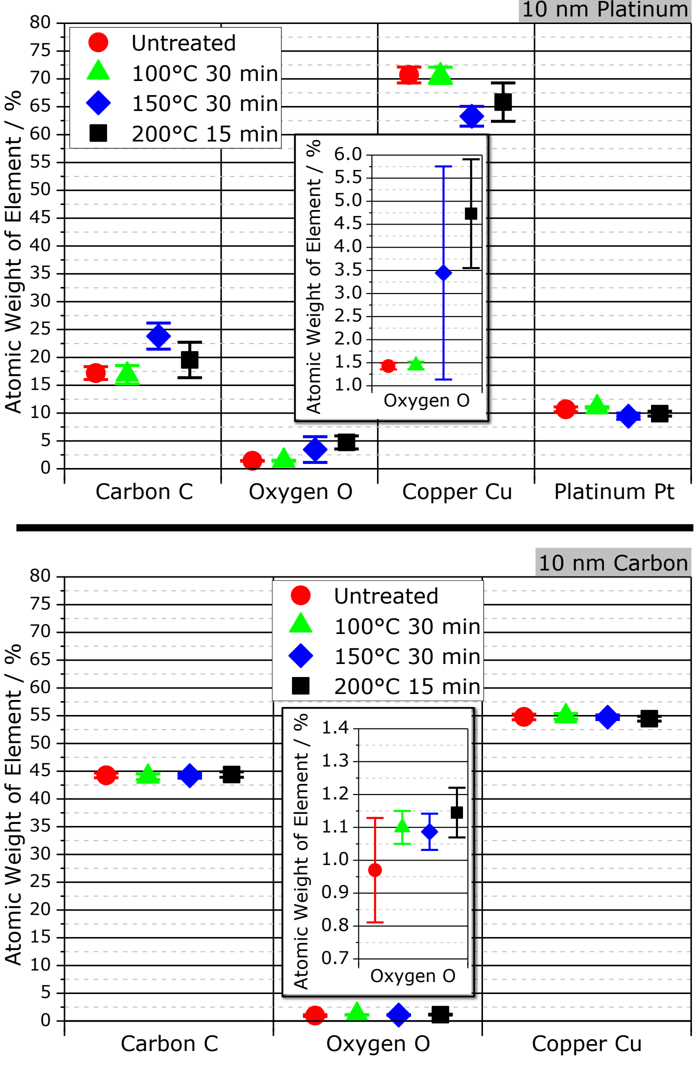

Figure 7.7. Atomic Weight of the individual elements of a Pt and a C coating treated by different temperatures derived by a quantitative EDX characterization at different surface areas. The distribution of the low oxygen weights is shown in detail in the respective inset.

However, especially the large variations of the Pt coating results show that for determining the exact weakness of the coating material a more detailed analysis must be performed because the covering of the coating material related to the topography must be considered.

7.3 Analysis at the nanoscale of the protective Pt layer

Consequently, in addition to SEM imaging of the topography, the material contrast derived by backscatter imaging was used to investigate the coated surfaces treated by the elevated temperatures. The resulting images of the Pt coating are depicted in Fig. 7.8. The topography exhibits already small particles grown on the surface after a stress of 150 °C. A further increase of the temperature leads to a much stronger change of the surface, although the stress time has already been reduced. The corresponding backscatter images show a significant difference between the surface and the particles. Moreover, beside the grown particles, the backscatter images show slight differences caused by the varying crystal orientations of the Cu surface.

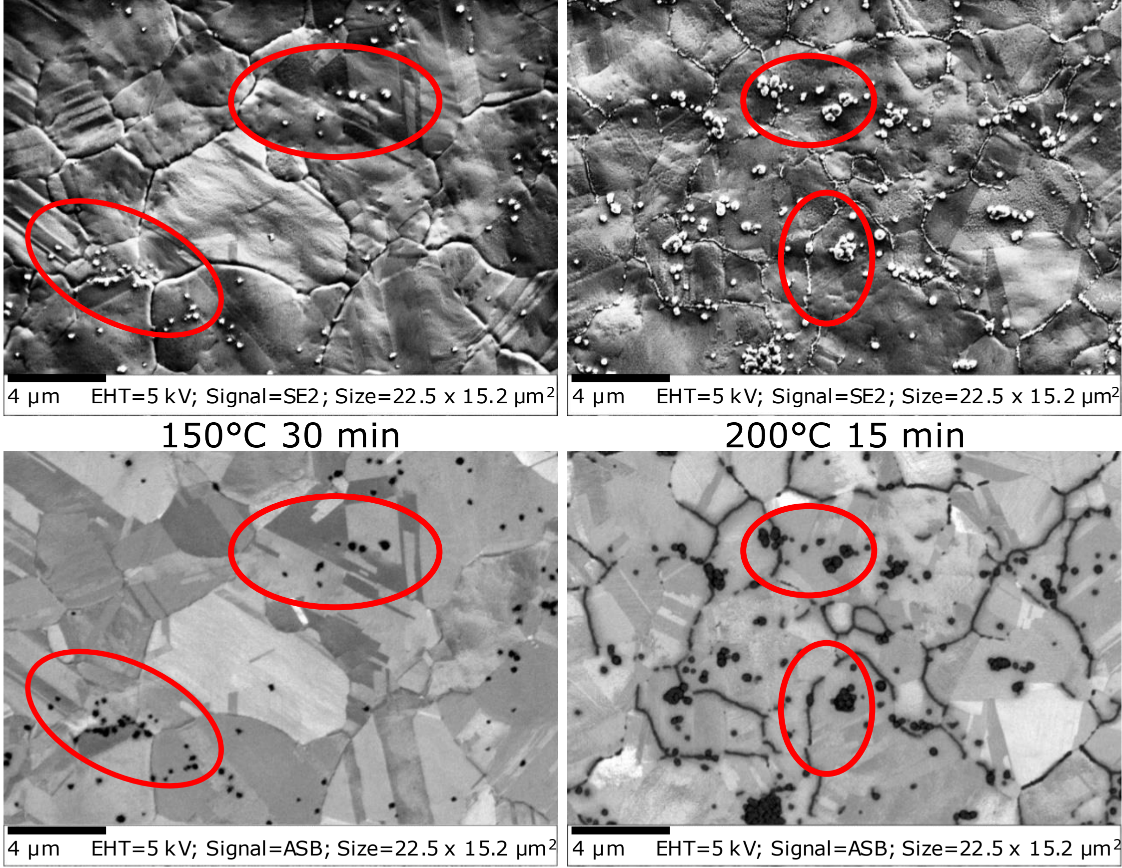

Figure 7.8. SEM topography image and material contrast achieved by backscatter imaging of a Cu surface protected by a 10 nm thick Pt coating after a temperature treatment of 150 °C and 200 °C. The red circles indicate some topography features and their correlation to the material contrast.

In detail, the results indicate that the particle growing is not supported by any topographic feature. It can be observed that the particles are grown in the very near of grain boundaries as well as inside a grain without any specific topographic change. However, the backscatter imaging or material contrast imaging in Fig 7.8 only specifies that the grown particles on the surface can be allocated to a different material. For a direct allocation of the grown topographic features to a possible oxidation an element mapping was performed.

In Fig 7.9, the result of this EDX element mapping for the Pt coating stressed at a temperature of 200 °C is displayed. For comparison, the corresponding topography can be seen in Fig. 7.8. The different mappings are allocated to the identified elements carbon C, copper Cu, oxygen O and the coating material platinum Pt. The oxygen mapping clearly indicates that the particles grown by the temperature stress resulted from oxidation because they consist mainly of oxygen. Furthermore, the Pt mapping shows that the Pt layer was decomposed at the regions of the oxide particles and was not able to protect the Cu surface effectively.

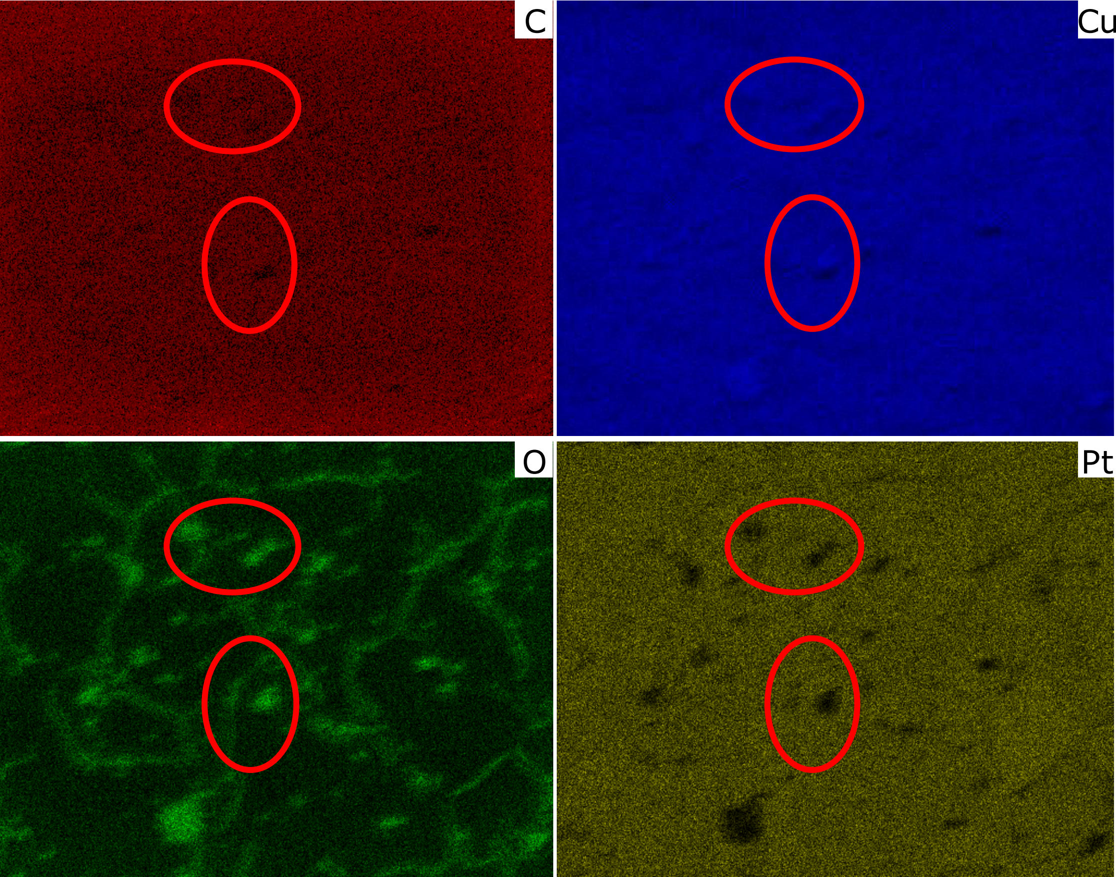

Figure 7.9. EDX element mapping of a Cu surface protected by the 10 nm thick Pt coating after a temperature treatment of 200 °C. Corresponding to the topographic image in Fig. 7.8 the red circles highlight areas of some topography features.

By comparing the images allocated to a stress temperature of 150 °C and 200 °C in Fig. 7.8, the kinetics of the oxide grain growth can be investigated. The 150 °C surface has only a few individual grown grains nonuniformly distributed. A further increase of the temperature results in an advanced oxidation of the surface. As introduced by the images in Fig. 7.8, the grains detected on the 200 °C surface form rather clusters than individual grains grow and cover the entire surface.

Summarized, it is important to note that the detected oxidation occurring despite the protective Pt coating demonstrates that the degradation caused by the temperature treatment is very different locally. However, the distribution of the oxide grains verifies that the coating does not fall off in quality at topographic features such as grain boundaries. Thus, the resulted degradation is characteristic for the Pt coating material.

The investigations so far provide important outcomes regarding the protective effect of the Pt coating. The SEM results (Fig. 7.8) and the element mappings achieved by EDX measurements (Fig. 7.9) clarify that the degradation of the Pt layer leads to the growth of oxide grains. However, because of the principle of these techniques, the detection of nanometer scale particles on the surface is limited and any degradation effects beside the detected oxide grains could not be realized. For this reason, an additional nanoscale characterization by PF-KPFM was performed.

The results in Fig. 7.10 show an AFM high-resolution topography image and the corresponding contact potential difference of the Pt coated Cu surface after a temperature treatment of 200 °C. The topography image clearly indicates an additional grain structure with different sized grains grown on top of the surface.

The grains are not oriented at the boundaries of the original Cu structure. This outcome agrees with the observations of the SEM and EDX characterizations. The contact potential difference (CPD) in Fig. 7.10 provides a significant contrast between the grains and the grain-free regions. The larger grain structure achieved by the SEM and EDX characterization could be assigned to oxidation. Consequently, because of the detected CPD contrast in Fig. 7.10, it can be concluded that the nanoscale particles are oxide grains. Additionally, the magnified area can emphasize that the larger grains at the borders and the smaller grains can be assigned to the same oxide because they have similar CPD values. These results complete the SEM and EDX characterization and show the degradation of the Pt coating provoking very different oxide grains grown on the surface. It is important to note that the introduced results are closely linked to the deposition process. It is known from the literature that Ion beam-assisted deposition (IBAD) could be able to create a gradual transition layer mixed with substrate material and depositing material between the substrate and the deposited film, thereby the coating adheres strongly to the substrate [157].

This increased adhesion strength could probably improve the protective effect, but simultaneously such a very strong adhesive layer could limit the applications of subsequent interconnection processes.

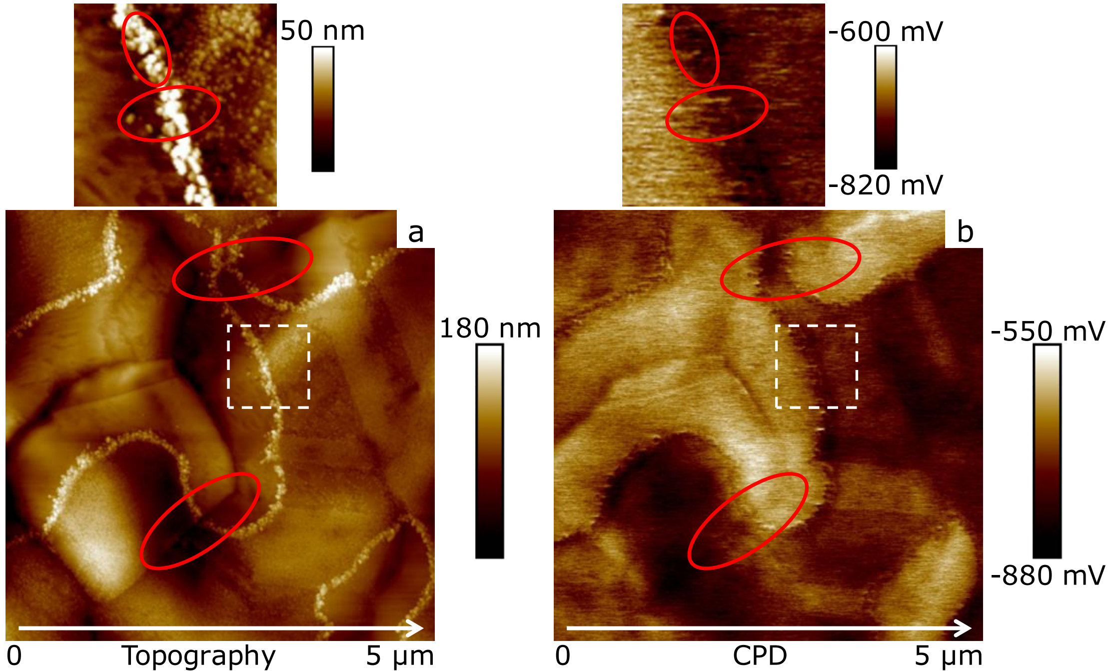

Figure 7.10. AFM topography (a) and corresponding PF-KPFM result (b) of a Cu surface protected by the 10 nm thick Pt coating after a temperature treatment of 200 °C. The red circles highlight the correlation of some topographic features (a) and the PF-KPFM results (b). The white dashed squares mark magnified areas presented in the above subsections.

7.4 Nanoscale characterization of the protective C layer

Beside platinum, carbon was introduced as coating material for very thin protection layers in the nanometer range. The EDX analysis in Fig. 7.7 already showed that the carbon coating does not yield any variation in the element contents caused by a probable degradation of the coating or a resulting oxidation. To confirm this assumption, additional research must be carried out. Like the investigations of the Pt coating, the SEM topography imaging and the material contrast achieved by backscatter imaging are suitable methods. The results are presented in Fig. 7.11. The topography as well as the material contrast images clearly illustrate that no parasitic particles were grown during the temperature treatment, confirming the previous examinations of the EDX analysis in Fig. 7.7.

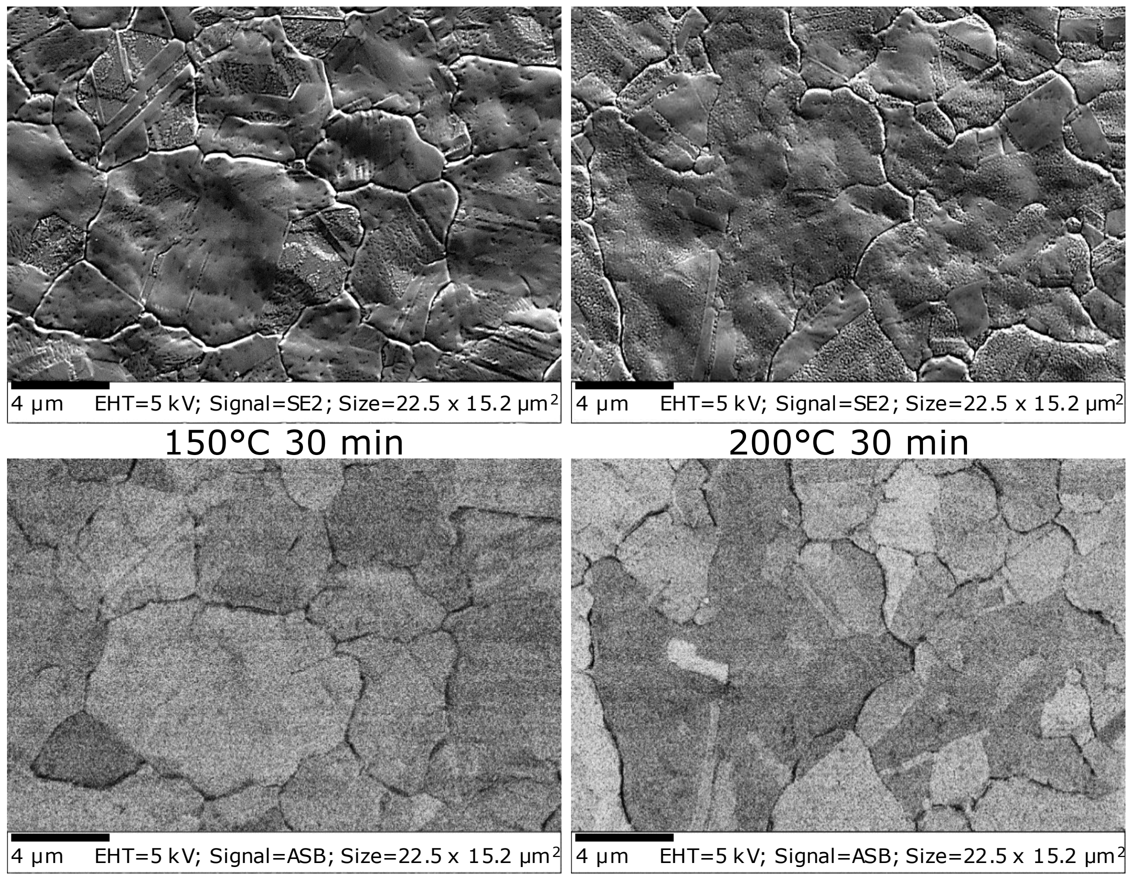

Figure 7.11. SEM topography image and material contrast achieved by backscatter imaging of a Cu surface protected by a 10 nm thick C coating after a temperature treatment of 150 °C and 200 °C.

Analogous to the investigations of the Pt coating, an EDX element mapping of the carbon coated surface stressed at 200 °C was performed and the results are imaged in Fig. 7.12. In agreement with the results of the EDX analysis (Fig. 7.7) and the investigation of the topography (Fig. 7.11), the EDX element mappings in Fig. 7.12 clearly present, that carbon C, oxygen O and copper Cu are uniformly distributed and that a local oxidation or degradation of the protective coating cannot be observed. Based on the results presented so far, the C coating is very promising. The investigations could not detect any degradation or oxidation of the Cu surface. For a confirmation of these outcomes, the advanced nanoscale characterization by PF-KPFM was performed.

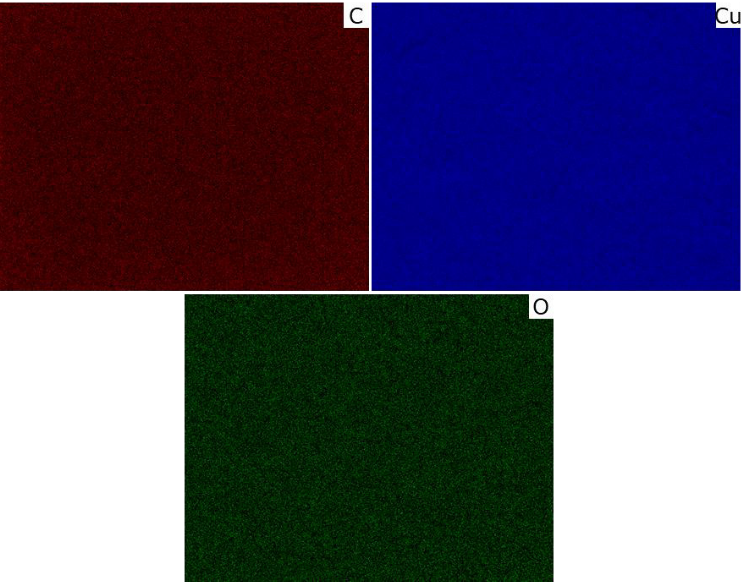

Figure 7.12. EDX element mapping of a Cu surface protected by the 10 nm C coating after a temperature treatment of 200 °C corresponding to the topographic image in Fig. 7.11.

The AFM topography and the corresponding PF-KPFM result of a 200 °C stressed Cu surface protected by the 10 nm thick C coating can be seen in the Fig. 7.13. In contrast to the Pt coating, the AFM topography image of the observed carbon layer does not yield any grown particles on top of the surface. The corresponding CPD image only shows slight variations at some topographic features such as grain boundaries. A more detailed insight can be gained by the enlarged subsections in Fig. 7.13. The subsection of the topography provides the improved display of the surface and enables the investigation of attributes near the grain boundary. The CPD result of the subsection only shows slight variations provoked by the grain boundary. The other topographic features did not provide a change of the CPD value. These important outcomes of the nanoscale investigation clearly demonstrate that the carbon layer did not degrade and that no oxidation of the protected Cu surface occurred. These conclusions agree with the SEM investigations of the topography and the corresponding EDX results. The findings clearly demonstrate the excellent performance of the 10 nm thick C coating regarding the protective effect even for elevated temperatures up to 200 °C. Based on these results the thickness of the protective layer can be further decreased. The 10 nm C coating did not show a detectable degradation and protected the Cu surface completely from oxidation.

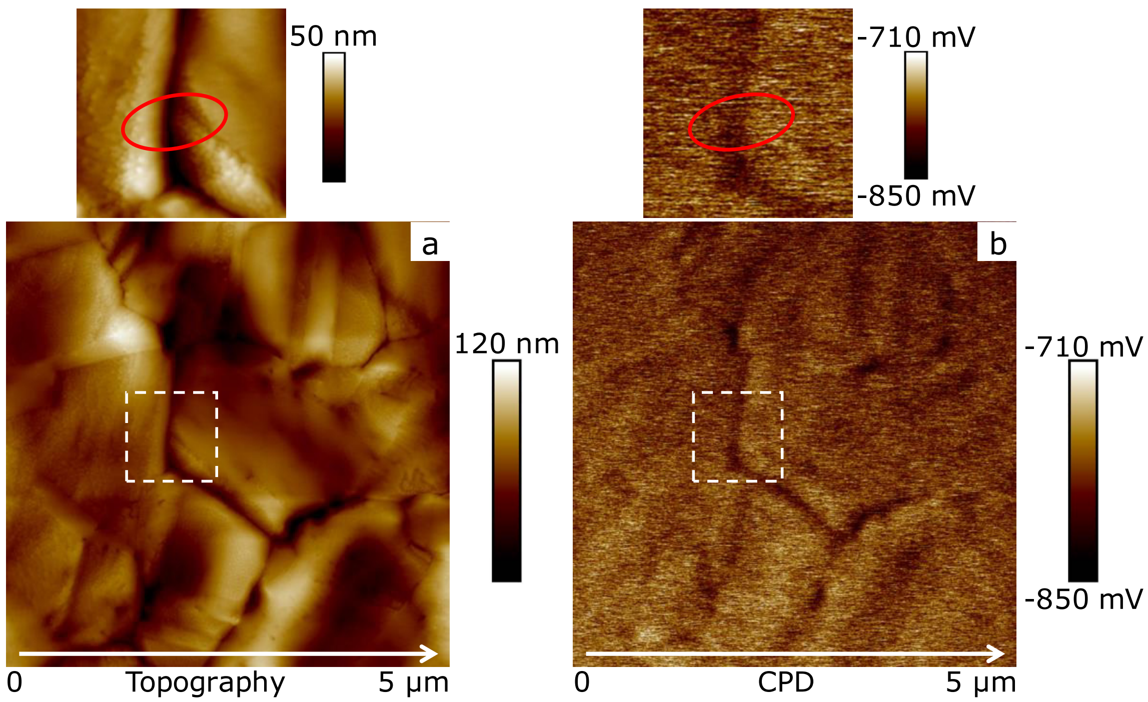

Figure 7.13. AFM topography (a) and corresponding PF-KPFM result (b) of a Cu surface protected by the 10 nm C coating after a temperature treatment of 200 °C. The white dashed squares mark magnified areas presented in the above subsections. The red circles in the subsections highlight the correlation of the grain boundary and the CPD change.

7.5 Decrease of the C layer thickness

The further decrease of the layer thickness ensures that further process steps such as interconnection techniques are not influenced by the additional layer. The results in Fig. 7.14 represent the SEM topography images as well as the BSE images of the different layer thicknesses. It is apparent that the additional coating layer does not influence the topography images. The deviations shown are due to the natural change in the surface structure. In contrast, the BSE images (Fig. 7.14a2, b2, c2) provide compelling evidence that the layer thickness is reduced.

The different grayscales in the BSE images indicate the variation of the crystal orientation of the individual Cu grains. It can be inferred therefore, that the contrast is damped by the C layer. The lower the thickness of the C layer the more detailed the Cu grain structure can be detected. But it can be concluded, that further investigations are necessary to rate the protective effect. Consequently, an EDX analysis of the coated surfaces was performed before and after a temperature treatment of 200 °C. The quantitative results of the element distribution are given in Fig. 7.15. The atomic weight of the fresh and untreated samples provides expected values. Due to the decreasing coating layer thickness, it is logical that the C value decreases and hence, as detailed in Fig. 7.15, the Cu value increases. The oxygen fractions indicating a possible oxidation of the fresh surface remain in the low range around 1% or even below

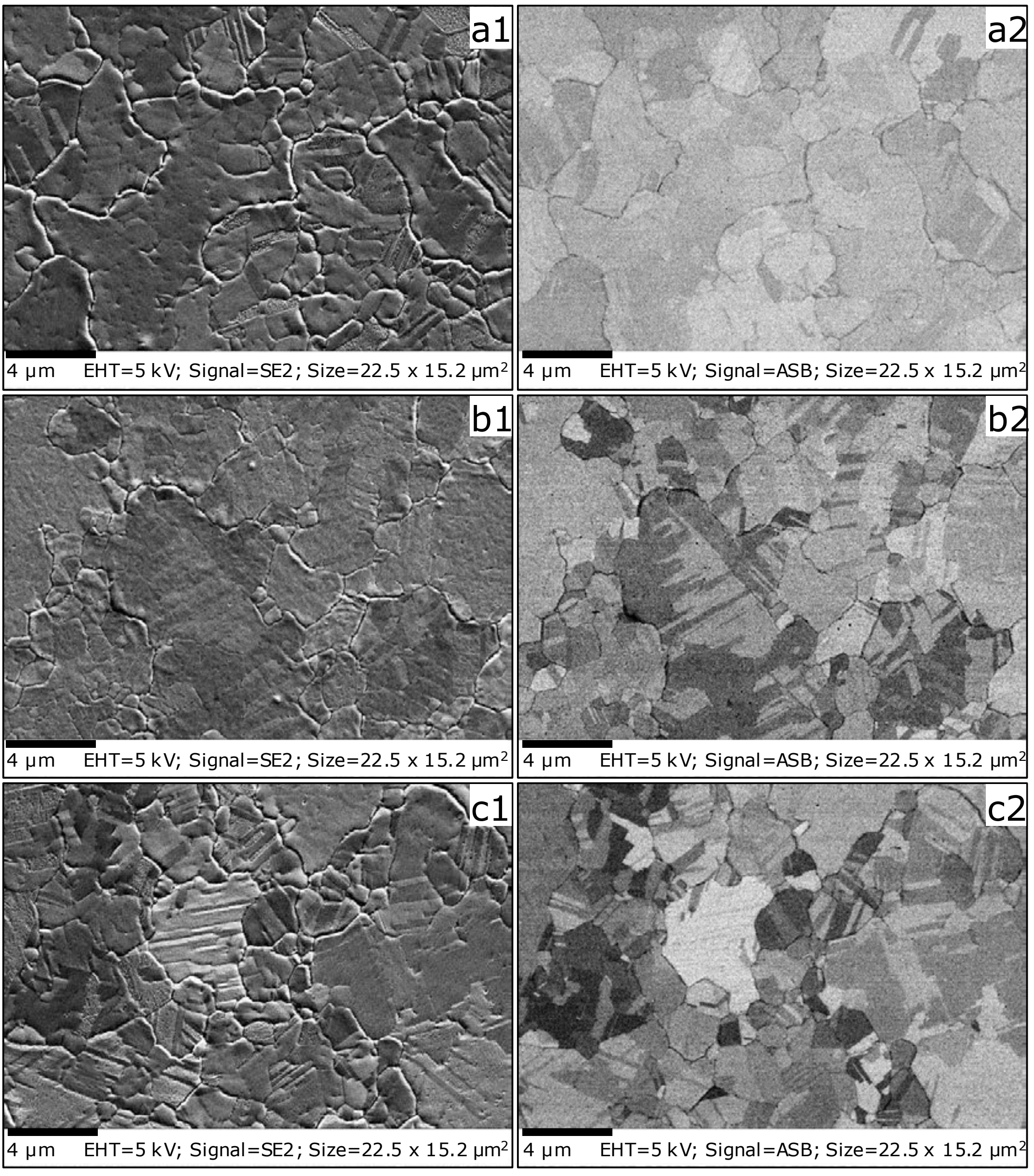

Figure 7.14. SEM topography image (a1, b1, c1) and material contrast images achieved by BSE imaging (a2, b2, c2) of a Cu surface protected by a C coating with a thickness of (a1, a2) 5 nm, (b1, b2) 3 nm and (c1, c2) 1 nm.

and a correlation with the coating layer thickness cannot be observed in the inset in Fig. 7.15. This expected behavior is in agreement with the topography and BSE results as inspected in Fig. 7.14. After stressing the protected surface with a temperature of 200 °C for 15 min, the atomic weight values of the elements evidence the protection of the Cu surface for layer thicknesses down to 3 nm.

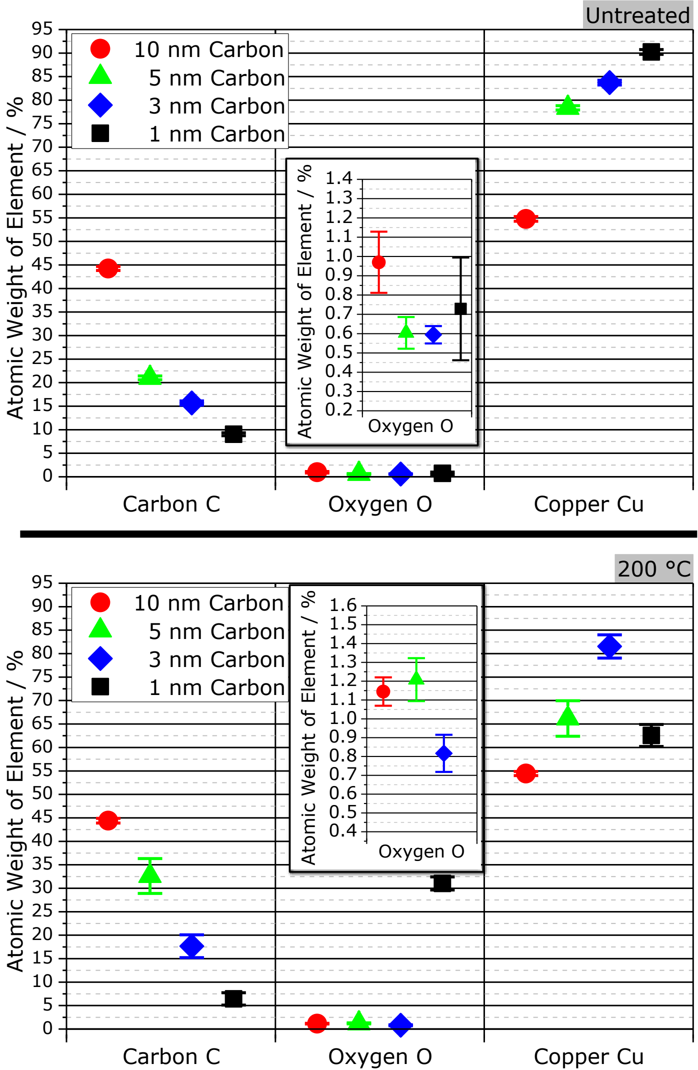

Figure 7.15. Atomic weight of the individual elements achieved by a quantitative EDX characterization of both, a fresh and untreated C coating and a 200 °C stressed C coating, with layer thicknesses varying from 10 nm to 1 nm. The stress time was 15 min. The distribution of the low oxygen weights is shown in detail in the respective inset.

The inset illustrating the low oxygen fractions in detail confirms that the 3 nm thick layer provides the same protection as the 10 nm or the 5 nm layer. The C and the Cu values provide much larger deviations compared to the unstressed samples, but it is important to note that the oxygen weights remain low. In contrast, the inspection of Fig. 7.15 indicates that the 1 nm thick C layer is substantially oxidized after the temperature stress. The achieved ratio of the Cu content related to the oxygen content can be stated to be approximately 2:1. This detected ratio provides compelling evidence that the grown oxide mainly consists of Cu_2O.

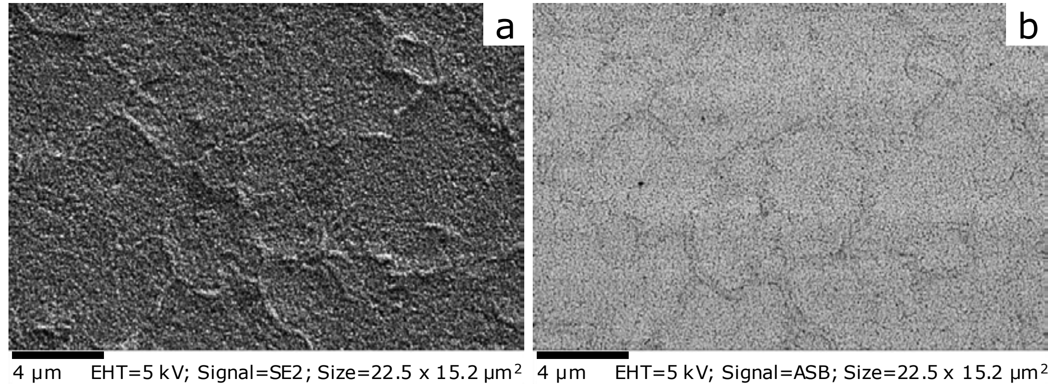

Figure 7.17. SEM topography image (a) and material contrast image achieved by BSE imaging (b) of a Cu surface coated by a 1 nm thick C layer stressed at 200 °C

The topography image of the oxidized surface and the material contrast image in Fig. 7.17 display the significant loss of the protective effect and verify the quantitative EDX characterization in Fig. 7.15.

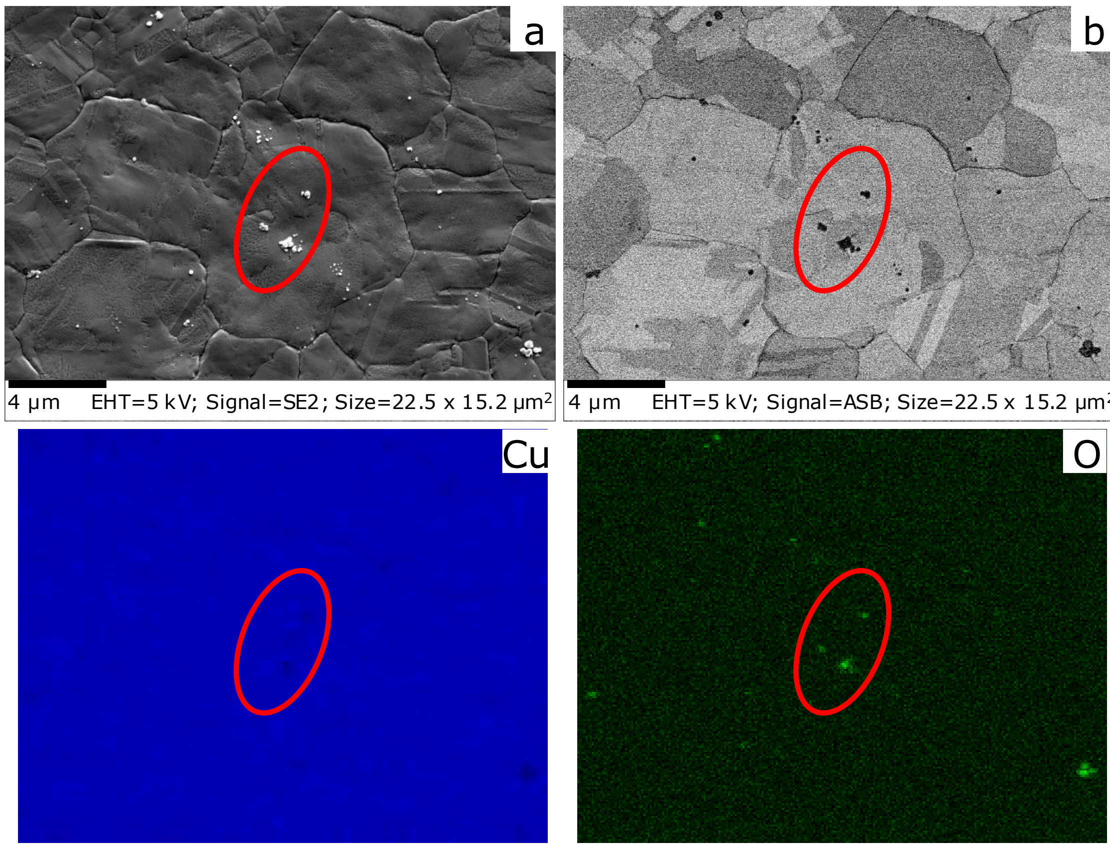

Figure 7.16. SEM topography image (a) and material contrast image achieved by BSE imaging (b) of a Cu surface coated by a 5 nm thick C layer stressed at 200 °C. The corresponding EDX mappings represent the distribution of Cu and O on the surface. The red circles clarify the correlation of specific surface areas.

Despite the fact that the atomic weights of the elements listed in Fig. 7.15 show that the 5 nm and the 3 nm thick C layer can protect the Cu surface from oxidation, very local oxide grains could occur on the surface. For the detection of such grains, the topography must be related to the element distribution over the surface.

The result of the investigations can be found in Fig. 7.16. The topography images provide very local grains and the material contrast images can obviously show that the grains can be defined to be a different material. The corresponding EDX mappings enable the assignment of the detected particles to oxygen and therefore, they can be defined to be oxide grains. The EDX spectrum of the whole area does not yield an increased oxygen content, but at some sporadic places, very local oxidation particles could be identified. The same examinations were performed for the 3 nm thick C layer and the outcomes are represented in Fig. 7.18. By inspecting the mentioned figure, it can be reasoned that parasitic particles could be detected on the surface and the material contrast image enables the correlation of these topographic features to a different material. The additional EDX mappings illustrated in Fig 7.18 allow a more precise specification of the material. It can be observed that the oxygen content rises significantly at the detected particles. This result provides compelling evidence that the detected particles are oxide

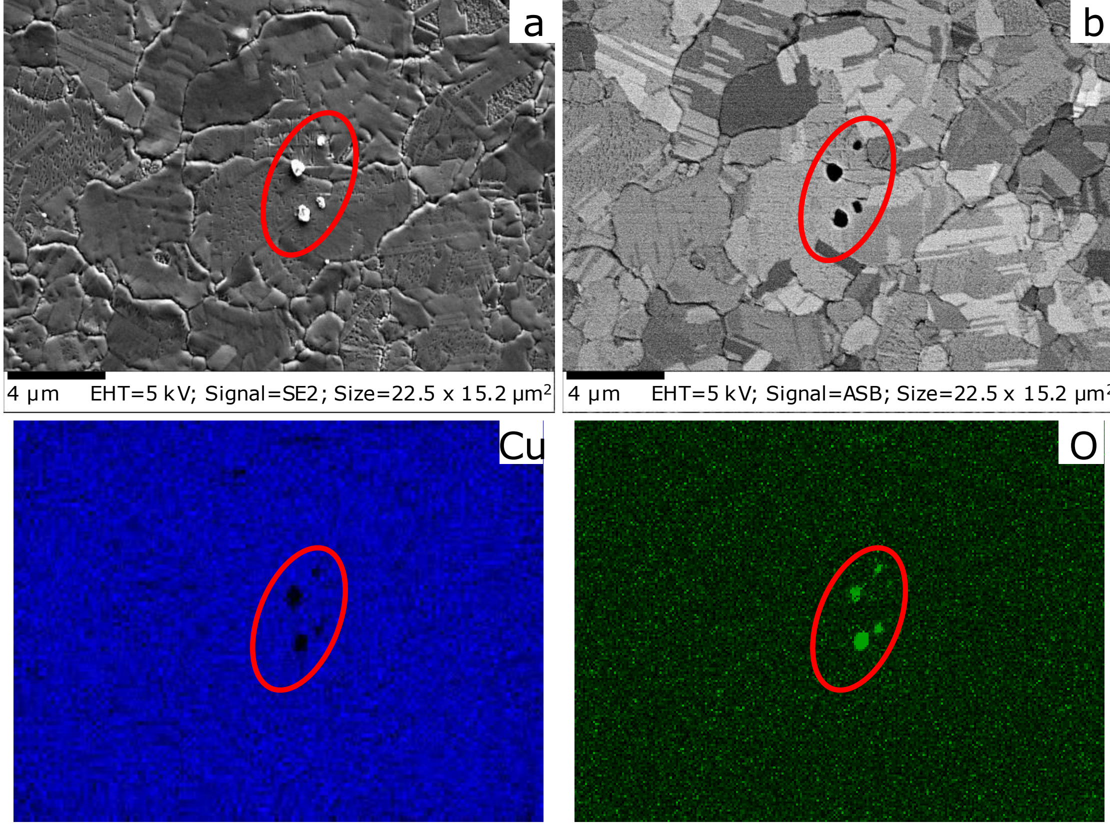

Figure 7.18. SEM topography image (a) and material contrast image achieved by BSE imaging (b) of a Cu surface coated by a 3 nm thick C layer stressed at 200 °C. The corresponding EDX mappings represent the distribution of Cu and O on the surface. The red circles clarify the correlation of specific surface areas.

grains. Similar to the results of the 5 nm thick C layer presented in Fig. 7.16, Fig. 7.18 indicates that only very local oxide grains were grown on the surface and a degradation of the remaining protection layer could not be detected.

In further investigations, the advanced nanoscale characterization by PF-KPFM was used to confirm the previous results. As shown in Fig. 7.19, AFM topography imaging provides a high-resolution image of the coated surface. The corresponding PF-KPFM results showing the CPD values reports only slight variations, but any correlation of grain structures grown on the surface and a CPD change cannot be observed. The subsections of the magnified areas in Fig. 7.19 also validate this conclusion. Comparing the Figs. 7.13 and 7.19, it can be seen that they provide very similar results, even the CPD values of the PF-KPFM results are approximately in the same region. Summarized, it can be reasoned that beside some very sporadic local oxide grains, the 5 nm thick C layer also enables the effective protection of the Cu surface from oxidation. The SEM imaging, the EDX analysis and the nanoscale PF-KPFM investigations did not detect a general degradation of the protection layer caused by the temperature stress.

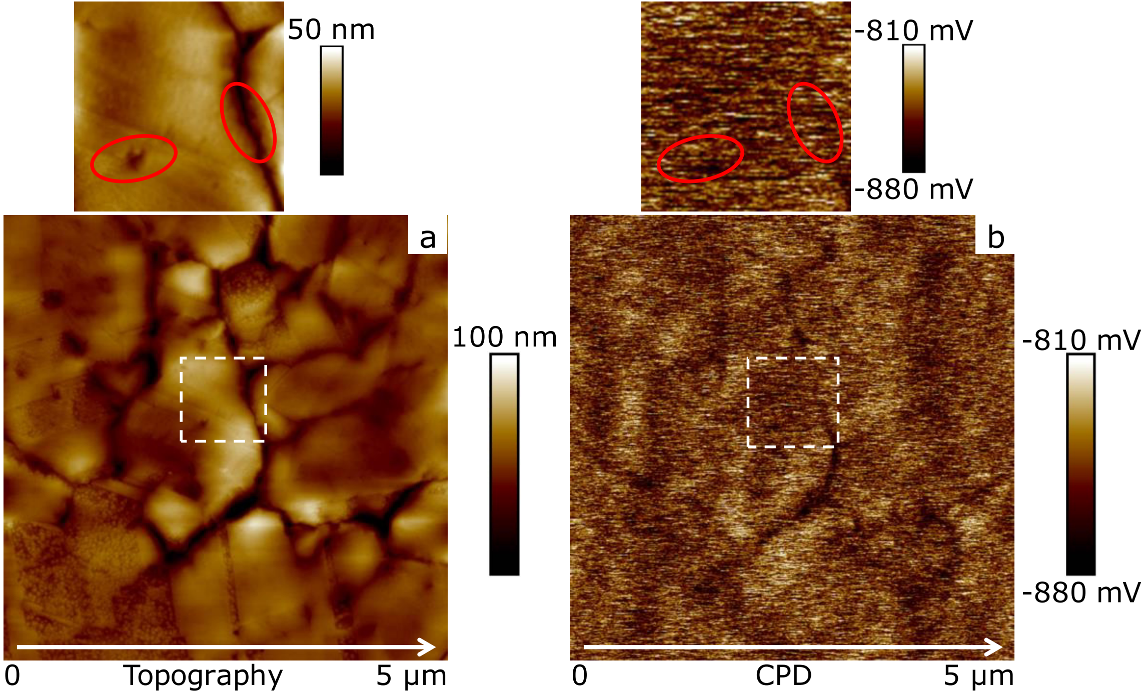

Figure 7.19. AFM topography (a) and corresponding PF-KPFM result (b) of a Cu surface protected by the 5 nm C coating after a temperature treatment of 200 °C. The white dashed squares mark magnified areas presented in the above subsections. The red circles in the subsections highlight the correlation of surface areas with topographic variations and the corresponding CPD change.

In a last step, the nanoscale characterization by PF-KPFM of the 3 nm thick C layer was performed. The results so far were comparable with the 5 nm thick layer. SEM imaging and EDX analysis illustrated in

the Figs. 7.15 and 7.18 the existence of sporadic local oxide grains, but a general degradation of the 3 nm thick C layer was not detected. PF-KPFM should enable the determination of a possible degradation of the coating layer. The result can be found in Fig. 7.20. The AFM topography image clearly displays the surface structure. The red circles in the image as well as in the magnified subsection highlight some very local features. But it is important to note that any clusters of grown oxide grains are not visible. In the corresponding PF-KPFM map the red circles mark the same areas and improve the correlation of the topographic features and their CPD values.

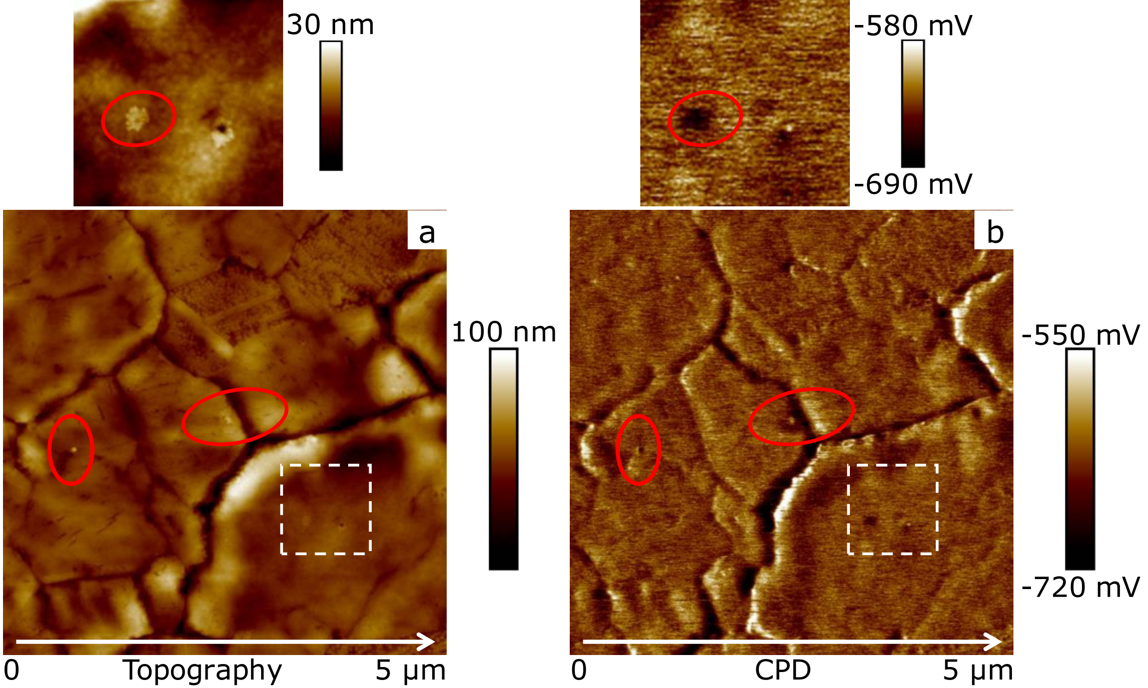

Figure 7.20. AFM topography (a) and corresponding PF-KPFM result (b) of a Cu surface protected by the 3 nm C coating after a temperature treatment of 200 °C. The white dashed squares mark magnified areas presented in the above subsections. The red circles highlight the correlation of surface areas with topographic variations and the corresponding CPD change.

It is evident from the images that the identified particles have a slightly different CPD value than the surrounding. It can be suggested that these particles were grown by oxidation, but a clear assignment is not possible. Beside the identified particles, the CPD image provides the evidence that any clusters of oxide grains were not grown on the surface and the protective effect of the C layer still exists. However, by comparing all PF-KPFM results presented in the Figs. 7.13, 7.19 and 7.20, it can be observed that the CPD range of the 3 nm thick C layer is very different. Such an exception especially in case of the 3 nm thick C layer could already be seen in the BSE images presented in Fig. 7.14. The thickness drop of 5 nm to 3 nm improved the BSE signal contrast significantly which could be explained by the lower damping of the thinner coating layer. It is important to note that the different CPD range is not resulted by the temperature treatment because the untreated samples provided PF-KPFM results with CPD values in the same range. For this reason, it can be speculated that the thinner coating layer has a lower packing

density and therefore, the PF-KPFM characterization provided lower CPD values more influenced by the underneath Cu material. Even though, it is an important outcome that the protective effect of the 3 nm thick coating layer is just as good as of the 5 nm thick layer. For any subsequent interconnection processes, the variation of the CPD range is a significant observation, because it can be assumed that if even non-contact measuring methods such as PF-KPFM can detect a change, following mechanical treatments are not affected. Finally, it can be concluded that the presented results could clearly evidence the protective effect of a 3 nm thick carbon coating layer for a Cu surface up to a temperature of 200 °C.

7.6 Summary

I found out that a 3 nm thick carbon layer deposited by Ion-beam sputtering deposition can clearly protect Cu surfaces from oxidation for a stress temperature up to 200 °C. SEM topography imaging, Backscatter Electron Imaging and corresponding EDX analysis are appropriate tools to monitor the general and local film degradation. An additional PF-KPFM characterization enables the nanoscale investigation of the coating degraded by the temperature treatment. It could be shown that a 10 nm thick Pt coating cannot successfully protect the Cu surface and provides already a local oxidation at a stress temperature of 150 °C. The degradation is characteristic for the Pt coating material and not linked to a drop in the coating quality at specific topographic features. The C coating layer provides a much better protective effect. Beside very local sporadically distributed oxide grains, a gradually degradation of the protective coating was even not observable in the nanoscale for a stress temperature of 200 °C and layer thicknesses down to 3 nm. A 1 nm thick C layer cannot protect the Cu surface sufficiently and provides a complete oxidation of the Cu surface after the 200 °C temperature stress. The PF-KPFM measurements show a significant change of the CPD value in the transition of the 5 nm to the 3 nm thick layer. I concluded that if even PF-KPFM can detect a change, following mechanical treatments are not affected. For semiconductor manufacturing, in general and copper wire bonding, in particular, the introduced carbon coating is a valuable process to protect the Cu surface from oxidation.

8. Oxidation and microstructural study of Cu free air ball formed in air

The electric flame-off (EFO) is the initial step in the thermosonic wire bonding process cycle [158] and forms the free air ball (FAB). Fig. 8.1 illustrates the FAB formation. The EFO step uses a low energy plasma discharge applied by an appropriate electrode to melt the wire tail of the Cu wire. Due to the surface tension the molten metal builds up a ball and afterwards the formed FAB cools down and solidifies.

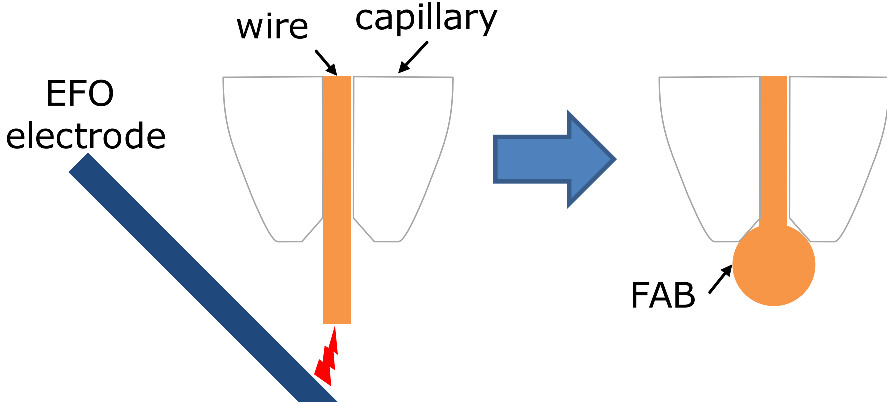

Figure 8.1. Schematic principle of the electric flame-off process step. A low energy plasma discharge is applied by an EFO electrode to melt the wire tail. Due to the surface tension the molten metal forms the free air ball.

For applications with gold wires, the different parameters affecting the Au FAB formation were researched in various publications [158,159,8]. For the implementation of Cu as bonding material, the heat transfer, cooling and solidification of the Cu wire during the EFO process were investigated. Hang et al. [35] reported in their study that the dominant heat loss mechanism is the conduction through the wire. In contrast to the Au wire, Cu is very reactive and susceptible to oxidation. Since the melting of the Cu wire and the solidification to the FAB are temperature related processes, the recrystallization and oxidation of the Cu FAB are important factors for the bonding process [160]. The majority of the researchers tried to neglect the oxidation during the formation of the FAB by implementing a shielding gas environment [14,161–163]. As schematically illustrated in Fig. 8.2, the shielding gas flows only around the wire tail for the ball formation. Pequegnat et al. [14] studied the gas type and the flow rate of the shielding gas. They reported that the flow rate must be optimized for each wire type to produce acceptable FABs and that a gas mixture of 95% N_2 and 5% H_2 significantly reduces the surface oxide rather than N_2. The realization of such a gas environment with a very distinct flow rate necessitates additional technical equipment. But, even with optimized settings the Cu oxidation could not be extinguished totally.

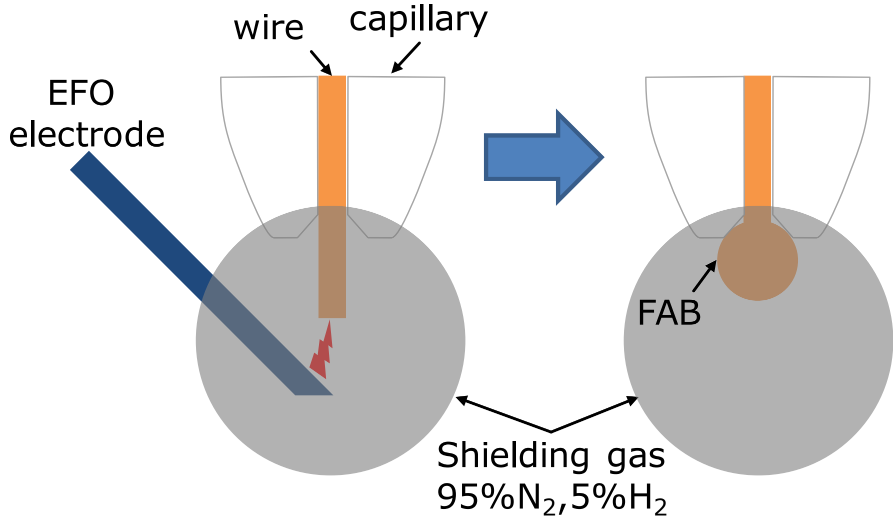

Figure 8.2. Related to Fig. 8.1 EFO process under shielding gas environment to prevent oxidation during the FAB formation.

In this study, the Cu FAB formation in a standard air environment was used. I explored not only the oxidation of the Cu FAB dependent on the EFO parameters, but also effects resulted from the recrystallization such as strain within the microstructure and the grain size distribution.

8.1 Experimental

For the FAB formation, an oxide-free Cu wire with a diameter of 25.4 µm was used. The low energy plasma discharge of the EFO process was provided by the Negative EFO module Model 238 from UTHE technology. This module offers a constant current output of 200 mA and an adjustable discharge voltage in the range of 2 kV to 5 kV. In addition, the EFO firing time of the voltage discharge can be varied from 0.2 ms to 10 ms. Related to the study of Hang et al. [162], the EFO firing time was set to 0.56 ms, because they declared that by using shorter firing times grains have less time to grow during the recrystallization. Consequently, the firing time enables a minimized heat affected zone and a reduced grain size. This microstructure is related to FABs with a lower hardness [35,160].

The FAB formation in this study was performed by a semi-automatic ball-wedge bonder model 1204B from Mech-El industries. The gap between the EFO electrode and the wire tail was set to 790 µm in agreement with the instrument parameters.

The Cu FABs were examined using a Zeiss Ultra 55 scanning electron microscope to observe the topography and FAB diameter. Oxidation as well as microstructural properties of the Cu FABs were analyzed by using energy dispersive X-ray spectroscopy (EDX) and electron backscatter diffraction (EBSD). The fundamental details of the SEM topography imaging and the further SEM based analytical techniques, EDX and EBSD, were described in section 3.2.

8.2 Surface morphology and elemental analysis of FAB

In a first advance, the surface topography and the resulting diameter of the FAB were investigated by using SEM imaging methods immediately after the formation. In Fig. 8.3 the SEM images of individual FABs formed by using different discharge voltages are represented. By comparing the different shapes, it can be noted that most of the discharge voltages resulted in well-formed balls and only the FAB formed at 2.6 kV provided significant deviations from the round shape.

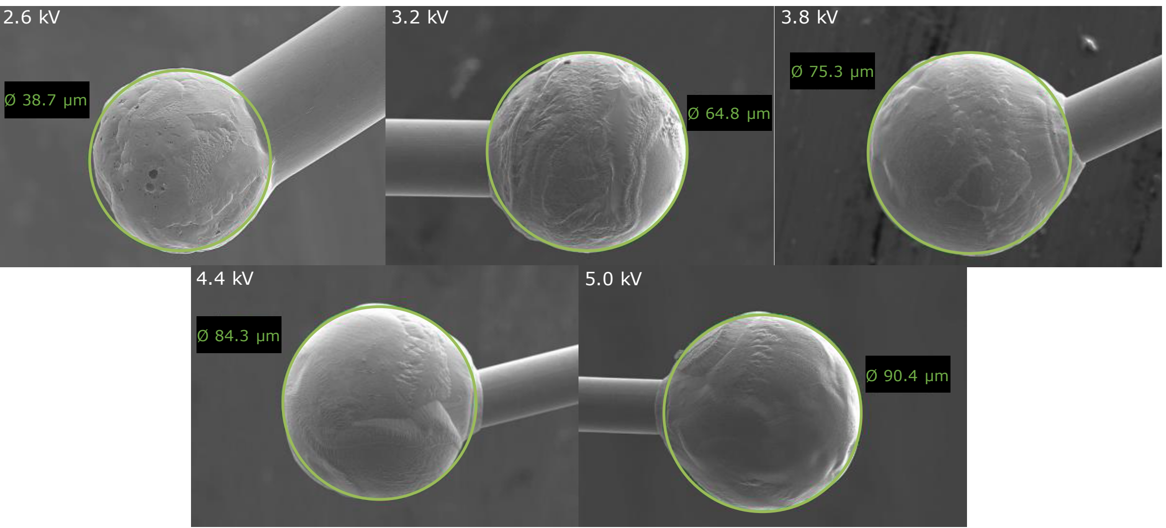

Figure 8.3. Surface topography of FAB and diameter in relation to the EFO discharge voltage.

Besides the topographical variations, the FAB diameters are specified in Fig. 8.3 and they clearly highlight that the FAB size increased for higher discharge voltages. The maximal FAB diameter is around 90 µm, which is about 3.5 times larger than the original Cu wire size of 25.4 µm. The statistical deviations of the individual FAB sizes could be determined by investigating between seven and 14 FABs generated at each single EFO voltage.

As a result, Fig. 8.4 shows the measured FAB diameters as well as the FAB size with respect to the original Cu wire diameter in relation to the electric flame-off voltage. It is obvious that the exponential trend of the best-fit line is very suitable for the relationship between the FAB diameter and the EFO voltage. The equation of the exponential fit line with the corresponding values as well as the coefficient of determination R^2 is stated in Fig. 8.4.

Pequegnat et al. [163] outlined in their study that FAB diameter and EFO firing time are related to a second-order polynomial. They achieved FAB diameters in a similar range of approximately 30 µm to 70 µm by using much shorter firing times of about 0.05 ms to 0.25 ms. This difference can be explained by the higher EFO current of 250 mA compared to 200 mA used in this work as well as by the use of forming gas containing 5% H_2 and 95% N_2. The hydrogen in the forming gas provides additional thermal energy to the EFO process which leads to an increased FAB size [14].

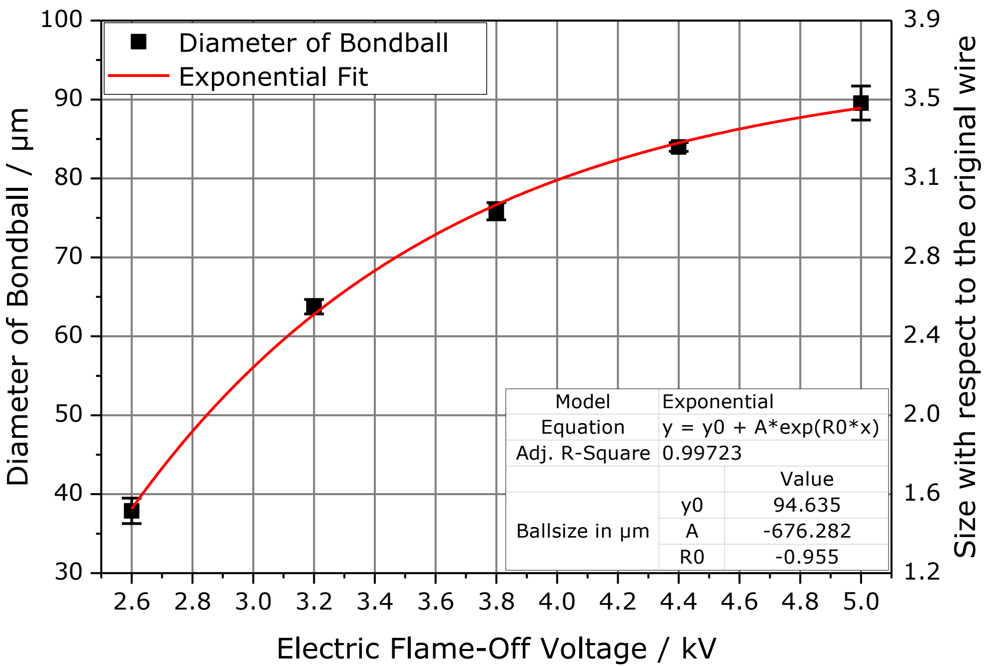

Figure 8.4. Diameter of the Cu FAB in relation to the electric flame-off voltage

In a first view the surface topography of the FABs in Fig. 8.3 looks quite similar. Fig. 8.5 provides a magnified area of the FABs shown in Fig. 8.3 which enables a more detailed investigation of the topographies. The transformation of the surface topography is clearly visible. With increasing EFO voltage, the microstructure of the FAB surface varies significantly. The 2.6 kV and 3.2 kV surfaces in Fig. 8.5 shows a coarse topography with comparative large topographic structures. A further increase of the EFO voltage to 3.8 kV and 4.4 kV, respectively, provides an additional microstructure to the remained coarser structured areas. The red circles in Fig. 8.5 highlight the areas indicating these different topographic features with varying structure size. The last topographic image corresponding to a EFO voltage of 5 kV indicates a further structural change and suggests that the previously observed microstructure has grown and expanded further. Since the FAB is formed by melting the Cu wire tail, it must be considered that the structural variation of the FAB surface could be due to the exposure to oxidation during the FAB formation. The melting point of Cu is known to be at a temperature of 1083 °C. In this temperature range the oxidation behavior is different and cannot be easily compared to the oxidation kinetics in the low temperature range up to 300 °C. For this reason, the high temperature oxidation is addressed in publications separately [164,165]. In this study, the oxidation behavior dependent on the used EFO voltage was investigated by employing the X-ray spectroscopy methodology EDX.

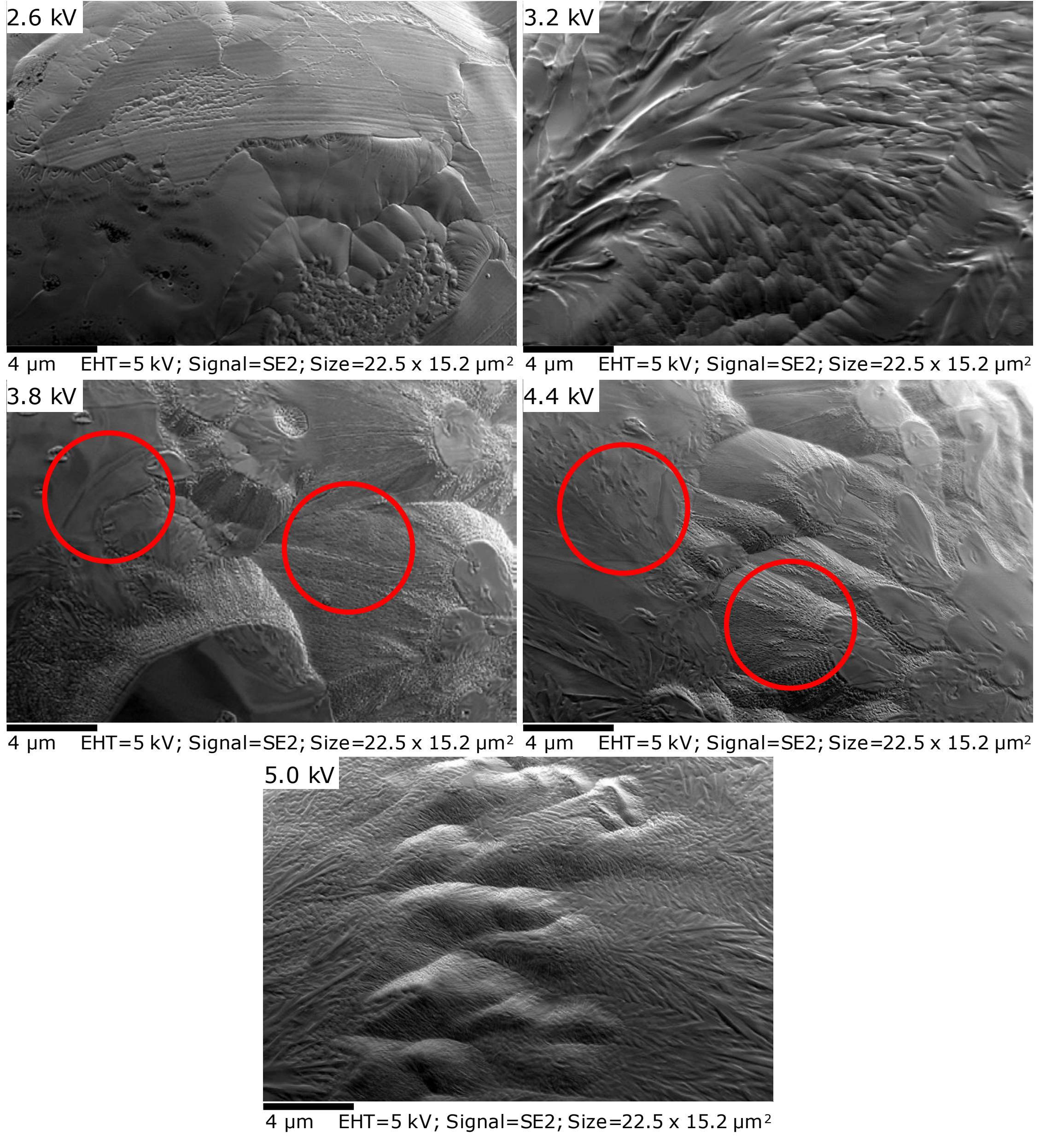

Figure 8.5. Magnified surface topography of the FABs corresponding to Fig. 8.3. The red circle highlight different topography features build up on the FAB surface.

A typical spectrum of a 5 kV FAB is illustrated in Fig. 8.6. The elements identified are carbon (C), oxygen (O) and certainly copper (Cu). Especially, the comparatively high oxygen peak indicates an oxidation of the Cu FAB. The acceleration voltage chosen for the EDX analysis of the FAB was 3 kV. Such a low voltage ensures that the penetration depth of the electron beam is reduced and the analytical area may be limited to the surface.

For the calculation of the X-ray generation depth in Cu, the formula of Castaing [129] can be used. The formula is given by

$$z_m = 0.033(E_0^{1.7} - E_C^{1.7})\frac{A}{\rho Z} \tag{8.1}$$

where z_m denotes the X-ray generation depth or analytical depth, E_0 is the electron energy related to the acceleration voltage in keV, E_C represents the minimum emission energy in keV for the bulk element, A denotes the atomic mass in g/mol of the bulk element, ρ is the density in kg/m³ and Z represents the atomic number of the bulk element. For Cu, O and C the corresponding parameters and the calculated analytical depth z_m are summarized in Table 8.1. z_m for pure copper was calculated to be 45 nm. The values derived for pure oxygen and carbon are only of theoretical importance because carbon or oxygen may only be present in a compound.

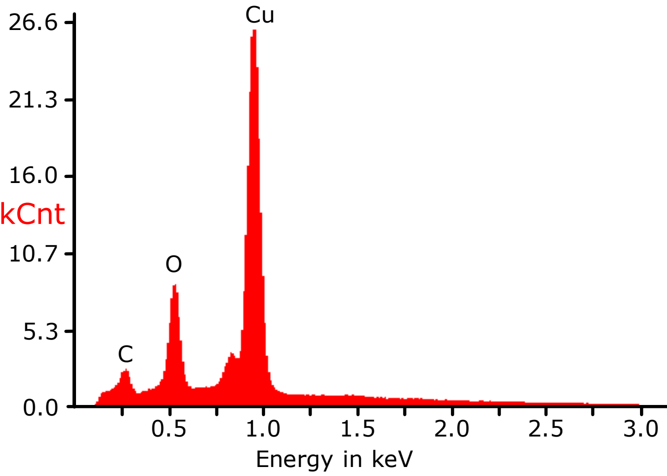

Figure 8.6. EDX spectrum achieved from the surface of a FAB formed at 5 kV.

Table 8.1. Parameter values for z_m calculation as introduced in Eq. 8.1 and the derived z_m values.

	Cu	O	C
E_0 (keV)	3	3	3
E_c (keV)	0.930	0.523	0.277
A (g/mol)	63.55	16.00	12.01
ρ (kg/m³)	8.93	1.57	2.25
Z	29	8	6
Z_m (nm)	45	258	187

For comparison, the derived value for Cu can be evaluated by performing a Monte Carlo simulation of electron trajectories using the software tool electron flight simulator (EFS). EFS simulates the electron beam penetration by the energy loss resulting from inelastic collisions in-between individual elastic scattering events [80]. The result of the Monte Carlo simulation in Fig. 8.7 shows that the electrons penetration depth and the derived analytical depth of 45 nm are slightly different. This difference can be explained by the energy loss of the electrons inside the material. Since the Cu X-ray quantum of the L-shell has a minimum emission energy of 0.93 keV, the remaining electron energy must have at least this value in order to be suitable for the excitation of the X-ray quantum. Consequently, it can be concluded that electrons penetrating deeper into the material than the analytical depth cannot excite the Cu X-ray quantum anymore and thus, that the computation and the simulation are in good agreement.

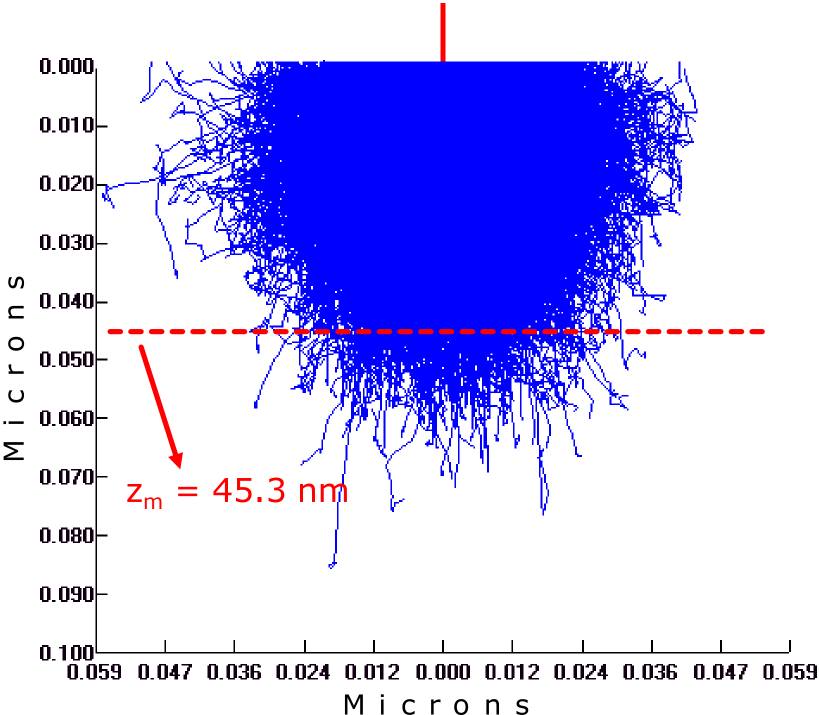

Figure 8.7. Monte Carlo simulation of electron trajectories for pure copper. The analytical depth of 45 nm derived by Eq. 8.1 is marked by the red dashed line.

As already mentioned related to Fig. 8.6, the clear O peak indicates the formation of Cu oxide on the FAB surface. Since the oxidation states of Cu, Cu_2O and CuO, have different material properties compared to pure Cu, the analytical depth may also be calculated for the Cu oxides. Therefore, the parameters according to Eq. 8.1 must be evaluated for Cu_2O and CuO. The density ρ for both materials is known and is 6.0 g/cm^3 for CuO and 6.32 g/cm^3 for Cu_2O.

For the evaluation of the analytical depth z_m the mean atomic mass A_{mean} and the mean atomic number Z_{mean} must be calculated. A_{mean} is defined by

$$A_{mean} = \frac{N_{Cu}}{N_{total}} \cdot A_{Cu} + \frac{N_O}{N_{total}} \cdot A_O \tag{8.2}$$

where N_{Cu} denotes the number of copper atoms, N_0 denotes the number of oxygen atoms and N_{total} the total number of atoms in the molecule. The atomic number corresponds to the atomic mass of the element. For this reason, the theoretical mean atomic number for CuO and Cu_2O must correspond to the molecular weight ratio of the compounds. Based on that, Z_{mean} is defined by

$$Z_{mean} = \frac{N_{Cu} \cdot A_{Cu}}{M} \cdot Z_{Cu} + \frac{N_O \cdot A_O}{M} \cdot Z_0 \tag{8.3}$$

where M denotes the molecular mass of CuO and Cu_2O, respectively. In Table 8.2 the emission energy E_C for the compounds Cu_2O and CuO was defined to be the value for Cu, because the remaining electron energy must be high enough for the excitation of the Cu X-ray quantum.

Table 8.2. Material parameters for Eq. 8.1 of Cu and O and the corresponding values for the molecules Cu_2O and CuO. [1]Calculated values according to equations 8.2 and 8.3.

	Cu	O	Cu_2O	CuO
E_0 (keV)	3	3	3	3
E_c (keV)	0.930	0.523	0.930	0.930
A (g/mol)	63.55	16.00	47.70[1]	39.78[1]
M (g/mol)	-	-	143.1	79.55
ρ (kg/m³)	8.93	1.57	6	6.32
Z	29	8	26.65[1]	24.78[1]

As a result, the calculation of the analytical depth with the data from Table 8.2 inserted in Eq. 8.1 provides z_m values for Cu_2O and CuO of 55.0 nm and 46.9 nm, respectively. Fig. 8.8 illustrates the comparison of the analytic depth z_m and the penetration depth of the electrons derived by a Monte Carlo simulation. Again both, the electron penetration depth and the calculated z_m values are in good agreement. Additionally, it is obvious from Fig. 8.8 that both Cu oxides provide different electron propagation characteristics. As an important outcome, the X-ray generation depth z_m as well as the appropriate propagation characteristics estimated by the Monte Carlo simulation of electron trajectories define the thickness limitations for the EDX analysis of oxide films.

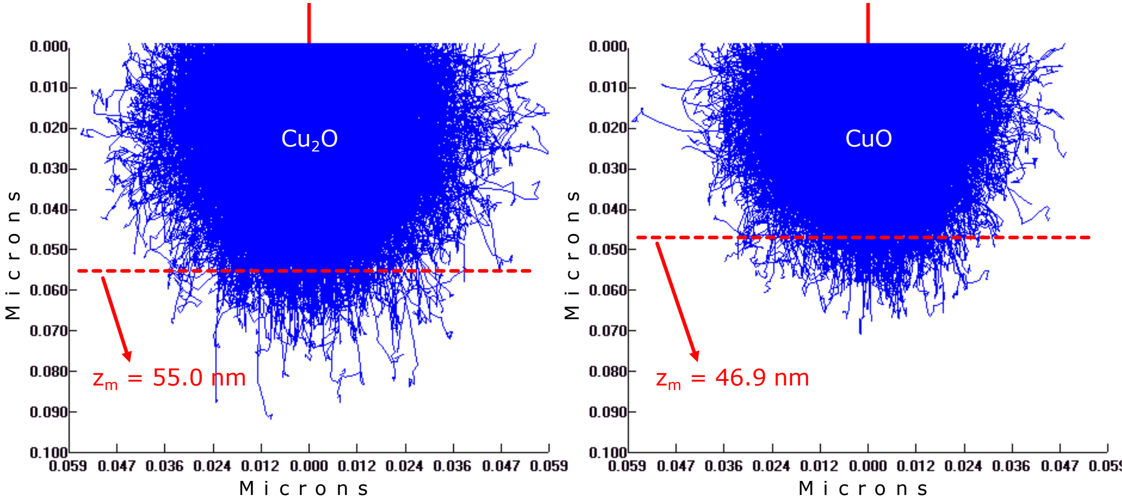

Figure 8.8. Monte Carlo simulation of electron trajectories for Cu_2O (left) and CuO (right). The analytical depth for the respective material, 55 nm for Cu_2O and 46.9 nm for CuO, is marked by the red dashed line in both graphs.

In detail, the element composition of at least five FABs were characterized to ensure that the result can be named as representative and does not refer to outlier. The quantitative analysis of each EDX spectrum is summarized in Fig. 8.9. Furthermore, the element composition of the Cu wire was also quantified and the quantities of the elements were added in Fig. 8.9. The results of the Cu wire provide significant variations. Especially, the oxygen content is much lower than the derived quantities of the FABs. The increased O content and the concurrent decreased Cu content at unchanged C values are a clear indication for the oxidation of the FABs. The average carbon contents of all FABs as well as the values

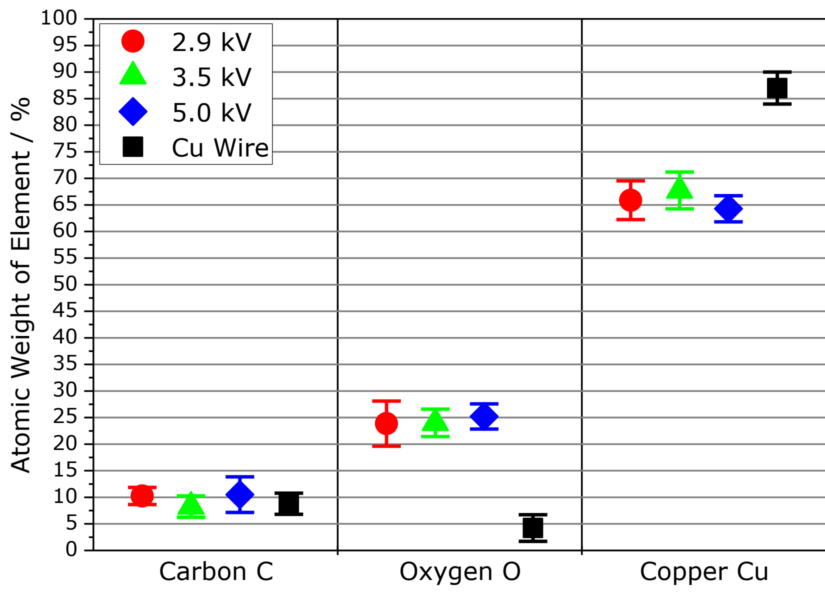

Figure 8.9. Quantitative evaluation of the EDX measurements showing the atomic weight in percentage of the detected elements.

of the pure Cu wire are pretty much the same. Only the FAB formed by the highest discharge voltage of 5 kV shows a larger deviation of the individual carbon contents. This high EFO voltage is thus more susceptible to an increased carbon contamination. However, as can be noticed by reviewing the O content, this increased C contamination does not influence the oxidation. As a more detailed indication for an occurring oxidation the ratio of Cu to O can be considered. The different Cu oxides, CuO and Cu_2O, can be identified by the ratio of the atomic weight of Cu and O. Accordingly, a ratio of 2:1 corresponds to Cu_2O and 1:1 corresponds to CuO, respectively.

Based on the quantified evaluation in Fig. 8.9 the statistical distribution of the atomic weight ratio of Cu:O is plotted in Fig. 8.10. The average values related to the Cu:O ratio of the lower EFO voltages are in the same range. A voltage of 5 kV provides slightly lower values. However, from these results, the type of oxide can not be inferred. Fig. 8.8 introduced the analytical depth for the respective Cu oxides. Since even the lowest Cu:O ratios in Fig. 8.10 are larger than 2:1, it can be noted that the oxide thickness grown on the FABs is significantly lower than the analytical depth derived in Fig. 8.8. This is an important outcome because due to the melting process during the FAB formation in ambient air a much thicker oxide layer was expected. However, providing that a Cu_2O film has formed, the Cu:O ratios (Fig. 8.10) clearly shows that a oxide layer below the analytical depth of 55 nm has grown on the FABs. Logically, this value is even much lower for an assumed CuO layer because of the lower analytical depth (Fig. 8.8) and the provided Cu:O ratios (Fig. 8.10) indicating a much higher Cu content than required for CuO.

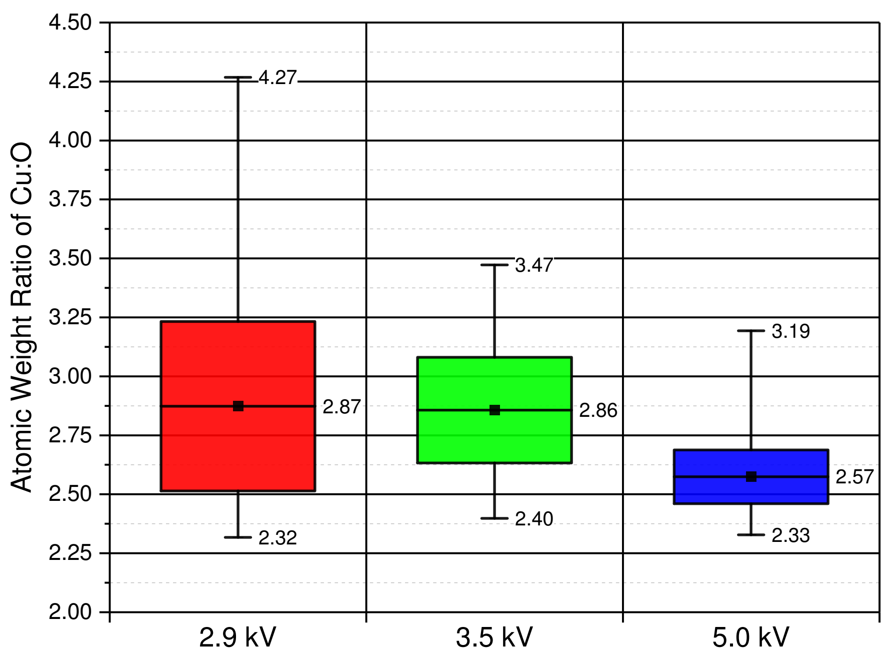

Figure 8.10. Statistical distribution with standard deviation from the mean value and minimum and maximum value of the atomic weight ratio of copper to oxygen measured at FABs shaped at different voltages.

The statistical distribution in Fig. 8.10 also shows that lower EFO discharge voltages result in much larger deviations of the Cu:O ratio. This means that the oxidation behavior of the FABs formed at identical conditions varies clearly. Summarized it could be shown that the topographical investigation as well as the X-ray analysis of the FAB surface revealed significant differences at the various EFO discharge voltages. Previously, the detailed image of the FAB surfaces in Fig. 8.5 indicated that lower EFO voltages provide various topographic patterns. It is worth noting that this surface structures go in line with the observed deviations of the atomic weight ratio of Cu:O (Fig. 8.10) and may be related to different oxidation states or oxide layer thicknesses. In addition, the 5 kV results of the surface topography (Figs. 8.3 and 8.5) and the EDX analysis (Fig. 8.10) fit together. The more balanced and increased microstructure of the 5 kV FAB and the lower deviations of the Cu:O ratios indicate a thicker and more consistent oxide layer covering the Cu FAB surface. These significant differences of the oxidations can be explained by the FAB size in relation to the original Cu wire diameter (Fig. 8.4). Hang et al. [35] reported that the dominant heat loss mechanism related to the cooling of the FAB in air is the conduction up to the wire. Therefore, smaller FABs with respect to the original Cu wire may cool down faster than larger FABs. In the present case, the FAB formed at 2.9 kV is 2.1 times larger, the 3.5 kV FAB is 2.8 times larger and the FAB formed at 5 kV is even 3.5 times larger than the original Cu wire (Fig. 8.4). Consequently, the heat loss through the Cu wire is much more effective for the 2.9 kV FAB than for the 5 kV FAB and the slower heat transport of the 5 kV results in a longer lasting temperature stress and thus, in an extended oxidation.

To confirm these assumptions, Fig. 8.11 shows the simulated temperature distribution of two different FABs formed at 3.2 kV and 5.0 kV with diameters of 63.75 μm and 89.54 μm, respectively, and the Cu wire 1ms after the FAB formation by the EFO process. The correlation of EFO voltage and FAB diameter were chosen referred to Fig. 8.4. The different color scales clearly illustrate that the larger FAB

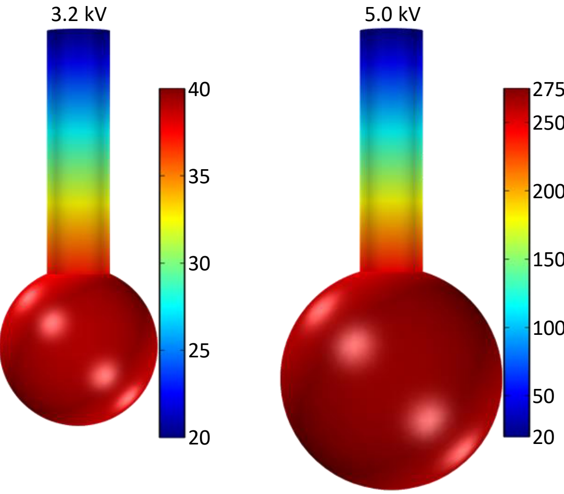

Figure 8.11. Temperature distribution 1ms after the FAB formation of two different sized FABs formed by other EFO voltages.

cooled down more slowly after 1 ms. These results confirm that the dominant heat transfer is the conduction up to the wire. Fig. 8.12 displays the whole temperature profile during the solidification phase after the Cu wire melting. It is evident that larger FABs formed by higher EFO voltages needs much more time to cool down.

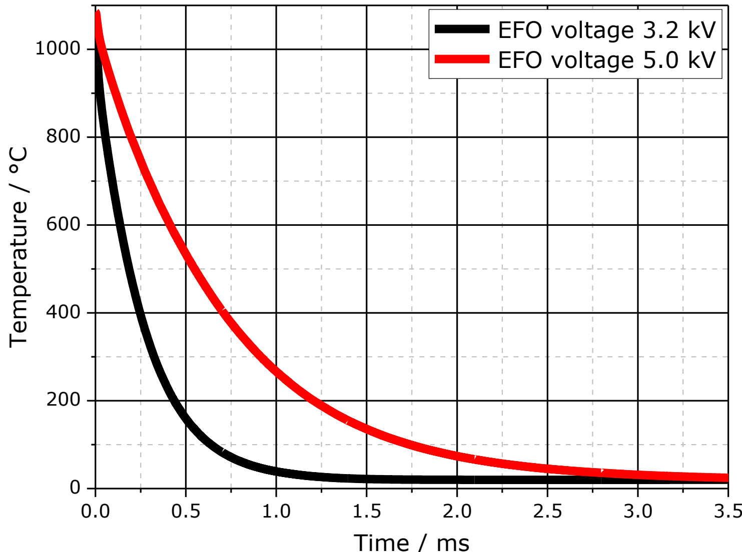

Figure 8.12. FAB temperature over time during the cooling phase for FABs formed by different EFO voltages.

8.3 Nanoscale characterization of the internal FAB structure

The present investigations focused on the general FAB size and on the FAB surface or at least on the area near to the surface, but due to the melting and solidification for the FAB formation, the inner FAB properties such as the crystal structure or the existence of oxidation areas must be considered. Consequently, in the next part results related to the inner structure of the FABs formed in ambient air are presented. For this investigation, a cross-section preparation of the FABs were done.

In a first approach the EDX results of the cross sectioned FABs were compared with the results of the FAB surfaces. The topography of the cross section and the corresponding elemental mapping of the EDX analysis are depicted in the Fig. 8.13. In the topography images the individual grains can be identified. The corresponding elemental mapping specifies the arrangement of carbon, oxygen and copper indicated by their respective color. The carbon content in the outer areas is due to the epoxy resin which was used for mounting the samples. It is obvious that inside the FAB only Cu is present and no oxide areas indicated by oxygen are visible.

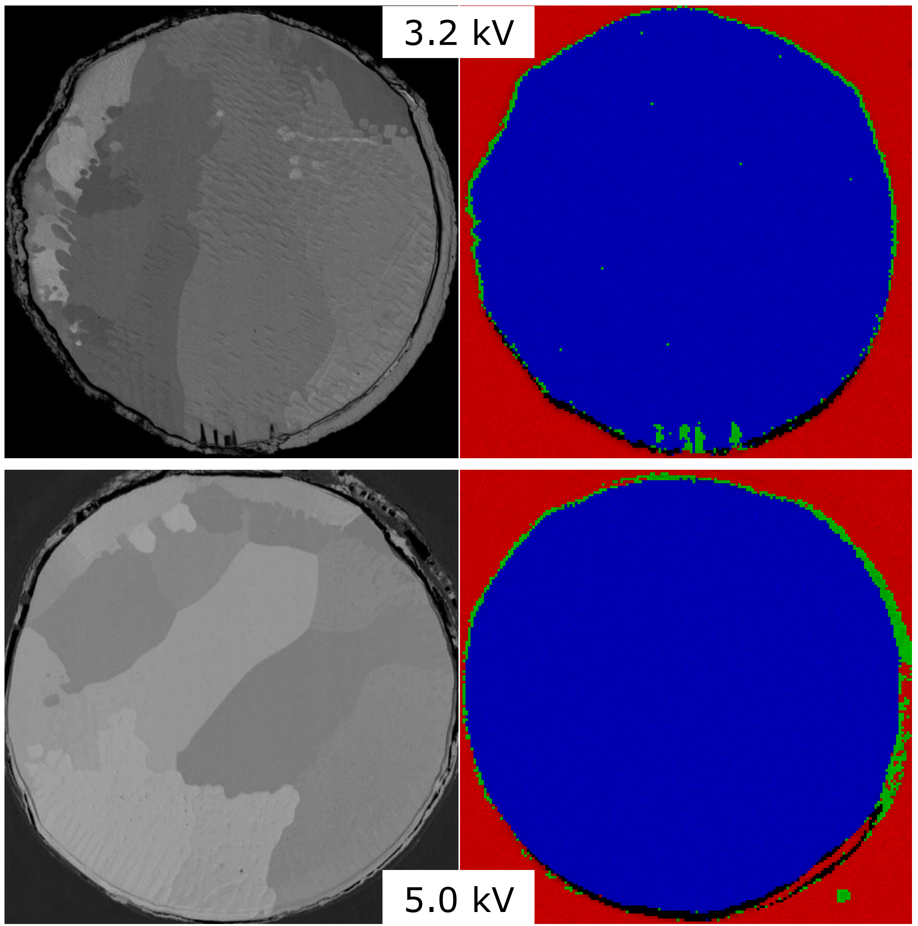

Figure 8.13. Surface topography (left) and corresponding elemental mapping of an EDX analysis (right) of the cross section of two FABs formed at different discharge voltages. FAB diameters can be read from the Fig. 8.4. In the elemental mapping, the red color corresponds to carbon C, green to oxygen O and blue to copper Cu.

Moreover, oxygen indicated by the green color is mainly existent at the border of the FAB. Compared with the EDX analysis of the FAB surface in Fig. 8.9 and 8.10, the elemental mapping in Fig. 8.13 also exhibits significant differences of the oxygen areas or rather the oxidation layer grown by the EFO process. The correlation between an increased EFO voltage and the thicker oxidation layer could be confirmed by the Cu:O ratio (Fig. 8.10) and the oxygen areas around the cross-section samples (Fig. 8.13). This is an important outcome for choosing the parameter settings of the EFO process in ambient air. An EFO voltage in the range of 3 kV produces a well formed spherical FAB with a very thin oxide layer grown on the surface.

Additionally, the EFO process probably also changes the crystallographic structure of the original Cu wire. Fig. 8.13 already suggests individual grains, but for a more detailed insight the exact crystal structure was determined by performing an EBSD characterization of the cross-sectioned FABs and the Cu wire.

The EBSD results in Fig. 8.14. indicate significant differences between the crystal structure of the FABs and the Cu wire. Each grain is related to a color which specifies the crystal orientation of that grain. The Inverse Pole Figure (IPF) map in Fig. 8.14 shows that the grain size of the FAB compared to the Cu wire increased significantly and that the larger grains in the FABs have different orientations. However, a preferred crystal orientation could not be observed. The IPF maps present the grain distribution inside the FABs and the Cu wire very well, but especially the grain size of the FABs is not comparable in this figure.

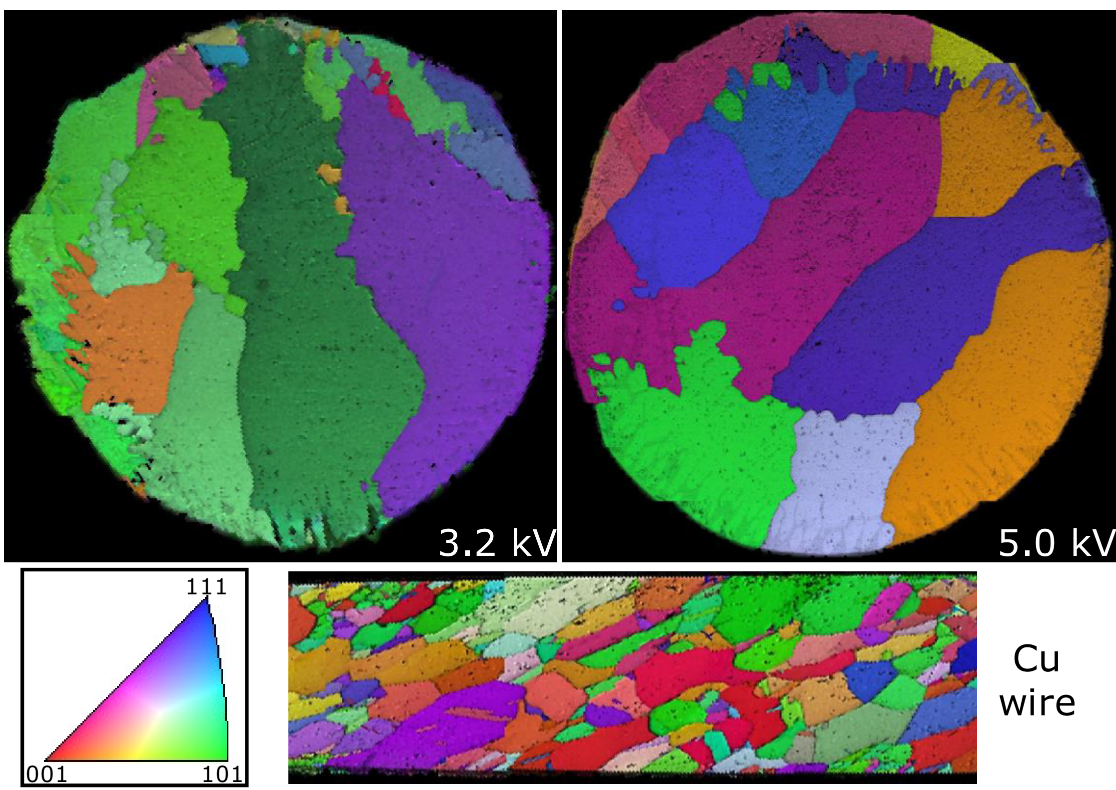

Figure 8.14. EBSD analysis of FABs formed by using different discharge voltages and of an original Cu wire showing the grayscale image quality map colored by the Inverse Pole Figure (IPF) data with respect to the [001] direction. FAB diameters can be read from Fig. 8.4.

Therefore, the exact grain size area was extracted and outlined in Fig. 8.15. The difference between the Cu wire grain size and the FAB could already be suggested in Fig. 8.14. Fig. 8.15 shows in detail the statistical distribution of the grain size areas. It could be indicated that the 5 kV FAB provided larger grains than the 3.2 kV FAB. However, it must be considered, that the 5 kV voltage results in a 41.6% larger FAB diameter compared to the 3.2 kV FAB. However, the difference in grain size between the 5 kV FAB and the 3.2 kV FAB does not match the increase of the FAB diameter. It can be observed that a maximum grain size of 547 μm^2 can be related to the 3.2 kV and 1237 μm^2 to the 5.0 kV, respectively. This corresponds to an enlargement of 126%, which is much more than the percental increase of 41.6% for the FAB diameter. Due to this significant difference, it can be noted that the EFO

voltage clearly influences the grain size of the recrystallized FAB. Since Hang et al. [162] reported that a finer grain structure is advantageous for the microhardness because of softer FABs and since the 3.2 kV FAB provided lower grain sizes, the EFO discharge voltage should be chosen in this range. Previously in this section, it was concluded that a voltage in the range of 3 kV produce a well formed spherical FAB with a very thin oxide layer grown on the surface. The results and the conclusions drawn for the observed crystal orientations (Fig. 8.14) and the evaluated grain sizes (Fig. 8.15) are consistent with the topographical and X-ray spectroscopic observations and verify the favored EFO voltage range of 3 kV.

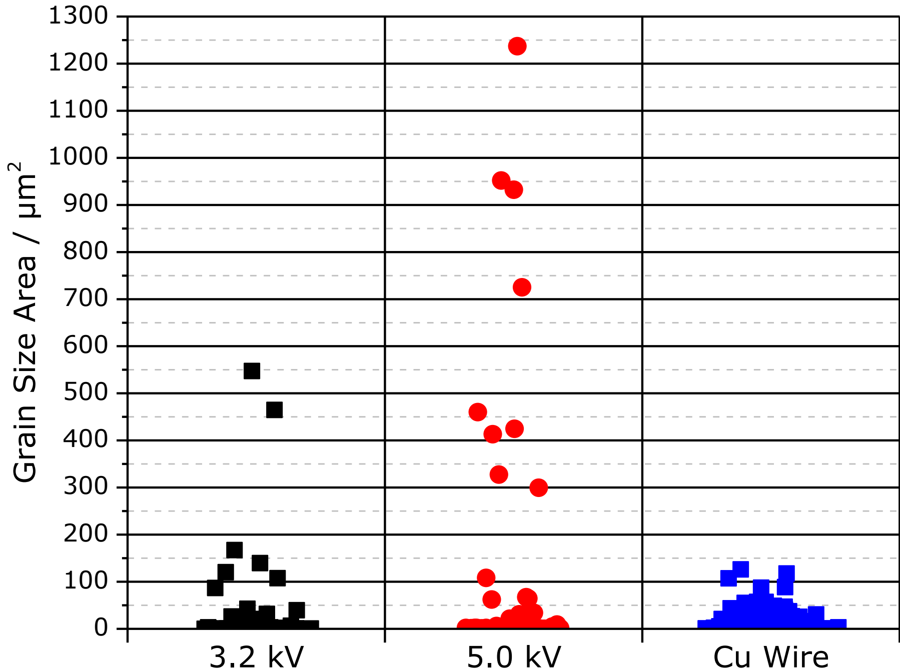

Figure 8.15. Statistical distribution of the grains size areas extracted from the EBSD results introduced in Fig. 8.14.

Besides the analysis of the crystal structure, the orientation and the grain size, the EBSD results can also be used to perform a plastic strain analysis caused by the deformation [166,167]. In their review article Wright et al. [166] examined the different technologies in terms of strain analysis using EBSD and explained in detail that plastic strain degrades the quality of the diffraction patterns. A diffraction volume within a region of a high dislocation density results in degraded patterns because local perturbations of the diffracting lattice planes lead to an incoherent scattering. This is shown schematically in Fig. 8.16 for a single dislocation. Thus, the higher the dislocation density is the stronger the degradation in pattern quality.

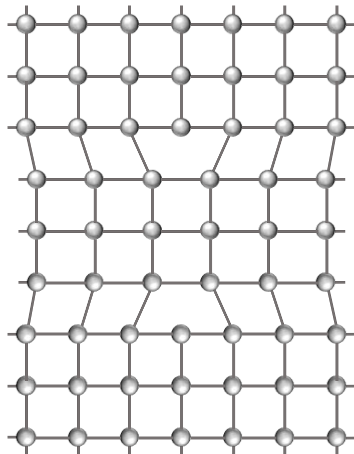

Figure 8.16. Schematic diagram demonstrating the disturbance in the crystal lattice caused by two opposing edge dislocations leading to a degraded EBSD pattern.

The visualization of such a dislocation density can be achieved by investigating the deviations in orientation between each measurement point in a grain and the average orientation of that grain. More plastic strain lowers the pattern quality and increased the orientation spread inside a grain significantly. The map for this kind of strain analysis is called the grain orientation spread (GOS) and is explained in detail in [166].

Applied to the EBSD results in Fig. 8.14, Fig. 8.17 represents the corresponding GOS map. The colors indicate an orientation deviation from 0 up to a maximum deviation of 6 degrees. The GOS map of the Cu wire features very low deviations and thus, the dislocation density or the plastic strain in the material is very low. A specific area for an increased strain may not be observed. In contrast to this, the GOS maps of the FABs in Fig. 8.17 indicates increased orientation deviations at the borders. This increased dislocation density at the borders was observed for both, the 3.2 kV and the 5.0 kV FAB, whereas the 3.2 kV FAB provided the largest dislocation density indicated by the measured deviation of around 6°. The GOS map of the 5.0 kV FAB resulted in a maximum deviation of around 2.7°. Based on these results, it can be concluded that FABs formed at lower voltages have more strain inside than FABs formed at higher voltages.

As a reason for the different GOS maps, the cool down procedure of the FABs may be stated. In the previous investigations related to the Cu oxide growth on the FAB surface, the heat loss mechanism (Figs. 8.11 and 8.12) could explain the detected differences in oxide layer thickness. In various studies [35,168,169,9] the researchers found out that during the FAB formation the main heat loss mechanism is the conduction up to the wire and thus the ball solidified rapidly by convective heat transfer. For the evaluation of the temperature distribution 1 ms after wire melting (Fig. 8.11) as well as for the complete temperature profile over time (Fig. 8.12) the convective heat transfer in the material up to the wire and the convective cooling over the ambient air were considered. The larger volume of the 5.0 kV FAB takes more time for the cooling phase compared to the 3.2 kV. The GOS maps in Fig. 8.17 provided reduced

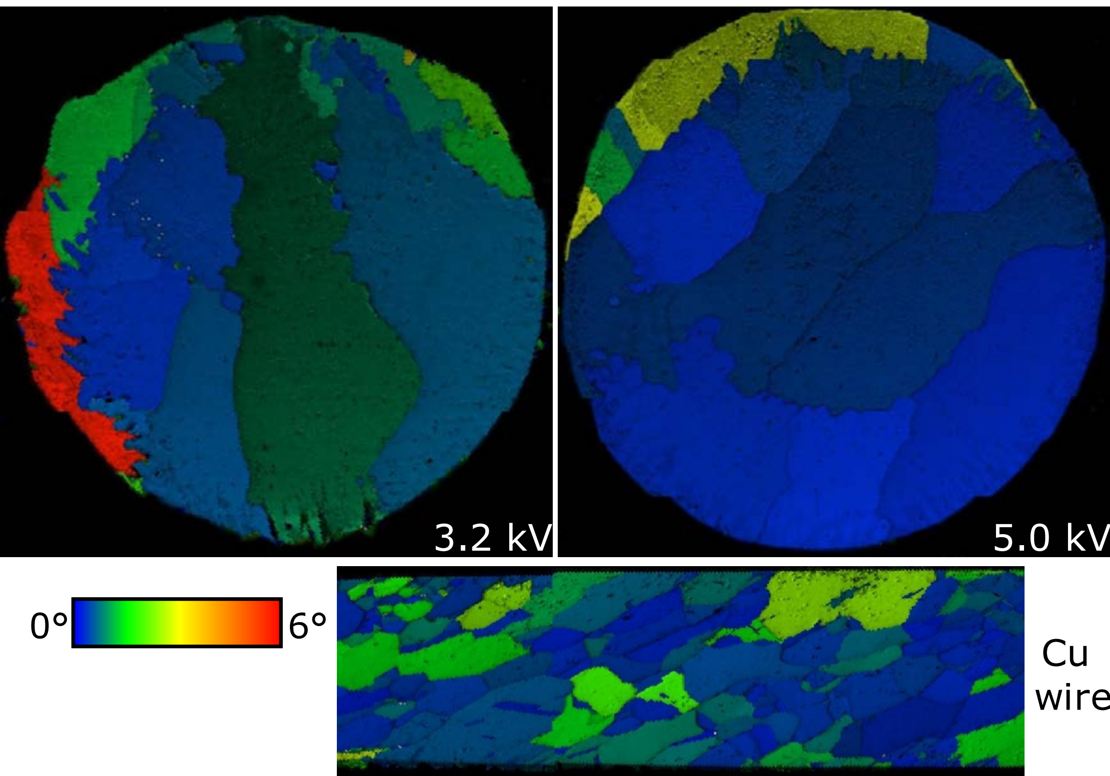

Figure 8.17. EBSD strain analysis of FABs formed by using different voltages and of the original Cu wire showing the grayscale image quality map colored by the grain orientation spread (GOS)

strain inside the FAB for higher EFO voltages because the internal stress could be lowered by the longer cooling phase.

8.4 Summary

In this study, the FAB formation in ambient air environment was investigated by using SEM topography imaging and further SEM based characterization techniques such as EDX and EBSD. The FAB diameter correlates clearly with the EFO voltage in an exponential trend. The measurements showed that various topographic regions on the FAB surface can be assigned to different Cu oxide layer thicknesses.

The X-ray generation depth could be calculated for pure Cu as well as for the Cu oxides, Cu_2O and CuO and the results could be confirmed by performing Monte Carlo simulations of electron trajectories. It could be shown that the thickness of the oxide layers grown on the FAB surface are below the derived analytical depth of 55 nm. The deviations of the Cu:O ratio at different FABs as well as at different FAB regions provided a significant correlation of the EFO voltage and the oxidation behavior.

Cross sectioned FABs showed that the oxidation occurs only on the surface and oxide areas inside the FAB can be excluded. EBSD measurements enabled the correlation of grain structure, grain size and strain inside the FAB with the EFO voltage. A finer grain structure and a lower grain size can be achieved

by lower EFO voltages. EBSD strain analysis indicated an increased dislocation density at outer area of the FAB and simultaneously higher EFO voltages yielded a lower dislocation density.

Both, the difference in oxidation behavior as well as the different dislocation density could be correlated to the heat transfer during the FAB formation. Since the main heat transfer mechanism is up to the wire, smaller FABs cooled down faster and they possessed thinner oxide layer. Related to the dislocation density, larger FABs provided reduced strain inside the FAB because the internal stress can be lowered by the extended cooling phase.

9. Conclusion

The progressive down scaling of semiconductor technologies has improved the performance of integrated circuits. For this consequent device shrinking and the needs for high-performance devices, the metallization material had to be changed to copper because of the much better electrical properties. Beside the metallization, the interconnection technology in the packaging process is also an important factor for the performance and reliability of the device. Although Cu has found one's way into the semiconductor manufacturing as metallization material, the mostly used interconnection material to connect a semiconductor chip and a leadframe is gold. The reasons providing gold as interconnection material are benefits such as self-cleaning, a high yield rate, flexibility and reliability. In IC packaging the three principal electrical interconnection methods are flip-chip, tape-automated bonding and thermosonic wire bonding, at which the thermosonic wire bonding alone has been applied for more than 96% of the IC interconnections. Since Cu is subject to oxidation, even at room temperature, the characterization of the Cu surface is an important aspect for the process development.

For manufacturing of reliable and predictable Cu wire bonds and the development of respective industrial processes, a novel method to research the oxidation behavior of the Cu bond pad in the nanoscale was developed by using combined characterization techniques. Different copper oxides, cupric oxide CuO and cuprous oxide Cu_2O, may clearly be distinguished by the CPD value measured by PF-KPFM at ambient conditions. The PF-KPFM results were validated by EDX and FTIR measurements. The statistical evaluation of the measured CPD values demonstrated that even the maximum and minimum values do not overlap, and therefore the Cu oxides may clearly be distinguished solely by PF-KPFM. For CuO PF-KPFM yields CPD values in the range of -859 mV to -709 mV and for Cu_2O in the range of -635 mV to -524 mV. Based on those results, the investigation of the oxidation at the bonding temperature of 200 °C yields that already after two minutes CuO has grown on top of a Cu_2O layer. The small CuO grains cover almost the whole surface. At five minutes of oxidation the small CuO grains apparently merged and build up larger grains. Additionally, the gap between the CuO grains increased and can clearly be identified to consist of Cu_2O indicating a Cu_2O sub-layer.

Novel thin passivation layer in the nanometer range are introduced to protect the Cu surface from oxidation without limiting the ability for applying interconnection processes. Such layers enable reliable and stable surface conditions. Studies show that thin organic Self-Assembled Monolayer (SAM) act as effective barrier to protect Cu from corrosion. As copper is exposed to elevated temperatures during the bonding process, integrity, degradation and temperature stability of the protective layers are critical issues.

For the characterization of these soft passivation films, advanced AFM techniques such as dCFM operated in a fluidic environment are introduced to detect chemical surface properties. Due to the operation in a fluid medium, hydrodynamic drag forces must be considered. A novel numerical integrated model was presented that is able to provide accurate predictions of the hydrodynamic drag forces present in AFM fluid imaging in general and in dCFM measurements in particular. The presented results included a wide range of cantilever types, cantilever oscillation amplitudes, liquids and further fluid properties such as temperature and ethanol concentration. The correctness of the numerical 3D model could be verified by comparing the predicted drag forces with published results of other researchers and good agreement was observed. The findings of this section confirmed that drag force dependence on tip speed is essentially linear in nature. The numerical results could show that the triangular cantilever geometry is preferable for AFM operations in liquid because it provides significant lower drag forces than the rectangular cantilever geometry. Beside the examination of different cantilevers and their oscillation amplitudes, the influence of fluid media such as ultrapure water or an ethanol-water mixture with varying ethanol concentration could be demonstrated. The results showed that ultrapure water provided the lowest drag forces, whereas with increasing ethanol concentration the drag forces increase. In addition, the presented fluid temperature dependence on the drag force clarified that beside the heating caused by the equipment, an additional heat source could be used for a further reduction of the parasitic hydrodynamic drag forces.

The results achieved by the introduced numerical model improved the ability of AFM measurements in a liquid environment and enabled the nanoscale characterization of passivation layer on Cu. I found that CH_3-terminated SAM films are able to protect Cu from oxidation. Subject to temperature stress, the films degrade and gradually lose their integrity. Torsional Resonance Tunneling AFM and dynamic Chemical Force Microscopy are appropriate tools to monitor film integrity and degradation on nanometer scale without damaging the film. High hydrophobicity and low tunneling current, respectively, correlate with intact film integrity and vice versa. By comparing my microscopic results with the macroscopic chemical film composition achieved by ATR-FTIR, I conclude that after 100 °C stress regions with high tunneling current and low hydrophobicity correlate with local SAM film disintegration and local oxidation of the Cu surface. With stress temperature up to 150 °C the grade of disintegration and oxidation increases and may finally lead to a complete decomposition of the SAM film. The film degradation observed is critical for the application of SAM films in wire bonding processes. For semiconductor manufacturing, in general and Cu wire bonding, in particular, TR-TUNA and dCFM are valuable tools for further research, predominately when sensitive surface layers are involved.

Passivation layer based on sputter techniques was evaluated. I found out that a 3 nm thick carbon layer deposited by Ion-beam sputtering deposition can clearly protect Cu surfaces from oxidation for temperatures up to 200 °C. SEM topography imaging, Backscatter Electron Imaging and corresponding EDX analysis are appropriate tools to monitor the general and local film degradation. An additional

PF-KPFM characterization enables the nanoscale investigation of the coating degraded by the temperature treatment. It could be shown that a 10 nm thick Pt coating cannot successfully protect the Cu surface and provides already a local oxidation at a stress temperature of 150 °C. The degradation is characteristic for the Pt coating material and not linked to a drop in the coating quality at specific topographic features. The C coating layer provides a much better protective effect. Beside very local sporadically distributed oxide grains, a gradually degradation of the protective coating was even not observable in the nanoscale for a stress temperature up to 200 °C and layer thicknesses down to 3 nm. A 1 nm thick carbon layer cannot protect the Cu surface sufficiently and provides a complete oxidation of the Cu surface. The PF-KPFM measurements show a significant change of the CPD value in the transition of the 5 nm to the 3 nm thick layer. I concluded that if even PF-KPFM can detect a change, following mechanical treatments are not affected. For semiconductor manufacturing, in general and copper wire bonding, in particular, the introduced carbon coating is a valuable process to protect the Cu surface from oxidation.

Beside the research of the Cu pad surface, the Cu free air ball (FAB) formation in the ambient environment was investigated by using SEM topography imaging and further SEM based characterization techniques such as EDX and EBSD. The FAB diameter correlates clearly with the electric flame-off (EFO) voltage in an exponential trend. The measurements show that topographic changes of the FAB diameters can be assigned to different oxidation layers. The results of the EDX analysis can be validated by combining the calculation of the X-ray generation depth and the Monte Carlo simulation of electron trajectories for pure copper as well as for the Cu oxides. The detected oxide layers are well below the derived generation depth of 55 nm of the EDX analysis and the deviations of the quantitative element composition provides a significant correlation of the EFO discharge voltage and the oxidation. Cross-sectioned FABs provide more details related to the internal structure. Element mappings of the cross-sectioned FABs could show that the oxidation occurs only on the surface and oxide areas inside the FAB can be excluded. EBSD measurements enabled the correlation of grain structure, grain size and strain inside the FAB with the EFO voltage. A finer grain structure and a lower grain size can be achieved by lower discharge voltages. In contrast, a lower dislocation density at the borders can be detected for higher EFO voltages. The heat transfer up to the wire and the convective cooling by the surrounding air can explain the introduced conclusions regarding the oxidation and the dislocation density.

References

[1] J.R. Lloyd, J.J. Clement, Electromigration in copper conductors, Thin Solid Films 262 (1995) 135–141.

[2] J. Lloyd, J. Clemens, R. Snede, Copper metallization reliability, Microelectron. Reliab. 39 (1999) 1595–1602.

[3] B. Li, T.D. Sullivan, T.C. Lee, D. Badami, Reliability challenges for copper interconnects, Microelectron. Reliab. 44 (2004) 365–380.

[4] M.M. Waldrop, The chips are down for Moore's law, Nature 530 (2016) 144–147.

[5] Alexander von Glasow, Zuverlässigkeitsaspekte von Kupfermetallisierungen in Integrierten Schaltungen. Dissertation, 2005.

[6] ITRS, Internetaional Technology Roadmap for Semiconductors: Assembly and Packaging (2009).

[7] Kulicke, Soffa (Eds.), Bonden mit Kupferdraht, 2004.

[8] H. Xu, C. Liu, V.V. Silberschmidt, Z. Chen, J. Wei, Initial bond formation in thermosonic gold ball bonding on aluminium metallization pads, J. Mater. Process. Technol. 210 (2010) 1035–1042.

[9] S. Murali, N. Srikanth, C.J. Vath, Grains, deformation substructures, and slip bands observed in thermosonic copper ball bonding, Materials Characterization 50 (2003) 39–50.

[10] J. Tan, B.H. Toh, H.M. Ho (Eds.), Modelling of free air ball for copper wire bonding, 711-717, 2004.

[11] G.G. Harman, C.E. Johnson, Wire bonding to advanced copper, low-K integrated circuits, the metal/dielectric stacks, and materials considerations, IEEE Trans. Comp. Packag. Technol. 25 (2002) 677–683.

[12] S. Murali, N. Srikanth, C.J. Vath, Effect of wire diameter on the thermosonic bond reliability, Microelectron. Reliab. 46 (2006) 467–475.

[13] C.C. Lee, T. Tran, D. Boyne, L. Higgins, A. Mawer, in: Electronic Components and Technology Conference (ECTC), 64th ed., 2014, pp. 1539–1548.

[14] A. Pequegnat, H.J. Kim, M. Mayer, Y. Zhou, J. Persic, J.T. Moon, Effect of gas type and flow rate on Cu free air ball formation in thermosonic wire bonding, Microelectron. Reliab. 51 (2011) 43–52.

[15] S. Kaimori, T. Nonaka, A. Mizoguchi, The Development of Cu Bonding Wire With Oxidation-Resistant Metal Coating, IEEE Trans. Adv. Packag. 29 (2006) 227–231.

[16] A.B. Lim, C.B. Boothroyd, O. Yauw, B. Chylak, C.L. Gan, Z. Chen, Interfacial evolution and bond reliability in thermosonic Pd coated Cu wire bonding on aluminum metallization, Microelectron. Reliab. 63 (2016) 214–223.

[17] B. Zhang, K. Qian, T. Wang, Y. Cong, M. Zhao, X. Fan, J. Wang (Eds.), Behaviors of Palladium in Palladium Coated Copper Wire Bonding Process, 662-665, 2009.

[18] I. Qin, A. Shah, C. Huynh, M. Meyer, M. Mayer, Y. Zhou, Role of process parameters on bondability and pad damage indicators in copper ball bonding, Microelectron. Reliab. 51 (2011) 60–66.

[19] Z.W. Zhong, Overview of wire bonding using copper wire or insulated wire, Microelectron. Reliab. 51 (2011) 4–12.

[20] C.J. Vath, M. Gunasekaran, R. Malliah, Factors affecting the long-term stability of Cu/Al ball bonds subjected to standard and extended high temperature storage, Microelectron. Reliab. 51 (2011) 137–147.

[21] H. Xu, C. Liu, V.V. Silberschmidt, Z. Chen, Growth of Intermetallic Compounds in Thermosonic Copper Wire Bonding on Aluminum Metallization, Journal of Elec Materi 39 (2010) 124–131.

[22] C.D. Breach, F.W. Wulff, A brief review of selected aspects of the materials science of ball bonding, Microelectron. Reliab. 50 (2010) 1–20.

[23] H. Xu, C. Liu, V.V. Silberschmidt, S.S. Pramana, T.J. White, Z. Chen, A re-examination of the mechanism of thermosonic copper ball bonding on aluminium metallization pads, Scripta Materialia 61 (2009) 165–168.

[24] S. Murali, N. Srikanth, C.J. Vath, An analysis of intermetallics formation of gold and copper ball bonding on thermal aging, Mater. Res. Bull. 38 (2003) 637–646.
[25] C.J. Hang, C.Q. Wang, M. Mayer, Y.H. Tian, Y. Zhou, H.H. Wang, Growth behavior of Cu/Al intermetallic compounds and cracks in copper ball bonds during isothermal aging, Microelectron. Reliab. 48 (2008) 416–424.
[26] C.D. Breach, F. Wulff, New observations on intermetallic compound formation in gold ball bonds, Microelectron. Reliab. 44 (2004) 973–981.
[27] A. Lassnig, R. Pelzer, C. Gammer, G. Khatibi, Role of intermetallics on the mechanical fatigue behavior of Cu–Al ball bond interfaces, Journal of Alloys and Compounds 646 (2015) 803–809.
[28] C.-L. Chuang, J.-N. Aoh, R.-F. Din, Oxidation of copper pads and its influence on the quality of Au/Cu bonds during thermosonic wire bonding process, Microelectron. Reliab. 46 (2006) 449–458.
[29] H.M. Ho, W. Lam, S. Stoukatch, P. Ratchev, C.J. Vath, E. Beyne, Direct gold and copper wires bonding on copper, Microelectron. Reliab. 43 (2003) 913–923.
[30] J.-N. Aoh, C.-L. Chuang, Thermosonic bonding of gold wire onto a copper pad with titanium thin-film deposition, Journal of Elec Materi 33 (2004) 290–299.
[31] S. Hymes, S.P. Murarka, C. Shepard, W.A. Lanford, Passivation of copper by silicide formation in dilute silane, J. Appl. Phys. 71 (1992) 4623.
[32] S. Hymes, K.S. Kumar, S.P. Murarka, P.J. Ding, W. Wang, W.A. Lanford, Thermal stability of copper silicide passivation layers in copper-based multilevel interconnects, J. Appl. Phys. 83 (1998) 4507–4512.
[33] C.M. Whelan, M. Kinsella, L. Carbonell, H. Meng Ho, K. Maex, Corrosion inhibition by self-assembled monolayers for enhanced wire bonding on Cu surfaces, Microelectron. Eng. 70 (2003) 551–557.
[34] Y.-R. Jeng, C.-M. Wang, S.-M. Chiu, C.-Y. Cheng, A Novel Method for Enabling the Thermosonic Wire Bonding of Gold Wire onto Chips with Copper Interconnects, Electrochem. Solid-State Lett. 7 (2004) G335.
[35] C.J. Hang, C.Q. Wang, Y.H. Tian, M. Mayer, Y. Zhou, Microstructural study of copper free air balls in thermosonic wire bonding, Microelectron. Eng. 85 (2008) 1815–1819.
[36] N. Hansen, Hall–Petch relation and boundary strengthening, Scripta Materialia 51 (2004) 801–806.
[37] C.S. Tan, D.F. Lim, X.F. Ang, J. Wei, K.C. Leong, Low temperature CuCu thermo-compression bonding with temporary passivation of self-assembled monolayer and its bond strength enhancement, Microelectron. Reliab. 52 (2012) 321–324.
[38] H. Derin, K. Kantarli, Optical characterization of thin thermal oxide films on copper by ellipsometry, Appl. Phys. A 75 (2002) 391–395.
[39] N. Cabrera, N.F. Mott, Theory of the oxidation of metals, Rep. Prog. Phys. 12 (1949) 163–184.
[40] J.C. Yang, B. Kolasa, J.M. Gibson, M. Yeadon, Self-limiting oxidation of copper, Appl. Phys. Lett. 73 (1998) 2841.
[41] C. Zhong, Y. Jiang, D. Sun, J. Gong, B. Deng, S. Cao, J. Li, Oxidation Kinetics of Nanoscale Copper Thin Films at Low Temperature Characterized by Sheet Resistance and Optical Transmittance, Chinese Journal of Physics 47 (2009) 253–260.
[42] S. Ghosh, D. Avasthi, P. Shah, V. Ganesan, A. Gupta, D. Sarangi, R. Bhattacharya, W. Assmann, Deposition of thin films of different oxides of copper by RF reactive sputtering and their characterization, Vacuum 57 (2000) 377–385.
[43] M. Honkanen, M. Vippola, T. Lepistö, Low temperature oxidation of copper alloys—AEM and AFM characterization, J Mater Sci 42 (2007) 4684–4691.
[44] B. Lefez, K. Kartouni, M. Lenglet, D. Rönnow, C.G. Ribbing, Application of reflectance spectrophotometry to the study of copper (I) oxides (Cu2O and Cu3O2) on metallic substrate, Surface and Interface Analysis 22 (1994) 451–455.
[45] M. Lenglet, K. Kartouni, J. Machefert, J.M. Claude, P. Steinmetz, E. Beauprez, J. Heinrich, N. Celati, Low temperature oxidation of copper: The formation of CuO, Mater. Res. Bull. 30 (1995) 393–403.
[46] L.D. Cocke, R. Schennach, A.M. Hossain, D.E. Mencer, H. McWhinney, J.R. Parga, M. Kesmez, J.A.G. Gomes, M.Y.A. Mollah, D.L. Cocke, M.A. Hossain, J. Gomes, M. Mollah, The low-

temperature thermal oxidation of copper, Cu3O2, and its influence on past and future studies, Vacuum 79 (2005) 71–83.
[47] D.E. Mencer, M.A. Hossain, R. Schennach, T. Grady, H. McWhinney, J. Gomes, M. Kesmez, J.R. Parga, T.L. Barr, D.L. Cocke, On the surface analysis of copper oxides: the difficulty in detecting Cu3O2, Vacuum 77 (2004) 27–35.
[48] K. Santra, C.K. Sarkar, M.K. Mukherjee, B. Ghosh, Copper oxide thin films grown by plasma evaporation method, Thin Solid Films 213 (1992) 226–229.
[49] M. Nair, L. Guerrero, O.L. Arenas, P. Nair, Chemically deposited copper oxide thin films: structural, optical and electrical characteristics, Appl. Surf. Sci. 150 (1999) 143–151.
[50] A. Musa, T. Akomolafe, M. Carter, Production of cuprous oxide, a solar cell material, by thermal oxidation and a study of its physical and electrical properties, Sol. Energy Mater. Sol. Cells 51 (1998) 305–316.
[51] Y. Abdu, A.O. Musa, Copper (I) Oxide (Cu2O) based Solar Cells - A Review, Bayero Journal of Pure and Applied Sciences 2 (2009) 8–12.
[52] A. Parretta, M.K. Jayaraj, A. Di Nocera, S. Loreti, L. Quercia, A. Agati, Electrical and Optical Properties of Copper Oxide Films Prepared by Reactive RF Magnetron Sputtering, Phys. Stat. Sol. (a) 155 (1996) 399–404.
[53] J.J. Diaz Leon, D.M. Fryauf, R.D. Cormia, M.-X.M. Zhang, K. Samuels, R.S. Williams, N.P. Kobayashi, Reflectometry-Ellipsometry Reveals Thickness, Growth Rate, and Phase Composition in Oxidation of Copper, ACS applied materials & interfaces 8 (2016) 22337–22344.
[54] P. Ratchev, S. Stoukatch, B. Swinnen, Mechanical reliability of Au and Cu wire bonds to Al, Ni/Au and Ni/Pd/Au capped Cu bond pads, Microelectron. Reliab. 46 (2006) 1315–1325.
[55] J. Li, J.W. Mayer, E.G. Colgan, Oxidation and protection in copper and copper alloy thin films, J. Appl. Phys. 70 (1991) 2820–2827.
[56] K. Choy, Chemical vapour deposition of coatings, Progress in Materials Science 48 (2003) 57–170.
[57] M.L. Chang, L.C. Wang, H.C. Lin, M.J. Chen, K.M. Lin, Investigation of defects in ultra-thin Al2O3 films deposited on pure copper by the atomic layer deposition technique, Applied Surface Science 359 (2015) 533–542.
[58] S. Mirhashemihaghighi, J. Światowska, V. Maurice, A. Seyeux, L.H. Klein, E. Salmi, M. Ritala, P. Marcus, The role of surface preparation in corrosion protection of copper with nanometer-thick ALD alumina coatings, Applied Surface Science 387 (2016) 1054–1061.
[59] K. Kukli, E. Salmi, T. Jõgiaas, R. Zabels, M. Schuisky, J. Westlinder, K. Mizohata, M. Ritala, M. Leskelä, Atomic layer deposition of aluminum oxide on modified steel substrates, Surf. Coat. Technol. 304 (2016) 1–8.
[60] N.T. Kirkland, T. Schiller, N. Medhekar, N. Birbilis, Exploring graphene as a corrosion protection barrier, Corros. Sci. 56 (2012) 1–4.
[61] R.K. Singh Raman, P. Chakraborty Banerjee, D.E. Lobo, H. Gullapalli, M. Sumandasa, A. Kumar, L. Choudhary, R. Tkacz, P.M. Ajayan, M. Majumder, Protecting copper from electrochemical degradation by graphene coating, Carbon 50 (2012) 4040–4045.
[62] S. Chen, L. Brown, M. Levendorf, W. Cai, S.-Y. Ju, J. Edgeworth, X. Li, C.W. Magnuson, A. Velamakanni, R.D. Piner, J. Kang, J. Park, R.S. Ruoff, Oxidation resistance of graphene-coated Cu and Cu/Ni alloy, ACS nano 5 (2011) 1321–1327.
[63] D. Prasai, J.C. Tuberquia, R.R. Harl, G.K. Jennings, B.R. Rogers, K.I. Bolotin, Graphene: corrosion-inhibiting coating, ACS nano 6 (2012) 1102–1108.
[64] D. Berman, S.A. Deshmukh, S.K.R.S. Sankaranarayanan, A. Erdemir, A.V. Sumant, Extraordinary Macroscale Wear Resistance of One Atom Thick Graphene Layer, Adv. Funct. Mater. 24 (2014) 6640–6646.
[65] J. Hu, Y. Ji, Y. Shi, F. Hui, H. Duan, M. Lanza, A Review on the use of Graphene as a Protective Coating against Corrosion, Ann. J. Materials Sci. Eng. 1 (2014) 16.
[66] Stokroos, Kalicharan, van der Want, Jongebloed, A comparative study of thin coatings of Au/Pd, Pt and Cr produced by magnetron sputtering for FE-SEM, J. Microsc. 189 (1998) 79–89.
[67] S. Zhang, X. Lam Bui, Y. Fu, Magnetron sputtered hard a-C coatings of very high toughness, Surf. Coat. Technol. 167 (2003) 137–142.
[68] D.A. Hutt, C. Liu, Oxidation protection of copper surfaces using self-assembled monolayers of octadecanethiol, Appl. Surf. Sci. 252 (2005) 400–411.

[69] P.E. Laibinis, G.M. Whitesides, Self-assembled monolayers of n-alkanethiolates on copper are barrier films that protect the metal against oxidation by air, J. Am. Chem. Soc. 114 (1992) 9022–9028.
[70] B.V. Appa Rao, Self-assembled 1-octadecyl-1H-1,2,4-triazole films on copper for corrosion protection, Prog. Org. Coat. 77 (2014) 202–212.
[71] G. Rajkumar, M.G. Sethuraman, Corrosion protection ability of self-assembled monolayer of 3-amino-5-mercapto-1,2,4-triazole on copper electrode, Thin Solid Films 562 (2014) 32–36.
[72] B. Balamurugan, B.R. Mehta, Surface-modified CuO layer in size-stabilized single-phase Cu2O nanoparticles, Appl. Phys. Lett. 79 (2001) 3176–3178.
[73] A. Njeh, T. Wieder, H. Fuess, Reflectometry studies of the oxidation kinetics of thin copper films, Surf. Interface Anal. 33 (2002) 626–628.
[74] G. Papadimitropoulos, N. Vourdas, V.E. Vamvakas, D. Davazoglou, Deposition and characterization of copper oxide thin films, J. Phys.: Conf. Ser. 10 (2005) 182–185.
[75] K. Akimoto, S. Ishizuka, M. Yanagita, Y. Nawa, G.K. Paul, T. Sakurai, Thin film deposition of Cu2O and application for solar cells, Solar Energy 80 (2006) 715–722.
[76] S. Han, H.-Y. Chen, L.-T. Kuo, C.-H. Tsai, Characterization of cuprous oxide films prepared by post-annealing of cupric oxide using an atmospheric nitrogen pressure plasma torch, Thin Solid Films 517 (2008) 1195–1199.
[77] R.M. Johan, M.S. Suan, N.L. Hawari, H.A. Ching, Annealing Effects on the Properties of Copper Oxide Thin Films Prepared by Chemical Deposition, International Journal of Electrochemical Science 6 (2011) 6094–6104.
[78] T. Iivonen, J. Hämäläinen, B. Marchand, K. Mizohata, M. Mattinen, G. Popov, J. Kim, R.A. Fischer, M. Leskelä, Low-temperature atomic layer deposition of copper(II) oxide thin films, Journal of Vacuum Science & Technology A: Vacuum, Surfaces, and Films 34 (2016) 01A109.
[79] İ.Y. Erdoğan, Ö. Güllü, Optical and structural properties of CuO nanofilm: Its diode application, Journal of Alloys and Compounds 492 (2010) 378–383.
[80] User, I. Kyriakou, D. Emfietzoglou, A. Nojeh, M. Moscovitch, Monte Carlo study of electron-beam penetration and backscattering in multi-walled carbon nanotube materials: The effect of different scattering models, J. Appl. Phys. 113 (2013) 84303.
[81] Ritchie, Nicholas W. M., A new Monte Carlo application for complex sample geometries, Surf. Interface Anal. 37 (2005) 1006–1011.
[82] A.B. Lim, A.C. Chang, O. Yauw, B. Chylak, C.L. Gan, Z. Chen, Ultra-fine pitch palladium-coated copper wire bonding: Effect of bonding parameters, Microelectron. Reliab. (2014).
[83] J. Lukose, V. Kulal, A. Bankapur, S.D. George, S. Chidangil, R.K. Sinha, Raman spectroscopy and surface wetting of self-assembled monolayer (SAM) of 1-octanethiol and 1,10-decanedithiol, Indian J Phys 90 (2016) 943–949.
[84] J.T. Chen, F. Zhang, J. Wang, G.A. Zhang, B.B. Miao, X.Y. Fan, D. Yan, P.X. Yan, CuO nanowires synthesized by thermal oxidation route, Journal of Alloys and Compounds 454 (2008) 268–273.
[85] V. Figueiredo, E. Elangovan, G. Gonçalves, P. Barquinha, L. Pereira, N. Franco, E. Alves, R. Martins, E. Fortunato, Effect of post-annealing on the properties of copper oxide thin films obtained from the oxidation of evaporated metallic copper, Appl. Surf. Sci. 254 (2008) 3949–3954.
[86] W. Melitz, J. Shen, A.C. Kummel, S. Lee, Kelvin probe force microscopy and its application, Surf. Sci. Rep. 66 (2011) 1–27.
[87] H.O. Jacobs, H.F. Knapp, S. Müller, A. Stemmer, Surface potential mapping: A qualitative material contrast in SPM, Ultramicroscopy 69 (1997) 39–49.
[88] B. Moores, F. Hane, L. Eng, Z. Leonenko, Kelvin probe force microscopy in application to biomolecular films: Frequency modulation, amplitude modulation, and lift mode, Ultramicroscopy 110 (2010) 708–711.
[89] T. Xu, S. Venkatesan, D. Galipeau, Q. Qiao, Study of polymer/ZnO nanostructure interfaces by Kelvin probe force microscopy, Sol. Energy Mater. Sol. Cells 108 (2013) 246–251.
[90] L. Kou, Y.J. Li, T. Kamijyo, Y. Naitoh, Y. Sugawara, Investigation of the surface potential of TiO2 (110) by frequency-modulation Kelvin probe force microscopy, Nanotechnology 27 (2016) 505704.
[91] H. Sugimura, Y. Ishida, K. Hayashi, O. Takai, N. Nakagiri, Potential shielding by the surface water layer in Kelvin probe force microscopy, Appl. Phys. Lett. 80 (2002) 1459.

[92] R. Chintala, P. Eyben, S. Armini, A. Maestre Caro, J. Loyo, Y. Sun, W. Vandervorst, Electrical properties of amino SAM layers studied with conductive AFM, Eur. Polym. J. 49 (2013) 1952–1956.

[93] A. Vecchiola, P. Chrétien, S. Delprat, K. Bouzehouane, O. Schneegans, P. Seneor, R. Mattana, S. Tatay, B. Geffroy, Y. Bonnassieux, D. Mencaraglia, F. Houzé, Wide range local resistance imaging on fragile materials by conducting probe atomic force microscopy in intermittent contact mode, Appl. Phys. Lett. 108 (2016) 243101.

[94] S. Weber, Electrical scanning probe microscopy on organic optoelectronic structures. Dissertation, Mainz, 2010.

[95] G. Binnig, C.F. Quate, Atomic Force Microscope, Phys. Rev. Lett. 56 (1986) 930–933.

[96] B. Bhushan, Springer Handbook of Nanotechnology, 2nd ed., Springer Berlin Heidelberg, Berlin, Heidelberg, 2007.

[97] A.L. Weisenhorn, P.K. Hansma, T.R. Albrecht, C.F. Quate, Forces in atomic force microscopy in air and water, Appl. Phys. Lett. 54 (1989) 2651.

[98] B. Pittenger, N. Erina, C. Su, Quantitative Mechanical Property Mapping at the Nanoscale with PeakForce QNM, Bruker Appl. Note 128 (2012) 1–12.

[99] B. Bhushan, H. Fuchs, M. Tomitori, A.M. Gigler, O. Marti, Applied scanning probe methods IX // Quantitative Measurement of Materials Properties with the (Digital) Pulsed Force Mode: Characterization, Springer, Berlin, New York, 2008.

[100] H. Schillers, I. Medalsy, S. Hu, A.L. Slade, J.E. Shaw, PeakForce Tapping resolves individual microvilli on living cells, J. Mol. Recognit. 29 (2016).

[101] J. Adamcik, A. Berquand, R. Mezzenga, Single-step direct measurement of amyloid fibrils stiffness by peak force quantitative nanomechanical atomic force microscopy, Appl. Phys. Lett. 98 (2011) 193701.

[102] M. Nonnenmacher, M.P. O'Boyle, H.K. Wickramasinghe, Kelvin probe force microscopy, Appl. Phys. Lett. 58 (1991) 2921.

[103] R. Shikler, T. Meoded, N. Fried, B. Mishori, Y. Rosenwaks, Two-dimensional surface band structure of operating light emitting devices, J. Appl. Phys. 86 (1999) 107.

[104] T. Glatzel, S. Sadewasser, M. Lux-Steiner, Amplitude or frequency modulation-detection in Kelvin probe force microscopy, Applied Surface Science 210 (2003) 84–89.

[105] S. Kitamura, M. Iwatsuki, High-resolution imaging of contact potential difference with ultrahigh vacuum noncontact atomic force microscope, Appl. Phys. Lett. 72 (1998) 3154.

[106] C. Li, S. Minne, Y. Hu, J. Ma, J. He, H. Mittel, V. Kelly, N. Erina, S. Guo, T. Mueller, PeakForce Kelvin Probe Force Microscopy, Bruker Appl. Note 140 (2013) 1–14.

[107] V. de Renzi, R. Rousseau, D. Marchetto, R. Biagi, S. Scandolo, U. Del Pennino, Metal work-function changes induced by organic adsorbates, Phys. Rev. Lett. 95 (2005) 46804.

[108] M. Korte, S. Akari, H. Kühn, N. Baghdadli, H. Möhwald, G.S. Luengo, Distribution and Localization of Hydrophobic and Ionic Chemical Groups at the Surface of Bleached Human Hair Fibers, Langmuir (2014).

[109] M. Schneider, M. Zhu, G. Papastavrou, S. Akari, H. Möhwald, Chemical Pulsed-Force Microscopy of Single Polyethyleneimine Molecules in Aqueous Solution, Langmuir 18 (2002) 602–606.

[110] S. Akari, D. Horn, H. Keller, W. Schrepp, Chemical imaging by scanning force microscopy, Adv. Mater. 7 (1995) 549–551.

[111] A. Noy, D.V. Vezenov, C.M. Lieber, CHEMICAL FORCE MICROSCOPY, Annu. Rev. Mater. Sci. 27 (1997) 381–421.

[112] G. Papastavrou, S. Akari, Specific detection of interactions between uncharged surfaces in different solvents, Nanotechnology 10 (1999) 453–457.

[113] G. Papastavrou, S. Akari, H. Möhwald, Interactions between hydrophilic and hydrophobic surfaces on microscopic scale and the influence of air bubbles as observed by scanning force microscopy in aqueous and alcoholic mediums, Europhys. Lett. 52 (2000) 551–556.

[114] C. Prastani, M. Nanu, D.E. Nanu, J.K. Rath, R.E. Schropp, Synthesis and conductivity mapping of SnS quantum dots for photovoltaic applications, Mater. Sci. Eng., B 178 (2013) 656–659.

[115] A. Vetushka, T. Itoh, Y. Nakanishi, A. Fejfar, S. Nonomura, M. Ledinský, J. Kočka, Conductive atomic force microscopy on carbon nanowalls, J. Non-Cryst. Solids 358 (2012) 2545–2547.

[116] L. Sun, E. Bonaccurso, in: C.S. Kumar (Ed.), Surface Science Tools for Nanomaterials Characterization, Springer Berlin Heidelberg, Berlin, Heidelberg, 2015, pp. 199–225.
[117] Y. Song, B. Bhushan, Atomic force microscopy dynamic modes, J. Phys.: Condens. Matter 20 (2008) 225012.
[118] D. McMullan, Scanning electron microscopy 1928-1965, Scanning 17 (1995) 175–185.
[119] S. NISHIKAWA, S. KIKUCHI, Diffraction of Cathode Rays by Mica, Nature 121 (1928) 1019–1020.
[120] T. Maitland, S. Sitzman, in: W. Zhou, Z.L. Wang (Eds.), Scanning microscopy for nanotechnology: Techniques and applications / edited by Weilie Zhou and Zhong Lin Wang, Springer, New York, London, 2007, pp. 41–75.
[121] R.A. Schwarzer, D.P. Field, B.L. Adams, M. Kumar, A.J. Schwartz, in: A.J. Schwartz, M. Kumar, B.L. Adams, D.P. Field (Eds.), Electron Backscatter Diffraction in Materials Science, Springer US, Boston, MA, 2009, pp. 1–20.
[122] D. Chen, J.-C. Kuo, W.-T. Wu, Effect of microscopic parameters on EBSD spatial resolution, Ultramicroscopy 111 (2011) 1488–1494.
[123] L. England, S.T. Eng, C. Liew, H.H. Lim, Cu wire bond parameter optimization on various bond pad metallization and barrier layer material schemes, Microelectron. Reliab. 51 (2011) 81–87.
[124] A.J. Strandjord, S. Popelar, C. Jauernig, Interconnecting to aluminum- and copper-based semiconductors (electroless-nickel/gold for solder bumping and wire bonding), Microelectron. Reliab. 42 (2002) 265–283.
[125] J.F. Rohan, G. O'Riordan, J. Boardman, Selective electroless nickel deposition on copper as a final barrier/bonding layer material for microelectronics applications, Appl. Surf. Sci. 185 (2002) 289–297.
[126] X. Fan, T. Wang, Y. Cong, B. Zhang, J. Wang (Eds.), Oxidation Study of Copper Wire Bonding, ICEPT-HDP, 246-249, 2010.
[127] K. Amikura, T. Kimura, M. Hamada, N. Yokoyama, J. Miyazaki, Y. Yamada, Copper oxide particles produced by laser ablation in water, Appl. Surf. Sci. 254 (2008) 6976–6982.
[128] A. Brandl, Aufnahme der Oxidationskinetic von dünnen Kupferschichten auf Silizium-Scheiben mittels Raman-Spektroskopie. Diploma Thesis in German, 2009.
[129] L.C. Yung, C.C. Fei, J.S. Mandeep, N. Amin, K.W. Lai, Bulk substrate porosity verification by applying Monte Carlo modeling and Castaing's formula using energy-dispersive x-rays, J. Electron. Imaging 24 (2015) 61105.
[130] B. Lefez, R. Souchet, K. Kartouni, M. Lenglet, Infrared reflection study of CuO in thin oxide films, Thin Solid Films 268 (1995) 45–48.
[131] L. Liao, Z. Zhang, B. Yan, Z. Zheng, Q.L. Bao, T. Wu, C.M. Li, Z.X. Shen, J.X. Zhang, H. Gong, J.C. Li, T. Yu, Multifunctional CuO nanowire devices: p-type field effect transistors and CO gas sensors, Nanotechnology 20 (2009) 85203.
[132] W.-Y. Yang, S.-W. Rhee, Effect of electrode material on the resistance switching of Cu2O film, Appl. Phys. Lett. 91 (2007).
[133] A. Noy, C.H. Sanders, D.V. Vezenov, S.S. Wong, C.M. Lieber, Chemically-Sensitive Imaging in Tapping Mode by Chemical Force Microscopy, Langmuir 14 (1998) 1508–1511.
[134] L. Zitzler, S. Herminghaus, F. Mugele, Capillary forces in tapping mode atomic force microscopy, Phys. Rev. B 66 (2002).
[135] D.L. Sedin, K.L. Rowlen, Adhesion Forces Measured by Atomic Force Microscopy in Humid Air, Anal. Chem. 72 (2000) 2183–2189.
[136] F. Wang, L. Zhao, Y. Zhang, Z. Qiao, Simplified Aeroelastic Model for Fluid Structure Interaction between Microcantilever Sensors and Fluid Surroundings, PLoS ONE 10 (2015) e0123860.
[137] M. Minary-Jolandan, M.-F. Yu, Nanomechanical imaging of soft samples in liquid using atomic force microscopy, J. Appl. Phys. 114 (2013) 134313.
[138] J.V. Mendez-Mendez, M.T. Alonso-Rasgado, E.C. Faria, E.A. Flores-Johnson, R.D. Snook, Numerical study of the hydrodynamic drag force in atomic force microscopy measurements undertaken in fluids, Micron 66 (2014) 37–46.
[139] H. Janovjak, J. Struckmeier, D.J. Muller, Hydrodynamic effects in fast AFM single-molecule force measurements, Eur. Biophys. J. 34 (2005) 91–96.

[140] J. Alcaraz, L. Buscemi, M. Puig-de-Morales, J. Colchero, A. Baró, D. Navajas, Correction of Microrheological Measurements of Soft Samples with Atomic Force Microscopy for the Hydrodynamic Drag on the Cantilever, Langmuir 18 (2002) 716–721.
[141] R. Liu, M. Roman, G. Yang, Correction of the viscous drag induced errors in macromolecular manipulation experiments using atomic force microscope, Rev. Sci. Instrum. 81 (2010) 63703.
[142] K. Sarangapani, H. Torun, O. Finkler, C. Zhu, L. Degertekin, Membrane-based actuation for high-speed single molecule force spectroscopy studies using AFM, Eur. Biophys. J. 39 (2010) 1219–1227.
[143] M. Encinar, S. Casado, A. Calzado-Martin, P. Natale, A. San Paulo, M. Calleja, M. Velez, F. Monroy, I. Lopez-Montero, Nanomechanical properties of composite protein networks of erythroid membranes at lipid surfaces, Colloids Surf B Biointerfaces 149 (2017) 174–183.
[144] H. Bonakdari, A.A. Zinatizadeh, Influence of position and type of Doppler flow meters on flow-rate measurement in sewers using computational fluid dynamic, Flow Measurement and Instrumentation 22 (2011) 225–234.
[145] M. Mortensen, H.P. Langtangen, G.N. Wells, A FEniCS-based programming framework for modeling turbulent flow by the Reynolds-averaged Navier–Stokes equations, Adv. Water Resour. 34 (2011) 1082–1101.
[146] W. Jones, B. Launder, The prediction of laminarization with a two-equation model of turbulence, Int. J. Heat Mass Transfer 15 (1972) 301–314.
[147] Kokkoli, Zukoski, Effect of Solvents on Interactions between Hydrophobic Self-Assembled Monolayers, J. Colloid Interface Sci. 209 (1999) 60–65.
[148] M. Yaacobi, A. Ben-Naim, Hydrophobic interaction in water-ethanol mixtures, J. Solution Chem. 2 (1973) 425–443.
[149] B. González, N. Calvar, E. Gómez, Á. Domínguez, Density, dynamic viscosity, and derived properties of binary mixtures of methanol or ethanol with water, ethyl acetate, and methyl acetate at T=(293.15, 298.15, and 303.15)K, J. Chem. Thermodyn. 39 (2007) 1578–1588.
[150] Y. Lu, Q. Ren, T. Liu, S.L. Leung, V. Gau, J.C. Liao, C.L. Chan, P.K. Wong, Long-range electrothermal fluid motion in microfluidic systems, Int. J. Heat Mass Transfer 98 (2016) 341–349.
[151] M. Dizechi, E. Marschall, Viscosity of some binary and ternary liquid mixtures, J. Chem. Eng. Data 27 (1982) 358–363.
[152] Nanocraft Coating GmbH, http://www.nanocraft.de/, accessed 13 April 2015.
[153] Y.D. Park, D.H. Kim, Y. Jang, J.H. Cho, M. Hwang, H.S. Lee, J.A. Lim, K. Cho, Effect of side chain length on molecular ordering and field-effect mobility in poly(3-alkylthiophene) transistors, Org. Electron. 7 (2006) 514–520.
[154] Y.T. Tao, Structural comparison of self-assembled monolayers of n-alkanoic acids on the surfaces of silver, copper, and aluminum, J. Am. Chem. Soc. 115 (1993) 4350–4358.
[155] V.F. Drobny, L. Pulfrey, Properties of reactively-sputtered copper oxide thin films, Thin Solid Films 61 (1979) 89–98.
[156] J. Siegel, O. Lyutakov, V. Rybka, Z. Kolska, V. Svorcik, Properties of gold nanostructures sputtered on glass, Nanoscale Res. Lett. 6 (2011) 96.
[157] Z.-Y. Qiu, C. Chen, X.-M. Wang, I.-S. Lee, Advances in the surface modification techniques of bone-related implants for last 10 years, Regen. Biomater. 1 (2014) 67–79.
[158] J.-L. Chen, Y.-C. Lin, A new approach in free air ball formation process parameters analysis, IEEE Trans. Electron. Packag. Manufact. 23 (2000) 116–122.
[159] S.-J. Hong, J.-S. Cho, J.-T. Moon, J. Lee, in: Advances in Electronic Materials and Packaging 2001, 19-22 Nov. 2001, pp. 52–55.
[160] Z.W. Zhong, H.M. Ho, Y.C. Tan, W.C. Tan, H.M. Goh, B.H. Toh, J. Tan, Study of factors affecting the hardness of ball bonds in copper wire bonding, Microelectron. Eng. 84 (2007) 368–374.
[161] F.-Y. Hung, T.-S. Lui, L.-H. Chen, H.-W. Hsueh, An investigation into the crystallization and electric flame-off characteristics of 20µm copper wires, Microelectron. Reliab. 51 (2011) 21–24.
[162] C.J. Hang, W.H. Song, I. Lum, M. Mayer, Y. Zhou, C.Q. Wang, J.T. Moon, J. Persic, Effect of electronic flame off parameters on copper bonding wire: Free-air ball deformability, heat affected zone length, heat affected zone breaking force, Microelectron. Eng. 86 (2009) 2094–2103.

[163] A. Pequegnat, C.J. Hang, M. Mayer, Y. Zhou, J.T. Moon, J. Persic, Effect of EFO parameters on Cu FAB hardness and work hardening in thermosonic wire bonding, J Mater Sci: Mater Electron 20 (2009) 1144–1149.

[164] S. Mrowec, A. Stokłosa, Oxidation of copper at high temperatures, Oxid Met 3 (1971) 291–311.

[165] K. Mimura, J.-W. Lim, M. Isshiki, Y. Zhu, Q. Jiang, Brief review of oxidation kinetics of copper at 350 °C to 1050 °C, Metall and Mat Trans A 37 (2006) 1231–1237.

[166] S.I. Wright, M.M. Nowell, D.P. Field, A review of strain analysis using electron backscatter diffraction, Microscopy and microanalysis the official journal of Microscopy Society of America, Microbeam Analysis Society, Microscopical Society of Canada 17 (2011) 316–329.

[167] C. Moussa, M. Bernacki, R. Besnard, N. Bozzolo, About quantitative EBSD analysis of deformation and recovery substructures in pure Tantalum, IOP Conf. Ser.: Mater. Sci. Eng. 89 (2015) 12038.

[168] I.M. Cohen, L.J. Huang, P.S. Ayyaswamy, Melting and solidification of thin wires, Int. J. Heat Mass Transfer 38 (1995) 1647–1659.

[169] L.J. Huang, P.S. Ayyaswamy, I.M. Cohen, Melting and solidification of thin wires, Int. J. Heat Mass Transfer 38 (1995) 1637–1645.